The University Of Sheffield.

CFD analysis of CO_2- and H_2O-diluted combustion in gas turbines

Andrea De Santis

A thesis submitted in partial fulfilment of the requirements for the degree of Doctor of Philosophy

The University of Sheffield

Department of Mechanical Engineering

December 2016

Acknowledgements

Throughout this PhD project I have received invaluable support and help from a great number of people. Firstly, I would like to express my gratitude to my supervisors Prof. Mohamed Pourkashanian and Prof. D. B. Ingham for their precious guidance and advice. I also want to acknowledge the support of Dr. Alessandro Pranzitelli and Dr. Alastair G. Clements for the constant motivation they provided through their advices (and criticisms!).

The useful discussions with my colleagues Kate, Eirini, Tom, Jujar, Oscar, Jaime, Johnnie, Poly and many others are gratefully acknowledged. Many of them have been good friends outside of the office as well, to celebrate during the good times and to cheer me up during the inevitable hardships of this PhD. Their support has been as valuable to me as the one provided by my long-standing friends back in Italy.

I also want to express my gratitude to my family for their love and unconditional support.

Last but not least, thank you to the love of my life, Chiara, just for being the person you are and for being there every time I was in need of encouragement.

The financial support from the GasFACTS project (ESPRC grant reference EP/J020788/1) is acknowledged.

Distribution of work and publications

The candidate confirms that the work contained in this thesis is his own, with the exceptions indicated below:

- The implementation of the SNB-CK model in Cantera described in Section 2.3 has been carried out by Dr. Alastair G. Clements.
- Credits for the experimental data employed to set-up and validate the numerical calculations have been given in Chapter 3 by citing the relevant publications.
- The process modelling calculations employed to obtain the boundary conditions reported in Table 3.6 have been performed by Dr. Maria Elena Diego de Paz and Usman Ali.

The work described in Chapter 5 has led to the following journal publication:

- A. De Santis, A. G. Clements, A. Pranzitelli, D. B. Ingham and M. Pourkashanian. LES of a partially-premixed swirling flame: impact of subgrid-scale stress models and mesh resolution. *Combustion and Flame*, under review.

The work described in Chapter 6 has been included in the following journal publication and international conferences:

- A. De Santis, D. B. Ingham, L. Ma, M. Pourkashanian. CFD analysis of exhaust gas recirculation in micro gas turbine combustor for CO_2 capture. *Fuel*, 173:146-154, 2016.
- T. Best, K. N. Finney, A. De Santis, D. B. Ingham, M. Pourkashanian. Exhaust gas recirculation and selective exhaust gas recirculation on a micro gas turbine for enhanced CO_2 capture performance. In *Proceedings of the 8th ETN International Gas Turbine Conference*, 2016.
- K. N. Finney, A. De Santis, A. G. Clements, T. Best, M. Pourkashanian. CFD analysis of selective exhaust gas recirculation in a micro gas turbine for enchanced CO_2 capture performance. *2017 ASME Turbo Expo*, abstract accepted.

Abstract

With the increasing evidence of the potential disastrous consequences arising from global warming, there is a need to reduce greenhouse gas emissions, and gas-fired power generation represents an attractive option due to its low carbon intensity. Nevertheless, gas is not a zero-emission fuel and therefore it is necessary to control the emissions associated with its usage.

Among the carbon capture techniques suitable for gas-fired generation, post-combustion is regarded as the most feasible in the short-term. The additional costs associated with the CO_2 capture process can be reduced by employing modified cycle concepts such as EGR and STIG, which are characterised by a diluted combustion environment. The development of accurate numerical models for the combustion process in industrial devices under diluted conditions can be very useful in assessing the impact of dilution on the combustion process, and represents the main goal of the present work.

Firstly, the impact of carbon dioxide and steam dilution on natural gas combustion has been assessed by means of detailed simulations of simple unidimensional laminar flames. It has been found that even the relatively low dilutions levels typical of EGR and STIG cycles have a significant impact on the combustion process. Also, the diluting species participate directly in the combustion chemistry, and therefore there is a need to include detailed chemistry and finite rate-effects in a CFD model for realistic configurations.

In this respect, the suitability of the RANS and LES FGM/presumed-PDF approach for the modelling of swirling partially-premixed flames has been assessed. The performance of different turbulence models with different levels of mesh refinement have been assessed against in-flame measurements in a lab-scale burner and guidelines for the CFD modelling of industrial devices have been inferred.

Finally, the previous findings have been employed to develop a complete CFD model for an industrial MGT combustor, which has been investigated under both air-fired and diluted operation. The numerical results have compared with the available experimental data. It has been concluded that the model is able to predict the impact of dilution on the heat release, flame stabilisation, flow-field and pollutant emissions

Contents

List of Figures

List of Tables

Nomenclature

B Pre-exponential factor (s^{-1})[1]

c Progress variable ($-$)

c Speed of light in the medium ($m\ s^{-1}$)

c_p Constant pressure specific heat ($J\ kg^{-1}\ K^{-1}$)

C Generic constant ($-$)

D Diffusion coefficient ($m^2\ s^{-1}$)

$\mathcal{D}$ SGS model differential operator ($-$)

Da Damköhler number ($-$)

E Activation energy (J)

F Body force ($N\ m^{-3}$)

g_{ij} Velocity gradient tensor (s^{-1})

h Specific enthalpy ($J\ kg^{-1}$)

h_t Specific total enthalpy ($J\ kg^{-1}$)

I Radiative intensity ($W\ m^{-2}\ sr^{-1}\ Hz^{-1}$)

k Thermal conductivity ($W\ m^{-1}\ K^{-1}$)

k Turbulent kinetic energy ($m^2\ s^{-2}$)

Ka Karlovitz number ($-$)

[1] For first-order reactions

k_B Boltzmann constant ($\mathrm{m^2\ kg\ s^{-2}K^{-1}}$)

L Flow length scale (m)

$\mathcal{L}$ Turbulent integral length scale (m)

ℓ Characteristic length (m)

Le Lewis number ($-$)

$\dot{m}$ Mass flow rate ($\mathrm{kg\ s^{-1}}$)

p Pressure (Pa)

P Probability density function ($-$)

Pr Prandtl number ($-$)

q Heat flux ($\mathrm{W\ m^{-2}}$)

r Radial coordinate (m)

$\mathbf{r}$ Position vector (m)

s Fuel split ratio ($-$)

s Path length (m)

s_L Laminar flame speed ($\mathrm{m\ s^{-1}}$)

s_T Turbulent flame speed ($\mathrm{m\ s^{-1}}$)

S Swirl number ($-$)

S_{ij} Strain rate tensor ($\mathrm{s^{-1}}$)

t Time (s)

T Temperature (K)

u Instantaneous velocity ($\mathrm{m\ s^{-1}}$)

u' Fluctuating velocity ($\mathrm{m\ s^{-1}}$)

U Mean velocity, axial velocity ($\mathrm{m\ s^{-1}}$)

$\mathcal{U}$ Velocity characteristic scale (m s^{-1})

V Volume (m^3)

W Molecular weight (kg $kmol^{-1}$)

W Tangential velocity (m s^{-1})

x Axial coordinate (m)

X_k Mole fraction of species k ($-$)

Y_k Mass fraction of species k ($-$)

z Axial coordinate (m)

Z Mixture fraction ($-$)

Greek letters

α Thermal diffusivity (m^2 s^{-1})

δ Dirac delta function ($-$)

δ_{ij} Kronecker delta ($-$)

Δ Filter width (m)

ϵ Turbulent kinetic energy dissipation rate (m^2 s^{-3})

η Wavenumber ($-$)

κ Absorption coefficient (m^{-1})

λ Wavelength (m)

μ Dynamic viscosity (N s m^{-2})

ν Kinematic viscosity (m^2 s^{-1})

ρ Density (kg m^{-3})

σ Schmidt number ($-$)

σ Stephen-Boltzmann constant (W m^{-2} K^{-4})

τ Characteristic time (s)

τ_{ij} Stress tensor ($m^2\ s^{-2}$)

ϕ Equivalence ratio, generic transported scalar ($-$)

χ Scalar dissipation rate (s^{-1})

ω Source term ($-$)

Subscripts

0 Energy-containing scales

η Komogorov scales

b Blackbody, burnt

c Chemical

eq Equilibrium

F Flame, fuel

oxi Oxidizer

st Stoichiometric

t Turbulent

u Unburnt

Acronyms

CCGT Combined Cycle Gas Turbine

CCS Carbon Capture and Storage

CFD Computational Fluid Dynamics

CHP Combined Heat and Power

CHT Conjugate Heat Transfer

CK Correlated-k

CNG Compressed Natural Gas

DLE Dry Low-Emissions

DNS Direct Numerical Simulation

EBU Eddy Break-Up

EDC Eddy Dissipation Concept

EGR Exhaust Gas Recirculation

FFT Fast Fourier Transform

FGM Flamelet Generated Manifold

FPI Flamelet Prolongated Instric (low dimensional manifold)

FSCK Full Spectrum Correlated-k

HRSG Heat Recovery Steam Generator

IRZ Inner Recirculation Zone

LBL Line-By-Line

LDV Laser Doppler Velocimetry

LES Large Eddy Simulation

LIF Laser Induced Fluorescence

MGT Micro Gas Turbine

ORZ Outer Recirculation Zone

PDF Probability Density Function

RANS Reynolds-averaged Navier-Stokes

RGT Recuperative Gas Turbine

RMS Root Mean Square

RSM Reynolds Stress Model

RTE Radiative Transfer Equation

RZ Recirculation Zone

S-EGR Selective Exhaust Gas Recirculation

SCGT Simple Cycle Gas Turbine

SGS Subgrid Scale Stress

SLFM Steady Laminar Flamelet Model

SNB Statistical Narrow Band

STIG Steam Injected Gas Turbine

UHC Unburned Hydrocarbon

WSGG Weighted-Sum of Grey Gases

Chapter 1

Introduction

Fossil fuels are expected to play a central role in meeting the growing power demand in the medium term, with gas becoming more and more important in the energy mix due to its lower carbon intensity compared to other fossil fuels. The coupling of gas-fired power generation with Carbon Capture and Storage (CCS) has the potential to reduce significantly the carbon dioxide emissions from power generation, thus assisting to meet the strict emissions limits necessary to mitigate the potentially disastrous consequences arising from anthropogenic greenhouse gases release in the atmosphere.

With a focus on the post-combustion capture techniques, the efficiency of the CO_2 capture process can be improved significantly by increasing the carbon dioxide concentration in the exhaust gases. This can be achieved by resorting to modified cycles solutions such as Exhaust Gas Recirculation (EGR) and Selective Exhaust Gas Recirculation (S-EGR). The Steam-Injected Gas Turbine (STIG) cycle also represents and attractive option to mitigate the energy penalty associated with the CO_2 capture process. All of these advanced cycles are characterised by an increased concentration of CO_2 and/or H_2O in the combustion environment with respect to traditional gas turbine operation, and this can have an impact on the combustion process itself as well as on the overall plant performance.

The aim of this work is the development of an accurate and reliable Computational Fluid Dynamics (CFD) model in order assess the impact of carbon dioxide and steam dilution on the combustion process in gas turbines. In addition to the typical challenges associated with the modelling of industrial combustion cham-

bers, e.g. the geometrical complexity of the devices, complex fluid dynamics phenomena, turbulence-chemistry interaction, etc., the presence of increased levels of CO_2 and H_2O in the combustor associated with EGR and STIG cycles has a significant impact on the combustion chemistry, heat transfer and flow field characteristics that has to be accounted for at the modelling stage.

In this chapter, the work carried out in the thesis is put in the framework of the current global energy outlook and the motivations behind the present study are presented. In Section 1.1, a description of the world energy demand, together with the concerns associated with global warming, is provided. A short introduction to power generation in gas turbines is given in Section 1.2 and in Section 1.3 a discussion on CCS with a focus on carbon capture techniques suitable for gas-fired power generation is carried out. Considerations on the peculiarities and challenges associated with the modelling of diluted combustion in gas turbines are discussed in Section 1.4 and the aims and objectives of the present work are presented in Section 1.5. Finally, a description of the thesis outline is provided in Section 1.6.

1.1 World energy demand and global warming

The world energy demand is expected to increase dramatically over the next few decades, with a predicted growth of 34% between 2014 and 2035 [1]. As reported in Figure 1.1, emerging economies will contribute more than 90% of the global energy growth, whilst the energy demand from OECD countries is expected not to vary significantly.

In this context, fossil fuels are forecast to play a major role in meeting the demand for cheap energy coming from developing countries, accounting for almost 80% of the primary energy in 2035, compared to a share equal to 86% in 2014 [1]. As shown in Figure 1.2, gas is the fossil fuel expected to experience the fastest growth in the medium term. Also, for non-fossil sources, renewables are predicted to be growing steadily, with their share increasing from the current 3% to 9% in 2035.

The massive reliance on fossil fuels usage depicted in Figure 1.1 is in stri-

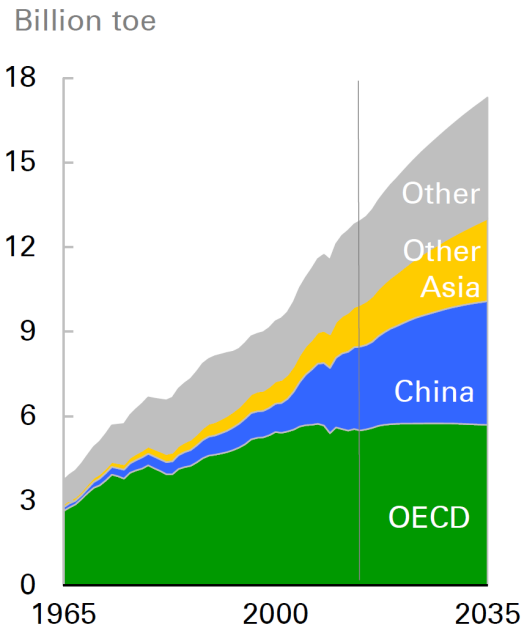

Figure 1.1: Global primary energy consumption (with forecast up to 2035) as reported in [1].

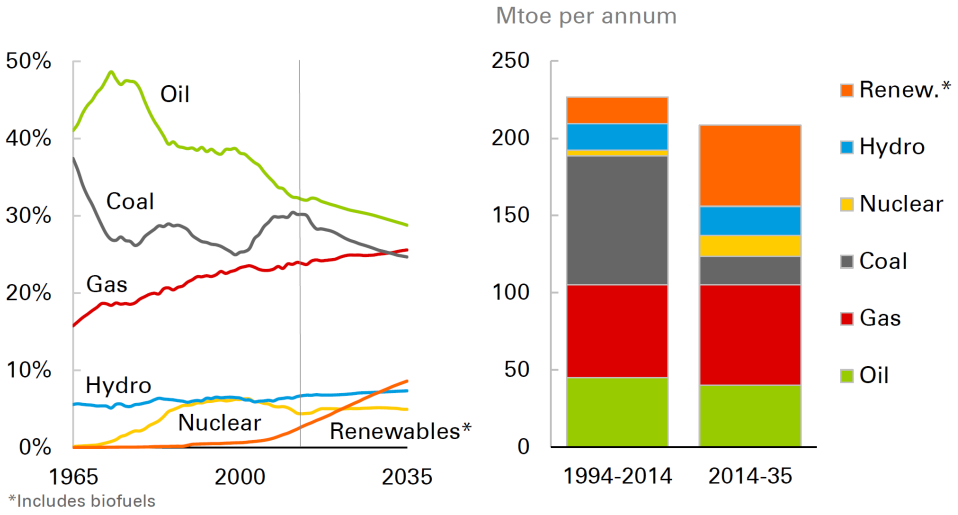

Figure 1.2: Shares of primary energy (left) and annual growth for different fuels according to [1].

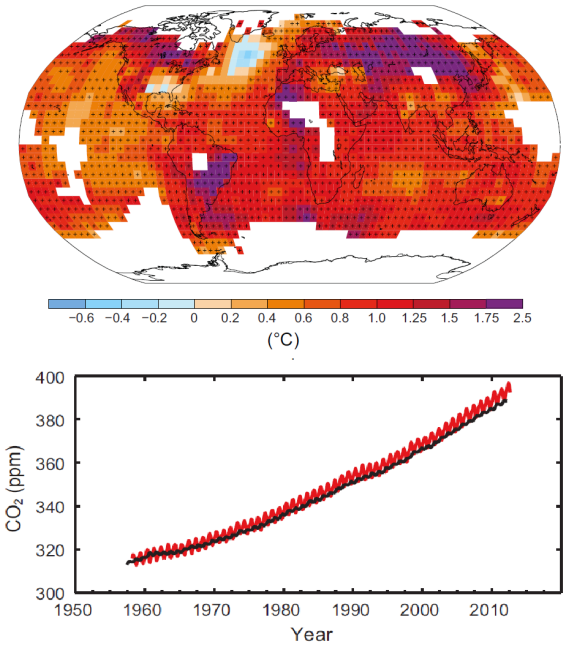

Figure 1.3: Observed surface temperature change from 1901 to 2012 (top) and measured atmospheric CO_2 concentration at two different locations [2].

dent contrast with the more and more stringent need to reduce greenhouse gases emissions. The necessity to reduce the release of greenhouse gases into the atmosphere is related to the need to limit the observed warming of the Earth's climate system known as global warming. An almost unanimous consent within the scientific community has been reached on the direct link between the observed global average surface temperature growth and the unprecedented levels of greenhouse gases [2] such as methane, nitrous oxide and carbon dioxide measured in the atmosphere (Figure 1.3). In particular, although it is characterised by a relatively small global warming potential with respect to other greenhouse gases, carbon dioxide is by far the greenhouse gas with the highest atmospheric concentration, which was equal to of 391 ppm in 2011, compared to 1803 ppb for methane and 324 ppb for nitrous oxide. Therefore, there is a stringent need to reduce global CO_2 emissions.

In order to avoid dangerous and potentially disruptive consequences arising from global warming, the limit of 2 °C in the rise of the global average surface temperature with respect to pre-industrial levels has been set by the scientific community [3] and accepted by policymakers [4].

The power generation sector accounts for more than half of the increase in the global primary energy demand, and currently generates more than two-thirds of the overall greenhouse gases emissions. The growing diffusion of low-carbon technologies and improvements in the efficiency of fossil fuel power plants are predicted to reduce the CO_2 emissions intensity of electricity generation from the 2011 overall value of 532 g_{CO_2}/kWh to 374 g_{CO_2}/kWh in 2035 [5]. Nevertheless, since fossil fuels are going to play a major role in the energy mix, it is of paramount important to control the emissions related to their usage.

Gas-fired power generation is less carbon intensive than coal, so it represents an attractive option for power generation in the current global energy scenario. Also, gas-fired power plants are less capital intensive than coal power plants, which makes them more attractive given the present uncertainties over future fossil fuel prices and energy policies. However, natural gas is not a carbon-free fuel. Within the 2 °C goal, by 2025 the average carbon dioxide emission intensity of global electricity generation will be below that of a gas-fired plant [6]. This means that, in a low-emission scenario, the only way to operate gas-fired plants is to equip many of them with carbon capture systems. Therefore, a gas plant with CCS can be considered as an attractive investment in the mid-term; IEA forecasts that by 2050 all gas plants providing base-load power will be fitted with CCS [5]. An overview on CCS and details on its application to gas-fired power plants are provided in the next sections.

1.2 Power generation in gas turbines

Gas turbine systems are a type of internal combustion engine. Depending on the nature of their application, gas turbine systems can be divided in two main categories, i.e. aero-propulsion and land-based gas turbines. With a focus on the latter, land-based gas turbines are mainly employed for power generation or direct-drive applications. This section provides a short introduction to the application of gas turbines to power generation. Even if the systems employed in today's gas-fired power plants are complex devices, a basic gas turbine consists of three main components [7]:

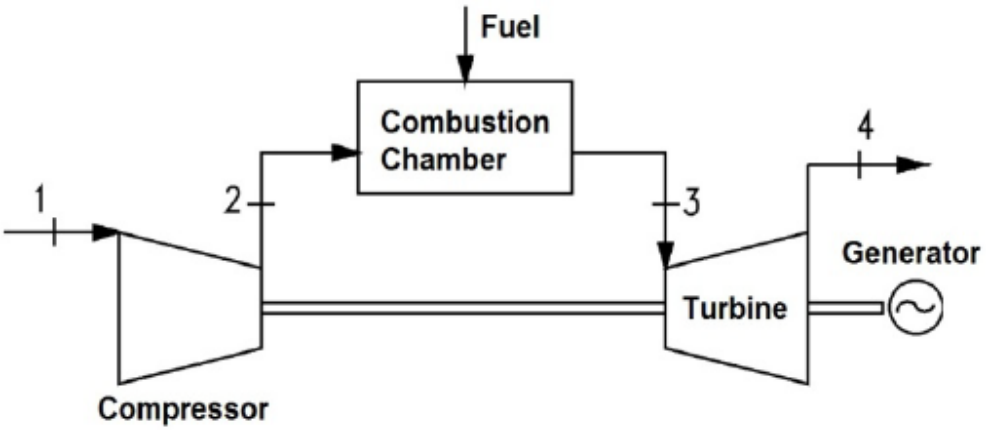

Figure 1.4: Schematic of a basic gas turbine.

- A compressor which is used to draw the working fluid (usually air) into the engine, pressurise it and feed it to the combustion chamber.
- A combustion section where a fuel stream is injected and mixed with the pressurised air coming from the compressor. The combustion process takes place in this section and a high pressure and temperature gas stream is produced.
- A turbine which is employed to expand the hot gases coming from the combustor. The turbine has the dual purpose of driving the compressor and to spin a generator in order to produce electric power.

The basic gas turbine system described above is referred to as Simple Cycle Gas Turbine (SCGT), for which a schematic is reported in Figure 1.4. The main factors affecting the efficiency of the SCGT are the efficiency of the single components and the firing temperature, which is defined as the temperature of the hot gases at the turbine inlet. The latter parameter is controlled by technological limits, i.e. by the maximum temperature that can be withstood by the blades of the turbine. Significant progresses have been made in this respect, with firing temperature rising from around 1000 K in the 1950s to above 1800 K in modern heavy-duty gas turbines [8].

Given the elevated firing temperature typical of modern systems, the exhaust gases at the turbine outlet are still characterised by a relatively high temperature, and therefore by a non negligible energy content which can be employed to

improve the efficiency of the system [7]. In the Recuperative Gas Turbine (RGT) the hot gases at the turbine outlet are employed to pre-heat the air downstream of the combustion section. In the Combined Cycle Gas Turbine (CCGT) the hot gases are employed to generate steam in a Heat Recovery Steam Generator (HRSG). The steam is then expanded in a steam turbine in order to increase the power output of system. In Combined Heat and Power (CHP) generation, the hot gases are used to produce high temperature water for industrial or heating applications. All of these modifications in the SCGT can result in a significant improvement in the overall efficiency of the system [8].

Regardless of the gas turbine application and specific configuration, environmental considerations are of paramount importance in the design of the system. In this respect, the combustor represents the critical component and the main pollutants that are of concerns for gas turbines are CO, NOx and smoke [8]. With the increasing need to reduce greenhouse gases emissions, there is also a growing requirement to control the amount of CO_2 released in the atmosphere by gas turbines, as will be detailed in the next section.

1.3 CCS and its application to gas turbines

CCS is a process consisting of the separation (capture) of carbon dioxide from a mixture of gases generated in industrial or power-generation processes, e.g. the flue gases of a power plant. This is followed by its compression to a liquid state and the transportation to a storage site where a long-term isolation from the atmosphere is achieved by the injection into suitable geological formations or for its reuse in industrial applications such as enhanced oil recovery.

CCS is widely recognised as an essential component in the portfolio of technologies necessary for substantially reducing carbon dioxide emissions. Other options include low-carbon technologies, such as nuclear and renewables, and energy efficiency.

There are multiple aspects contributing to the importance of CCS as an option for mitigating carbon dioxide emissions. Firstly, as fossil fuels are still expected to play a key role in the global energy market in the future, CCS offers a solution

for dealing with emissions from fossil fuel use. The present estimated reserves of fossil fuels, if combusted, would release in the atmosphere approximately 2860 Gt of CO_2 [6]. If the limit of 2 °C long term increase in temperature is to be satisfied, a cumulative total of 884 Gt of carbon dioxide should be emitted from the power sector up to the year 2050. This means that less than one-third of the global fossil fuel reserves can be actually consumed without the need for the substantial use of CCS technologies. It has been estimated that if CCS is not taken into consideration as an option in the energy sector, then the cost to meet the same emission limit is increased by about 40% [9]. This is because CCS is the only technology which is able to preserve the value of fossil fuel reserves and of the related infrastructures.

Finally, CCS can also be applied for reducing carbon dioxide emissions due to industrial sectors such as cement, iron and steel, chemicals and refining. For details about the application of CCS to such sectors refer to [10].

Despite the previous observations, the development of CCS technology is progressing quite slowly, and there is a need to progress CCS demonstration projects around the world. The Global CCS Institute has identified the following key points to enhance the development and the spreading of the technology [11]:

- Implementing policies that include long-term support to low-CO_2 technologies and strong market-based emission trading schemes.
- Enhancing short term support for demonstration projects.
- Dealing with remaining critical regulatory uncertainties.
- Providing significant funding support for CCS research and development.

The processes involving the capture of the carbon dioxide can be categorised, according to the modifications to the industrial process needed to achieve CO_2 separation [6], as follows:

- **Post-combustion capture**: Carbon dioxide is separated from the mixture of gases at the end of the combustion process, usually by employing a chemical separation technique.

- **Pre-combustion capture**: The fossil fuel is partially oxidized to produce syngas, which is then shifted to obtain a gas containing H_2 and CO_2. The carbon dioxide is separated before combustion takes place. This technology is applied in gaseous fuel and fertilizer production, as well as in power production.

- **Oxy-fuel combustion**: Pure oxygen is used as an oxidizer in combustion in place of air, giving rise to the production of a flue stream containing only carbon dioxide and water, which can be easily condensed by cooling. In this technology, there is no requirement for a specific CO_2 separation step, but the energy penalty is largely determined by the separation of the oxygen from air.

The application of CCS to electricity production yields an increase in the energy generation cost. This is largely related to the modification required to the standard process by the chosen capture technology and to the loss of efficiency arising from the CO_2 capture process [6]. Among the different carbon capture technologies suitable for gas turbines, oxy-fuel combustion is regarded as feasible in the medium term, mainly because of the need to develop a gas turbine able to operate with CO_2 instead of nitrogen as the major component of the working fluid. On the other hand, post-combustion separation is the one which is currently receiving the most attention due to its feasibility in the short term [12].

The additional costs associated with CCS can be reduced by improving the efficiency of the carbon capture process; in particular, post-combustion carbon capture application to a gas turbine is a challenging task due to the following reasons:

- Low carbon dioxide concentration in the exhaust gases, which results in an inefficient capture process.

- Elevated oxygen concentration in the flue gases, due to the lean combustion process typical of gas turbines, which can imply solvent degradation due to oxidation.

- High flue gases flowrate (again due to the lean combustion process) which results in the need of large capture plants and thus in a cost increase.

In order to reduce the cost of the post-combustion carbon capture process, various advanced cycle solutions for gas turbine power generation have been proposed. EGR and S-EGR represent suitable solutions, already tested in industrial applications (see, for instance, [13] and [14]). The higher carbon dioxide concentration in the exhaust gas observed with EGR and S-EGR with respect to conventional air-firing results in a significant increase in the efficiency of the post-combustion CO_2 capture process [15]. EGR consists in the recirculation of a portion of the exhaust gases back into the inlet of the gas turbine. In S-EGR, the exhaust gases are passed through a separation system in order to separate carbon dioxide from other species and recirculate only the former into the gas turbine. The portion of exhaust gases recirculated into the system is defined in terms of the EGR ratio, R

$$R = \frac{\dot{m}_{rec}}{\dot{m}_{air} + \dot{m}_{rec}} \tag{1.1}$$

Several studies, e.g. [15, 13, 14], reported that it is possible to attain a significant increase of carbon dioxide concentration in the exhaust gases with an EGR ratio between 30% and 50%. Also, a reduction in the O_2 content in the exhaust has been observed.

The STIG cycle, similar to the combined cycle, has been proposed as a method to increase the power output of the conventional gas turbines operated with a basic Brayton cycle [16]. It consists in the generation of steam in a HRSG unit and in its injection in the combustion section (or in a different location depending on the considered cycle) of the gas turbine. The steam injection increases the total mass flow rate through the turbine, thus leading to an increased power output and improved overall efficiency [17, 18]. The increased power output can be employed to reduce the energy penalty associated with the carbon capture process; also, a reduced carbon dioxide content in the oxidizer stream is obtained (when evaluated on a dry basis).

Although EGR and STIG cycles can be regarded as viable approaches to reduce the cost of carbon capture in gas turbines, both these solutions modify the combustion environment by introducing a non-negligible amount of diluting species, i.e. carbon dioxide or steam, in the oxidizer stream issuing into the combustion chamber. For these reasons, the suitability of existing combustion devices

for these modified cycles has to be verified. In the next section, an overview of the effects of carbon dioxide and steam dilution on natural gas combustion is presented, together with an assessment of the impact on the modelling strategy of such diluted combustion processes in gas turbines.

1.4 Modelling of diluted combustion in gas turbines

CFD is the science involving the numerical modelling of fluid motion and of the related phenomena. The governing equations, e.g. conservation of mass, momentum, energy and chemical species, are discretised over a numerical grid representing the domain of interest and solved using suitable numerical techniques. Due to the increasing power of modern computers, it is possible to employ CFD to analyse more and more complex problems [19].

The modelling of turbulent combustion is an important branch of CFD. The complex nature of reactive flows, the strong coupling between chemistry and turbulence and the different characteristic scales of turbulence and combustion makes CFD modelling of turbulent combustion processes an extremely challenging task [20].

The difficulties related to turbulent combustion modelling are even greater when considering its application to industrial gas turbine combustors, due to the peculiarities of these devices. In fact, modern Dry Low-Emissions (DLE) gas turbine combustors rely on the lean-premixed technology to control NO_x emissions; in these devices most of the fuel is premixed with air before the mixture enters the combustion chamber and is burned in lean conditions in order to reduce the flame temperature and thus NO_x production [21]. This results in the operating point of the combustor to be moved closer to the lean flammability limit with respect to conventional non-premixed devices, with possible issues related to flame stability and CO emissions. For these reasons, while most of the combustion process follows the lean-premixed approach, a small percentage of the fuel is usually injected into the combustion chamber with little if no premixing in order to create a stable pilot flame to enhance the overall combustion stability in the device [8]. Thus,

the overall combustion process cannot be regarded as either purely premixed nor non-premixed; this condition is referred to as partially-premixed combustion and represents the most challenging combustion regime from a modelling point of view [22].

Also, practical combustion devices are characterised by a complicated geometry (with multiple fuel injection points, swirling vanes, dilution jets) leading to the need to employ unstructured numerical grids and advanced meshing techniques like hybrid meshes and non-conformal interfaces.

Finally, the flow features typical of swirl-stabilised DLE combustors comprise complicated phenomena such as swirling flows, vortex breakdown, recirculating flows and the possible presence of aerodynamic instabilities [23].

Therefore, the CFD modelling of combustion in industrial gas turbines can be regarded as a noticeably challenging task, even without the additional complications associated with carbon dioxide and steam dilution.

In this context, steady-state Reynolds-Averaged Navier-Stokes (RANS) calculations still represents the workhorse for CFD modelling of gas turbine combustion, due to their moderate computational cost as well as to the experience gained in decades of use and model calibrations [24, 25, 26, 27]. Nevertheless, due to the increasing computational power coming from massive parallel computers together with a significant research effort to develop suitable sub-grid scale (SGS) models for turbulent combustion, Large Eddy Simulation (LES) is becoming an attractive option for the modelling of both lab-scale burners and industrial combustors [28, 29, 30]. In fact, LES can provide more accurate results with respect to RANS for both non-reactive and reactive swirling flows, due to its ability to account for the unsteady nature of such flows as well as to its capacity to better predict the mixing process, which is of paramount importance in turbulent combustion modelling [31]. On the other hand, LES is characterised by a significantly higher computational cost with respect to steady-state RANS calculations.

The application of EGR of STIG cycles to enhance carbon capture in gas turbines poses additional challenges due to the increased levels of CO_2 and H_2O in the combustion environment with respect to conventional air-fired operation. The impact of the diluting species on the combustion process is due to both

thermal and chemical effects [32]. The thermal effects are related to the different physical properties of the diluting species with respect to air. In particular, the higher heat capacity of both carbon dioxide and steam compared to air results in lower temperature levels with respect to conventional air-fired combustion. Chemical effects are due to the chemical reactivity of the diluting species, and involve both a direct participation in the combustion chemistry as well as in a participation as third body in termolecular reactions with a significantly higher efficiency with respect to nitrogen.

In addition to these basic effects on the combustion process, the enhanced presence on diluting species has an impact also on the heat transfer mechanism and on the flow field within the combustor [33, 34, 35, 36].

All these effects have to be accounted for at the modelling stage, and the main aim of the present thesis is to develop a complete and accurate CFD model for diluted combustion in gas turbines and its application in the modelling of an industrial device.

1.5 Aims and objectives

From the analysis presented in the previous sections, it can be inferred that the use of advanced cycles such as EGR and STIG in gas turbines will become more and more popular in the future, in order to reduce the efficiency penalty associated with post-combustion carbon capture in these devices. In this context, CFD modelling can represent a powerful tool to investigate the effects of dilution in existing combustion chambers as well as to assist in the design of novel devices. Therefore, the main objectives of the present work are the following:

- Assessment of the effects CO_2 and H_2O dilution of natural gas combustion and development of an accurate CFD model for diluted combustion in gas turbines accounting for the dilution effects on heat release, flame stabilization and pollutant emissions.

- CFD investigation of an industrial micro gas turbine (MGT) combustor under air-fired and diluted conditions and the assessment of the effects of carbon dioxide and steam dilution on the operation of the device.

1.6 Thesis outline

In this chapter the motivation behind the present study has been presented. Modified gas turbine cycles such as EGR and STIG have been proposed in order to improve the efficiency of carbon capture for gas-fired power generation. Both these solutions imply the presence of diluting species in the combustion environment. This can cause issues in the operation of the combustion section of the plant. CFD analyses can be employed to assess the effects of CO_2 and steam dilution in existing combustion chambers and also for the design of new devices. Therefore there is a need for the development of accurate numerical models for this purpose. In Chapter 2, a literature review on the existing CFD techniques that are suitable for gas combustion and on the studies dealing with the impact of carbon dioxide and H_2O dilution on gas combustion is presented.

Chapter 3 provides an overview of the experimental data used for the validation of the numerical results. Firstly, detailed in-flame experimental measurements from a lab-scale burner have been employed in order to assess the suitability of the models employed in the present study for complex partially-premixed flames. Further, the data obtained from the experimental investigation of the operation of a micro gas turbine (MGT) system under air-fired, CO_2- and steam-diluted conditions have been used to set up and validate the CFD modelling of the combustion chamber employed in the system.

In Chapter 4, the effects of dilution on gas combustion have been assessed through the numerical simulation of basic one-dimensional laminar flames employing a detailed chemical mechanism for natural gas combustion. Also, the influence of radiative heat transfer has been evaluated in air-fired and diluted 1D flames.

Chapter 5 contains a description of the modelling of a lab-scale burner flame, that is employed to validate the tabulated chemistry/presumed-PDF approach for partially premixed swirling flames in both RANS and LES frameworks. Further, general guidelines are obtained for the numerical investigation of complex flames similar to those found in industrial devices.

Chapter 6 describes the results obtained from a CFD investigation of the combustor of a MGT system under air-fired and diluted conditions.

Finally, Chapter 7 summarises the conclusions of the present thesis and outlines some possible future work that may be performed.

Chapter 2

Literature review

A critical review of the literature regarding the modelling of turbulent gas-phase combustion is presented in this chapter, with a focus on the aim of the present work, i.e. the modelling of diluted combustion in industrial devices. The governing equations for the problem are presented in Section 2.1. Details on the turbulent flows modelling are presented in Section 2.2 and a review of the approaches for turbulent combustion modelling is reported in Section 2.3, with a focus on their suitability for diluted combustion. Finally, a short introduction to radiative heat transfer modelling is reported in Section 2.4.

2.1 Governing equations

Under the continuum hypothesis [37], reactive flows are described by partial differential equations expressing the physical principles of conservation for mass, momentum, species and energy.

The mass conservation principle is expressed by the continuity equation, which takes the general form

$$\frac{\partial \rho}{\partial t} + \frac{\partial}{\partial x_j}\left(\rho u_j\right) = 0 \tag{2.1}$$

Newton's second law of dynamic states that momentum is conserved in a closed system, and therefore it can only be changed by the action of external forces. This principle is expressed by the momentum conservation equation, also known as the Navier-Stokes equation

$$\frac{\partial}{\partial t}\left(\rho u_i\right) + \frac{\partial}{\partial x_j}\left(\rho u_i u_j\right) = \frac{\partial}{\partial x_j}\tau_{ij} - \frac{\partial p}{\partial x_i} + F_i \tag{2.2}$$

where, for Newtonian fluids, the stress tensor τ_{ij} is given by

$$\tau_{ij} = \mu\left(\frac{\partial u_i}{\partial x_j} + \frac{\partial u_j}{\partial x_i} - \frac{2}{3}\frac{\partial u_k}{\partial x_k}\delta_{ij}\right) \tag{2.3}$$

For reactive flows, a transport equation for the mass fraction of species k, Y_k, can be expressed as

$$\frac{\partial}{\partial t}\left(\rho Y_k\right) + \frac{\partial}{\partial x_j}\left(\rho Y_k u_j\right) = -\frac{\partial J_j^k}{\partial x_j} + \omega_k \tag{2.4}$$

where the source term ω_k represents the net mass reaction rate of species k per unit volume.

The molecular diffusive flux J_j^k is usually evaluated according to the dilute approximation (i.e. Fick's first law) as [38]

$$J_j^k = -\rho D_k \frac{\partial Y_k}{\partial x_j} \tag{2.5}$$

where the molecular diffusivity of species k relative to the major species is calculated from the Schmidt number

$$\sigma_k = \frac{\mu}{\rho D_k} \tag{2.6}$$

In the cases where the diluted approximation cannot be employed, more complex expressions can be used to account for full multicomponent diffusion [39]. Soret effect and molecular diffusion related to pressure gradients are usually neglected [38].

Energy conservation can be expressed in terms of total enthalpy $h_t = h + u_i u_i/2$ as

$$\frac{\partial}{\partial t}\left(\rho h_t\right) + \frac{\partial}{\partial x_j}\left(\rho h_t u_j\right) = -\frac{\partial}{\partial x_j}\left(J_j^{h_t} + u_i\tau_{ij}\right) + \frac{\partial p}{\partial t} + u_j F_i + \omega_{h_t} \tag{2.7}$$

The enthalpy diffusive flux $J_j^{h_t}$ can be evaluated using the Fourier law as [20]

$$J_j^{h_t} = -\frac{\mu}{Pr}\left(\frac{\partial h_t}{\partial x_j} + \sum_{k=1}^{N}\left(\frac{1}{Le_k} - 1\right)h_{t,k}\frac{\partial Y_k}{\partial x_j}\right) \tag{2.8}$$

where the Lewis number for species k is equal to

$$Le_k = \frac{\sigma_k}{Pr} = \frac{k}{\rho c_p D_k} \tag{2.9}$$

and expresses the ratio between thermal and mass diffusivity. The Prandtl number is defined as

$$Pr = \frac{c_p \mu}{k} \tag{2.10}$$

and represents the ratio between diffusive transport of momentum and temperature.

The assumption of unity Lewis number for all species greatly simplifies the formulation of Equation (2.8) and is common practice in turbulent combustion modelling. This stems from the observation that molecular transport plays an important role only in a small region nearby the reaction zone, whilst turbulent transport is largely predominant elsewhere [40, 41]. Assuming unity Lewis number, and neglecting the terms $\frac{\partial p}{\partial t}$, $u_i \tau_{ij}$ and $u_j F_i$ under the low-Mach assumption [38], the energy conservation equation takes the form

$$\frac{\partial}{\partial t}\left(\rho h_t\right) + \frac{\partial}{\partial x_j}\left(\rho h_t u_j\right) = \frac{\partial}{\partial x_j}\left(\frac{\mu}{Pr}\frac{\partial h_t}{\partial x_j}\right) + \omega_{h_t} \tag{2.11}$$

which is formally identical to the species transport Equation (2.4).

The system formed by Equations (2.1), (2.2), (2.4) and (2.11) describes the evolution of any turbulent reactive flow in the limit of the considered assumptions. Unfortunately, the analytical solution of the system is only possible in a few very simple and laminar configuration that are of little practical interest. Furthermore, a direct numerical solution of the instantaneous balance equations is often not feasible even for relatively simple configurations. Therefore, an averaged or filtered formulation of the governing equations is usually introduced in order to reduce the computational effort required to solve the problem. The averaging and the filtering operations introduce new unknown terms and thus a significant modelling effort is often required to close the system, as it will be detailed further in the following sections.

2.2 Turbulence modelling

Since most flows in engineering applications are turbulent, it is crucial to understand the main characteristics of turbulence and the related modelling techniques. Fluid flows show a turbulent character when inertial, buoyancy, centrifugal or

other forces are dominant over the viscous force that tends to suppress inhomogeneities and flow instabilities. The ratio between inertial and viscous forces is expressed by the Reynolds number, Re, which is equal to

$$Re = \frac{UL}{\nu} \tag{2.12}$$

where U and L are the characteristic velocity and length of the considered flow, respectively, and ν is the kinematic viscosity of the fluid.

When Re is higher than a critical value, the inertial forces overcome the viscous effects and the flow starts to show a turbulent behaviour. Although no universal definition of turbulence exists, all turbulent flows are characterised by the same peculiar features. Bradshaw in [42] proposed to following definition of turbulence to highlight its main characteristics:

> Turbulence is a three-dimensional time dependent motion in which vortex stretching causes velocity fluctuations to spread to all wavelengths between a maximum determined by the boundary conditions of the flow and a minimum determined by viscous forces. It is the usual state of fluid motion except at low Reynolds number.

The previous definition contains some of the features typical of turbulent flows, which can be summarised as follows [43, 44]:

- Randomness: meaning turbulent flows show random velocity fluctuations and are not repeatable.
- High vorticity: turbulent flows contain high vorticity regions, which undergo vortex stretching, elongation and breakup. In particular vortex stretching is the main mechanism responsible for the energy transfer from large to small turbulent eddies.
- Three-dimensionality: even in cases where mean velocity and pressure only change in two dimensions, turbulent flows always have a three-dimensional nature. This is due to the fact that vortex stretching is not possible in two dimensions.

- Effective mixing: although molecular diffusion is always responsible for the mixing at the molecular level [45], turbulent eddies advect and wrinkle the molecular mixing layer, thus greatly increasing the effectiveness of the mixing process with respect to laminar flows.

- Continuity of the eddy spectrum: turbulent flows are characterised by the presence of turbulent structures covering the entire spectrum between the largest eddies (having a characteristic dimension comparable to that of the flow scale L) to the smallest ones in which the turbulent kinetic energy is eventually dissipated into heat by viscous effects.

- Presence of coherent structures: the presence of spotty regions of high vorticity or dissipation rate has been observed both experimentally and numerically in turbulent flows. Such regions, usually referred to as turbulent coherent structures, present a characteristic coherent pattern and are significantly larger than the smallest eddies.

One of the peculiar features of turbulence is the presence of turbulent eddies of different size and characteristics, as can be appreciated from the picture of the turbulent water jet shown in Figure 2.1. The largest eddies have characteristic length, L, and velocity, U, scales similar to those of the main flow field [37]. These largest eddies are usually weak and have a low energy content [44].

Turbulence production occurs by mean flow deformation and its interaction with the most energetic eddies. These eddies, often referred to as energy containing eddies, are similar in size to the largest ones, having a characteristic length ℓ_0 slightly smaller than L. Their characteristic velocity u_0 scales with the main velocity fluctuations u' and is comparable to U. Therefore, the Reynolds number associated with the energy containing eddies $Re_0 = \ell_0 u_0/\nu$ is large and of the some order of magnitude of Re [37]. In his description of the so called energy cascade process, Richardson [46] assumed that these energy containing structures are unstable and tend to break up and transfer their energy to smaller eddies. The energy transfer process continues until the Reynolds number associated with the turbulent eddies $Re = \ell u/\nu$ is small enough for the viscous forces to be able to stabilise the eddy motion and dissipate the turbulent energy into heat. Therefore,

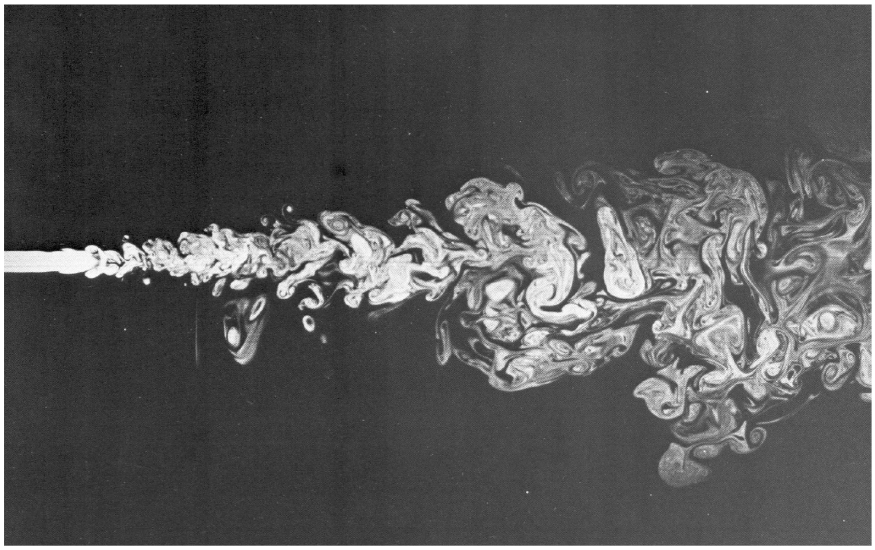

Figure 2.1: Turbulent water jet issuing into quiescent water, with turbulent eddies of different scales visualized by laser-induced fluorescence [47].

according to this theory, dissipation happens at the end of the energy cascade process in the smallest eddies.

The energy dissipation rate ϵ is determined by the first process in the energy cascade, i.e. the energy extraction from the mean flow by the most energetic eddies. The time scale associated with these eddies is $\tau_0 = \ell_0/u_0$ and their energy content is of the order u_0^2. Thus, the dissipation rate ϵ can be assumed to scale as

$$\epsilon \propto \frac{u_0^3}{\ell_0} \approx \frac{U^3}{L} \tag{2.13}$$

and does not depend on ν under the assumption of high Reynolds number, consistently with experimental findings in free shear flows [37].

Kolmogorov [48] elaborated a theory for the definition of the characteristic scales for different eddies on the basis of three hypotheses. The first one, called Komogorov's hypothesis of local isotropy, states that at high Reynolds number the small-scales ($\ell << \ell_0$) are statistically isotropic. This is in contrast with the large-scale eddies which are usually non-isotropic and whose characteristics depend on the flow boundary conditions. Following Pope [37], it is possible to define a scale ℓ_{EI} that separates the large non-isotropic eddies from the small isotropic scales.

The second hypothesis assumes that the statistics of the small-scale turbulent eddies are characterised by a universal behaviour determined by ϵ and ν only. This range size corresponds to $\ell < \ell_{EI}$ and is called the universal equilibrium range. The timescales associated with the equilibrium range are smaller than τ_0, and therefore these eddies can adapt quickly and are in dynamic equilibrium with the energy transfer rate imposed by the large eddies [37].

It is possible to obtain a unique definition for length, velocity and time scales for the small eddies on the basis of ϵ and ν, usually referred to as the Kolmogorov scales. The Kolmogorov length, velocity and time scales are defined as

$$\ell_\eta = \left(\nu^3/\epsilon\right)^{\frac{1}{4}} \tag{2.14}$$

$$u_\eta = \left(\nu\epsilon\right)^{\frac{1}{4}} \tag{2.15}$$

$$\tau_\eta = \left(\nu/\epsilon\right)^{\frac{1}{2}} \tag{2.16}$$

It can be noticed that the Reynolds number associated with the Kolmogorov scale, $Re_\eta = \ell_\eta u_\eta/\nu$ is equal to one, which agrees with the assumption that the energy cascade proceeds to smaller and smaller scales until the Reynolds number is low enough for the viscous effects to overcome the inertial forces.

The ratios between the energy containing scales and the Kolmogorov scales can be determined by the expressions for the latter and the scaling rule $\epsilon \propto u_0^3/\ell_0$ as

$$\frac{\ell_\eta}{\ell_0} \propto Re^{-\frac{3}{4}} \tag{2.17}$$

$$\frac{u_\eta}{u_0} \propto Re^{-\frac{1}{4}} \tag{2.18}$$

$$\frac{\tau_\eta}{\tau_0} \propto Re^{-\frac{1}{2}} \tag{2.19}$$

Equation (2.17) confirms that, for high Reynolds number, $\ell_0 >> \ell_\eta$. Also, since the ratio ℓ_η/ℓ_0 decreases with increasing Re, at high Reynolds number there exists a range of scales that are very small compared ℓ_0 and yet significantly larger than the Kolmogorov scale. The third Kolmogorov hypothesis states that at sufficiently high Reynolds number the statistics of the motion of the scales ℓ in the range $\ell_{EI} > \ell > \ell_{DI}$ are uniquely determined by ϵ and are thus independent from ν.

The lengthscale $\ell_{DI} \approx 60\ell_\eta$ [37] divides the universal equilibrium range into two sub-parts: the inertial subrange, corresponding to $\ell_{EI} > \ell > \ell_{DI}$, that is governed by inertial effects with negligible viscosity influence, and the dissipation range, corresponding to $\ell < \ell_{DI}$, where the viscous dissipation process takes place.

The randomness of the velocity field in turbulent flows is in contrast with the deterministic character of the governing equations. This apparent paradox is due to the presence of perturbations in initial and boundary conditions and in material properties, and to the fact that the governing equations, due to their non linear character, have a very high sensibility to such perturbations. In other words, the instantaneous velocity field obtained from a given experiment (i.e. a realisation of the turbulent flow field) is non-repeatable due to the high sensitivity of turbulent flows to small perturbations in the experiment's settings.

Given the random character of turbulence, it comes natural to describe it from a statistical point of view. A random variable u is characterised by its probability density function (PDF), $P(u)$, such that $P(u)du$ is the probability of observing u within the range of values between u and $u + du$. Clearly, P must satisfy the normalization condition

$$\int_{-\infty}^{\infty} P(u)du = 1 \tag{2.20}$$

The mean, or expected value, of a random variable u is denoted with U and can be calculated as

$$U = \int_{-\infty}^{\infty} uP(u)du \tag{2.21}$$

The variance associated with u is the mean-square fluctuation

$$var(u) = \int_{-\infty}^{\infty} (u - U)^2 P(u)du \tag{2.22}$$

and the root mean square (RMS) value of u is the square root of the variance

$$u_{RMS} = \sqrt{var(u)} \tag{2.23}$$

In order to simplify the description of turbulent flows, Reynolds [49] proposed to decompose the instantaneous random variable u into into a mean $\bar{u}$ and a fluctuating u' part as

$$u = \bar{u} + u' \tag{2.24}$$

where the overbar indicates the application of a Reynolds-averaging operator to the instantaneous variable. The Reynolds-averaging operation can assume different forms depending on the properties of the considered turbulent flow field [50]. In particular, time averaging is usually employed for statistically stationary turbulence. In this case the Reynolds-averaged variable is expressed as

$$\bar{u} = \lim_{T\to\infty} \frac{1}{T} \int_{t}^{t+T} u dt \tag{2.25}$$

where, in practical applications, T is chosen such as it is much longer than the characteristic time of the slowest fluctuations, that are associated with the largest eddies [19].

If the flow is not statistically stationary, ensemble averaging over a number of N realisations can be employed, thus obtaining

$$\bar{u} = \lim_{N\to\infty} \frac{1}{N} \sum_{i=1}^{N} u_i \tag{2.26}$$

The Reynolds-averaged quantities introduced so far characterise the mean flow field, but give no information on the turbulence. A scale based on velocity fluctuations would be a natural choice to characterise the turbulence. Direct averaging of the fluctuating velocity appearing in Equation (2.24) leads to

$$\bar{u'} = 0 \tag{2.27}$$

and thus is not a viable choice. Therefore, the RMS value of u is defined as

$$u_{RMS} = \sqrt{\overline{(u')^2}} \tag{2.28}$$

and this can be employed as a velocity scale for turbulence.

The turbulent kinetic energy per unit mass is defined as the kinetic energy associated with the turbulent velocity fluctuations and it can be expressed as

$$k = \frac{1}{2}\overline{u_i' u_i'} \tag{2.29}$$

In isotropic turbulence, by definition, it results $\overline{(u_1')^2} = \overline{(u_2')^2} = \overline{(u_3')^2}$ and therefore velocity fluctuations can be characterised by a single RMS value $u' = u_{RMS}$. For non-isotropic turbulence, the scale for velocity fluctuations can be taken equal to

$$u' = \sqrt{\frac{2}{3}k} = \sqrt{\frac{\overline{(u_1')^2} + \overline{(u_2')^2} + \overline{(u_3')^2}}{3}} \tag{2.30}$$

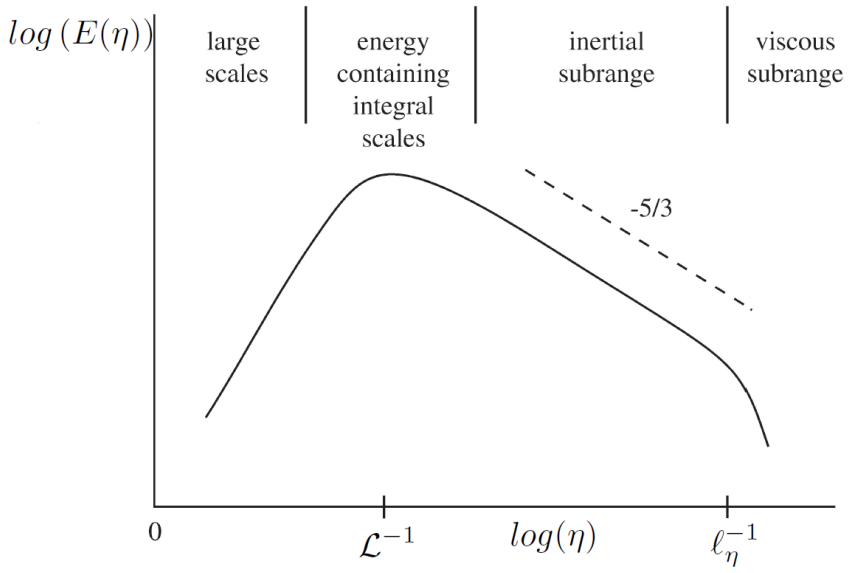

Figure 2.2: Sketch of a typical turbulent energy spectrum. The dashed line represent the $-5/3$ slope expressed in Equation (2.32).

The distribution of the turbulent kinetic energy over the different scales of the turbulent eddies can be obtained by considering the energy spectrum function $E(\eta)$ where $\eta = 2\pi/\ell$ is the wavenumber associated with the eddy of size ℓ. The integral of $E(\eta)$ over the entire wavelength range is equal to the turbulent kinetic energy [37], i.e.

$$\int_0^\infty E(\eta)d\eta = \frac{1}{2}\overline{u_i' u_i'} = k \tag{2.31}$$

where, in reality, the lowest bounding value of η is of the order of $2\pi/L$, whilst the upper bounding value corresponds to the wavenumber associated with the Kolmogorv scale $2\pi/\ell_\eta$.

From the Kolmogorov first hypothesis, it follows that in the universal equilibrium range, the spectrum is only a function of ϵ and ν. Further, from the third hypothesis, in the inertial subrange the spectrum is only a function of ϵ and can be expressed as [37]

$$E(\eta) = C\epsilon^{2/3}\eta^{-5/3} \tag{2.32}$$

where C is a universal constant. A sketch of a typical turbulent energy spectrum is provided in Figure 2.2, where the characteristic $-5/3$ slope in the inertial subrange is highlighted.

As mentioned in Section 2.1, it is possible to obtain an analytical solution of the governing equations only for some simple laminar flow configurations [51]. For all the other cases, and especially for practical turbulent flows of engineering interest, the system has to be solved by means of numerical techniques [19].

Among the possible approaches to predict turbulent flows, the most accurate one is to solve the governing equations as they are, without the introduction of any averaging or approximation, apart from the numerical discretisation technique employed to solve the equations. This approach is referred to as Direct Numerical Simulation (DNS) and resolves all the scales contained in the flow, such that the calculated solution is equivalent to a single realisation of the turbulent flow [43]. Thus, the numerical discretisation in space and time for DNS has to be fine enough to resolve all the eddies in the turbulent spectrum up to the Kolmogorov scales. As it can be noted from Equations (2.14) and (2.16), as the flow Reynolds number increases then this approach involves a formidable computational cost, and its use is limited to the investigation of simple configurations at low or moderate Reynolds number.

In order to simplify the problem and make it treatable even in cases involving complex configurations at elevated Reynolds number, which are very common in practical applications, it is possible to employ the Reynolds decomposition outlined in Equation (2.24). By applying the Reynolds-averaging operator to the governing system of equations, a new set of equations, called the RANS equations, is obtained. In this approach, the solution contains only the mean Reynolds-averaged flow variables, and all the information about the turbulence spectrum are lost [43]. Furthermore, as it will be detailed further in the following section, RANS equations contain unknown terms arising from the averaging operation, thus the introduction of a model is required in order to close the system. Despite its shortcomings, RANS still represents the most common approach for the modelling of complex industrial flows. This is due to its reduced computational costs and the ability to provide reasonable results for the mean flow parameters that are usually of interest for engineers.

Another approach, which lies between RANS and DNS in terms of complexity and computational costs, consists in resolving the largest, energy containing

eddies in the turbulent flow, and to employ a suitable model to account for the effects of the smallest scales. This approach is referred to as LES, and involves a spatial filtering operation of the governing equations in order to introduce a scale separation between the large scales to be resolved and the small scales [52]. Similarly to Reynolds-averaging, the filtering operation leads to the introduction of unknown terms in the filtered equations, representing the effects of the unresolved small scales on the filtered field, and thus require modelling in order to close the system. LES offers clear advantages with respect to RANS, being able to account for the natural unsteadiness of turbulent flows, and to predict the presence of coherent structures and flow instabilities [53]. Further, since in LES the large scales that are responsible for most of the scalar transport are resolved, the modelling of the mixing process with LES can be significantly more accurate with respect to RANS [31]. On the other hand, LES is characterised by a significantly higher computational cost with respect to RANS, due to the fact that the LES simulations are inherently three-dimensional and unsteady, and the numerical discretisation needs to be able to resolve a sufficient part of the turbulent energy spectrum, leaving only the small scales to be modelled [54].

The choice of the appropriate turbulence model is not trivial and depends on both the complexity of the flow and the goal of the investigation. Whilst DNS is ruled out for the investigation of practical high-Reynolds flows due to the prohibitive computational effort required, in the last few years LES has become a viable option for industrial applications due to the increased power of modern computers [55]. Nevertheless, the RANS approach still represents the workhorse for industrial CFD analyses, especially when the scope of the investigation is the evaluation of averaged flow field properties (e.g. average heat transfer coefficient over a surface, lift generated by an airfoil profile, etc.). The use of LES, which implies significantly higher computational cost with respect to RANS, can be justified when there is a need for increased accuracy in the modelling of specific phenomena (e.g. prediction of the mixing process in non-premixed flames [31]) or when the aim of the CFD analysis rules out the use of steady RANS models (e.g. investigation of flow instabilities, presence of coherent structures, etc.). Wilcox [50] stated that *"an ideal model should introduce the minimum amount of*

complexity while capturing the essence of the relevant physics", bearing in mind that the relevant physics is generally dictated by the application and aims of the numerical investigation.

2.2.1 RANS approach

The RANS approach to turbulence modelling is based on the decomposition of the instantaneous flow field variable in a mean and a fluctuating component, following the Reynolds decomposition described in Equation (2.24). In the governing equations for variable density flows, which characterise combustion modelling, convective transportation is expressed by ρu_i rather than just u_i. For this reason, a density-weighted average $\tilde{u}$, called the Favre average, is introduced [45], such that all the relevant field variables, except the pressure, are density weighted. The Favre-averaging operator is defined as

$$\tilde{u} = \frac{\overline{\rho u}}{\bar{\rho}} \tag{2.33}$$

and u can now be expressed as

$$u = \tilde{u} + u' \tag{2.34}$$

where the the fluctuating quantities associated with Favre-averaging are still indicated with u', although they have a different definition with respect to the one in Equation (2.24).

Now consider a typical convection term in the Navier-Stokes equations for a non-constant density flow, with the form $\rho u_1 u_2$. By using the Reynolds-averaging one obtains

$$\overline{\rho u_1 u_2} = \bar{\rho}\bar{u_1}\bar{u_2} + \bar{\rho}\overline{u_1' u_2'} + \bar{u_1}\overline{\rho' u_2'} + \bar{u_2}\overline{\rho' u_1'} \tag{2.35}$$

whereas, using the Favre-averaging operator, the averaged convection term is given by

$$\widetilde{\rho u_1 u_2} = \bar{\rho}\tilde{u}_1\tilde{u}_2 + \bar{\rho}\widetilde{u_1' u_2'} \tag{2.36}$$

Comparing Equations (2.35) and (2.36), it can be noticed that the three additional terms involving density fluctuations present in Equation (2.35) do not appear in the Favre-averaged form of the convective term. Furthermore, Equation

(2.36) has the same form as the Reynolds-averaged convective term for constant density flows, which is $\overline{uv} = \bar{u}\bar{v} + \overline{u'v'}$ [56].

In order to obtain the averaged version of the governing equations, the Favre-averaging operator has to be applied to the instantaneous governing equations. The resulting Favre-averaged continuity and momentum equations are given by [20]

$$\frac{\partial \bar{\rho}}{\partial t} + \frac{\partial}{\partial x_j}\left(\bar{\rho}\tilde{u}_j\right) = 0 \tag{2.37}$$

$$\frac{\partial}{\partial t}\left(\bar{\rho}\tilde{u}_i\right) + \frac{\partial}{\partial x_j}\left(\bar{\rho}\tilde{u}_i\tilde{u}_j\right) = -\frac{\partial}{\partial x_j}\left(\bar{\rho}\widetilde{u_i'u_j'}\right) + \frac{\partial}{\partial x_j}\overline{\tau}_{ij} - \frac{\partial \bar{p}}{\partial x_i} + \bar{F}_i \tag{2.38}$$

The Favre-averaged continuity Equation (2.37) has exactly the same form as its instantaneous counterpart, Equation (2.1). On the other hand, the averaging of the non-linear term in the instantaneous momentum Equation (2.2) leads to the introduction of the unknown term $\widetilde{u_i'u_j'}$. This term is referred to as the Reynolds stress tensor and has to be accounted for by resorting to a suitable model. This is commonly referred to as the "closure problem" in turbulence modelling, and will be addressed more in detail below.

The averaged conservation equations for species Y_k and total enthalpy h_t take the form

$$\frac{\partial}{\partial t}\left(\bar{\rho}\tilde{Y}_k\right) + \frac{\partial}{\partial x_j}\left(\bar{\rho}\tilde{Y}_k\tilde{u}_j\right) = -\frac{\partial}{\partial x_j}\left(\bar{\rho}\widetilde{Y_k'u_j'}\right) - \frac{\partial \overline{J_j^k}}{\partial x_j} + \bar{\omega}_k \tag{2.39}$$

$$\frac{\partial}{\partial t}\left(\bar{\rho}\tilde{h}_t\right) + \frac{\partial}{\partial x_j}\left(\bar{\rho}\tilde{h}_t\tilde{u}_j\right) = -\frac{\partial}{\partial x_j}\left(\bar{\rho}\widetilde{h_t'u_j'}\right) - \frac{\partial \overline{J_j^{h_t}}}{\partial x_j} + \bar{\omega}_{h_t} \tag{2.40}$$

By analysing Equations (2.39) and (2.40), it can be inferred that the Favre-averaged transport equation for a generic scalar ϕ can be expressed as

$$\frac{\partial}{\partial t}\left(\bar{\rho}\tilde{\phi}\right) + \frac{\partial}{\partial x_j}\left(\bar{\rho}\tilde{\phi}\tilde{u}_j\right) = -\frac{\partial}{\partial x_j}\left(\bar{\rho}\widetilde{\phi'u_j'}\right) - \frac{\partial \overline{J_j^{\phi}}}{\partial x_j} + \bar{\omega}_{\phi} \tag{2.41}$$

in which the laminar diffusive flux $\overline{J_j^{\phi}}$ is usually small compared to the turbulent flux $\bar{\rho}\widetilde{\phi'u_j'}$ and can be neglected or modelled according to Equation (2.5)[38]. The turbulent flux in Equation (2.41) is not expressed in a closed form and is usually

modelled by employing a gradient transport hypothesis, which is the analogue of Fick's law for molecular diffusion (Equation (2.5)), as [37]

$$\bar{\rho}\widetilde{\phi' u_j'} = -\frac{\mu_t}{\sigma_{t,\phi}}\frac{\partial \tilde{\phi}}{\partial x_j} \tag{2.42}$$

where $\sigma_{t,\phi}$ is the turbulent Schmidt number and μ_t is the turbulent viscosity. Although this assumption is very common in turbulent combustion modelling, it might not hold in some particular cases. For instance, counter-gradient turbulent transport has been observed in some premixed turbulent flames [57].

The evaluation of the source term $\bar{\omega}_\phi$ is not discussed here, since it depends on the nature of the considered variable ϕ. For example, turbulent combustion modelling is concerned with the evaluation of the chemical source term in the species transport equation.

The closure problem

Turbulence modelling in the context of RANS approach is mainly concerned with the modelling of the unknown Reynolds stress tensor that appears as a consequence of the averaging operation applied to the Navier-Stokes equations. Two possible levels of closure are most used in present CFD codes [44]:

- First-order or eddy-viscosity closure.
- Second-order or Reynolds Stress Models (RSM) closure.

In the first order-order approach, the Reynolds stress tensor is modelled by an analogy with the gradient-diffusion process and the introduction of an eddy (or turbulent) viscosity [50]. Thus, the unknown tensor $\tau_{ij}^t = -\rho\overline{u_i' u_j'}$ is modelled using the Boussinesq hypothesis as [1] [58]

$$-\rho\overline{u_i' u_j'} + \frac{2}{3}\rho k = \rho\mu_t\left(\frac{\partial \bar{u}_i}{\partial x_j} + \frac{\partial \bar{u}_j}{\partial x_i}\right) = 2\mu_t \bar{S}_{ij} \tag{2.43}$$

where μ_t is the turbulent viscosity and $\bar{S}_{ij}$ is the averaged rate of strain tensor. In the Boussinesq hypothesis, the turbulent stress tensor is expressed in the same

[1] Since most RANS turbulence models have been originally developed for constant density flows, the derivation for such flows is reported here. This can be readily extended to variable density flows and Favre-averaged variables [38].

way as the viscous stress for Newtonian fluids in Equation (2.3), but the molecular viscosity is replaced by the eddy viscosity μ_t. It has to be noted that, different from the molecular viscosity, the eddy viscosity is not a physical property of the fluid but is a field variable.

From dimensional arguments, the eddy viscosity can be expressed as the product between a characteristic turbulent length $\mathcal{L}$ and velocity $\mathcal{U}$, that have to be determined. Different models have been proposed to evaluate the eddy viscosity in Equation (2.43). The earliest model were based on Prandtl's mixing-length hypothesis and are referred to as algebraic or zero-equation models, since they do not require the solution of any additional transport equation [50]. Successively, one-equation models have been introduced, requiring the solution of a differential transport equation for the turbulent kinetic energy or a related quantity [59, 60]. Currently, the most common approach is based on two-equation models which involve the solution of two additional transport equations for turbulent variables that are then combined in order to evaluate the turbulent length and velocity scales.

The use of the square root of the turbulent kinetic energy k is a straightforward way to define the velocity scale and is common to all the two-equation eddy viscosity models. The evaluation of the length scale is somehow more difficult, and a number of different models has been developed using different definition for the turbulent length scale [50, 44]. Probably the most popular choice for the turbulent variables are the turbulent kinetic energy k and the its dissipation rate ϵ, as firstly proposed by Launder and Spalding [61] in their $k-\epsilon$ model. The characteristic turbulent length and velocity scales are then defined as

$$\mathcal{L} = \frac{k^{3/2}}{\epsilon} \tag{2.44}$$

$$\mathcal{U} = k^{1/2} \tag{2.45}$$

and, consequently, the turbulent viscosity is evaluated as

$$\mu_t = C_\mu \rho \frac{k^2}{\epsilon} \tag{2.46}$$

where C_μ is a model constant that can be evaluated out of a calibration procedure, together with the other model constants contained in the transport equations for k and ϵ [44].

The application of two-equation models to wall-bounded turbulent flows requires the specification of boundary conditions at the walls for the velocity as well as for the turbulent variables, k and ϵ for instance. The no-slip condition is usually applied to impose a zero velocity at the walls, whilst a zero-gradient Neumann boundary condition is used for k [62], i.e.

$$\frac{\partial k}{\partial x_n} = 0 \tag{2.47}$$

where x_n indicates the coordinate normal to the wall. Unfortunately, the ϵ transport equation in the $k - \epsilon$ model is derived under a fully turbulent flow assumption, which does not hold in the proximity of solid walls, where viscous effects are significant. For this reason most two-equation models, including the $k - \epsilon$, are not able to reproduce the correct law-of-the-wall [44]. This issue is usually overcome by not solving the ϵ conservation equation up to the wall. In this approach the first grid point is located in the fully-turbulent region away from the solid boundary and semi-empirical relationships, called wall-functions, are used to connect the solution in the fully-turbulent region to the wall region, which is affected by the viscosity [50]. In the the standard wall-functions formulation [62], the law-of-the wall is used to link the calculated solution for velocity, temperature and other scalars at the computational point closest to the wall (but located in the fully-turbulent region) and the corresponding quantities at the wall, whilst an algebraic expression based on the local equilibrium hypothesis is used for ϵ. Different formulations for the wall-functions exist, such as scalable and non-equilibrium wall functions [63].

An alternative to the use of wall-functions is represented by the use of two-equation closures whose formulation is suitable for low-Reynolds number regions as well as in fully turbulent flows. In this approach the computational grid has to cover the entire wall boundary-layer, including the viscous sub-layer, and all the equations can be integrated up to the wall. More information on low-Reynolds two-equation closures can be found in [44].

Other two-equation models rely on a different choice for the second transported variable, and thus employ a different expression for the turbulent length with respect to Equation (2.44). For instance, the Wilcox's $k - \omega$ model [64] is obtained by introducing a transport for $\omega = \epsilon/k$ instead of ϵ. Regardless of the

choice for the two transported variables, all two-equation models based on the Boussinesq assumption are characterised by well-known shortcomings (which add up with the limitations intrinsically associated with the RANS approach), such as [65, 66]:

- Linear algebraic stres-strain relationship resulting in poor performances in all the situations where stress transport is significant (e.g.: separating, buoyant, non-equilibrium flows).
- Scalar nature of the eddy viscosity, which is insensible to the orientation of turbulent structures.
- Inability to account for stress anisotropy and related phenomena (e.g. secondary motions in channel flows).
- Definition of only one characteristic scale for length and velocity to describe the entire turbulent spectrum.
- Failure to account for all the physical processes involved in the transport of the scale-defining variable ϵ.

A number of modified versions of the original basic two-equation models have been proposed in the past years in order to overcome some of the previous limitations and improve the models' performances. Among those improved versions it is worth mentioning the realizable $k-\epsilon$ model [67], the modified $k-\epsilon$ based on the Renormalization Group Theory [68], the SST model resulting from a blending of the $k-\epsilon$ and $k-\omega$ approaches from Menter [69] and its transition modification [70] and the models based on the elliptic-relaxation concept from Durbin [71]. A summary of the main characteristics and improvements over the basic models for some of these more advanced formulations can be found in the review paper from Hanjalić [66].

Some of the drawbacks listed above can be overcome by resorting to second-order closure models. In this approach, originally proposed by Rotta [72], a transport equation is solved for every single component of the Reynolds stress tensor τ_{ij}^t, thus allowing us to avoid the limitations related to the linear stress-strain

relationship in the Boussinesq assumption and to account for stress anisotropy. More details on RSM models can found in [73] and [50].

2.2.2 LES approach

The basic concept underlying LES is to resolve directly the large energy containing scales and to model the remaining smaller structures up to the Kolmogorov scales. This approach stems from the observation that large eddies are usually non-isotropic and highly dependent on the flow boundary conditions, whilst small scales can be generally regarded as isotropic and having a more universal behaviour, and thus are more suitable for modelling [74]. The scale separation between the large resolved eddies and the small modelled structures is obtained by introducing a suitable filter $G(\mathbf{x}, \mathbf{x}')$, and thus defining of the filtered (or resolved) generic variable [75]

$$\bar{\phi}(\mathbf{x}) = \int \phi(\mathbf{x}', t) G(\mathbf{x} - \mathbf{x}') d\mathbf{x}' \tag{2.48}$$

Therefore, the instantaneous variable ϕ can be decomposed into a resolved part $\bar{\phi}$ and and a residual, or SGS, part ϕ' as

$$\phi = \bar{\phi} + \phi' \tag{2.49}$$

This decomposition is similar to its Reynolds-averaged counterpart, Equation (2.24). Differently from the latter, $\bar{\phi}$ in Equation (2.49) is a random field variable, and also the filtered residual term is not generally equal to zero [37].

The filtering operation can be defined explicitly or implicitly. In the first approach, the filtering operation is defined in an explicit way and is then applied to the governing equations [74]. The resulting filtered system is then resolved numerically. An exhaustive review of the most common definitions employed for the filtering function can be found in [37]. In the explicit approach, since the filtering and the discretisation operations are separated, it is possible to achieve grid independence [76, 77]. On the other hand, the size of the numerical grid has to be significantly smaller than the width of the filter Δ. Therefore, explicit filtering requires a significantly higher computational effort with respect to the implicit approach, and will not be considered further in the present work.

When implicit filtering is employed, the filter width is defined implicitly by the numerical grid and the discretisation procedure [74]. A common approach, employed in the framework on the finite volume discretisation method [78], is to relate the filter size Δ directly to the grid size as [79]

$$\Delta = \sqrt[3]{V} \tag{2.50}$$

where V is the mesh cell volume. Therefore, the definition of a grid independent solution for implicit LES is not possible, since the solution changes with the mesh resolution [77]. A more convenient definition for the implicit approach is mesh convergence, meaning that a well-posed LES should converge towards a DNS when the mesh size, and therefore the size of the smallest resolved eddy, tends towards the Kolmogorov scale [80]. This is due to the fact that the SGS model contribution should vanish when the filter size is equal to the Komogorov length and therefore all the scales are directly resolved and $\phi \approx \bar{\phi}$.

The filtered balance equations can be obtained by applying the filtering operation to the instantaneous conservation equations. Similarly to the approach followed with RANS, it is possible to define a Favre-filtering operations suitable for variable density flows as [28]

$$\bar{\rho}\tilde{\phi}(\mathbf{x}) = \int \rho\phi(\mathbf{x}', t)G(\mathbf{x} - \mathbf{x}')d\mathbf{x}' \tag{2.51}$$

and the Favre-filtered mass conservation equations takes the form [20]

$$\frac{\partial \bar{\rho}}{\partial t} + \frac{\partial}{\partial x_j}\left(\bar{\rho}\tilde{u}_j\right) = 0 \tag{2.52}$$

which is formally identical to its instantaneous and Reynolds-averaged counterparts.

The Favre-filtered momentum conservation equation is given by

$$\frac{\partial}{\partial t}\left(\bar{\rho}\tilde{u}_i\right) + \frac{\partial}{\partial x_j}\left(\bar{\rho}\tilde{u}_i\tilde{u}_j\right) = -\frac{\partial}{\partial x_j}\left(\bar{\rho}\left(\widetilde{u_i u_j} - \tilde{u}_i\tilde{u}_j\right)\right) + \frac{\partial}{\partial x_j}\overline{\tau}_{ij} \tag{2.53}$$

The filtering operation results in the introduction of the unknown term $\tau_{ij}^{SGS} = \bar{\rho}\left(\widetilde{u_i u_j} - \tilde{u}_i\tilde{u}_j\right)$, called SGS stress tensor. Therefore, a suitable model for τ_{ij}^{SGS} is needed in order to close the system.

The filtered conservation equations for the chemical species Y_k and the total enthalpy h_t are given by

$$\frac{\partial}{\partial t}\left(\bar{\rho}\tilde{Y}_k\right) + \frac{\partial}{\partial x_j}\left(\bar{\rho}\tilde{Y}_k\tilde{u}_j\right) = -\frac{\partial}{\partial x_j}\left(\bar{\rho}\left(\widetilde{Y_k u_j} - \tilde{Y}_k\tilde{u}_j\right)\right) - \frac{\partial \overline{J_j^k}}{\partial x_j} + \bar{\omega}_k \tag{2.54}$$

and

$$\frac{\partial}{\partial t}\left(\bar{\rho}\tilde{h}_t\right)+\frac{\partial}{\partial x_j}\left(\bar{\rho}\tilde{h}_t\tilde{u}_j\right)=-\frac{\partial}{\partial x_j}\left(\bar{\rho}\left(\widetilde{h_t u_j}-\tilde{h}_t\tilde{u}_j\right)\right)-\frac{\partial\overline{J_j^{h_t}}}{\partial x_j}+\bar{\omega}_{h_t} \tag{2.55}$$

respectively.

Similarly to Equation (2.41) for Reynolds-averaging, a Favre-filtered transport equation for a general transported variable ϕ can be obtained, and it has the form

$$\frac{\partial}{\partial t}\left(\bar{\rho}\tilde{\phi}\right)+\frac{\partial}{\partial x_j}\left(\bar{\rho}\tilde{\phi}\tilde{u}_j\right)=-\frac{\partial}{\partial x_j}\left(\bar{\rho}\left(\widetilde{\phi u_j}-\tilde{\phi}\tilde{u}_j\right)\right)-\frac{\partial\overline{J_j^{\phi}}}{\partial x_j}+\bar{\omega}_{\phi} \tag{2.56}$$

Apart from the source term $\bar{\omega}_\phi$, whose evaluation depends on the definition of ϕ, the unclosed terms in Equation (2.56) are represented by the filtered molecular diffusion flux $\overline{J_j^{\phi}}$ and the SGS flux $\bar{\rho}\left(\widetilde{\phi u_j}-\tilde{\phi}\tilde{u}_j\right)$. The former, likewise to the RANS approach, can be neglected or modelled according to Fick's first law as in Equation (2.5), whilst for the latter a gradient transport approximation is employed, having the form [81]

$$\bar{\rho}\left(\widetilde{\phi u_j}-\tilde{\phi}\tilde{u}_j\right)=-\frac{\mu_{SGS}}{\sigma_{t,\phi}}\frac{\partial\tilde{\phi}}{\partial x_j} \tag{2.57}$$

where μ_{SGS} is the turbulent or SGS viscosity, which is now defined.

SGS stress models

The SGS stress tensor arising from the filtering operation of the momentum equation can be decomposed as [2] [52]

$$\tau_{ij}^{SGS}/\bar{\rho}=(\overline{u_i u_j}-\bar{u}_i\bar{u}_j)=L_{ij}+C_{ij}+R_{ij} \tag{2.58}$$

where $L_{ij}=\overline{\bar{u}_i\bar{u}_j}-\bar{u}_i\bar{u}_j$ are the Leonard stresses, $C_{ij}=\overline{\bar{u}_i u_j'}+\overline{u_i'\bar{u}_j}$ are the cross-stresses and $R_{ij}=\overline{u_i'u_j'}$ are the Reynolds stresses. The Leonard stresses represent the interaction between resolved scales that result in SGS effects, the cross stresses represent the interaction between the resolved and the SGS scales, and the Reynolds stresses represent the interaction between the SGS scales [75]. Speziale [82] demonstrated that L_{ij} and C_{ij} are not Galilean-invariant and thus

[2] Similarly to RANS, most SGS stress models for LES have been originally derived under the assumption of constant density, and thus the formulation for such flows is reported. The formulation can be readily extended to variable density flows and Favre-averaged variables [38].

the decomposition shown in Equation (2.58) is not usually considered. The most common approach is to ignore Leonard and cross-stresses and include their effects in the modelling of the Reynolds SGS stress tensor [79].

Counter-gradient transport of SGS stresses has been observed in DNS simulations of premixed flames, and this phenomenon cannot be accounted for by classical eddy viscosity models developed for isothermal non-reacting flows [83]. Nevertheless, the impact of SGS counter-gradient diffusion is usually neglected under the assumption that the LES filter is small enough to directly resolve most of this phenomenon. Therefore, the SGS stress tensor is usually modelled through a Boussinesq relationship similar to the one employed for RANS models, following the assumption that its deviatoric part is locally aligned with the resolved strain rate tensor [84], i.e.:

$$\tau_{ij}^{SGS} - \frac{1}{3}\tau_{kk}^{SGS}\delta_{ij} = 2\mu_{SGS}\left(\bar{S}_{ij} - \frac{1}{3}\bar{S}_{kk}\delta_{ij}\right) \tag{2.59}$$

By analogy with the mixing-length hypothesis, the eddy viscosity $\nu_{SGS} = \mu_{SGS}/\rho$ can be evaluated as

$$\nu_{SGS} = (C_m\Delta)^2\,\mathcal{D}_m \tag{2.60}$$

where C_m is a model constant and $\mathcal{D}_m$ is a differential operator acting on the resolved velocity field $\bar{U}_i$. The straightforward choice of the strain rate as the differential operator leads to

$$\mathcal{D}_m = \mathcal{D}_s = \left(2\bar{S}_{ij}\bar{S}_{ij}\right)^{1/2} \tag{2.61}$$

which corresponds to the Smagorinsky model [85], with $C_m = C_s = 0.1$. This has been the most popular SGS model in the past years, due to its simplicity and robustness. On the other hand, the Smagorinsky model is characterised by well-known drawbacks: mainly, a single universal value for the model constant results in a non-vanishing eddy viscosity at the walls and in laminar shear flows, which can lead to inaccuracies when it is applied to model wall-bounded or transitional flows.

These major drawbacks led to the introduction of the dynamic procedure [86] to estimate the model constant or to the derivation of more advanced differential

operators based on the velocity gradient tensor invariants, in order to obtain a correct near-wall behaviour or to meet other desirable properties. Although the definition of a list of desirable properties that the differential operator should meet is difficult and somehow arbitrary, some of these properties can be defined on the grounds of practical and physical considerations. Nicoud et al. [87] argued that the operator should be defined locally (its calculation involving only local gradients of the resolved field) and positive (to improve numerical stability), should reproduce the correct $\mathcal{O}(y^3)$ asymptotic near-wall behaviour, should vanish for any two-dimensional and two-component flows (i.e. should return a zero eddy viscosity for laminar 2D shear flows as well as for solid body rotation) and for axisymmetric (e.g. laminar jet impinging on a solid plate) or isotropic (e.g. laminar spherical premixed flame) expansion/contraction.

The Wall-Adapting Local Eddy Viscosity (WALE) [88] employs the following definition for the differential operator:

$$\mathcal{D}_m = \mathcal{D}_w = \frac{\left(\bar{S}^d_{ij}\bar{S}^d_{ij}\right)^{3/2}}{\left(\bar{S}_{ij}\bar{S}_{ij}\right)^{5/2} + \left(\bar{S}^d_{ij}\bar{S}^d_{ij}\right)^{5/4}} \tag{2.62}$$

where $\bar{S}^d_{ij}$ is the traceless symmetric part of the square of the velocity gradient tensor $g^2_{ij} = g_{ik}g_{kj}$:

$$\bar{S}^d_{ij} = \frac{1}{2}\left(g^2_{ij} + g^2_{ij}\right) - \frac{1}{3}g^2_{kk}\delta_{ij} \tag{2.63}$$

and the model constant $C_m = C_w$ is taken to be 0.325. The differential operator defined in Equation (2.62) gives the correct theoretical near-wall behaviour and vanishes in the case of pure shear flow. However, it can be shown that the WALE model returns a non-zero SGS viscosity value in the case of solid body rotation.

The Sigma SGS stress model, proposed by Nicoud et al. [87], meets all the properties listed above. The differential operator for this model is based on three singular values $\sigma_1 \geqslant \sigma_2 \geqslant \sigma_3$, defined as the square roots of the eigenvalues of the tensor $\mathbf{G} = \mathbf{g^t g}$. The three singular values are defined as

$$\sigma_1 = \left(\frac{\mathcal{I}_1}{3} + 2\sqrt{\alpha_1}cos\alpha_3\right)^{1/2} \tag{2.64}$$

$$\sigma_1 = \left(\frac{\mathcal{I}_1}{3} - 2\sqrt{\alpha_1}cos\left(\frac{\pi}{3} + \alpha_3\right)\right)^{1/2} \tag{2.65}$$

$$\sigma_1 = \left(\frac{\mathcal{I}_1}{3} - 2\sqrt{\alpha_1}cos\left(\frac{\pi}{3} - \alpha_3\right)\right)^{1/2} \tag{2.66}$$

where

$$\alpha_1 = \frac{\mathcal{I}_1^2}{9} - \frac{\mathcal{I}_2}{3} \tag{2.67}$$

$$\alpha_2 = \frac{\mathcal{I}_1^3}{27} - \frac{\mathcal{I}_1\mathcal{I}_2}{6} + \frac{\mathcal{I}_3}{2} \tag{2.68}$$

$$\alpha_1 = \frac{1}{3} arccos \frac{\alpha_2}{\alpha_2 \alpha_1^{3/2}} \tag{2.69}$$

and

$$\mathcal{I}_1 = tr\left(\mathbf{G}\right) \tag{2.70}$$

$$\mathcal{I}_2 = \frac{1}{2}\left(tr\left(\mathbf{G}\right)^2 - tr\left(\mathbf{G^2}\right)\right) \tag{2.71}$$

$$\mathcal{I}_3 = det\left(\mathbf{G}\right) \tag{2.72}$$

The Sigma model differential operator is then defined as

$$\mathcal{D}_\sigma = \frac{\sigma_3\left(\sigma_1 - \sigma_2\right)\left(\sigma_2 - \sigma_3\right)}{\sigma_1^2} \tag{2.73}$$

and the model constant C_σ is taken to be 1.5. This SGS stress model has been reported to perform consistently better than the standard Smagorinsky model and as good as or better than the Dynamic model in some base test cases [89]. Also, it has been successfully applied to the modelling of a piloted spray flame in a lab-scale burner [90] and of a model gas turbine combustion chamber [91].

The dynamic procedure detailed in [92] employs an explicit test filter $\hat{\bullet}$ to evaluate the model constant using a least squares approach, namely

$$\left(C_D\Delta\right)^2 = -\frac{1}{2}\frac{L_{ij}M_{ij}}{M_{kl}M_{kl}} \tag{2.74}$$

where

$$L_{ij} = \widehat{\bar{u}_i\bar{u}_j} - \hat{\bar{U}}_i\hat{\bar{U}}_j \tag{2.75}$$

and M_{kl} depends on the definition of the differential operator $\mathcal{D}_m$ as

$$M_{kl} = \frac{\hat{\Delta}}{\Delta}\hat{\bar{\mathcal{D}}}_m\hat{\bar{S}}_{kl}\widehat{\bar{\mathcal{D}}_m\bar{S}_{kl}} \tag{2.76}$$

Usually both the numerator and the denominator in Equation (2.74) are locally averaged and the resulting C_D value is clipped at 0 and to a maximum value (equal to 0.23 in ANSYS Fluent [63]) in order to improve numerical stability. The dynamic procedure illustrated above can be applied not only to the Smagorinsky model, but also to other eddy viscosity-based SGS models, by using

the related differential operator in Equation (2.76). However, the application of a locally-averaged dynamic procedure to SGS that are characterized by the correct $\mathcal{O}(y^3)$ asymptotic near-wall behaviour has been shown to lead to numerical instabilities [93]. Instead, a global dynamic procedure is advised for these models [87]. Also, [89] reported that the application of the local dynamic procedure did not show any improvement in the performances of the Sigma model. Therefore, the dynamic procedure has not been applied to the WALE and Sigma models in the present work.

LES mesh requirements, wall treatment and boundary conditions

The total error associated with LES calculations is given by the sum of two major components, i.e. the numerical discretisation error ϵ_{num} and the modelling error related to the modelling of SGS effects ϵ_{SGS} [94]. Theoretically, for a given filter width Δ, the grid should be refined enough in order to obtain $\epsilon_{num} << \epsilon_{SGS}$. Since in most practical application as ϵ_{num} decreases ϵ_{SGS} diminishes as well, it is very difficult to satisfy the previous requirement. This is particularly true in the context of implicit filtering, when the filter width is directly related to mesh size [95].

To assess the quality of LES, a direct comparison with experimental or DNS results can be performed, usually in terms of mean and RMS velocity components, turbulent stresses and turbulence energy spectrum. This approach is usually referred to as a-posteriori assessment [96]. A more fundamental approach is to compare directly the results from the SGS model with filtered DNS or experimental data. This approach requires data with an elevated spectral resolution, usually obtained from DNS, and it represents the so called a-priori analysis [53, 83].

It is desirable to develop some form of quality assessment for LES that does not rely on external data. This is due to the fact that the aforementioned methodologies rely on experimental or DNS data that are usually only available for simple flow configurations. Also, the need for experimental or DNS data for every possible application of LES analysis would greatly undermine its predictive purpose and its employment as a viable engineering tool [94]. Therefore, a quality indicator can be introduced, in order to provide a mean to assess the suitability

of a given numerical grid for LES. It must be noted that a good grid resolution resulting from the use of these quality indicators does not imply that an accurate solution will be obtained [94], therefore these quality indicators should be regarded only as a viable tool to assess the suitability of the numerical grid for LES, and not for results validation.

A natural choice for such a quality indicator is the ratio between the modelled and the total turbulent kinetic energy [95, 97], i.e.

$$M = \frac{k_{SGS}}{k_{SGS} + k_{res}} \tag{2.77}$$

where k_{res} is the resolved turbulent kinetic energy. For this criterion $M = 0$ corresponds to the DNS limit (all the turbulent kinetic energy is resolved) and $M = 1$ corresponds to RANS, where all the energy is modelled. By assuming that, in order for a LES to be "well-resolved", 80% of the total turbulent kinetic energy has to be resolved [37], the previous criterion can be summarised as

$$M \begin{cases} \leq 0.2 & \text{satisfied} \\ > 0.2 & \text{not satisfied} \end{cases} \tag{2.78}$$

The definition for the quality indicator in Equation (2.77) is based on the analysis of the results of the LES calculations. An a-priori estimation for the mesh quality can be introduced based on the estimation that the length dividing the large anisotropic scales and the universal equilibrium range ℓ_{EI} can be related to the turbulent integral length scale $\mathcal{L}$ as $\ell_{EI} \approx \frac{1}{6}\mathcal{L}$ [37]. A characteristic length associated with the numerical grid can be defined as $\mathcal{L}_{mesh} = \sqrt[3]{V}$, which is equal to the filter width Δ as defined in Equation (2.50). A quality indicator can be introduced by assuming that a filter size $\Delta \approx \mathcal{L}/12$ (which corresponds to resolve all the lengthscales within the spectrum up to ℓ_{EI}) is required to resolve 80% of the turbulent kinetic energy in the case if isotropic turbulence at very high Reynolds numbers [37, 94]. Under these assumptions, the criterion can be expressed as

$$\frac{\mathcal{L}_{mesh}}{\mathcal{L}/12} \begin{cases} \leq 1 & \text{satisfied} \\ > 1 & \text{not satisfied} \end{cases} \tag{2.79}$$

and $\mathcal{L}$ can be determined, for instance, from a precursor RANS simulation.

The presence of solid boundaries in the domain poses additional challenges and needs to be addressed carefully. For LES of wall-bounded flows at high-Reynolds number, most of the computational resources are dedicated to the resolution of the wall boundary layers. For this reason, the solution of the near-wall region represent a major bottleneck in the application of LES to complex highly turbulent flows [98]. A substantial saving of computational resources can be obtained by not resolving the viscous wall region, and employing an approach similar to those described for RANS wall-functions. The near-wall models are usually based on the impermeability condition for the velocity component normal to the wall, whilst the tangential components are evaluated implicitly by imposing a condition on the wall shear-stress [37] in order for the velocity to satisfy either the log-law [99] or a power-law [100]. More details about available wall treatments for LES can be found in [101, 102]. If any kind of wall-treatment is employed, then the mesh assessment provided by quality metrics such as the ones in Equations (2.78) and (2.79) does not apply to the near-wall regions.

The specification of realistic boundary conditions is of paramount importance for the accuracy of LES results [75]. In RANS, the inflow boundary conditions contain information about the mean velocity field and turbulence (i.e. k and ϵ), whilst the specification of the inflow in LES is much more complicated, since information about the stochastic time-varying component of the velocity field should be included [103]. Whenever detailed experimental or DNS data are available, these should be employed to specify realistic boundary conditions [104]. When there are no detailed measurements available, an artificial stochastic component can be added to the mean values by means of numerical algorithms such as the vortex method [105] or the algorithm proposed by Kempf et al. [106].

2.3 Gas-phase combustion modelling

In this section the different approaches available for turbulent combustion modelling in the gaseous phase are critically reviewed, with a focus on the application to diluted combustion in gas turbines. Combustion modelling is mainly concerned with the formulation of a suitable closure for the chemical reaction source terms

in the governing equations. Given the strong coupling and interaction between chemistry and turbulence and the great variety of scales involved, the modelling of turbulent combustion processes is an extremely challenging task [38]. The description of the various combustion models refers to the RANS framework, and the particular implications for LES modelling will be pointed out in the text when necessary. This approach is justified by the observation that, since in most cases the combustion process takes place at scales smaller than the LES filter size, the filtered chemical source term is not resolved and it is necessary to resort to a suitable SGS combustion model [29]. Thus, because the chemical source term has to be entirely modelled in both RANS and LES, most combustion models available for LES are directly derived from those originally proposed for RANS [28].

2.3.1 Classification of flames

In order to simplify the problem, some kind of flame classification can be introduced, and suitable models can be derived for different classes of combustion processes. In this context, it is useful to introduce the classical distinction between premixed, non-premixed and partially premixed flames, since their significantly different peculiarities lead to different modelling approaches [22]. A more detailed description of combustion theory can be found in well-known books [107, 56, 108], whilst comprehensive reviews of turbulent combustion modelling are reported in [38, 39].

In premixed flames, fuel and oxidizer are uniformly mixed prior to combustion and the flame front propagates into the fresh gas mixture. This combustion regime is found, for example, in spark combustion engines and Bunsen burners. In non-premixed combustion, fuel and oxidizer enter the system separately and they must mix at the molecular level before combustion can occur, as is the case in conventional gas turbine combustors and in Diesel engines. Diffusion plays a key role in mixing the two streams in non-premixed flames, and therefore they are also referred to as diffusion flames. All the combustion processes that do not fall into the previous definitions are classified as partially-premixed.

Both premixed, non-premixed and partially-premixed flames can be further

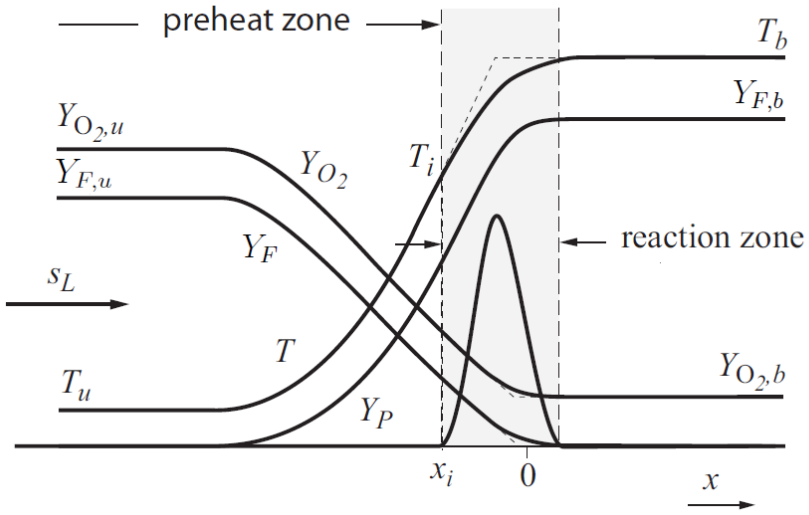

Figure 2.3: Schematic of a laminar 1D lean premixed flame [31].

classified as laminar or turbulent depending on the flow regime characterising the process. Heat and mass transfer in laminar flames occur by molecular diffusion, whilst turbulence transport usually plays a dominant role in turbulent combustion [21].

Laminar premixed flames

A laminar premixed flame can be seen as a deflagration wave propagating in a mixture of unburnt fuel and oxidizer. Although the classical experimental device to generate a premixed flame is the Bunsen burner [31], from a theoretical point of view it is convenient to consider a unidimensional flame, as sketched in Figure 2.3. The unburnt mixture and the burnt gases are separated by a thin reaction zone (with a typical thickness between 0.1 and 1 mm). The small pressure decrease through the flame is usually neglected, so that temperature and density are directly related through the ideal gas law [109]. The density ratio across the flame ρ_u/ρ_b is usually in the range 6-8 for typical unburnt temperatures and gas mixtures [45], and is equal to the temperature ratio T_b/T_u.

In the propagation of a laminar premixed flame the products are heated up by the energy released by the chemical reactions. Due to the elevated temperature gradient across the flame, part of this energy is transported into the fresh

cold mixture by means of thermal conduction. Therefore, the temperature of the unburnt mixture increases until it reaches the ignition temperature T_i and the chemical reactions are triggered. Ahead of the the flame front, the burnt mixture is in chemical equilibrium at the temperature T_b, and no chemical reactions take place [3]. In addition to the thermal conductive flux, a diffusive flux of reactants and combustion products into the reaction zone is present, due to the concentration gradient. Therefore, flame propagation is controlled by the diffusive transport of heat and species and by the chemical reactions [45].

The main parameter that characterises flame propagation is the laminar flame speed s_L, representing the velocity at which the flame propagates normal to itself in the unburnt mixture [31]. It is possible to derive an expression for the laminar flame speed in the case of a 1D unperturbed steady adiabatic flame, following the classical analysis of Zel'dovich and Frank-Kamenetskii, known as the thermal flame theory [110].

The Zel'dovich analysis is based on the assumption of a single-step global reaction with high activation energy. It is also assumed that the heat capacity is constant and equal for all species and the Lewis number is equal to unity. The irreversible one-step reaction has the form

$$\nu_{\mathrm{F}}\mathrm{F} + \nu_{\mathrm{O_2}}\mathrm{O_2} \longrightarrow \nu_{\mathrm{P}}\mathrm{P} \tag{R 2.1}$$

with a reaction rate given by

$$\omega = B\frac{\rho Y_F}{W_F}\frac{\rho Y_{O_2}}{W_{O_2}} exp\left(-\frac{E}{RT}\right) \tag{2.80}$$

The one-step analysis reported here is of great importance not only because of its simplicity and physical meaning, but also because it serves as a basis for the development of many models for premixed combustion. Modern analysis of unperturbed and perturbed propagation of premixed laminar flames usually rely on multi-step chemistry and a summary of the various approaches and the results obtained is reported in the review by de Goey et al. [111].

[3] This description assumes a single-step irreversible reaction. When multi-step chemistry is considered, an oxidation layer is present after the thin reaction zone, where the oxidation of the combustion products H_2 and CO to H_2O and CO_2 is completed [31].

In turbulent combustion modelling it is common practice to define a progress variable Y_c in order to track the reaction progress between the unburnt and the burnt states [112]. The normalised progress variable c can be defined as a reduced mass fraction, for instance [20]

$$c = \frac{Y_P - Y_{P,u}}{Y_{P,b} - Y_{P,u}} \tag{2.81}$$

so that $c = 0$ corresponds to the fresh gases and $c = 1$ corresponds to the burnt products. The transport equation for c under the assumptions of the thermal flame theory is given by[45]

$$\rho_u s_L \frac{dc}{dx} = \frac{d}{dx}\left(\rho D \frac{dc}{dx}\right) + \omega \tag{2.82}$$

where the continuity equation

$$\rho u = \rho_u u_u = \rho_u s_L = \rho_b u_b \tag{2.83}$$

has been used. The continuity equation in the form $\rho_u s_L = \rho_b u_b$ expresses the balance between the rate of consumption of the reactants and the rate of formation of the products per unit area of the flame surface.

The reaction rate ω in Equation (2.82) can be expressed as [45]

$$\omega = \frac{\rho(1-c)}{\tau_c} exp\left(-\frac{E}{RT}\right) \tag{2.84}$$

where

$$T = T_u + (T_b - T_u)c \tag{2.85}$$

and ρ can be evaluated from the state equation $\rho T = \rho_u T_u$. The term τ_c is the time scale associated with the chemistry.

The integration of the previous equation leads to the following expression for the laminar flame speed [45]

$$s_L = \sqrt{2D \int_0^1 \frac{\omega}{\rho_u} dc} \tag{2.86}$$

which confirms that the laminar flame propagation is controlled by molecular transport and the chemical reactions. From this observation and dimensional considerations one would obtain the expression

$$s_L \propto \sqrt{\frac{D}{\tau_c}} \tag{2.87}$$

which leads to the following definition of the chemical timescale

$$\frac{1}{\tau_c} = 2\int_0^1 \frac{\omega}{\rho_u} dc \tag{2.88}$$

Since the laminar flame is composed of a preheat zone and a reaction zone, and usually the reaction zone thickness is negligible compared to the preheat zone, the flame thickness ℓ_F can be assumed to be equal to that of the preheat zone. Different definitions for the flame thickness can be found in the literature [31], but the most common one is based on the maximum gradient method and defines the flame thickness as

$$\ell_F = \frac{T_b - T_u}{|dT/dx|_{max}} \tag{2.89}$$

which, in the framework of the Zel'dovich theory, can be expressed as [45]

$$\ell_F = \frac{D}{s_L} = \frac{\alpha_u}{s_L} = \frac{k_u}{\rho_u c_p s_L} \tag{2.90}$$

The flame characteristic time, τ_F, can be defined as the time required for the flame front to propagate for a distance equal to the flame thickness, i.e.

$$\tau_F = \frac{\ell_F}{s_L} \tag{2.91}$$

Laminar non-premixed flames

In non-premixed flames, the fuel and oxidizer streams enter separately into the combustion chamber where they have to mix at the molecular level before combustion can take place. Therefore mixing is of paramount importance in non-premixing flames and is the rate controlling phenomenon, since the chemical reactions are usually much faster than the mixing process. The rate controlling process can be identified through the Damköhler number, Da, which is defined as the ratio between a characteristic diffusion time and the chemical time scale, i.e. [107]:

$$Da = \frac{\tau_D}{\tau_C} \tag{2.92}$$

For $Da >> 1$, which is the case in common applications, the chemical reactions are much faster than molecular diffusion, so the process is diffusion limited and the chemical reactions can be assumed to be infinitely fast. On the other hand,

for $Da << 1$, diffusion occurs much faster with respect to chemical reactions, so the combustion process is limited by the chemical reaction kinetics.

Given the importance of mixing in non-premixed combustion, it is convenient to introduce a conserved scalar quantity to describe the mixing process between the fuel and oxidizer [113]. The most common choice for the conserved scalar is the mixture fraction Z. The mixture fraction is defined at any point within the system as the local mass fraction originating from the fuel stream. For a homogeneous mixture and a single-step reaction for hydrocarbon combustion, the mixture fraction Z can be defined as [31]

$$Z = \frac{\nu Y_F - Y_{O_2} + Y_{O_{2,2}}}{\nu Y_{F,1} + Y_{O_{2,2}}} \tag{2.93}$$

where ν is the stoichiometric oxygen-to-fuel mass ratio. From Equation (2.93) it can be seen that $Z = 0$ corresponds to pure oxidizer and $Z = 1$ corresponds to pure fuel. The stoichiometric mixture fraction value Z_{st} can then be evaluated as

$$Z_{st} = \left(1 + \frac{\nu Y_{F,1}}{Y_{O_{2,2}}}\right)^{-1} \tag{2.94}$$

It is worth noting that Z is just an alternative expression for the local equivalence ratio value ϕ, since it can be shown [31] that the following relationship holds

$$\phi = \frac{Z}{1 - Z} \frac{(1 - Z_{st})}{Z_{st}} \tag{2.95}$$

A more general definition for Z can be derived based on local elemental mass fractions following, for instance, the approach of Bilger [113]. Since chemical elements are conserved during chemical reactions, Z is a conserved scalar and, assuming equal diffusivity for all species, its transport equation becomes [31]

$$\frac{\partial}{\partial t}(\rho Z) + \frac{\partial}{\partial x_j}(\rho Z u_j) = \frac{\partial}{\partial x_j}\left(\rho D \frac{\partial Z}{\partial x_j}\right) \tag{2.96}$$

In the limit of infinitely fast chemistry, an infinitely thin non-equlibrium layer is located at $Z = Z_{st}$, and outside of this layer Y_F and Y_{O_2} are either zero or a piecewise function of Z, according to Equation (2.93). Under the assumptions of unity Lewis number and constant specific heat it can be shown that the temperature is also a piecewise function of Z. The resulting profiles for the temperature and species in functions of Z are referred to as the Burke-Schumann solution [114], and are depicted in Figure 2.4.

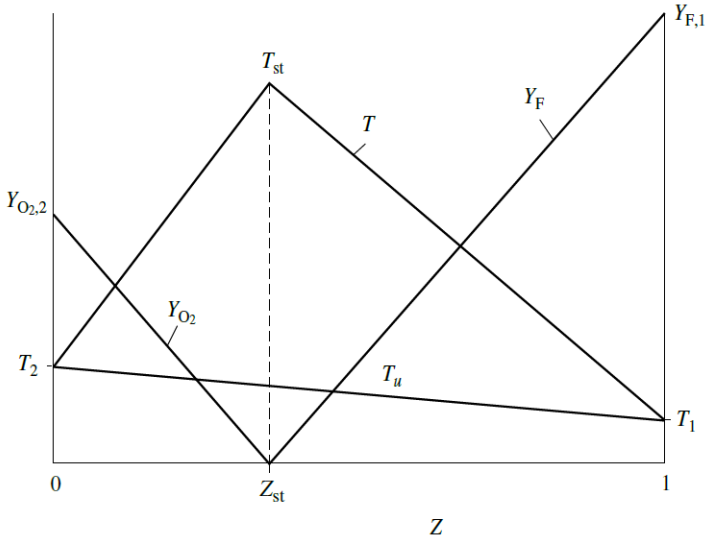

Figure 2.4: Graphical representation of the Burke-Schumann solution [39].

In many practical cases the infinitely fast chemistry hypothesis may not be satisfied locally, even if in general the condition $Da >> 1$ is met. If locally the diffusion time scale becomes of the same order of magnitude as the chemical time scale, non-equilibrium effects must be accounted for and even local quenching may occur. A further reduction in τ_D can lead to flame lift-off and blow-off of the entire flame. Also, the assumption of a single-step irreversible reaction for the chemistry is a great simplification. In reality the combustion of light hydrocarbons, such as methane and propane, involves hundreds of species and thousands of reactions, associated with a broad range of chemical time scales [107]. For example, the oxidation of propane might be considered fast compared to the diffusion time scale, whilst the reactions leading to NO formation or the oxidation of CO to CO_2 in the burnt gases are relatively slow processes characterised by a time scale comparable to the diffusion process. In this cases the mixture fraction Z alone is no longer sufficient to describe the system, and a new parameter has to be introduced in order to account for non-equilibrium effects.

One of the configurations commonly employed to investigate non-premixed combustion is the planar counterflow configuration depicted in Figure 2.5, since it results in an essentially 1D flame structure [115]. The overall strain rate a_s for

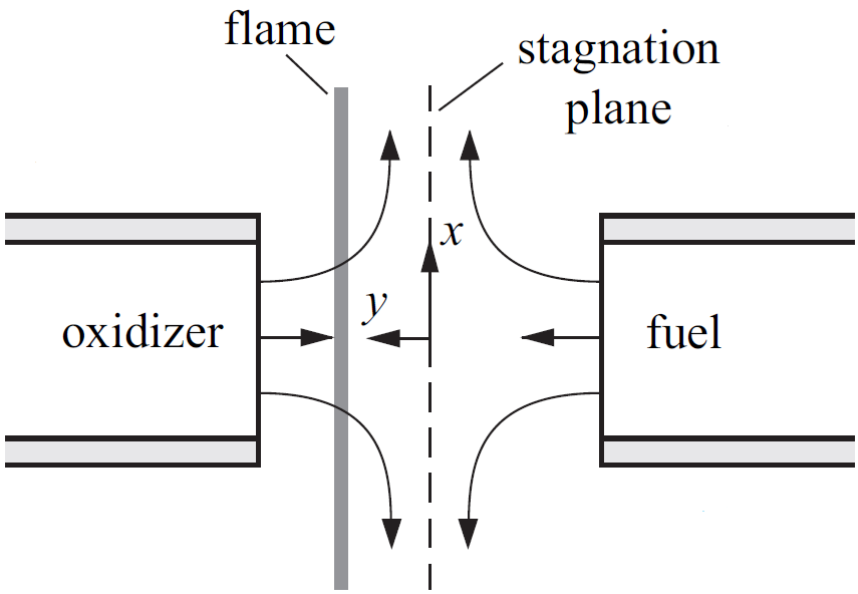

Figure 2.5: Schematic of a counterflow non-premixed flame [39].

a counterflow diffusion flame can be evaluated as

$$a_s = \frac{v}{2d} \tag{2.97}$$

where v is the relative speed of the undisturbed fuel and oxidizer jet and d is the distance between the jet nozzles. Most of the heat release takes place in the reaction zone, which is located in the vicinity of the $Z = Z_{st}$ isosurface. In a steady counterflow flame the amount of heat transported away from the reaction zone is equal to the heat released by the chemical reactions [20]. Increasing the jet velocity, and therefore the strain rate, eventually leads to flame quenching, when the heat leaving the reaction zone overcomes the chemical heat generation. Therefore the structure of the flame depends on the ratio between diffusion and chemical heat release, i.e. on the value of the Damköhler number.

It is possible to rearrange the balance equations for species and temperature from the physical space to a new reference frame, where Z is one of the coordinates, by defining a local orthogonal coordinate system attached to $Z = Z_{st}$. By assuming unity Lewis number and constant heat capacity [4] for all species, the

[4]The formulation for the general case accounting for variable Lewis number and c_p can be found in [116].

species and temperature conservation equations can be recast as [117]

$$\rho\frac{\partial Y_k}{\partial t} - \rho\frac{\chi}{2}\frac{\partial^2 Y_k}{\partial Z^2} - \omega_k = 0 \tag{2.98}$$

and

$$\rho\frac{\partial T}{\partial t} - \rho\frac{\chi}{2}\frac{\partial^2 T}{\partial Z^2} - \frac{1}{c_p}\frac{\partial p}{\partial t} + \sum_{k=1}^{N} h_k\omega_k = 0 \tag{2.99}$$

where χ is the scalar dissipation rate of the mixture fraction

$$\chi = 2D\left(\frac{\partial Z}{\partial x_j}\frac{\partial Z}{\partial x_j}\right) \tag{2.100}$$

and represents a key parameter in the description of non-premixed combustion. The inverse of the scalar dissipation rate at $Z = Z_{st}$ can be used as a representative diffusive time scale, $\tau_D = \chi_{st}^{-1}$ [31], and the Damköhler number can therefore be expressed as

$$Da = \frac{1}{\tau_c \chi_{st}} \tag{2.101}$$

Also, following the coordinate change, the scalar dissipation includes the influence of convection and diffusion normal to $Z = Z_{st}$ and is directly related to the strain rate a_s through [118]

$$\chi_{st} = \frac{a_s exp\left(-2\left(erfc^{-1}\left(2Z_{st}\right)\right)^2\right)}{\pi} \tag{2.102}$$

Therefore, χ_{st} can be employed as an expression for the characteristic strain rate of the flame. Thus, it is possible to represent the flame by means of Z and χ_{st} only, where the latter parameter is employed to represent non-equilibrium effects due to the aerodynamic strain of the flame.

Equations (2.98) and (2.99) can be employed in the analysis of the counterflow diffusion flame configuration depicted in Figure 2.5 in order to characterise non-premixed flames between the infinitely fast reactions and the quenching limits. The reaction rate response to variation in the Damköhler number is depicted in the S-shaped curve in Figure 2.6. A point located in the lower branch of curve before the ignition corresponds to a slowly reacting state in which the effect of diffusion prevents a thermal runaway. By increasing the Damköhler number, eventually the ignition point corresponding to Da_i is reached. If Da is further increased, a rapid transition to the upper side of the curve close to the equilibrium

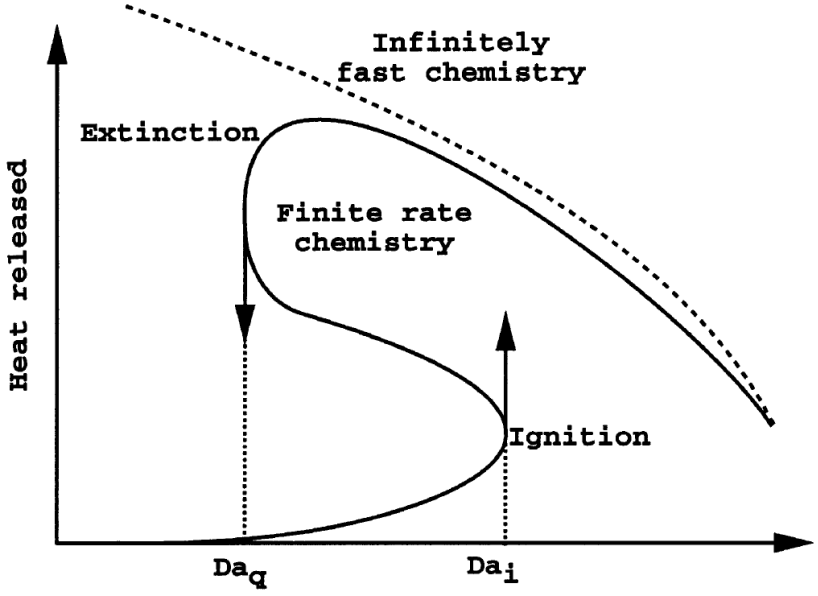

Figure 2.6: Heat release as a function of the Damköhler number for a strained counterflow diffusion flame [20].

state occurs. If from the upper branch one diminishes the Damköhler number, the quenching point corresponding to Da_q is reached and a sudden transition to the lower non-reacting branch takes place. Therefore, the middle branch between Da_i and Da_q is unstable whilst the two stable branches correspond to the two limits of pure mixing with no combustion ($Da \to 0$) and infinitely fast chemistry ($Da \to \infty$) [31].

Turbulent premixed flames

From empirical evidence it results that the flame speed is highly increased by turbulence, as demonstrated by the very high burning rates observed in spark ignited engines and gas turbines [21]. Although the mechanisms and the extent of the impact of turbulence on flame characteristics are not completely understood yet, it is commonly accepted that the higher burning rates associated with turbulent flames are due to the distortion and wrinkling of the flame front associated with turbulent fluctuations. This results in an increased flame specific surface area and thus in a boosted capability to consume the fresh mixture. The turbulent flame brush appears thick compared to a laminar flame, and can contain a large

amount of unburnt gases [45].

It is possible to identify different regimes in turbulent premixed combustion, on the basis of the comparison between the different scales characterising turbulence and chemical reactions [119, 120, 121]. For this purpose, the turbulent Reynolds number Re_t is defined as

$$Re_t = \frac{u'\ell}{\nu} \tag{2.103}$$

where the characteristic length ℓ is chosen to be equal to integral length scale $\mathcal{L}$, Equation (2.44). Therefore, the turbulent time scale is $\tau_t = \ell/u'$ and the Damköhler number can be expressed as

$$Da = \frac{\ell}{\ell_F}\frac{s_L}{u'} \tag{2.104}$$

For large Da values, the chemical time scale is much shorter that the turbulent one, and this corresponds to a thin reaction zone slightly distorted and wrinkled by the turbulent flow field. The internal structure of the flame is not significantly affected by turbulence and therefore resembles a laminar flame structure, called flamelet, and the corresponding regime is called flamelet regime. The other limit, corresponding to low Damköhler number values, is characterised by slow chemistry and thus reactant and product species are mixed by turbulence before the chemical reactions occur. This situation is referred to as the perfectly stirred reaction limit [20].

By introducing the Kolmogorov scales for turbulence, Equations (2.14), (2.15) and (2.16), two non-dimensional numbers can be introduced, called first and second Karlovitz numbers [31]. The first Karlovitz number is defined as

$$Ka = \frac{\tau_F}{\tau_\eta} = \frac{l_F^2}{\ell_\eta^2} = \frac{u_\eta^2}{s_L^2} \tag{2.105}$$

and expresses the ratio of the flame time scale to the Komogorov scale. The second Karlovitz number, Ka_δ represents the ratio between the inner layer thickness and the Kolmogorov scales, and is given by

$$Ka_\delta = \frac{l_\delta^2}{\ell_\eta^2} \tag{2.106}$$

where ℓ_δ is the thickness of the inner layer zone within the flame [122].

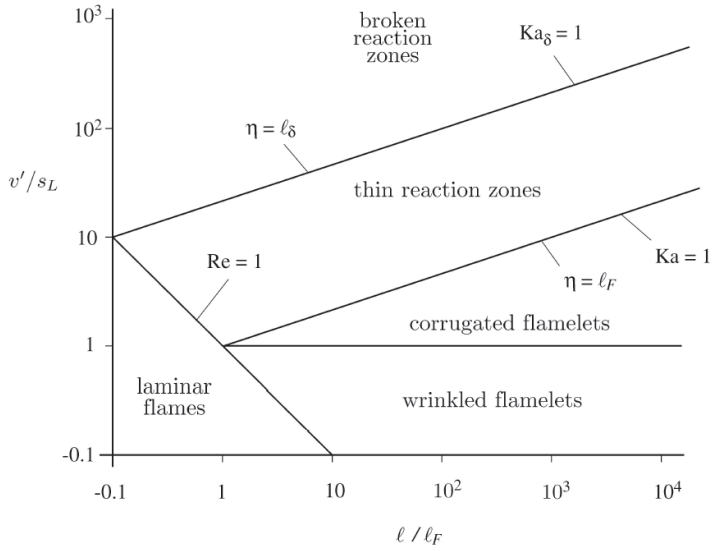

Figure 2.7: Borghi-Peters turbulent premixed combustion diagram [39].

A regime diagram for turbulent premixed combustion, referred to as Borghi-Peters diagram, can be obtained on the basis of the different values assumed by the non-dimensional numbers defined above, as shown in Figure 2.7. The line $Re = 1$ separates the laminar regime ($Re < 1$) from the turbulent one ($Re > 1$). With reference to turbulent flames, the following combustion regimes can be identified [31, 20]:

- Wrinkled flamelet regime (corresponding to $Ka < 1$ and $u'/s_L < 1$): since u' represents the turnover velocity of the large eddies, turbulent structures are not able to wrinkle the flame surface significantly, and the flame front is not affected by turbulence. Therefore turbulence/chemistry interactions are weak and the flame has a predominantly laminar character. Most practical combustion processes take place at high Reynolds number, and thus this regime is of little practical interest.

- Corrugated flamelet regime (corresponding to $Ka < 1$ and $u'/s_L > 1$): since the Kolmogorov scale is larger than the flame thickness, the flame still shows a laminar structure but the flame front is now noticeably wrinkled by its interaction with the large eddies.

- Thin reaction zones (corresponding to $Ka > 1$ and $Ka_\delta < 1$): in this regime

the smallest eddies can interact with and thicken the preheat zone within the flame, but do not affect the reaction zone that still presents a laminar nature.

- Broken reaction zones (corresponding to $Ka_\delta > 1$): the smallest turbulent eddies can now interact with the preheat and the reaction zones and no laminar structure can be identified. The heat losses from the reaction zone to the preheat zone are greatly enhanced, thus leading to flame extinction.

From the previous analysis, it is clear that the most common regimes found in practical combustion applications corresponds to the corrugated flamelet and the thin reaction zones.

Finally, although a classification such as the one provided in the diagram in Figure 2.7 can be quite useful to understand the different processes associated with various turbulent premixed combustion regimes, it is worth pointing out that it represents a qualitative analysis relying on numerous simplifying assumptions, e.g. neglecting of curvature effects, isotropic turbulence not affected by heat release, and therefore it should be used with care [20].

Turbulent non-premixed flames

The main effects of turbulence on non-premixed flames are an increase in the area of the stoichiometric surface due the distortions caused by velocity fluctuations, and changes in the structure of the reaction zone attached to to the $Z = Z_{st}$ surface.

Since non-premixed flames do not propagate, it is impossible to define a unique characteristic speed as for premixed flames. Also, the flame thickness depends on local strain rate determining the thickness of the local mixing layer, and therefore the identification of a fixed characteristic flame length for such flames is complicated as well. As a consequence, several different definitions for the characteristic scales of non-premixed flames have been proposed [123, 124, 125].

Despite some similarities between turbulent premixed and non-premixed combustion, the modelling of the latter is a much easier task thanks to the dominant role played by turbulent mixing [22]. Non-premixed combustion can therefore

be described with reasonable accuracy by the turbulent transport of a conserved scalar, as will be illustrated in the next sections.

Partially-premixed flames

Premixed and non-premixed combustion represent two limits and somehow idealised cases of perfectly mixing and complete separation between fuel and oxidizer, respectively. In most practical applications the combustion process does not fall into any of these two categories, and these cases are referred to as partially-premixed combustion [39].

Two different burning modes can be identified within the partially-premixed regime. In a lean-premixed gas turbine combustor, the fuel and oxidizer are mixed before entering the combustion. Nevertheless the inevitable presence of inhomogeneities in the mixture leads to non-uniform values of the equivalence ratio in the domain [45]. Therefore, the combustion process cannot be regarded as purely premixed, since the mixture composition is not constant, but nowhere in the domain is the mixture characterised by a stoichiometric composition. Such a regime is referred to as stratified combustion [22]. The local combustion process can be regarded as premixed, with additional flame wrinkling due to fluctuations in the burning rate arising from inhomogeneities in the mixture composition.

On the other hand, some configurations exist (e.g: rich fuel-air jet flame surrounded by a lean fuel-air jet, lean-premixed gas turbine combustor with non-premixed pilot flame) where both non-premixed and premixed burning modes are present, and such a regime is referred to as premixed/non-premixed combustion [22]. The mixture includes stoichiometric composition, with the equivalence ratio in the domain ranging from lean ($\phi < 1$) to rich ($\phi > 1$) values, even beyond the flammability limits. Since premixed and non-premixed burning modes coexist in premixed/non-premixed flames, these can be regarded as the most challenging from the modelling point of view.

Lifted turbulent jet flames [126, 127, 128] represent a typical test case employed to investigate the premixed/non-premixed combustion, since partially-premixed burning is observed at the lift off height of diffusion jet flames [129]. Triple flames [130] are commonly regarded as a key structure in partially-premixed

burning and have been the object of several studies as well [131, 132, 133].

2.3.2 Modelling of turbulent premixed combustion

Most models for turbulent premixed combustion are based on a single one-step irreversible reaction, as the one in Reaction (R 2.1). Furthermore, the changes in pressure are usually neglected, a unity Lewis number is assumed for all species and the system is considered to be adiabatic [38].

The key variable employed in the modelling of turbulent premixed combustion is the same as that introduced for describing laminar premixed flames, i.e. the progress variable c [45]. Therefore, in the context of the RANS approach, the governing equations used to describe turbulent premixed combustion are the Favre-averaged continuity and momentum equations and the transport equation for $\tilde{c}$, that can be derived by considering $\phi = c$ in Equation (2.41), namely

$$\frac{\partial}{\partial t}\left(\bar{\rho}\tilde{c}\right) + \frac{\partial}{\partial x_j}\left(\bar{\rho}\tilde{c}\tilde{u}_j\right) = \frac{\partial}{\partial x_j}\left(\bar{\rho}\bar{D}\frac{\partial \tilde{c}}{\partial x_j} - \bar{\rho}\widetilde{c'u'_j}\right) + \bar{\omega}_c \tag{2.107}$$

The modelling of the averaged chemical source term $\bar{\omega}$ is the main aim of turbulent combustion modelling. Unfortunately, the exponential term in the Arrhenius expression for ω, Equation (2.80), results in a highly non-linear behaviour of the reaction rate. This rules out the possibility of solving the problem by using a standard perturbation method based on the Taylor expansion [45]. Therefore, more advanced modelling approaches, derived from physical analysis of the combustion process, have been derived in order to close the mean reaction rate term.

Eddy-Break-Up and derived models

The Eddy-Break-Up (EBU) model proposed by Spalding [134, 135] has been developed under the assumption of high Reynolds and Damköhler numbers. This model assumes that chemical kinetics does not play any explicit role in the determination of the reaction rate, which is governed only by the turbulent mixing and the progress variable fluctuations. Therefore, in the EBU the mean chemical source term is evaluated as

$$\bar{\omega} = -C_{EBU}\rho\frac{\sqrt{\widetilde{c'^2}}}{\tau_t} \tag{2.108}$$

where C_{EBU} is a constant of the order of unity, τ_t is a characteristic turbulence time assumed to be equal to k/ϵ and the progress variable turbulent fluctuations are evaluated using its variance $\widetilde{c'^2}$. The progress variable variance can be estimated from a suitable transport equation, or modelled assuming an infinitely thin flame front [20]. A simple model can be derived by assuming an infinitely thin flame front, and therefore imposing that c is equal to either 0 or 1. Then. the progress variable variance can the be easily estimated from

$$\bar{\rho}\widetilde{c'^2} = \overline{\rho\left(c-\bar{c}\right)^2} = \bar{\rho}\bar{c}(1-\tilde{c}) \tag{2.109}$$

The square root in the expression for $\bar{\omega}$ has been originally introduced from dimensional arguments, but leads to mathematical inconsistencies when considering the derivative of the mean reaction rate with respect to the progress variable. Therefore, the following expression is used in practical applications [20]

$$\bar{\omega} = C_{EBU}\rho\frac{\epsilon}{k}\tilde{c}(1-\tilde{c}) \tag{2.110}$$

The EBU model is very attractive since it provides a simple expression for the reaction rate in terms of known quantities without the need to solve any additional transport equations. Since it results in a single value for the reaction rate, regardless of the considered chemical kinetics, it should not be used in combination with multi-step chemical mechanisms. Also, the EBU model tends to overestimate the reaction rate in regions characterised by elevated strain [20]. Finally, tuning of the model constant C_{EBU} is needed in order to obtain reasonable results for different applications [136].

The expression for the reaction rate in the EBU model has been modified in the Eddy Dissipation model from Magnussen and Hjertager [137], by expressing the reaction rate as a function of the mean mass fraction of the deficient species, i.e. fuel in lean combustion and oxygen in rich combustion.

In the context of LES, the turbulent time scale τ_t is assumed to be given by [38]

$$\tau_t \approx \frac{\Delta}{u'_{SGS}} \approx \frac{\Delta}{\sqrt{k_{SGS}}} \tag{2.111}$$

A further extension of the model to include finite-rate kinetics effects and allow the use of multi-step chemistry has been carried out by Magnussen and

co-workers [138, 139] in the Eddy Dissipation Concept (EDC) model. This model stems from the observation that chemical reactions usually occur within a thin reaction zone that is smaller than the size of the numerical grid. Therefore the EDC assumes that, within a single mesh element, the chemical reaction takes place within small turbulent structures referred to as "fine scales" surrounded by a molecular mixing region where no chemical reactions take place. The influence of turbulence is accounted for by relating the fine scales definition to turbulent quantities scales as [140]

$$\ell^* = C_{\ell^*} \left(\frac{\nu \epsilon}{k^2} \right) = C_{\ell^*} \left(Re_t \right)^{-1/4} \tag{2.112}$$

and

$$\tau^* = C_{\tau^*} \left(\frac{\nu}{\epsilon} \right)^{1/2} = C_{\tau^*} \left(Re_t \right)^{-1/2} \frac{k}{\epsilon} \tag{2.113}$$

where ℓ^* and τ^* are the characteristic length and time, respectively, associated with the fine scales. The fine scales are then treated as a constant pressure plug flow reactor, with initial conditions taken as the current species and temperature in the cell, and the Arrhenius rates are integrated over a time interval equal to τ^* and the species source terms are evaluated accordingly. Therefore, the EDC model is able to account for finite-rate effects and can be employed with multi-step chemical mechanisms. However, the highly non-linear Arrhenius reaction rates result in a numerically stiff system, which usually requires special numerical treatment to be solved (e.g. the ISAT algorithm [38]). Also, since a transport equation has to be solved for every chemical species in the system, the use of detailed chemical mechanisms results in elevated computational costs.

Turbulent flame speed models

Turbulent flames can be characterised by the value of the turbulent flame speed s_T. The progress variable source term can then be expressed as a function of s_T as

$$S_c = \rho_u s_t \left| \nabla c \right| \tag{2.114}$$

Alternatively, the flame front propagation can be described by means of the G-equation as [141]

$$\bar{\rho} \frac{\partial G}{\partial t} + \bar{\rho} \tilde{u}_j \frac{\partial G}{\partial x_j} = \rho_u s_T \left| \nabla G \right| \tag{2.115}$$

in which the position of the flame is indicated by the isosurface $G = G_0$. A comprehensive description of the G-equation approach and the related level-set formalism can be found in [121] and [39].

Unfortunately, the exact definition of turbulent flame speed can be tricky, since a large scatter is observed in the experimental data due to its dependence on various parameters related to the chemistry, turbulent scales and geometry characteristics [142]. Popular models for the evaluation of the turbulent flame speed have been proposed by Zimont et al. [143] and Peters [39].

Bray-Moss-Libby model

The Bray-Moss-Libby (BML) model combines a statistical approach with physical analysis and is well-known in turbulent premixed combustion modelling, since it can highlight peculiar features such as the relationship between the mean reaction rate and the scalar dissipation rate and the possible presence of counter-gradient transport [20]. A one-step irreversible chemical reaction is considered, together with the simplifying assumptions of perfect gases, incompressible flow and unity Lewis number.

The main concept at the basis of the BML model is to express the PDF of the progress variable at a given space location and time as the sum of contributions coming from unburnt, burnt and reacting gases as

$$P(c, \mathbf{x}, t) = \alpha(\mathbf{x}, t)\delta(c) + \beta(\mathbf{x}, t)\delta(1 - c) + \gamma(\mathbf{x}, t)f(c, \mathbf{x}, t) \tag{2.116}$$

where α, β and γ denote the probability to find unburnt, burnt and burning gases at $(\mathbf{x}, t)$, respectively, and $\delta(c)$ and $\delta(1 - c)$ are the Dirac delta functions corresponding to fresh and burnt gases, respectively.

If the PDF $P(c, \mathbf{x}, t)$ is known, then the mean reaction rate in Equation (2.107) can be expressed as

$$\bar{\omega}(\mathbf{x}, t) = \int_0^1 \omega(c)P(c, \mathbf{x}, t)dc \tag{2.117}$$

The BML model [144, 145, 146] has been derived under the assumption $Re >> Da >> 1$, corresponding to $\gamma << 1$. Therefore, the reaction zone can be assumed to be infinitely thin and an intermittent behaviour is associated with the progress variable, assuming values equal either to 0 or 1. Since this analysis assumes that

γ is negligible in Equation (2.116), the resulting PDF cannot be employed to evaluate the mean reaction rate. On the other hand it can be shown, from physical consideration and mathematical manipulation of the governing equations, that the mean reaction rate under the considered assumptions can instead be evaluated as [144]

$$\bar{\omega} = 2\frac{\overline{\rho\chi}}{2c_m - 1} \tag{2.118}$$

which highlights the close connection between the chemical source term and the dissipation rate. The term c_m in Equation (2.118) represents a modified expression for the progress variable [20]. It is possible to derive and resolve a transport equation for the scalar dissipation rate $\overline{\rho\chi}$ [147]. Alternatively, an algebraic expression can be employed to evaluate the scalar dissipation term in Equation (2.118), and the EBU model expression for the reaction rate, Equation (2.110), is recovered from the BML assumptions [20].

The hypothesis of intermittency between burnt and unburnt state leads to an expression for the Favre-averaged valued of the generic quantity ϕ based on its conditional averaged values in the fresh gases

$$\bar{\phi}^u = \int \phi \bar{P}_c(\phi|c=0)d\phi \tag{2.119}$$

and in the burnt gases

$$\bar{\phi}^b = \int \phi \bar{P}_c(\phi|c=1)d\phi \tag{2.120}$$

where $\bar{P}_c(\phi|c)$ is the conditional PDF of ϕ for the given value of the progress variable. Based on the previous definitions, the Favre-averaged value of ϕ can be expressed as [20]

$$\tilde{\phi} = (1-\tilde{c})\bar{\phi}^u + \tilde{c}\bar{\phi}^b \tag{2.121}$$

The turbulent flux of c, present in an unclosed form in Equation (2.107) can thus be expressed as

$$\widetilde{\bar{\rho}u_i'c'} = \bar{\rho}\tilde{c}(1-\tilde{c})\left(\bar{u}_i^b - \bar{u}_i^u\right) \tag{2.122}$$

This expression allows us to explain the presence of counter-gradient turbulent transport in turbulent premixed flames that has been observed both theoretically [148] and experimentally [57, 149], and is one of the most remarkable results of the BML analysis. Although an exact evaluation of conditioned velocities is

not straightforward, it usually results in $\bar{u}_i^b > \bar{u}_i^u$ due to the thermal expansion through the flame front. Therefore the turbulent flux of the the progress variable has the same sign as the gradient $\frac{\partial \tilde{c}}{\partial x_i}$, which is in contrast with the gradient transport hypothesis (Equation (2.42)) usually employed to model turbulent fluxes. Counter-gradient diffusion is often disregarded in the modelling of turbulent combustion and the gradient transport hypothesis is commonly employed. The inaccuracy introduced by the use of the gradient transport hypothesis, and therefore the neglect of counter-gradient diffusion, is usually smaller in LES with respect to the RANS approach, since unresolved fluxes in the former are usually smaller, and a portion of the counter-gradient diffusion is described in LES through direct solution of the resolved scales [38].

Flame surface density and coherent flame model

Given the assumed intermittency between burnt and fresh gases in the BML approach, Bray et al. [145] proposed to evaluate the mean reaction rate as the product between the flame crossing frequency and a local reaction rate per flame crossing. However, although the flame crossing frequency can be easily evaluated experimentally, the quantification of the reaction rate associated with flame crossing is not straightforward [20]. Therefore, the model has been modified [146, 150] in order to express the mean reaction rate as a function of the flame surface density Σ and the reaction rate per unit surface area, which is related to the laminar flame speed s_L.

The flame surface density is a measure of the flame convolution, and high values of Σ correspond to elevated turublent reaction rates. One of the main advantage of the flame surface density approach is that the exact transport equation for Σ can be obtained from basic principles and all of its terms can be directly evaluated through experiments or DNS [22]. The most common approaches to close the transport equation for Σ are those employed in the coherent flame model [151] and its derivation. An in-depth analysis of the Σ transport equation and the related modelling approaches is reported in [20] and [38].

Thickened flame model

As reported in the previous sections, laminar premixed flames are characterised by a flame thickness of the order of 1 mm or even less and, since the flame speed depends on molecular diffusion and chemical reactions within the flame, a sufficient mesh resolution is necessary within the flame in order to properly resolve it. Such a small size for the numerical grid is often not feasible in practical applications. An attractive solution for resolving the flame front propagation on coarse (relatively to the flame thickness) grids has been proposed by O'Rourke and co-workers [152, 153].

Following the simple theory of premixed laminar flame propagation, it can be shown [38] that the laminar flame speed s_L is proportional to

$$s_L \propto \sqrt{DB} \tag{2.123}$$

and flame thickness ℓ_F can be expressed as

$$\ell_F \propto \frac{D}{s_L} = \sqrt{\frac{D}{B}} \tag{2.124}$$

where D is the thermal diffusivity (equal to mass diffusivity under the unity Lewis number assumption) and B is the pre-exponential factor of the one-step reaction considered to represent the chemistry. If the diffusivity is multiplied by a factor F, called the thickening factor, and the pre-exponential factor is divided by the same factor, the value of the laminar flame speed is kept constant while the flame thickness is increased by a factor equal to F. In this procedure, the value of F can be evaluated as

$$F = \frac{N\Delta}{\ell_F} \tag{2.125}$$

where N is the number of computational points used to resolve the flame.

Since the reaction rate is still expressed using the Arrhenius law, the thickened flame model can account for various effects related to the chemical kinetics (e.g. ignition, flame stabilization). The model is usually employed with a single-step global reaction, but can also be used together with multi-step chemistry although, as in the case of the EDC model, special care in the treatment of the resulting stiff system is necessary. Also, it has to be pointed out that by increasing the flame thickness from ℓ_F to $F\ell_F$ the Damköhler number is reduced by a factor F, and

therefore the interactions between the chemical and turbulent scales are modified. This effect is usually compensated by the introduction of factor E, called efficiency function, that corresponds to a SGS wrinkling factor in the context of LES [38].

Presumed-PDF and transported-PDF approaches

The knowledge of the PDF associated with a given variable of interest, e.g. temperature, species mass fractions, etc., allows the evaluation of its mean, variance and higher-order moments through expressions having the form of Equations (2.21) and (2.22). Although theoretically the PDF function can assume any arbitrary shape, in most combustion applications the PDFs have common characteristics, and therefore it can be assumed that they can be expressed as a function of a limited number of control parameters [38]. The obvious choice for these parameters is represented by the moments of the considered variable, e.g. its mean value and the variance. Since the control variable for premixed combustion is the progress variable c, the presumed-PDF function is defined by the mean progress variable value and its variance at any given point within the domain [154]. As will be detailed further in the next section, the same approach can be employed for non-premixed combustion, where the control variable is represented by the mixture fraction Z.

Therefore, according to this approach the PDF function can be evaluated at any point, providing that $\tilde{c}$ and $\widetilde{c'^2}$ are known. The progress variable variance $\widetilde{c'^2}$ can be evaluated by means of a suitable transport equation or by employing a simplified algebraic expression, as the one in Equation (2.142). Details on the transport equation for the progress variable variance and the modelling assumptions usually employed in its closure can be found in [38].

Various presumed-PDF shapes can be found in the literature [124]. Among the different possible options, the most commonly employed in turbulent combustion modelling is the β-function [155], defined as

$$P(c) = \frac{(c)^{a-1}\,(1-c)^{b-1}}{\int (c)^{a-1}\,(1-c)^{b-1} dc} \tag{2.126}$$

where the two parameters a and b are a function of the progress variable mean

and variance only, i.e [20].

$$a = \tilde{c}\left(\frac{\tilde{c}(1-\tilde{c})}{\widetilde{c'^2}} - 1\right) \tag{2.127}$$

and

$$b = a\left(\frac{1}{\tilde{c}} - 1\right) \tag{2.128}$$

The β-function can approximate various PDF shapes from a Gaussian distribution to a bimodal PDF in the limit $a << 1$ and $b << 1$. The latter case represents the BML approach, in which only two states, $c = 0$ and $c = 1$, are possible.

The presumed-PDF approach is a very attractive model since it allows the determination of the PDF in a simple way. Nevertheless, accuracy issues can be associated with the use of the β-function, especially in its bimodal limit, in the calculation of the averaged chemical source term [45, 156]. Also, the suitability of the β-function for different applications and combustion regimes is somehow arbitrary, since its choice is not based on any solid physical argument [157].

The alternative to the presumed-PDF approach is the formulation and solution of a balance equation for the PDF itself, as proposed by Pope in [158] [5]. It is possible to derive an exact transport equation for the PDF of the progress variable or, in case of a multi-species system, for the PDF $P(Y_1, ..., Y_N)$. It is also possible to formulate a transport equation for the joint velocity/species PDF $P(\mathbf{u}, Y_1, ..., Y_N)$. In the latter case, the transport equation does not contain a turbulent flux term, and therefore it is not necessary to employ a turbulence model for the mean flow field. On the other hand, the transport equation for the joint velocity/species PDF contains additional unclosed terms that require an appropriate model [20].

The main advantage of the transported-PDF method is that the chemical source term in the PDF transport equation is expressed in a closed form and therefore does not require modelling, allowing the use of complex detailed chemical mechanisms. Unfortunately, the molecular diffusion term is unclosed and needs to be modelled, which results to be a challenging task [38].

Usually the PDF transport equation is not resolved directly, but by means of stochastic approaches such as the Monte-Carlo method [159]. The transported-

[5] As in the case of the presumed-PDF technique, the transported-PDF approach is also suitable for the modelling of non-premixed (and partially premixed) combustion processes.

PDF approach represents a general and powerful tool for the modelling of turbulent combustion, provided that a suitable model for molecular transport is provided. Unfortunately its application to complex configuration remains complicated and computationally expensive [38]. A detailed description on transported-PDF methods is reported in [158] and [160].

2.3.3 Modelling of turbulent non-premixed combustion

In the description of laminar non-premixed flames it has been shown that, under some assumptions, the chemical species and the temperature can be directly related to the mixture fraction Z and its scalar dissipation rate χ. Most of models for turbulent diffusion flames are based on this concept. Therefore, even if it is possible to model turbulent non-premixed combustion by means of a suitable closure for the mean reaction rate, e.g. Eddy Dissipation model in the framework of the infinitely fast chemistry and EDC, presumed-PDF or transported-PDF in the context of finite-rate chemistry, the present review will focus on the models based on the mixture fraction approach. In these models the transport equations for the chemical species and temperature are not solved for, and therefore there is no need to formulate a closure for the mean reaction rate [38].

The Favre-averaged transport equation for the mixture fraction can be obtained from Equation (2.41), bearing in mind that the mixture fraction is a conserved scalar and therefore its source term is equal to zero, and it is given by

$$\frac{\partial}{\partial t}\left(\bar{\rho}\tilde{Z}\right)+\frac{\partial}{\partial x_j}\left(\bar{\rho}\tilde{Z}\tilde{u}_j\right)=\frac{\partial}{\partial x_j}\left(\overline{\rho D\frac{\partial Z}{\partial x_j}}-\bar{\rho}\widetilde{Z'u'_j}\right) \tag{2.129}$$

where the molecular diffusive flux has been accounted for using the Fick's law and the turbulent flux $-\bar{\rho}\widetilde{Z'u'_j}$ is usually modelled according to the gradient transport hypothesis. The gradient transport assumption seems more appropriate in the case of non-premixed flames with respect to premixed combustion, since evidence of counter-gradient transport in the former cases is less evident compared to the latter [38].

Infinitely fast chemistry

Under the assumptions of infinitely fast chemistry, unity Lewis number, adiabatic combustion process and constant specific heat the instantaneous temperature T and species mass fractions Y_k depend only on the mixture fraction and can be expressed as $T = T(Z)$ and $Y_k = Y_k(Z)$ [31]. Therefore, the related Favre-averaged values can be expressed as [6]

$$\tilde{T} = \int T(Z)P(Z)dZ \tag{2.130}$$

and

$$\tilde{Y_k} = \int Y_k(Z)P(Z)dZ \tag{2.131}$$

Thus, the problem of estimating $\tilde{T}$ and $\tilde{Y_k}$ is reduced to the determination of the mixture fraction PDF $P(Z)$, under the present assumption of infinitely fast chemical reactions [39].

Likewise to turbulent premixed flames, the PDF can be either presumed or evaluated through a suitable transport equation. For practical applications, the most common approach is to employ a β-function to approximate the shape of $P(Z)$. The β-function has been found to be a more appropriate approximation of the experimentally observed PDFs for non-premixed combustion with respect to premixed flames [157]. More flexible PDF shapes have been proposed that can overcome these shortcomings, but their definition usually involves high-order moments of the considered variable, and therefore their use in practical applications is complicated [161].

The β-function is completely determined by the first and second moments of the mixture fraction. Therefore, similarly to the presumed-PDF approach for premixed combustion, a transport equation or a suitable algebraic expression for the mixture fraction variance $\widetilde{Z''^2}$ has to be employed, in addition to Equation (2.129) for $\tilde{Z}$. An in-depth analysis of the mixture fraction variance transport equation and of the related modelling assumptions can be found in [38]. It is worth pointing out that the transport equation for $\widetilde{Z''^2}$ contains the scalar dissipation

[6] The evaluation of Favre-averaged quantity actually requires the Favre-averaged PDF $\tilde{P}(Z) = \frac{\varrho}{\bar{\rho}}P(Z)$. For the sake of simplicity the Favre-averaged PDF $\tilde{P}(Z)$ will be indicated by $P(Z)$ in the text.

rate of the mixture fraction fluctuations

$$\bar{\rho}\tilde{\chi}_f = \overline{2\rho D \frac{\partial Z'}{\partial x_j}\frac{\partial Z'}{\partial x_j}} \tag{2.132}$$

In the literature, different expressions are associated with the definition of the scalar dissipation rate [20]. In fact, the scalar dissipation rate can refer to the mixture fraction Z, as in the laminar case of Equation (2.100), or to the mixture fraction fluctuations, as in Equation (2.132). For constant density flows, the total scalar dissipation rate can be written as

$$\bar{\rho}\tilde{\chi}_{tot} = 2\overline{\rho D\left(\frac{\partial Z}{\partial x_j}\right)^2} = 2\overline{\rho D}\left(\frac{\partial \tilde{Z}}{\partial x_j}\right)^2 + 2\overline{\rho D\left(\frac{\partial Z'}{\partial x_j}\right)^2} = \bar{\rho}\chi_m + \bar{\rho}\chi_f \tag{2.133}$$

In RANS the scalar dissipation rate contribution due to mean mixture fraction gradients, χ_m, is usually neglected [20] and therefore

$$\tilde{\chi}_{tot} \approx \tilde{\chi}_f \tag{2.134}$$

Since χ_f plays the same role for Z as the turbulent kinetic energy dissipation ϵ does for k, χ_f is usually modelled as [38]

$$\tilde{\chi}_f = C_\chi \frac{1}{\tau_t}\widetilde{Z'^2} = C_\chi \frac{\epsilon}{k}\widetilde{Z'^2} \tag{2.135}$$

In LES, the equilibrium hypothesis leads to the following expression for χ_f [20]

$$\chi_f = C_\chi \frac{\nu + \nu_{SGS}}{\sigma_t}\left(\frac{\partial \tilde{Z}}{\partial x_j}\right)^2 \tag{2.136}$$

In CFD codes, the PDF integrations in Equations (2.130) and (2.131) are usually performed at the pre-processing stage for different values of $\tilde{Z}$ and $\widetilde{Z'^2}$ and the results are stored in a look-up table where they can be retrieved at run-time based on the local values of $\tilde{Z}$ and $\widetilde{Z'^2}$ in order to obtain $\tilde{T}$ and $\tilde{Y}_k$ [63].

Finite-rate chemistry

The assumption of infinitely fast chemistry is clearly not adequate to describe important phenomena such as flame quenching and pollutants formation. The flamelet concept is widely employed to solve, at least partially, this issue and incorporate finite-rate chemistry effects into mixture fraction-based models for

turbulent non-premixed combustion [38]. The flamelet concept assumes that the turbulent non-premixed flame can be represented as an ensemble of thin, laminar diffusion flames called flamelets, embedded in the turbulent flow [118, 117, 162]. In order for this assumption to be valid, the reaction zone has to be small compared to the turbulent scales, corresponding to a large Damköhler number condition.

The widely used steady laminar flamelet model (SLFM) assumes that the local structure of the laminar flamelets embedded in the turbulent flow can be approximated by a steady planar counterflow diffusion flame, such as the one depicted in Figure 2.5. The steady version of the flamelet Equations (2.98) and (2.99) can be solved and the results can be used to parametrise the instantaneous values of T and Y_k as a functions of only the mixture fraction Z and χ_{st} [38], under the condition that a model for χ across the flamelet as function of χ_{st} and Z is provided [163]. It has to be pointed out that, as it will be explained in more detail in the next sections, other parameters can be included in the parametrisation of the variables of interest. If, for instance, the time dependence is retained in the flamelet equations, the so called unsteady flamelet models are obtained [164, 165].

Therefore, in the SLFM approach, the evaluation of the Favre-averaged temperature and species mass fractions requires an expression for the joint-PDF $P(Z, \chi_{st})$. Usually, statistically independence of Z and χ_{st} is invoked, based on the observation that the mixture fraction is a measure of the mixing between fuel and oxidizer which is governed by large scale effects, while χ_{st} is related to the local flame structure and therefore depends on small scale effects [45]. The mixture fraction PDF is usually approximated with a β-function shape, whilst a Dirac-delta function can be employed for χ_{st}, assuming that the scalar dissipation does not change significantly along the flame front [38]. Under these assumptions the joint-PDF can be expressed as

$$P(Z, \chi_{st}) = P(z)\delta(\chi_{st} - \tilde{\chi}_{st}) \tag{2.137}$$

At this point, $\tilde{\chi}_{st}$ has still to be defined, and it can be expressed as a function of the mean scalar dissipation rate $\tilde{\chi}$ as [38]

$$\tilde{\chi} = \tilde{\chi}_{st} \int \frac{F(Z)}{F(Z_{st})} P(Z) \tag{2.138}$$

where

$$F(Z) = exp\left(-2\left(erfc^{-1}\left(2Z-1\right)\right)^2\right) \tag{2.139}$$

Therefore, since $\tilde{\chi}$ can be evaluated as in Equation (2.135), it is possible to express all the mean scalar quantities as functions of known resolved variables.

With respect to infinitely fast chemistry models, the SLFM approach introduces the additional quantity χ_{st} to account for finite-rate effects. This improves the prediction of some features related to the chemical kinetics, such the prediction of intermediate species in diffusion flames [45]. Also, since the chemistry is resolved in simple laminar configurations, detailed chemical mechanisms can be employed with a limited computational cost. One of the main drawbacks of the SLFM is that its range of validity cannot be identified clearly, due to the difficulty of defining combustion regimes in turbulent diffusion flames. More details on the limitations of the model are discussed in [22, 45].

Another approach to account for finite-rate effects in the context of primitive variable models has been proposed independently by Klimenko [166] and Bilger [167] and is referred to as Conditional Moment Closure (CMC). It is based on the hypothesis that the fluctuations in T and Y_k are mainly controlled by the fluctuations in the mixture fraction. This approach is not described in detail here, since it is associated with a considerably high computational cost and therefore is not suitable for most practical combustion problems [38]. More details on the CMC approach can be found in [168].

The PDF concept introduced in the context of RANS can be readily extended to the LES approach. The Favre-filtered scalar ϕ can be expressed as in Equations (2.130) and (2.131) where, in the context of LES, $P(Z)$ represent the subgrid-scale PDF [169], which is sometimes referred to as Filtered Probability Density Function (FPDF) [7]. The conceptual differences between the PDF employed in the context of RANS and the FPDF invoked for LES are summarised by Pitsch in [29].

The β-function is usually employed to represent the mixture fraction FPDF. The presumed FPDF is then defined by the filtered mixture fraction $\tilde{Z}$ and its

[7] The case of infinitely fast chemistry is reported here, but the concept can be easily extended to joint-PDFs such as $P(Z, \chi)$

SGS variance $\widetilde{Z''^2}$. Cook and Riley [170] observed that the β-function represents a good approximation for the mixture fraction FPDF, and it better mimics the actual observed statistical distribution with respect to its use as a PDF for RANS. Also, the inability of the β-function to account for intermittency has less negative consequences with respect to RANS, since most of the intermittent behaviour takes place at the resolved scales and therefore can be captured by LES regardless of the SGS closure [31].

The most common approach in LES is not to resolve a transport equation for the SGS mixture fraction variance. Instead, an equilibrium assumption is made between the production and the scalar dissipation terms in the transport equation, leading to the following expression for $\tilde{\chi}$ [29]

$$\tilde{\chi} = 2D_{SGS}\left(\frac{\partial \tilde{Z}}{\partial x_j}\right)^2 \tag{2.140}$$

where D_{SGS} is a diffusion SGS coefficient that can be evaluated as $C_{D_{SGS}}\nu_{SGS}$. From Equation (2.140) and the model for $\tilde{\chi}$ in Equation (2.135), the following expression for $\widetilde{Z''^2}$ can be obtained [171]

$$\widetilde{Z''^2} = C_{Z,v}\Delta^2\left(\frac{\partial \tilde{Z}}{\partial x_j}\right)^2 \tag{2.141}$$

Following the same reasoning, a similar expression can be derived for the progress variable SGS variance for premixed combustion modelling, i.e.

$$\widetilde{c''^2} = C_{c,v}\Delta^2\left(\frac{\partial \tilde{c}}{\partial x_j}\right)^2 \tag{2.142}$$

2.3.4 Effects of carbon dioxide and steam dilution on gas combustion

Both the advanced gas turbine cycles considered in the present work, i.e. EGR and STIG, are characterised by the presence of diluent species in the combustion environment with respect to standard air-fired operation. The main diluting species considered here are carbon dioxide and steam. The enhanced presence of these two chemical species is also common in other technical solutions such as Moderate or Intense Low-oxygen Dilution (MILD) [172] and oxy-fuel combustion

Substance	O_2	N_2	CO_2	H_2O
ρ (kg m^{-3})	0.385	0.337	0.529	0.217
c_p (10^{-3} J kg^{-1} K^{-1})	1.09	1.17	1.23	2.29
k (10^3 W m^{-1} K^{-1})	79.7	66.0	70.6	97.1
μ (10^6 N s m^{-2})	49.1	41.6	41.3	37.6

Table 2.1: Properties of oxygen, nitrogen, carbon dioxide and steam at 0.1 MPa and 1000 K [36, 175].

[173]. Consequently, the impact of dilution on gas combustion has been investigated both numerically and experimentally in several studies, and a review of the main findings is reported here. Since these studies concern the fundamental impacts of dilution on combustion characteristics, they are usually carried out in simple laminar configurations, and rely on the use of detailed chemical mechanisms to describe the combustion chemistry.

In the case of adiabatic flames, it is observed that the presence of reactive diluent species, such as carbon dioxide and steam, affects the combustion process in two ways [32, 174, 36]:

- Thermal effects are related to the different physical properties (e.g. different specific heat, density and transport properties) of the diluting species with respect to the replaced species. A comparison between the physical properties of different species at 0.1 MPa and 1000 K is reported in Table 2.1. In the case of CO_2 and H_2O dilution, thermal effects usually result in reduced flame temperature and flame speed.

- Chemical effects due to the chemical reactivity of CO_2 and H_2O. Chemical effects comprise direct participation of the diluting species in elementary reactions or their action as a third body in termolecular reactions.

Although these two phenomena are interconnected, with the reduced temperature due to the thermal effects having an impact on the kinetics of the chemical effects, various researchers [176, 177, 32, 178] have employed a technique based on the introduction of a "fake" diluent species in order to distinguish between chemical and thermal effects in numerical investigations. The fictitious diluting

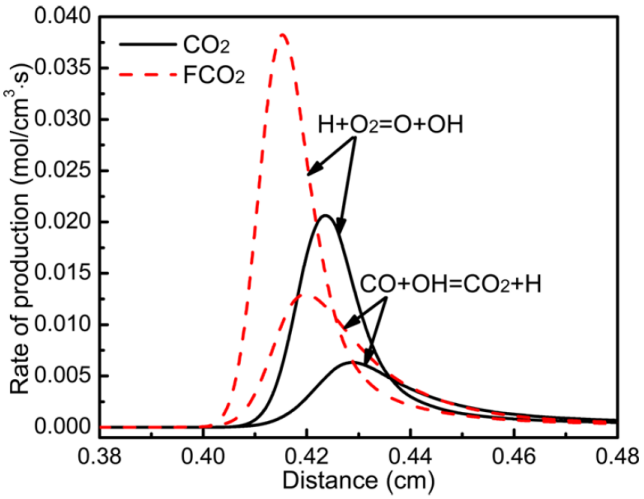

Figure 2.8: Rate of Reactions (R 2.2) and (R 2.3) with CO_2 and FCO_2 dilution, calculated using the GRI3.0 mechanism [176].

species, usually referred to as fake-CO_2 (FCO_2) and fake-H_2O (FH_2O), have the same thermal and transport properties of the actual diluent species but do not participate in the chemical reactions. In this procedure, the differences observed between the standard operation and the diluted operation with the fictitious species are due only to thermal effects.

An example of such an investigation is reported in Figure 2.8 from [176], reporting the calculated reaction rates for the chemical reactions

$$H + O_2 \rightleftharpoons O + OH \qquad \text{(R 2.2)}$$

and

$$CO + OH \rightleftharpoons CO_2 + H \qquad \text{(R 2.3)}$$

with both CO_2 and FCO_2 dilution in laminar 1D premixed flames. The calculations are carried out for a $CH_4/CO_2/O_2$ mixture at an equivalence ratio of 0.6, a mole fraction of CO_2 in the oxidizer of 0.5 and at unburnt temperature and pressure equal to 300 K and 0.1 MPa, respectively. The combustion process has been simulated employing a detailed chemical scheme for natural gas combustion, the GRI3.0 mechanism, consisting of 325 reactions and 53 species [179].

The difference between the red dashed curves and the black solid curves in Figure 2.8 can be thought of as being a measure of the impact of CO_2 on the combustion process due to chemical effects, since CO_2 and FCO_2 are characterised by

the same thermodynamic properties and therefore can be considered to produce the same thermal effects.

The chain-branching Reaction (R 2.2) has been reported to have the highest sensitivity coefficient to laminar flame speed for both hydrocarbon/air flames and CO_2-diluted systems [180, 176]. Reaction (R 2.3) has been identified as the main way in which carbon dioxide participates in the combustion chemistry. Its effect is to inhibit the combustion process by competing for the H radical with the chain-branching Reaction (R 2.2) via the reverse of Reaction (R 2.3) [176, 177, 181, 182].

A relatively small number of studies have addressed the impact of steam dilution, mainly because of the experimental difficulties arising in accurately controlling the amount of steam added to the reactive mixture [33]. Nevertheless, most studies [33, 32] agree that the impact of steam on the combustion chemistry is mainly due to its elevated third-body efficiency in the reaction

$$H + O_2 + M \rightleftharpoons HO_2 + M \qquad (R\,2.4)$$

which, similarly to the CO_2 effects, inhibits the chain-branching Reaction (R 2.2) by consuming H radicals.

The relative importance of thermal and chemical effects and the overall impact of dilution on the combustion process depends on the system operating conditions. Most of the works cited previously refer to ambient temperature and pressure levels, whilst only few studies, e.g. [183, 176, 182], addressed the elevated temperatures and pressures that are relevant to gas turbines.

From the modelling point of view, since both the carbon dioxide and steam dilution impact on the combustion chemistry at the radical level, it is clear that a detailed description of the chemistry is necessary to account for this effects at the modelling stage. The GRI3.0 mechanism gives overall satisfactory predictions for such diluted systems under a wide range of conditions, although a discrepancy with the experimental data has been observed for oxy-fuel mixtures at low levels of carbon dioxide and/or steam dilution, resulting in elevated adiabatic flame temperatures [33]. At adiabatic flame temperatures higher than about 2500 K significant thermal dissociation of CO_2 takes place, and the chemical mechanism needs to be revised in order to correctly account for this effect [176].

In addition to the aforementioned effects observed in simplified laminar con-

figurations, the presence of diluting species in more realistic swirl-stabilised turbulent flames has been observed to have an impact on the flow field, modifying the characteristics of the recirculation zones (RZs), as well as on the flame stabilisation mechanism and therefore on the stability limits of the device [36, 184].

2.3.5 Chemistry tabulation

The dual need to account for finite-rate effects and detailed chemistry on one side and reduce the computational costs associated with CFD simulations of combustion in complex configurations on the other side has led to the development of tabulation methods for the chemistry such as the Flamelet Prolongated Instrinsic Low Dimensional Manifold (FPI) [185] and the Flamelet Generated Manifold (FGM) [186]. Tabulated chemistry method are becoming more and more popular and have been employed in the CFD modelling of both lab-scale burners [187, 188, 189, 128] and industrial devices [26, 190, 191].

In both these methods it is assumed that the trajectories in the compositional space in turbulent flames can be approximated by the trajectories followed in the compositional space in laminar one-dimensional flamelets. A number of one-dimensional flamelets are solved and the scalar of interests (e.g: species mass fractions, reaction rates, temperature) are tabulated as a function of suitable controlling variables (e.g. mixture fraction, progress variable, enthalpy, scalar dissipation), likewise to the parametrisation of laminar non-premixed flamelets in terms of Z and χ_{st} in the SLFM model.

For instance, Pierce and Moin [192] employed the mixture fraction and the progress variable as tracking variables to map non-premixed flamelets, and successfully predicted flame lift-off in a coaxial jet combustor in a LES calculation using a presumed-PDF approach for combustion modelling.

An arbitrary number of tracking variables can be employed to map the 1D solutions in the manifolds [193], although the most common choice is to limit the number of variables to two, i.e. the mixture fraction and the progress variable. Theoretically, the choice of two control parameters is appropriate under a global one-step reaction assumption, since only two independent variables (i.e. fuel and oxidizer) exist in this case. Nevertheless, a priori evaluation of Z-Y_c manifolds

calculated with detailed chemistry shows excellent agreement with experimental data for partially-premixed methane-air jet flames even for minor species, provided that the flamelet type and the molecular transport model resemble the configuration to be investigated [194].

In general, both premixed and non-premixed flamelets can be used to generate the manifolds. Steady non-premixed flamelets are not suitable to predict premixed and partially-premixed flame propagation mode and do not cover the entire range of possible thermochemical states between $Y_c = 0$ and $Y_c = Y_{c,eq}$. On the other hand, premixed flamelets do not consider inhomogeneities in the mixture, and fluxes through Z iso-surfaces observed in diffusion flames or in curved partially-premixed flame fronts are not accounted for [193]. In the modelling of purely premixed or diffusion flames, it is clear that is convenient to employ flamelets corresponding to the regime of the turbuelnt flame that is going to be investigated. On the other hand, in the case of partially-premixed combustion the choice of the flamelet type to be employed to generate the manifold is not straightforward [112].

In both FGM and FPI the flamelet library is usually built from 1D steady premixed flamelets, and therefore fluxes in the mixture fraction are neglected. Premixed flamelets have the significant advantage of covering the full range of thermochemical states between unburnt and fully burnt conditions, unlike steady non-premixed manifolds [193]. Premixed flames can only be calculated between the lean and rich flammability limits, and therefore the solution is extrapolated from the flammability limits to $Z = 0$ and $Z = 1$ [195]. Although premixed manifolds are characterised by the inherent limitations discussed above, they have been successfully employed in the modelling of both non-premixed and partially premixed flames. Fiorina et al [196] carried out a systematic evaluation of premixed manifolds in predicting partially premixed and diffusion counterflow flames. When the equivalence ratio of the fuel/air mixture jet is between the flammability limits, the premixed manifold is in excellent agreement with the numerical results obtained with a fully detailed chemistry. Outside of the flammability limits, the presence of diffusive fluxes in the mixture fraction space result in a discrepancy between the tabulated premixed database and the detailed calculations.

Vreman et al. [197] employed both premixed and non-premixed generated manifolds in a LES simulation of different non-premixed jet flames. Although the considered flames are predominantly non-premixed, premixed and non-premixed tabulations gave similar results for main species and temperature predictions. Also, since premixed manifolds cover the non equilibrium range of the reaction progress, they provide better results in the prediction of flames characterised by extensive presence of local non-equilibrium, such as Sandia flame F.

Olbricht et al. [189] also employed a premixed flamelet database in LES calculations of non-premixed and partially-premixed swirling flames, obtaining good results for main species and temperature for both combustion regimes. Also in this case, the premixed manifold has been able to predict the presence of local extinction observed experimentally.

The transport equation for species and temperature for a steady premixed 1D flame can be solved in either the physical or the reaction progress space. The governing equations in the reaction progress space under the assumption of unity Lewis number have the form [193]

$$\frac{\partial Y_k}{\partial Y_c}\omega_{Y_c} = \rho\frac{\chi_{Y_c}}{2}\frac{\partial^2 Y_k}{\partial Y_c^2} + \omega_k \tag{2.143}$$

$$\frac{\partial T}{\partial Y_c}\omega_{Y_c} = \rho\frac{\chi_{Y_c}}{2}\frac{\partial^2 T}{\partial Y_c^2} - \frac{1}{c_p}\sum_{k=1}^{N} h_k\omega_k + \frac{\rho\chi_{Y_c}}{2c_p}\left(\frac{\partial c_p}{\partial Y_c} + \sum_{k=1}^{N} c_{p,k}\frac{\partial Y_k}{\partial Y_c}\right)\frac{\partial T}{\partial Y_c} \tag{2.144}$$

The scalar dissipation term χ_{Y_c} depends on the spatial distribution of the progress variable and therefore needs to be modelled when the equations are solved in the compositional space. The scalar dissipation term within one flamelet at different equivalence ratio values can be modelled as [193]

$$\chi_{Y_c}(Z,c) = \chi_{max}^{st} exp\left(-2\left(erfc^{-1}(\left(\frac{Z}{Z_{st}}\right)\right)^2\right) exp\left(-2\left(erfc^{-1}(2Y_c)\right)^2\right) \tag{2.145}$$

where χ_{max}^{st} is the maximum value of the scalar dissipation within the stoichiometric premixed flamelet, and can be evaluated from data available in the literature or from a physical space solution.

The definition of the progress variable is usually based on a combination of product mass fractions. The progress variable has to be monotonous between the unburnt and the equilibrium states and should provide a unique description

of the thermochemical state along the premixed flamelet. For instance, Proch and Kemp [91] suggested that the following definition for the progress variable provided a good representation of the manifold over the entire flammability range for a methane/air flame [8]

$$Y_c = Y_{CO_2} + Y_{H_2O} + Y_{CO} + Y_{H_2} \tag{2.146}$$

When tabulated chemistry is used in conjunction with PDF methods, it is necessary to estimate the joint-PDF $P(Z, Y_c)$. In order to split the joint-PDF into two single varialble PDFs for the mixture fraction and the progress variable, statistically independence between the mixture fraction and the progress variable has to be assumed. This is a strong assumption and has not been verified experimentally. In order to reduce the statistical dependence between Z and the progress variable it is common practice to employ the normalised progress variable c [155, 188]

$$c = \frac{Y_c - Y_c^{min}}{Y_c^{max} - Y_c^{min}} \tag{2.147}$$

When tabulated chemistry is coupled with the presumed-PDF approach, the PDFs for both Z and c are usually approximated with a β-function, and the mean scalar quantities are evaluated from the chemical database as

$$\tilde{\phi} = \iint \phi(Z, c) P(Z) P(c) dZ dc \tag{2.148}$$

The combustion process in many practical applications actually involves heat transfer to walls and radiation, and therefore cannot be regarded as adiabatic. In order to avoid the complication to account for non-adiabatic effects when generating the flamelet library, adiabatic flamelets can be employed in the modelling of non-adiabatic systems by assuming that heat loss/gain have a negligible effect on the species mass fractions within the flame brush, i.e. for values of the progress variable between 0 and 1, so that the mixture composition can be evaluated as in non-adiabatic calculations [198]. The local mean temperature $\tilde{T}$ is evaluated from the local value of the mean total enthalpy from the relationship [199]

$$\sum_{k=1}^{N} \tilde{Y}_k h_{t,k}(\tilde{T}) = \tilde{h}_t \tag{2.149}$$

[8] Other more refined definitions for the progress variable are possible. For an in-depth discussion about the progress variable definition refer to [193].

where the local mean total enthalpy $\tilde{h}_t$ is evaluated with a suitable transport equation, having the form of Equation (2.41). The source term in this equation accounts for heat losses due to heat transfer to the walls and radiation.

Since premixed manifolds include all the thermo-chemical states from the unburnt to the equilibrium conditions, theoretically they are suitable to evaluate the formation of "slow" pollutant species, such as CO and NO_x. In practical systems, where the combustion process usually falls into the partially premixed regime, the limitations linked with the representation of such complex phenomena with a simple premixed manifold can result in inaccuracies in the evaluation of minor species [198].

Further, the evaluation of NO_x employing a detailed chemical mechanism including nitrogen chemistry such the GRI3.0 can be problematic. In fact, if the progress variable is defined as a combination of major products species as in Equation (2.146), when the progress variable has nearly reached its maximum value within a flamelet, the mass fractions of NO and of NO_2 are still far from their equilibrium values. Consequently, very high gradients arises in the manifold for these species, resulting in significant interpolation errors during data retrieving from the chemical database [200]. The model can modified in order to account for this issue by including relevant species such as NO and NO_2 in the definition of Y_c and solving for an additional transport equation for these species [200, 201, 202].

An alternative approach for the evaluation of NO_x, quite popular in commercial CFD codes, stems from the observation that nitrogen oxides concentrations are usually very small (of the order of ppm) and negligible with respect to main species. Therefore they do not have a significant impact on global balances, main species mass fractions and temperature and can be evaluated via a post-processing technique [38]. In this approach, transport equations for NO and other species involved in NO_x chemistry (such as N_2O and HCN) can be solved using the frozen resolved field for velocity, temperature and other species. The source terms in these equations can be evaluated from rate expressions representative of the various paths leading to NO_x creation and destruction (i.e. thermal, prompt and N_2O-intermediate formation paths [9] and NO reburn). The averaged (or filtered)

[9]The nitrogen oxides production coming from fuel nitrogen content is usually neglected when

source terms are then obtained by averaging the resulting instantaneous values by means of a suitable presumed-PDF [38].

2.3.6 Radiative heat transfer modelling

The total radiative heat transfer in gas combustion can be split into two different contributions [21]:

- Non-luminous radiation due to the emissivity of the participating species such as CO_2, H_2O, CO, CH_4.
- Luminous radiation coming from particles (mainly soot) present in the flame.

Although the latter contribution can be significant at high operating pressures that are found in modern gas turbines and in the presence of non-premixed burning mode [203], it will be neglected in this study, since the main focus here is to assess the implications of the enhanced presence of carbon dioxide and steam on the non-luminous radiative mechanism. Also, the numerical prediction of soot is a very challenging task, mainly due to complexity of its formation process, and it is still an open research field [203, 204].

The interaction of gas molecules with photons is governed by quantum mechanics [205]. Even if the energy associated with a photon varies smoothly with its wavelength λ, the interaction of photons with the medium are restricted by quantum mechanics to discrete energy levels allowed for the considered molecule. It follows that a given molecule will only interact with photons with given energy levels, i.e. with given wavelengths. Thus, the absorption coefficient of a gas molecule shows characteristic peaks at well-defined wavelengths, whilst an almost transparent behaviour is observed outside of these absorption bands [206].

Furthermore, in order for a particular gas species to interact with thermal radiation, which typically falls in the infrared part of the electromagnetic spectrum, the presence of a permanent dipole moment in the gas molecule is necessary [205]. Therefore, monatomic and symmetrical diatomic molecules such as O_2 and N_2

dealing with natural gas combustion, whilst it can give a significant contribution to the overall NO_x production for other fuels such as coal.

can be considered transparent to thermal radiation. On the other hand, other molecules, such as CO_2, H_2O, CO and CH_4, can absorb and emit thermal radiation at given wavelengths [207]. In particular, carbon dioxide and H_2O are always present in air and represent the two final products of natural gas combustion. Also, in the diluted combustion processes considered in the present work, significantly higher concentrations of these species can be found in the combustion environment with respect to typical air-fired combustion. The enhanced presence of participating species results in higher radiation absorption and emission with respect to conventional air-firing, which can have a direct impact on flame temperature and heat transfer to the walls.

The transport of radiation energy in the direction $\mathbf{s}$ can be expressed by the radiative transfer equation (RTE). For a non-scattering environment under the equilibrium assumption it takes the form [206]

$$\frac{dI_\eta}{d\mathbf{s}} = \kappa_\eta \left(I_{b\eta} - I_\eta\right) \tag{2.150}$$

where I_η is the spectral radiative intensity associated with the wavenumber $\eta = 1/\lambda$, κ_η is the spectral absorption coefficient and $I_{b\eta}$ is the spectral blackbody intensity. Scattering effects in gaseous medium are usually negligible, and therefore the corresponding terms have not been included in Equation (2.150) [208, 209]

The spectral blackbody intensity $I_{b\eta}$ can be evaluated through the Planck function [206]

$$I_{b\eta}(T) = 2hc^2\eta^3 \frac{1}{exp\left(hc\eta/(k_B T)\right) - 1} \tag{2.151}$$

and the total blackbody emission can evaluated by integration of the Planck function over the entire spectrum as

$$I_b(T) = \int_0^\infty I_{b\eta}(T) d\eta = \frac{2\pi^4 k_B^4}{15h^3c^2} T^4 = \frac{\sigma}{\pi} T^4 \tag{2.152}$$

where σ is the Stefan-Boltzmann constant. Equation (2.152) highlights the fourth-power dependence of radiative emission on the temperature, which explains the importance of radiative heat transfer at high temperatures.

The radiative heat transfer is coupled to the governing equations via the source term in the energy equation. The radiative source term is represented

by the divergence of the radiative heat flux through the medium, and can be expressed in terms of the radiative intensity as [206]

$$\omega_{rad} = \int_0^\infty \kappa_\eta \left(4\pi I_{b\eta} - \int_{4\pi} I_\eta(\mathbf{s}) d\Omega \right) d\eta \tag{2.153}$$

If radiation is assumed to be independent of the wavenumber η, then the integration over the spectrum can be avoided, corresponding to the so called "grey" approximation.

The RTE can be resolved analytically only in very simple configurations that are of little practical interest. In all practical applications it is necessary to solve Equation (2.150) employing approximate methods, and several different solution techniques have been proposed for this purpose including Monte-Carlo [206], Discrete Ordinate [210], discrete transfer [211] and spherical harmonics (or P_N) [212] methods. A review of the various RTE solving methods can be found in [206].

Regardless of the employed solution method, the spectral absorption coefficient κ_η is affected by local properties such pressure, temperature and mixture composition and its evaluation is necessary in order to solve the RTE. The calculation of the spectral absorption coefficient can be challenging due to its high variability over the spectrum.

The most accurate approach for the evaluation of κ_η is referred to as the line-by-line (LBL) method [213]. In this approach the radiative intensity is resolved at a very high resolution using spectral absorption coefficient values from highly-resolved spectroscopic databases. More than one million intervals are required to discretise the infrared spectrum in LBL calculations [209], making this approach extremely expensive from the computational point of view, and therefore not affordable for most practical problem. In order to reduce the computational burden associated with the calculation of κ_η, the statistical narrow-band (SNB) model [214] has been introduced, in which the whole spectrum is discretised into hundreds of intervals with a spectral resolution of 10-50 cm^{-1} [209] and the average trasmissivity associated with every band is evaluated through a statistical representation of the optical properties. Although the SNB model is not suitable to evaluate radiative heat transfer in the presence of scattering or non-black walls, in most cases it is in very close agreement with LBL and experimental

measurements [215]. On the other hand, since the SNB model describes the radiative properties of the medium in terms of a path-dependent quantity, it is only compatible with integral methods for the resolution of the RTE.

The latter drawback of the SNB approach is overcome in the correlated-k model (CK), which is a narrow-band model that expresses the optical properties of the medium in terms of κ_η rather than the gas transmissivity, and is therefore compatible with all the resolution methods for the RTE. In this model the spectrum is divided into narrow bands in which $I_{b\eta}$ is assumed to be constant. Within each band, the spectral absorption coefficient is rearranged into a k-distribution as [216]

$$f(\boldsymbol{\phi}, k) = \frac{1}{\Delta\eta} \int_0^\infty \delta(k - \kappa_\eta(\phi)) d\eta \tag{2.154}$$

where $\boldsymbol{\phi}$ represents a vector including the local variables affecting the absorption coefficient (i.e. temperature, pressure, composition). The distribution represents the fraction of the narrow-band having an absorption coefficient equal to k. Therefore, it regroups all the spectral regions of similar absorption coefficient, which can be represented by the same RTE. In order to simplify its integration, it is convenient to arrange the the k distribution into a cumulative distribution $g(\boldsymbol{\phi}, k)$ as

$$g(\boldsymbol{\phi}, k) = \int_0^k f(\boldsymbol{\phi}, k') dk' \tag{2.155}$$

The g distribution is a smooth monotonically increasing function bounded between 0 and 1 and, therefore, can be easily integrated [209]. In the CK model the distribution in Equation (2.155) is inverted to produce a $k - g$ distribution. The intensity is expressed as a function of g, which is then integrated using a Gauss quadrature scheme.

If the $g(\boldsymbol{\phi}, k)$ distribution is evaluated from SNB parameters rather than from LBL data, the so called SNB-CK model is obtained [217]. In the present work, the SNB-CK model has been used to evaluate the Planck-averaged absorption coefficient of the mixture κ_{PL} in the optically thin model implemented in Cantera [218]. Under the optically thin assumption, the local intensity in Equation 2.153 is neglected, and the radiative heat source term can be expressed as

$$\omega_{rad} = 4\pi \int_0^\infty \kappa_\eta I_{b\eta} = 4\pi \kappa_{PL} I_b = 4\kappa_{PL} \sigma T^4 \tag{2.156}$$

The Planck-averaged absorption coefficient κ_{PL} is evaluated according to the SNB-CK model as

$$\kappa_{PL} = \frac{\sum_i^{N_b} \Delta\eta_i \sum_j^{N_q} w_j k_i(g_j) I_{b\eta_i}}{I_b} \tag{2.157}$$

where N_b is the number of narrow bands, $\Delta\eta_i$ is the width of band i, N_q is the number of quadrature points, $k_i(g)$ is the $k-g$ distribution of band i, and w_j is the quadrature weight for point j. The SNB model parameters employed to evaluate the g distribution are taken from [219].

Narrow-band models still requires the resolution of hundreds of RTEs (one for each interval used to discretise the wavenumber spectrum) and therefore they are often used in simplified configurations to generate benchmark data for the validation of less computationally-intensive global approaches, such as the weighted-sum of grey gas (WSGG) and the full-spectrum correlated-k (FSCK) models [215].

In the WSGG model [220], the total emissivity of the gas mixture ϵ is evaluated through a weighted average of the contributions coming from fictitious grey gases as

$$\epsilon = \sum_{k=0}^{K} a_k \epsilon_k = \sum_{k=0}^{K} a_k \left(1 - exp(-\kappa_k p s)\right) \tag{2.158}$$

where a_k is the weighting factor for the fictitious gas k, K is the number of fictitious grey gases used in the model (usually less than 5), p is the sum of the partial pressure of the participating species (usually CO_2 and H_2O) and s the path length. In order to account for windows between regions of high absorption in the spectrum, $K = 0$ corresponds to a transparent gas.

The previous assumption leads to the following form of the RTE equation for the WSGG model [220]

$$\frac{dI_k}{ds} = \kappa_k \left(a_k I_b - I_k\right) \tag{2.159}$$

which represent the RTE for a gray gas with the blackbody intensity I_b replaced by the weighted intensity $a_k I_b$. The WSGG model requires the solution of a number of RTEs equal to the number of grey gases used in equation (2.158). The overall radiation intensity is then evaluated as the sum of the grey gases intensities

$$I = \sum_{k=0}^{K} I_k \tag{2.160}$$

The model parameters, i.e. the weighting factors a_k and the absorptions coefficients κ_k, are usually evaluated by fitting Equation (2.158) to tabulated experimental or calculated emissivity values [209]. In the most common approaches the correlations for a_k and κ_k are limited to specific operating conditions and molar ratio between CO_2 and H_2O [221]. More advanced formulations in order to account for broader ranges of molar ratios, corresponding to the conditions typical of diluted and oxy-combustion, have been proposed [222, 223].

In commercial CFD codes (e.g. [63]) the model is further simplified in order to represent the medium with a single grey gas and reduce the number of RTE to be solved to one. The path length is Equation (2.158) is estimated as a beam length characteristic of the whole domain as

$$s = \frac{3.6V}{A} \tag{2.161}$$

where V is the domain volume and A the total internal surface area of the domain. The path length evaluated through Equation (2.161) is then employed to convert the emissivity given by Equation 2.158 into an effective grey absorption coefficient κ_e as

$$\kappa_e = -\frac{ln(1-\epsilon)}{s} \tag{2.162}$$

Although neglecting the spectral dependence of κ does not have a sound physical justification, it leads to a great simplification of the problem and calculations carried out with this approach still show an acceptable accuracy in some cases [224].

The limited range of applicability of the set of coefficients of the model and its reliance on generic definitions for important quantities such as the path length s lead to issues related to the generalisability of the WSGG approach. Nevertheless this model is extremely popular in CFD codes due to its simplicity and low computational cost.

The FSCK model employs the same approach as the CK model, but in this case the reordering takes place over the entire spectrum. Different wavenumbers are weighted through the Planck function in order to account for the variation of $I_{b\eta}$ across the spectrum [215]. It has been reported [215, 225] that the FSCK approach is more accurate with respect to the grey WSGG model with coefficients

from Smith et al. [221] when the considered operating conditions depart from the standard air-fired combustion at atmospheric pressure considered in [221].

When considering the prediction of radiative heat transfer in turbulent combustion, the mutual effects of the turbulent eddies on the radiative intensity and the dependence of the turbulent flow field on the radiative impact on the flame temperature are referred to as turbulence-radiation interaction (TRI) [226]. The effects of TRI are still not fully understood and represent an active research field at the moment.

2.4 Summary

In the present chapter a survey on the state of the art of gas-phase turbulent combustion modelling has been presented. Even if RANS still represents the workhorse for CFD modelling of combustion devices of industrial relevance, LES is becoming a more viable option due to the increased computational power of modern computers. Although neither LES nor RANS directly resolve the scales at which the combustion processes take place, the former approach still offers significant advantages over the latter due to its ability to cope with the natural unsteadiness of the combustion process. Nevertheless, the increased accuracy than can be obtained in LES calculations comes at the cost of a noticeably higher computational cost, and therefore LES is not always a viable option in the modelling of complex industrial problems.

Further, an analysis of the peculiarities of diluted combustion and the implications from the modelling point of view has been carried out. CO_2 and H_2O dilution impact on the combustion process is due to both thermal and chemical effects. In particular, since the participation of the diluting species in the combustion chemistry takes place at the radical production level, a detailed chemical description of the combustion process is necessary to account for these effects, which can be associated to very high computational cost in realistic turbulent configurations. The use of tabulated chemistry appears to offer a good compromise between a detailed description of the chemistry and the control of the computational cost associated with the CFD modelling of the combustion process

in industrial devices.

Although CFD is widely used for the modelling of combustion systems, most of the models commonly employed have been developed in the context of air-fired combustion. The relatively small dilution levels observed in EGR and STIG gas turbine operations are still expected to have an impact on combustion chemistry that has to be accounted for at the modelling stage. Therefore, there is a need to understand the effects of dilution on the combustion process and include them in reliable CFD models of combustion devices. In this context, the following tasks will be addressed in the next chapters:

- Fundamental study of the impact of carbon dioxide and steam dilution of natural gas combustion and assessment of the effects of the enhanced presence of participating species on radiative heat transfer.

- Validation of numerical models for the investigation of swirled partially-premixed flames.

- Development of a complete CFD model for the investigation of the air-fired and diluted operation of an industrial gas turbine combustor.

Chapter 3

Experimental facilities and data

This present chapter presents a short description of the experimental facilities employed to generate the data used to set up and validate the CFD calculations carried out in this thesis. Firstly, the lab-scale burner employed to generate the detailed in-flame measurements used in the numerical investigation outlined in Chapter 5 is described. Secondly, the industrial MGT system object of the CFD modelling outlined in Chapter 6 is presented, with details on the boundary conditions and the validation data employed in the CFD analysis of the combustion chamber.

3.1 Lab-scale burner

The complex nature of reactive flows, the strong coupling between chemistry and turbulence, and the different characteristic scales of these phenomena, makes the modelling of turbulent combustion processes a challenging task [20]. The difficulties related to turbulent combustion modelling are even greater when considering its application to complex swirling flames. This is due to the complicated flow features associated with these flows, such as vortex breakdown, recirculation and the possible presence of aerodynamic instabilities [23].

The validation of models that are suitable for such complicated reactive swirling flows requires the availability of extensive experimental measurements, together with well defined geometry and boundary conditions. A number of laboratory-scale swirled burners have been developed for this purpose [227]. Among the

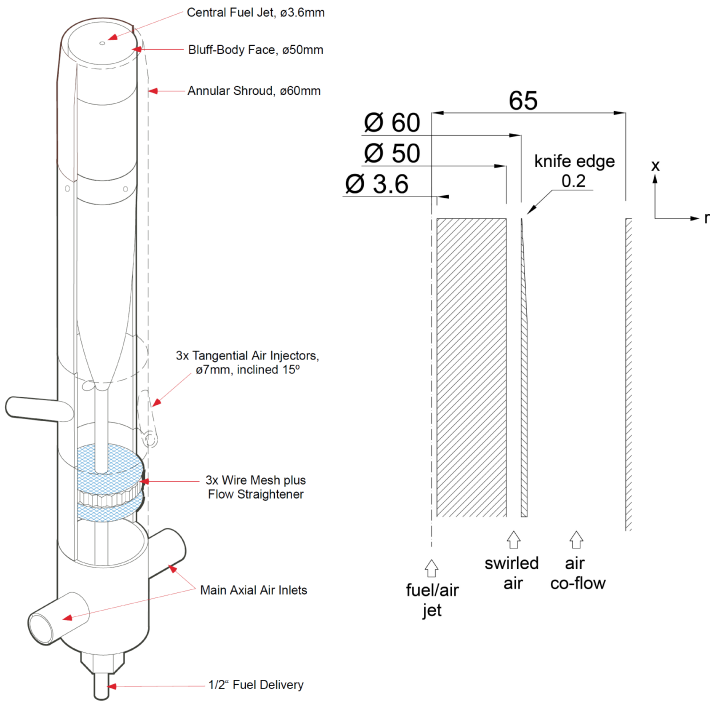

Figure 3.1: Schematic of the Sydney bluff-body burner (left) and detail of the burner outlet (right).

available experimental datasets, the Sydney burner flames series provides an extensive experimental database for two non-reactive and eight reactive cases [228]. In the modelling work described in Chapter 5, a non-reactive and a reactive cases have been numerically investigated in order to assess the potential of different numerical models against detailed in flame measurements.

The bluff-body burner used for the Sydney swirl flame series experimental campaign is characterized by a relatively simple geometry and is provided with well-defined boundary conditions. The burner produces complex swirling flows with features similar to those found in practical combustion chambers [228]. A schematic of the burner together with a more detailed representation of the burner outlet are reported in Figure 3.1.

The fuel jet is not swirled and is injected through a central pipe with a 3.6 mm inner diameter and is inserted into the bluff body, which has a diameter of 50 mm. The primary swirled oxidizer flow is fed through an annular channel having an outer diameter of 60 mm with a 0.2 mm thick knife edge at the outlet. The

Case	Fuel mixture (vol ratio)	U_s (m/s)	W_s (m/s)	U_j (m/s)	S_g
N29S054	air	29.7	16.0	66.0	0.54
SMA1	CNG-air (1:2)	32.9	21.6	66.3	0.66

Table 3.1: Flow parameters for the non-reactive N29S054 and the reactive SMA1 cases.

swirl on the primary oxidizer is induced aerodynamically via three tangential air injectors positioned 300 mm upstream of the burner exit plane. The burner assembly is located within a wind tunnel, having a square section with a side of 130 mm, which provides a secondary non-swirled air coflow. The coflow has a bulk axial velocity of 20 m/s for all of the cases. The jet, annulus and coflow velocity profiles are fully developed at the burner outlet [229].

The cases are characterized by different values for the three controlling parameters, i.e. the bulk axial velocity of the jet flow U_j and the bulk axial U_s and tangential W_s velocity components of the swirling primary oxidizer flow, as well as by different fuel mixture compositions. The geometric swirl number, S_g, is defined as the ratio between the tangential and the axial bulk velocities, which are measured at the annulus outlet. The values of the different parameters for both the non-reactive and the reactive cases considered in the present work are reported in Table 3.1.

Detailed LDV measurements of the velocity components and RMS fluctuations are available for both the non-reactive [229] and the reactive cases [228], and were employed in this study to validate the CFD flowfield predictions. Also, for the reactive case, the numerical results were validated against detailed temperature and species mass fraction measurements performed at the Sandia National Laboratory with a single-point Raman-Rayleigh-LIF technique [230]. Finally, time-resolved measurements (acquired by high-speed imaging of laser Mie scattering and shadowgraph) with a focus on flow instabilities are reported for the non-reactive [231] and the reactive cases [232], and were used to assess the capability of the numerical models to predict such instabilities. Since no estimation of the accuracy of the measurements is provided in the relevant publications, the

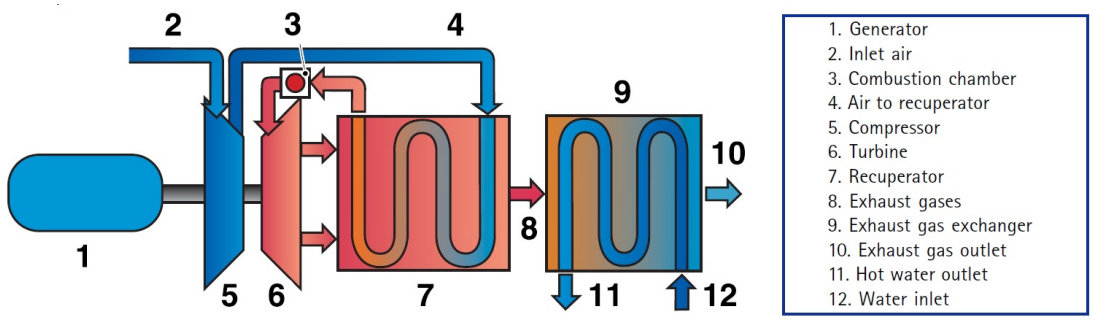

Figure 3.2: Schematic of the Turbec T-100 micro gas turbine [234].

experimental data in the plots in Chapter 5 will be presented without error bars. This should be kept into account when comparing the experimental data with the numerical results.

3.2 Turbec T-100 micro gas turbine

In the context of small-scale power generation, MGTs represent an attractive option for CHP generation, with the possibility to attain overall efficiencies above 90%. The main advantages of MGT systems are represented by the compact size and low weight, the small number of moving parts with the associated benefits in terms of maintenance, and the possibility to attain lower pollutant emissions with respect to gas and diesel engines [233].

This section is focused on the description of the Turbec-T 100 MGT system. The combustion chamber of this system is the object of a detailed CFD investigation, carried out under both air-fired and diluted operation, described in Chapter 6. The Turbec T-100 MGT is a system for the combined generation of heat and power. The nominal electrical power output is 100 kW, corresponding to a thermal power output of about 165 kW, with an electrical and overall nominal efficiency of about 33% and 80%, respectively [234].

A schematic of the system is shown in Figure 3.2. The air, at ambient temperature and pressure, is drawn into the system by the compressor, which operates at a nominal pressure ratio equal to 4.5. The compressed air is fed to a gas-to-air heat exchanger (i.e. the recuperator) where it is pre-heated before being injected into the combustor. The heated air is then fed to the combustor, where it is

mixed with the fuel in order to generate a flammable mixture. The hot combustion products are expanded through the turbine, which is mounted on the same shaft as the compressor and the electrical generator. The gases exiting from the turbine are fed firstly to the recuperator and, afterwards, to a gas-water heat exchanger where the production of hot water takes place. A short description of the main components of the system is provided below:

- **Compressor:** the system uses a radial centrifugal compressor, mounted on the same shaft as the turbine, with a pressure ratio of about 4.5.
- **Recuperator:** is a gas-to-air heat exchanger used to preheat the air coming from the compressor before injecting it into the combustion chamber.
- **Combustor:** the combustion process takes place in a DLE combustor which will be described in the detail below.
- **Turbine:** a centripetal turbine drives both the compressor and the electrical generator.
- **Electrical generator:** the electric power is generated by a water-cooled two-poled permanent magnet generator rotating at high speed (70000 rpm), thus producing high frequency electricity. It can also act as an electric starter.
- **Exhaust gas heat exchanger:** is a gas-water counter-current heat exchanger. It uses the exhaust gas coming from the recuperator to heat up water. The resulting outlet water temperature depends on the inlet water conditions, temperature and mass flow.

The Turbec T-100 also includes an electrical system for converting the high frequency AC power to the desired grid voltage and frequency and a supervision and control system which allows the operation of the Turbec T-100 without personal attendance under normal operation.

The system performances at nominal conditions are summarized in Table 3.2. The combustion process takes place in a reverse-flow DLE combustion chamber. NOx emissions are reduced by controlling the in-flame temperature by means of

Fuel type	Natural gas
Fuel LHV	49 MJ/Nm^3
Combustor operating pressure	4.5 bar
Fuel consumption	333 kW
Electrical output	100 kW
Electrical efficiency	30 %
Thermal output	165 kW
Total efficiency	80 %
NOx at 15% O_2	$<$ 15 ppm
CO at 15% O_2	$<$ 15 ppm

Table 3.2: Turbec T-100 system performance at nominal power output [234].

a lean-premixed combustion process. A non-premixed pilot flame, located in a dome, is present to enhance flame stability at stationary working points as well as during transient maneuvers. A section view of a CAD model of the combustor is shown in Figure 3.3.

With reference to the section view in Figure 3.3, the air coming from the recuperator enters the combustion chamber through the annular section comprised between the outer casing (in yellow in Figure 3.3) and the flame tube (shown in red in the figure) and is split into a dilution stream, the mean combustion air and the pilot flame air.

The flame tube encompasses the main combustion process and is provided with nine dilution holes (9 x 19.6 mm) used to cool down the hot combustion products before the turbine inlet. The pilot fuel flows through a dedicated pipe and is injected without swirl into the pilot flame region using six nozzles (6 x 1 mm). The main fuel injection system (depicted in blue in Figure 3.3) is used for both supplying air to the pilot flame zone by means of 12 jet holes (12 x 3.5 mm) and to distribute the main fuel into a toroidal chamber. The main fuel is then injected from the toroidal chamber directly into the premixing vanes by means of 15 nozzles (15 x 1.2 mm).

The main swirler is equipped with 15 radial swirling vanes, where the premix-

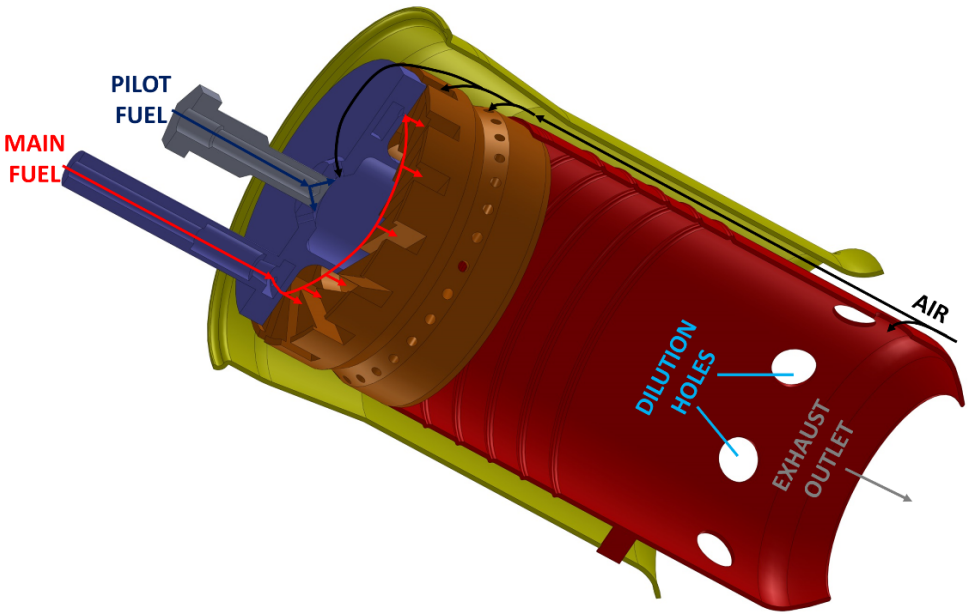

Figure 3.3: Section view of the CAD model for the Turbec T-100 combustor.

ing between the main fuel and the oxidizer takes place. A secondary axial/radial swirler, consisting of a series of 30 air jet holes distributed circumferentially, is present further downstream close to the burner outlet.

3.2.1 Experimental datasets

The datasets from two independent experimental campaigns have been employed in the present work to set-up and validate the CFD model of the Turbec T-100 combustion chamber. The first experimental investigation has been carried out by the Institute of Combustion Technology of the German Aerospace Center (DLR). This experimental campaign has employed the gas turbine in both its original configuration and in a modified configuration, in which the MGT has been equipped with a modified optically accessible combustion chamber [235]. In the former configuration, flue gas composition at the combustor outlet has been monitored [236]. The experimental techniques employed for the measurements of the different species in the exhausts are described in [237]. The reported accuracy of the measurements for carbon monoxide, NOx and UHC is summarised in Table 3.3.

In the optically accessible configuration, in addition to flue gas species mea-

	CO ppmv	NOx ppmv	UHC ppmv
Range 1	0-8	0-24	0-9
Accuracy 1	0.1	0.5	0.1
Range 2	8-80	24-238	9-90
Accuracy 2	1	5	1
Range 3	80-400		
Accuracy 3	5		

Table 3.3: Range and corresponding accuracy for the measurements of pollutant species in the flue gas [237].

N (%)	p_{abs} (bar)	$\dot{m}_F$ (kg/s)	$\dot{m}_{oxi}$ (kg/s)	T_{oxi} (K)	s (-)
92.5	3.30	0.006651	0.658	829.15	9.2
75.0	2.27	0.003578	0.446	802.15	3.6

Table 3.4: Boundary conditions for the case from the DLR dataset [236]

surements, the flame was analysed through visual inspection, as well as with OH* chemiluminescence and OH-PLIF measurements [236, 235]. The data from this experimental campaign have been employed to validate the performance of the CFD model under air-fired conditions at two stationary working points. The boundary conditions for these cases are reported in Table 3.4, where N is expressed as the percentage of the nominal shaft rotating speed (equal to 70000 rpm), p is the absolute pressure at the combustor inlet and s is the fuel split between the main and the pilot stages, defined as

$$s = \frac{\dot{m}_{F,main}}{\dot{m}_{F,pilot}} \tag{3.1}$$

The natural gas composition used to characterise the fuel stream is taken from [236].

The second dataset comes from the experimental campaign carried out at the UKCCSRC PACT Facility [1] and consists of different cases including air-fired,

[1] `http://www.pact.ac.uk/`

CO_2-diluted, H_2O-diluted and combined CO_2- and steam-diluted operation at different power output levels. Temperature, pressure and mass flow rates have been monitored at different locations in order to characterise the MGT system at different working points. In particular, temperature and pressure were monitored at the compressor inlet and outlet (points 2 and 4 in Figure 3.2, respectively), between the turbine and the recuperator and at the exhaust outlet (point 10 in Figure 3.2). Further, air, fuel, diluting species and exhaust mass flow rates were measured, together with the gas composition at the exhaust outlet (point 10 in Figure 3.2). More details on the experimental setup and the measurement techniques can be found in [238].

In order to analyse the system performance under EGR and STIG operation, the MGT has been modified to allow for CO_2 and/or H_2O injection in the system. The carbon dioxide, coming from a cryogenic CO_2 storage tank, is fed to the compressor inlet through a copper pipe. It is possible to inject up to 175 kg/h of CO_2. By injecting the carbon dioxide in this way it is possible to account for the effects of CO_2 dilution on the system operation and, at the same time, to avoid the technical issues related to the actual recirculation of the exhaust gases back to the compressor intake.

The steam injection takes place at the compressor outlet. The steam at high temperature and pressure is produced in a boiler located on site, which is able to guarantee steam mass flow rates up to 150 kg/h.

Since no direct measurements are taken at the combustor inlet and outlet sections, the boundary conditions for the CFD model of the combustion chamber for the different cases have been obtained through a process model of the system. Further, since it was not feasible to take a direct measurement of the air flow rate at the compressor intake in the considered experimental configuration [238], this parameter has been calibrated in the process modelling calculations in order to match the measured CO_2 content at the exhaust outlet. The air and natural gas composition considered in the process modelling calculations are reported in Table 3.5. The process model has been setup employing the experimental measurements for the different cases considered here [239, 240]. A summary of the boundary conditions obtained for the cases modelled in Chapter 6 is reported in

Air		Fuel	
Species	X_i	Species	X_i
N_2	0.7732	CH_4	0.9114
O_2	0.2074	C_2H_6	0.0512
Ar	0.0092	C_3H_8	0.0131
CO_2	0.0003	N_2	0.0106
H_2O	0.0099	CO_2	0.0137

Table 3.5: Air and natural gas compositions considered in the process simulation of the PACT cases.

Case	p_{abs} (bar)	$\dot{m}_F$ (kg/s)	$\dot{m}_{air}$ (kg/s)	$\dot{m}_{CO_2}$ (kg/s)	$\dot{m}_{H_2O}$ (kg/s)	T_{oxi} (K)
80 kW BAS	4.135	0.007168	0.7415	-	-	814.1
80 kW CO2	4.055	0.007482	0.7831	0.03472	-	800.8
65 kW BAS	3.645	0.005950	0.6565	-	-	828.1
65 kW CO2	3.615	0.006033	0.7196	0.03472	-	813.6
65 kW H2O	3.445	0.005890	0.6740	-	0.01111	821.2
65 kW COMB	3.485	0.005925	0.6585	0.03472	0.01111	819.7

Table 3.6: Boundary conditions for the PACT cases.

Table 3.6, where BAS, CO_2, H_2O and COMB stand for baseline air-fired, carbon dioxide-dilute, steam-diluted and combined CO_2- and H_2O-diluted operation, respectively.

It should to be pointed out that the fuel mass flow rate figure reported in Table 3.6 represents the sum of the pilot and main fuel streams, since the fuel flow meter is installed upstream of the split between the two lines. Consequently, no direct information on the value of fuel split s are available for the PACT cases. Therefore, the value of s for these cases has been retained constant and equal to 5.7 (which is equal to the fuel split value at nominal power output as reported in [241]), although it would be advisable to modify the measurement system of the fuel mass flow rate in order to be able to evaluate the fuel split for the different cases in the future.

3.3 Summary

The experimental rigs and the related data employed to set up and validate the CFD calculations carried out in this thesis have been introduced in this chapter. Firstly, a short description of the Sydney burner has been presented. The detailed in flame measurements available for the Sydney swirl flames dataset have been employed to set up and validate the calculations described in Chapter 5. Secondly, a description of the Turbec T-100 MGT system has been provided. The combustion chamber of the system is the topic of the CFD investigation reported in Chapter 6. The CFD model of the system has been validated against the experimental data obtained by the Institute of Combustion Technology at DLR. The same CFD model has been employed to numerically investigate the operation of the combustion chamber, under air-fired and diluted conditions at two different power outputs, for a total of six different cases which have been investigated experimentally at the UKCCSRC PACT Facilities.

Chapter 4

Effects of CO_2 and H_2O dilution on natural gas combustion

The effects of diluting species, such as carbon dioxide and steam, on natural gas combustion can be investigated in detail, both numerically and experimentally, in simple configurations. In numerical calculations it is common practice to employ detailed chemical schemes to assess the effects of dilution in simple representative configurations such as 1D freely propagating premixed flames, planar counterflow diffusion flames, plug flow and perfectly stirred reactors, as reported in Section 2.3. Most studies refer to highly diluted combustion processes such as MILD [172] and oxy-combustion [173].

In this chapter the effects of CO_2 and H_2O at the relatively low dilution levels that are typical of EGR and STIG applications in gas turbines are investigated. In particular, dilution levels comparable to those employed in the experimental campaign carried out at PACT and described in Section 3.2 are considered. The representative configuration chosen for this study is a 1D adiabatic freely propagating premixed flame. All the calculations were carried out with Cantera [218] and employing the GRI3.0 mechanism [179] to describe the chemistry of the problem. The governing equations are solved in the physical space considering a domain length equal to 0.12 m. Details on the governing equations and the numerical techniques employed for their solution can be found in [242]. For simplcity, the natural gas composition has been considered to be equal to pure methane.

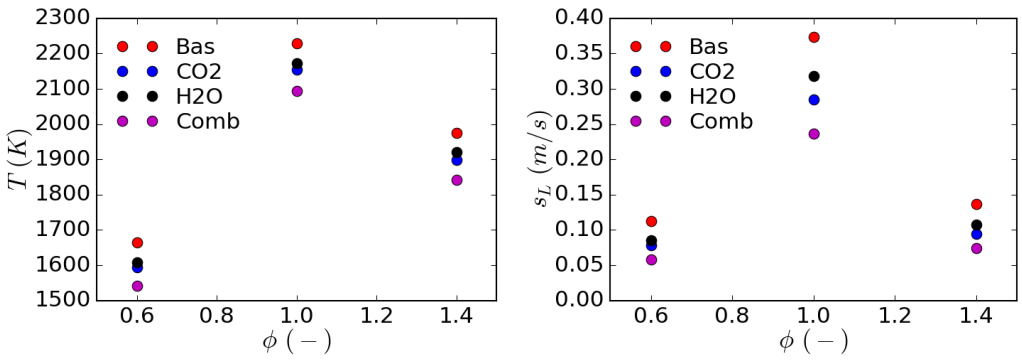

Figure 4.1: Calculated adiabatic flame temperature (left) and laminar flame speed (right) as a function of the equivalence ratio at atmospheric pressure and T_u = 298 K.

A 4% concentration of CO_2 or H_2O in the oxidizer stream is considered. Also, combined dilution with both carbon dioxide and steam is investigated, with $X_{CO_2,oxi} = X_{H_2O,oxi} = 0.04$. Two different operating conditions are evaluated: the first one is representative of ambient conditions, i.e. $p = 1$ atm and $T_u = 298$ K, whilst the second one corresponds to the operating conditions typical of a MGT, i.e. $p = 4$ bar and $T_u = 800$ K. Further, the effects of dilution on the radiative heat transfer in 1D premixed flames has been assessed by employing an optically thin approach and the SNB-CK model to evaluate the mixture optical properties, as detailed in Section 2.3.

Finally, the impact of dilution on the combustion process at the conditions corresponding to the six PACT experimental cases reported in Section 3.2 is considered.

4.1 Ambient operating conditions

In this section the results obtained at atmospheric pressure and with an unburnt mixture temperature equal to 298 K are reported. Figure 4.1 shows the calculated adiabatic flame temperature and laminar flame speed for three different equivalence ratio values (i.e. ϕ equal to 0.6, 1.0 and 1.4) that are representative of lean, stoichiometric and rich mixtures.

From Figure 4.1 it can be seen how, even at the relatively low dilution levels

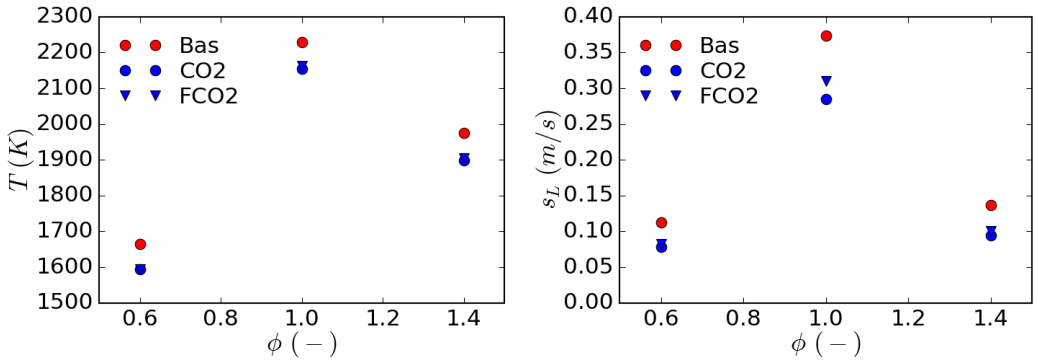

Figure 4.2: Calculated adiabatic flame temperature (left) and laminar flame speed (right) as a function of the equivalence ratio at atmospheric pressure and T_u = 298 K with CO_2 and FCO_2 dilution.

considered here, carbon dioxide and steam dilution have a non-negligible impact on both the adiabatic flame temperature and the laminar flame speed. In detail, the calculated reductions in both T_{ad} and s_L with CO_2 dilution are slightly higher with respect to steam dilution. The more pronounced difference between carbon dioxide and steam dilution is observed in the laminar flame speed at stoichiometric conditions. As expected, when combined CO_2 and H_2O dilution is considered, the effects on the combustion process are more evident. Furthermore, it is observed that the effects of dilution on the laminar flame speed appears to be more marked at stoichiometric conditions, with respect to both lean and rich mixtures.

The reasons behind the latter observation can be inferred from Figure 4.2, which shows the adiabatic flame temperature and the laminar flame speed values for three different cases. In detail, a baseline case, a case with CO_2 dilution and one with FCO_2 dilution, where FCO_2 is a fictitious species introduced in order for us to be able to distinguish between thermal and chemical effects of carbon dioxide dilution as detailed in Section 2.3, are reported. Since FCO_2 has the same thermal and transport properties as carbon dioxide, but does not participate in any chemical reaction, the differences between the baseline and the FCO_2-diluted cases in Figure 4.2 can be regarded as being only due to thermal effects. On the other hand, the discrepancy between the FCO_2- and the CO_2-diluted cases represents the effects due to the direct participation of carbon dioxide in the combustion chemistry. It can be observed that thermal effects are, in general,

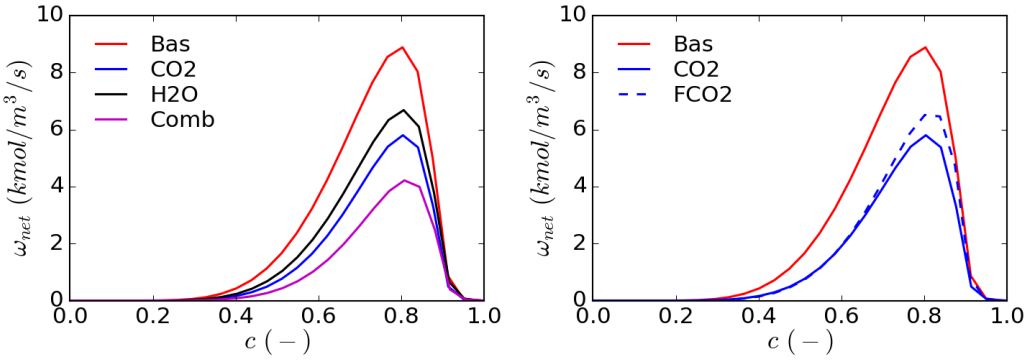

Figure 4.3: Net reaction rate of the chain-branching reaction (R 2.2) as a function of the progress variable c at atmospheric pressure, $T_u = 298$ K, and $\phi = 1$.

predominant over the chemical effects. Being characterised by a higher combustion temperature with respect to lean and rich mixtures, the chemical effects are more marked at stoichiometric conditions. Therefore, the significant difference in the the laminar flame speed values at stoichiometric conditions observed in Figure 4.1 can be due to the the fact that the carbon dioxide chemical effects are more pronounced with respect to H_2O dilution [32], and this difference is more marked at the higher temperature levels reached at $\phi = 1$.

It has been observed in Section 2.3 that the most significant chemical effects of both carbon dioxide and steam dilution is the inhibition of the chain-branching reaction (R 2.2) by boosting the reactions that compete with the former for the H radical. The overall effects of dilution on reaction (R 2.2) at stoichiometric conditions are shown on the left hand side of Figure 4.3, where the net rate of reaction is reported as a function of the progress variable c. The progress variable is defined according to Equation (2.146). It can been seen that dilution has a significant impact on the chain-branching reaction. The curves reported on the left hand side of Figure 4.3 include both thermal and chemical effects. The chemical effects of CO_2 can be assessed by analysing the right hand side of the figure, where the results obtained with FCO_2 dilution are included. The difference between the solid and the dashed blue curves represent the reduction in the chain-branching reaction rate due to chemical effects alone. Although thermal effects are more significant with respect to the influence of the chemical reactivity of CO_2, the latter cannot be neglected, especially at stoichiometric condition.

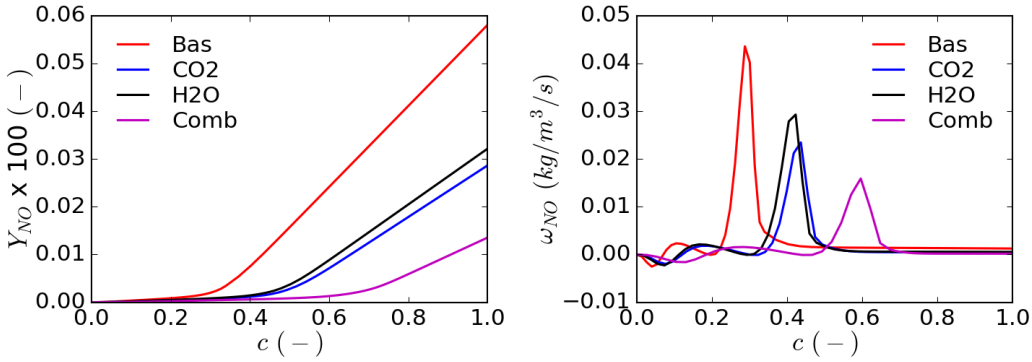

Figure 4.4: NO mass fraction (left) and NO source term (right) as function of the progress variable c at atmospheric pressure, $T_u = 298$ K, and $\phi = 1$.

In addition to improving the efficiency of carbon dioxide post-combustion capture, advanced cycles such as EGR and STIG can result in reduced nitrogen oxides emissions due to the lower combustion temperature observed with CO_2 and H_2O dilution. In fact, thermal NO_x production is extremely sensitive to the temperature due to the very high activation energy of the reaction [243]

$$N_2 + O \rightleftharpoons NO + N \qquad \text{(R 4.1)}$$

The reduction in NO_x production associated with the considered dilution levels is highlighted in Figure 4.4, showing the mass fraction of NO and its source term as a function of the progress variable at stoichiometric conditions. It is evident how even the relatively small reduction in the temperature associated with the considered levels of dilution results in a significant decrease in the NO mass fraction and in its source term. For instance, the adiabatic flame temperature in the baseline case, assumed to be equal to the temperature corresponding to $c = 1$, is equal to 2228 K, and it is lowered to 2094 K in the combined case, with a reduction of about 6%. The corresponding final NO mass fraction drops from 0.000581 in the baseline case to 0.000135 in the combined case, with a reduction of about 77%. The significant decrease in NO levels associated with such a relatively small reduction in temperature is due to the very high sensitivity to the temperature shown by reaction (R 4.1).

Although the considered domain length of 0.12 m is enough to ensure that the main product species, such as CO, CO_2, H_2 and H_2O, have reached equilibrium

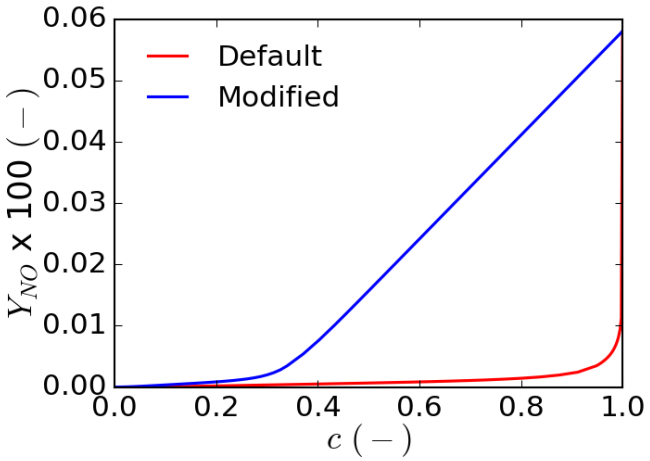

Figure 4.5: NO mass fraction for the baseline case at stoichiometric conditions as a function of the default progress variable definition c_{Def} (left) and of the modified definition c_{Mod} (right).

at $c = 1$, given the very slow character of the NO formation, the domain has been extended to 0.25 m for the calculations shown in Figure 4.4, in order for NO to be closer to its equilibrium concentration for the given cases. Also, the progress variable in the aforementioned calculations has been modified as follows

$$Y_{c,Mod} = Y_c = Y_{CO_2} + Y_{H_2O} + Y_{CO} + Y_{H_2} + \alpha Y_{NO} = Y_{c,Def} + \alpha Y_{NO} \tag{4.1}$$

where a value of α equal to 1000 has been considered according to [200]. As reported in Section 2.3, a definition of the progress variable based on the main product species, such as the one in Equation (2.146), leads to very high gradients in the vicinity of the $c = 1$ limit for NO. The definition reported in Equation (4.1) allows us to avoid this issue and therefore it is more suitable when employing a progress variable approach to analyse NO_x. This is highlighted in Figure 4.5 where Y_{NO} for the stoichiometric baseline case is plotted as a function of c_{Def}, Equation (2.146), and c_{Mod}, Equation (4.1). It is evident how employing the modified formulation for the progress variable allows the reduction of the Y_{NO} gradient and therefore the interpolation error associated with the use of tabulated chemistry to evaluate the NO_x production.

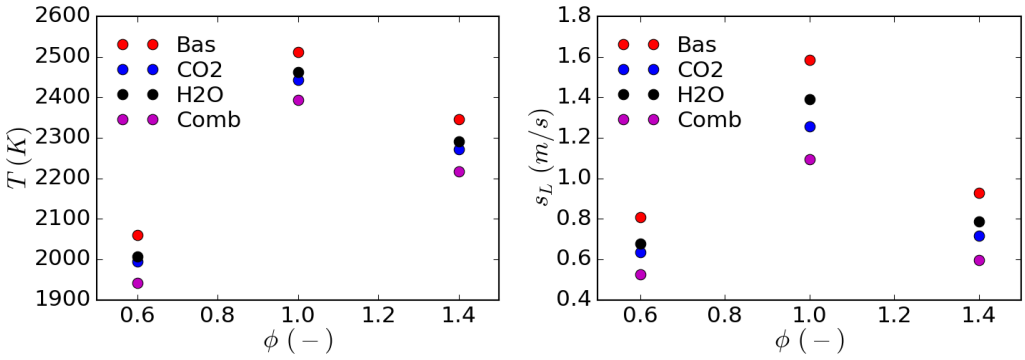

Figure 4.6: Calculated adiabatic flame temperature (left) and laminar flame speed (right) as a function of the equivalence ratio at $p_{abs} = 4$ bar and $T_u = 800$ K.

4.2 MGT-like operating conditions

The results obtained at MGT-like operating conditions, i.e. $p_{abs} = 4$ bar and $T_u = 800$ K, are reported in this section. The calculated adiabatic flame temperature and laminar flame speed at the considered pressure and temperature conditions are shown in Figure 4.6. In general, the same considerations made for the ambient operating conditions apply to this case. A comparison between the laminar flame speed values reported in Figures 4.1 and 4.2 highlights how the differences between carbon dioxide and steam dilution are more evident at MGT-like operating conditions. This is due to the fact that the elevated temperature of the unburnt gases leads to a higher combustion temperature and therefore more pronounced chemical effects, whilst the effect of the increased pressure is generally negligible with respect to that of temperature.

The increased importance of the chemical effects with higher temperature levels is depicted in Figure 4.7, where the calculated adiabatic flame temperature and laminar flame speed for the baseline, CO_2- and FCO_2-diluted cases are reported. It can be seen how the chemical effects on the laminar flame speed are visible, not only at $\phi = 1$ but also for lean and rich mixtures. Also, the relative importance of the chemical effects with respect to thermal effects at stoichiometric conditions is increased. At ambient conditions, the calculated laminar flame speed at $\phi = 1$ for the baseline case is 0.37 m/s, and is lowered to 0.28 m/s with carbon dioxide dilution, corresponding to a reduction of about 24%. About 71% of the total

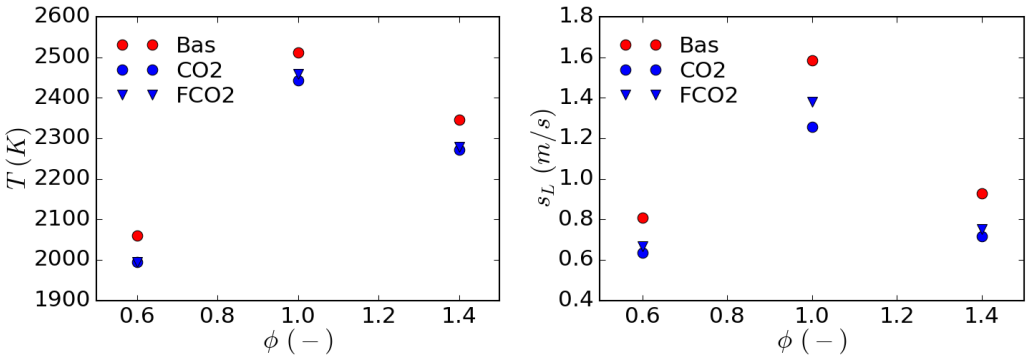

Figure 4.7: Calculated adiabatic flame temperature (left) and laminar flame speed (right) as a function of the equivalence ratio at $p_{abs} = 4$ bar and $T_u = 800$ K with CO_2 and FCO_2 dilution.

reduction in the laminar flame speed is due to thermal effects, and the remaining 29% is related to the chemical reactivity of CO_2. At elevated temperature and pressure conditions, the laminar flame speed for the stoichiometric non-diluted and the CO_2-diluted cases are 1.59 m/s and 1.25 m/s, respectively, with a total reduction of about 21% between the two. At these operating conditions, the share of the chemical effects in the total laminar flame speed reduction is increased to 38%, with the remaining 62% being associated with thermal effects.

The impact of dilution on the chain-branching reaction (R 2.2) at MGT-like operating conditions is depicted in Figure 4.8. From the left hand side of the figure it can be seen how at these operating conditions the considered dilution levels have a significant impact on the combustion chemistry. Due to the elevated unburnt gas temperature in the MGT-like conditions, the overall reaction rates are considerably higher with respect to the values reported in Figure 4.3 for the ambient operating conditions. Also, from the right hand side of the figure, it can be noted how the chemical effects have a non-negligible impact on the combustion process and this has to be accounted for in the modelling of the diluted operation of real combustors.

Finally, the impact of dilution on nitrogen oxides production at MGT-like conditions is summarised in Figure 4.9, showing the NO mass fraction and NO source term as a function of the progress variable c at stochiometric conditions. Due to the elevated sensitivity of the thermal NO_x production to the temperature,

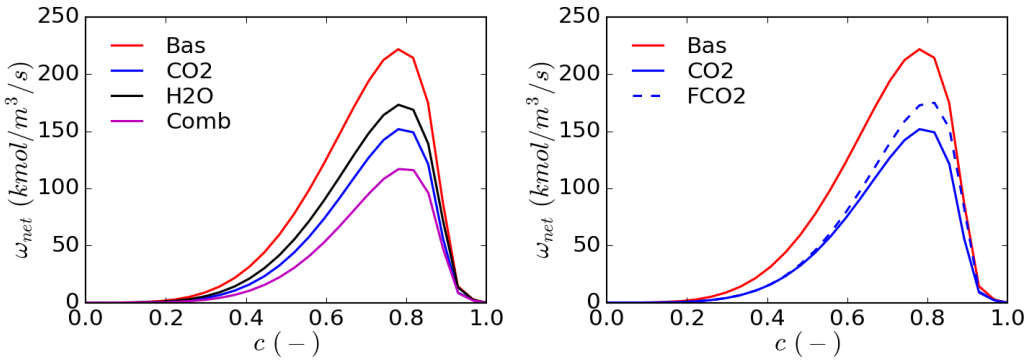

Figure 4.8: Net reaction rate of the chain-branching reaction (R 2.2) as a function of the progress variable c at $p_{abs} = 4$ bar, $T_u = 800$ K and $\phi = 1$.

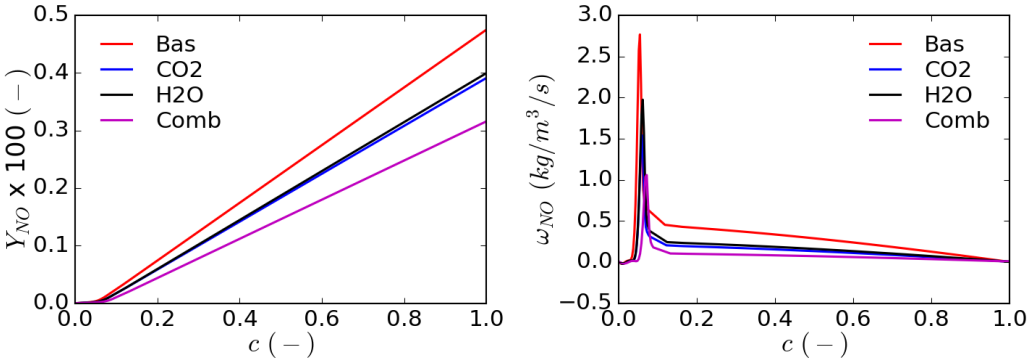

Figure 4.9: NO mass fraction (left) and NO source term (right) as a function of the progress variable c at $p_{abs} = 4$ bar, $T_u = 800$ K and $\phi = 1$.

the reduced temperature levels obtained with dilution have a significant impact on the NO source term and on Y_{NO}. The calculated adiabatic flame temperatures in the baseline and in the combined cases are equal to 2511 K and 2392 K, respectively, corresponding to a decrease of about 5% when combined CO_2 and H_2O injection is considered. The corresponding NO mass fractions at $c = 1$ are equal to 0.00475 and 0.00316, respectively, with a reduction of about 33% between the two cases. As in the ambient operating conditions case, the results shown in Figure 4.9 have been obtained with an extended domain of 0.25 m and on employing the modified expression of the progress variable reported in Equation (4.1).

4.3 Radiative heat transfer assessment

The effects of CO_2 and steam dilution on the radiative heat transfer have been evaluated by comparing the baseline and the combined dilution cases, at both ambient and MGT-like conditions, in the same representative configuration considered in the previous sections, i.e. 1D freely propagating flames. The radiative heat transfer has been evaluated in the optically thin limit and the Planck-averaged absorption coefficient κ_{PL} has been calculated according to the SNB-CK model, as detailed in Section 2.3.

The calculated temperature profiles along the domain are reported in Figure 4.10 for both adiabatic and non-adiabatic, i.e. including radiation, calculations, at ambient and MGT-like conditions for both air-fired and diluted flames. It can be noted how the impact of radiation in the diluted cases is higher with respect to the air-fired flames under both operating conditions. Also, for the considered configuration, the impact of radiative heat loss on the temperature becomes more evident when the domain is extended significantly behind the reaction zone. In fact, this region is characterised by elevated temperatures and high concentration of participating species and, at the same time, by a reduced contribution of the chemical heat release, which takes place mainly within the reaction zone. Therefore the impact of the radiative losses on the temperature can be expected to be significant in this region. Also, it can be noted that radiation appears to have a more marked impact on the temperature field at ambient conditions with respect to MGT-like conditions although, due to the dependence of the radiation loss on the fourth-power of the temperature, ω_{rad} is expected to be higher when MGT-like conditions are considered.

The high sensitivity of the radiative source term to the temperature, resulting from the aforementioned fourth-power dependence, can be inferred from the left hand side of Figure 4.11, where the radiative source term at MGT-like conditions is almost one order of magnitude higher with respect to ambient conditions. Further, it can be seen how the radiative source term is nearly negligible ahead of the flame, and it increases steeply within the reaction zone, following the temperature increase due to the onset of the chemical reactions. Behind the reaction zone, the chemical heat source term decreases rapidly, whilst ω_{rad} decreases slowly due to

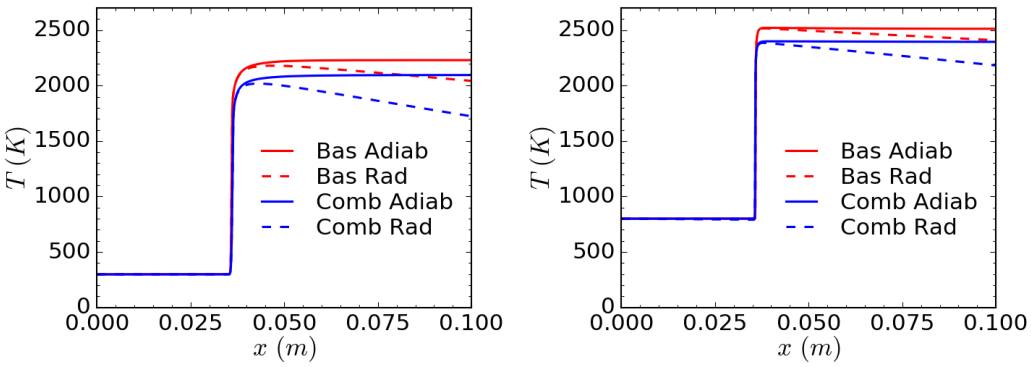

Figure 4.10: Calculated temperature profiles at ambient (left) and MGT-like (right) conditions.

the cooling of the gases by radiative heat loss. It is also worth noting that the radiative heat loss is higher in the diluted cases, although these cases are characterised by lower temperature values with respect to the air-fired cases. This is due to the higher concentration of the participating species in the former flames. The calculated chemical heat source term ω_{chem} within and in the proximity of the reaction zone for the four considered flames is reported in the right hand side of Figure 4.11. The chemical heat source term peaks sharply once the flame is ignited and, as opposed to ω_{rad}, decreases quickly outside of the reaction zone. The elevated temperatures reached at MGT-like conditions result in significantly higher chemical heat release rates compared to ambient conditions.

The latter observation can explain why radiation appears to have a more marked effect on the calculated temperature at ambient conditions, although these conditions are characterised by smaller radiative heat loss compared to MGT-like conditions. In fact, even if the flames at MGT-like conditions are characterised by a higher radiative source term, its effect on temperature is counterbalanced by the higher heat release rate and heat capacity rate observed at these conditions with respect to ambient temperature and pressure.

Nevertheless, even in diluted cases, the chemical heat release rate within the reaction zone is about three orders of magnitude higher than the radiative heat source term, and therefore radiation is found to have a significant impact on the temperature field only if the region of high temperature and elevated participating species concentration extends for a significant distance outside of the reaction

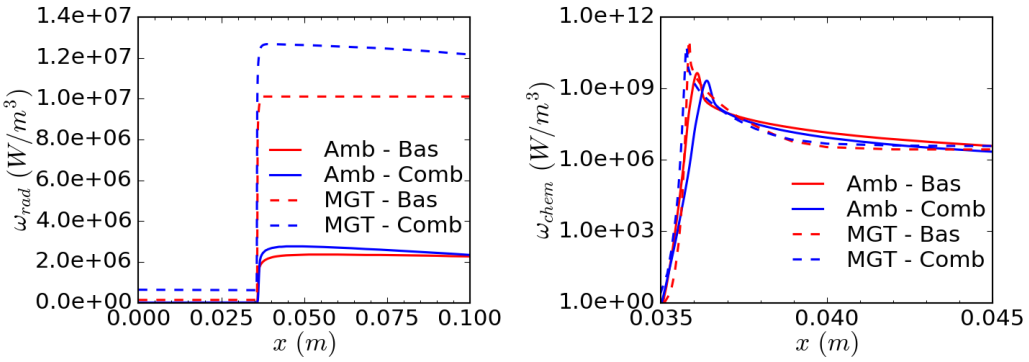

Figure 4.11: Calculated radiative (left) and chemical (right) source terms for the four considered flames.

zone.

The extension of the previous considerations to real combustion devices is cumbersome. Firstly, the optically thin model employed here neglects absorption in the gas mixture, which can be significant especially in the diluted cases. Unfortunately, an accurate evaluation of the optical properties of the mixture is necessary in order to obtain an accurate evaluation of the radiative heat transfer under diluted and oxy-combustion conditions [244]. Such an evaluation has to rely on computationally expensive models, such as the SNB-CK model employed in the present study, and therefore it is usually not feasible when performing a numerical analysis of complex devices. Also, soot can give a significant contribution to the overall radiative heat transfer in gas turbines, especially when a pilot non-premixed flame is present [21]. Given the fact that, for the considered dilution levels, the radiative source term is considerably smaller with respect to the chemical heat release in the reaction zone, radiation is not included in the CFD calculations. Nevertheless, the relative importance of radiation with respect to chemical reaction can be significantly higher when highly diluted conditions are considered, as in MILD and oxy-combustion. The choice of neglecting radiative heat transfer in the CFD calculations carried out in the present work is also justified by the significant computational effort that would be associated with an accurate prediction of the radiative heat transfer in an actual gas turbine combustor and by the difficulties associated with the specification of a sensible boundary condition for the combustor outlet section.

4.4 Experimental Turbec T-100 cases

From the calculations reported above, it is clear that carbon dioxide and steam dilution has a significant influence on the combustion chemistry. Further, both thermal and chemical effects have a non negligible impact. Therefore, when considering the diluted combustion processes in real combustors, both these effects must be accounted for at the modelling stage. The thermal effects are related to the the different physical properties, namely the different specific heat of the diluting species with respect to the replaced air, and therefore can be included in the model by accounting for the different mixture composition in the calculation of the physical properties.

Chemical effects are more complicated to be included in the model. As highlighted above, the participation of carbon dioxide and steam in the combustion chemistry takes place mainly at the radical level and affects the chemical kinetics of the combustion process. Therefore, there is a need to include detailed chemistry in the CFD model, together with finite-rate effects. Tabulated chemistry represents an attractive option to account for both these effects at a reasonable computational cost.

In the present work, the FGM method has been employed to parametrise the combustion chemistry as a function of the mixture fraction Z and progress variable c only, as detailed in Section 2.3. One-dimensional premixed adiabatic flamelets have been used as the representative configuration for the combustion process. A flamelet database ranging from pure oxidizer ($Z = 0$) to pure fuel ($Z = 1$) has been generated for each experimental case identified in Section 3.2. Since nitrogen oxides production will be evaluated at the post-processing stage, the progress variable definition reported in Equation (2.146) is employed in the generation of the flamelet libraries.

The governing equations for the baseline and the CO_2-diluted cases at 80 kW power output have been solved in both the physical space by employing Cantera and in the reaction progress space using the flamelet solver embedded in ANSYS Fluent [63], in order to assess the suitability of Equation (2.145) as a model for the scalar dissipation term within the reaction progress space. Since no significant differences were observed between the physical and the reaction progress space

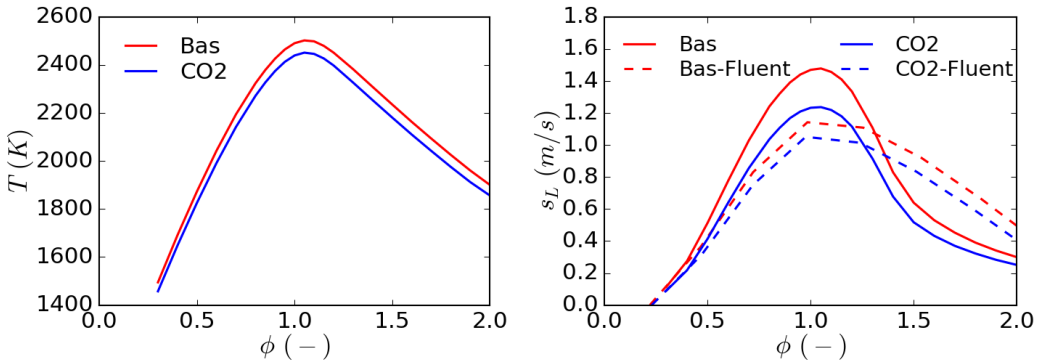

Figure 4.12: 80 kW power output: final temperature (left) and laminar flame speed (right) as a function of the equivalence ratio for the baseline and the CO_2-diluted cases.

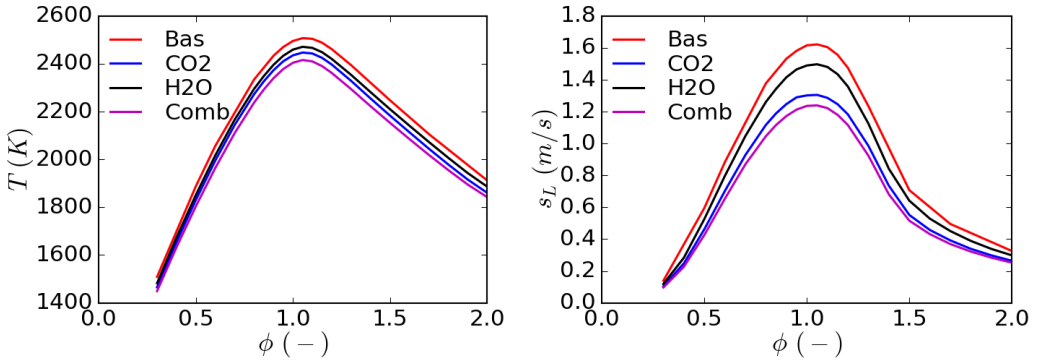

Figure 4.13: 65 kW power output: final temperature (left) and laminar flame speed (right) as a function of the equivalence ratio for the baseline, H_2O-diluted and combined CO_2/H_2O-diluted cases.

solutions, the latter has been employed in the remaining cases that have been investigated. The governing equations have been solved for each flamelet database between the lean and rich flammability limits. The solution has been extrapolated outside of the flammability limits in order to cover the entire mixture fraction range in the database between $Z = 0$ and $Z = 1$.

Since fuel and oxidizer are injected into the system at different temperatures, the unburnt mixture temperature at different mixture fraction values is evaluated as [31]

$$T_u(Z) = T_{oxi} - Z(T_{oxi} - T_F) \tag{4.2}$$

The resulting laminar flame speed and burnt gas temperature at $c = 1$ are reported in Figures 4.12 and 4.13 for the cases at 80 kW and 65 kW power outputs, respectively. It can be seen that even in these realistic cases, whose boundary conditions are obtained from the experimental tests and therefore account for the influence of dilution on the overall MGT operation, the considered dilution levels can be expected to have a significant impact on both the combustion temperature and the flame speed. It is interesting to note that the combined injection of carbon dioxide and steam has a slightly lesser effect with respect to sum of the individual impact of CO_2 and H_2O dilution. This can be due to the fact that the higher reduction in temperature observed with combined dilution hinders the direct participation of the diluting species in the combustion chemistry, resulting in less pronounced chemical effects.

The dashed curves on the right hand side of Figure 4.12 represent the laminar flame speed calculated by ANSYS Fluent for the two 80 kW cases. ANSYS Fluent uses correlations from [245] to evaluate the laminar flame speed at a given mixture fraction value. These correlations are only valid for combustion in air of the pure fuels H_2, CH_4, C_2H_2, C_2H_6 and C_3H_8, for unburnt mixture temperature up to 800 K, equivalence ratio ranging from the lean limit to unity and pressure from 1 bar to 40 bar. It can be seen how the laminar flame speed values evaluated by Fluent according to [245] are not suitable for the present application, failing to predict the correct peak value of s_L in the stoichiometric region and not being valid in the rich part of the flammability range. This has to be kept in mind if a turbulent flame speed model, Equation (2.114), is employed to model the source term in the progress variable transport equation, since all the models for s_T require the laminar flame speed as an input parameter.

4.5 Summary

This chapter presented the results obtained from the numerical investigation of the effects of H_2O and CO_2 dilution on methane combustion. The investigation has been performed in a representative simple configuration, i.e. a freely propagating 1D flame using a detailed chemical mechanism for natural gas combus-

tion. Two different operating conditions, corresponding to ambient and MGT-like temperature and pressure, have been considered. A dilution level of 4% in the oxidizer, similar to the experimental cases reported in Section 3.2 has been investigated for both carbon dioxide and steam dilution, together with a case with combined dilution using both CO_2 and H_2O. It has been found that dilution has a significant impact on the combustion process, even at the relatively low dilution levels considered. In detail, dilution has been found to have an impact due to both thermal and chemical effects, the former being related to the physical properties of the diluting species and the latter due to their participation in the chemical reactions. Although the thermal effects have been found to be more significant than the chemical ones, the latter cannot be neglected, especially at high unburnt gases temperature and for stoichiometric mixtures. This suggest that both these effects have to accounted for in the modelling of diluted combustion in practical combustion devices.

Furthermore, a fundamental study on the impact of radiative heat transfer has been carried out by employing the optically thin approximation and the SNB-CK model to evaluate the optical properties of the mixture. It has been found that the enhanced presence of CO_2 and H_2O in the combustion environment in the diluted cases results in a higher radiative source term and in a more marked impact on the temperature field. Nevertheless, this impact is small with respect to the effects of the chemical heat release within the reaction zone, and is less evident at MGT-like conditions. For this reason, together with the complications and the significant computational cost associated with an accurate calculations of radiative heat transfer under diluted conditions in complex configurations, radiation is neglected in the CFD analyses carried out in the present work.

Finally, it has been shown that dilution has a significant impact on the combustion process even under the realistic operating conditions taken from the PACT experimental dataset for the air-fired and diluted operation of the Turbec T-100 MGT. The impact of dilution on the operation of the combustor of this MGT will be assessed in detail through 3D CFD calculations in Chapter 6.

Chapter 5

Modelling of a lab-scale burner

This chapter presents the results obtained for the modelling of two cases of the Sydney burner swirling flames series described in Section 3.1. The non-reactive case N29S054 and the reactive SMA1 case have been selected for the present investigation. The non reactive case has been selected due to the presence of a characteristic secondary RZ having the form of a closed bubble and due to vortex breakdown. The vortex-breakdown mechanism [246] is often employed in combustion devices to generate a RZ in order to stabilise the flame [23]. The reactive case has been selected for being characterised by a partially-premixed combustion regime, which is often found in gas turbine combustors.

The main aim of this chapter is the assessment of the numerical techniques employed in the present thesis against detailed experimental data. For the reasons outlined in Section 2.3.5, the combustion chemistry is tabulated using the FGM method, and turbulence-chemistry interaction is accounted for using a presumed-PDF approach. In order to assess the main advantages and drawbacks of the two approaches, both steady-state RANS and LES have been employed for turbulence modelling.

The steady-state RANS calculations have been carried out using the realizable $k-\epsilon$ model from Shih et al. [67]. This model is expected to perform better than the standard and the RNG $k-\epsilon$ formulations in the modelling of jet flows and of flows characterised by strong streamlines curvature [63, 247, 140]. Also, the realizable $k-\epsilon$ model has been observed to perform similarly to RSM closures in some test cases, with the advantage of requiring less computational cost with

respect to second-order models [247, 248, 249].

With a focus on the LES approach, whilst a substantial effort has been put into the development and validation of SGS combustion models [29, 30], a relatively small attention has been given to the systematic assessment of SGS stress models and mesh resolution in the modelling of swirling flames. Due to the complex fluid dynamics nature of swirling flows, SGS stress models can be expected to have a significant impact in the prediction of such reactive swirling flows.

Therefore, four SGS models, i.e. the Smagorinsky, Dynamic Smagorinsky, WALE and Sigma models, have been tested in this thesis, employing three numerical grids with different levels of refinement in the modelling of both the non-reactive and the reactive cases. A total of 24 LES calculations have been carried out in the current work. The impact of mesh resolution, quantified using an a-priori quality metric, and of the SGS stress models has been assessed for the non-reactive and reactive cases with an extensive comparison with the experimental measurements. Also, general guidelines for LES-FGM calculation of partially-premixed swirling flames have been inferred.

Finally, in order to assess the benefits and drawbacks of both approaches, the LES results have been compared against the findings from steady-state RANS calculations of the same cases.

5.1 Computational domain and numerical settings

The computational domain used in the present calculations is cylindrical, with a height of 0.35 m and a radius of 0.22 m. During preliminary calculations it was found that further extending the domain in the axial and radial directions does not have a significant impact on the numerical results. The inflow plane is shifted 0.08 m upstream of the burner outlet section, following the observation from [250] that extending the domain upstream of the burner outlet improves the results accuracy with respect to applying the boundary conditions directly at the burner outlet section.

Three numerical grids, with different levels of refinement, have been generated

	Mesh #1	**Mesh #2**	**Mesh #3**
Jet diameter	27	29	29
Annulus radius	11	17	17
Annulus circumf.	79	87	87
Bluff-body radius	39	49	49
Axial (up to 0.2 m)	219	349	449
Total cell count	3.17×10^6	4.19×10^6	6.02×10^6

Table 5.1: Number of elements used to resolve different geometrical features and total cell count for the three numerical grids.

using a structured blocking method in ANSYS ICEM 15.0. The numerical grids were applied to both the non-reactive and the reactive cases. The number of elements employed to resolve the main geometrical features and the total cell count are summarised in Table 5.1.

The main differences between the first two meshes is an increased resolution in the radial direction within the annulus and across the bluff-body, as well as the refinement in the axial direction, in order to better resolve the shear layers in the near-burner region. The distinction between mesh #2 and mesh #3 is the increased axial resolution of the latter, with the objective to have a more accurate resolution away from the burner.

Fully developed velocity profiles based on the experimental flow rates were used for the inlet boundary conditions, together with stochastic unsteady perturbations generated using the vortex method [105]. For the exit of the domain a Dirichlet condition was employed for the pressure and a zero-gradient condition was enforced for all of the other flow variables. The wall treatment from [100] was employed for the near-wall regions in order to relax the mesh requirements to resolve the wall boundary layer and thus reduce the overall cell count.

All of the calculations have been carried out using the commercial CFD code ANSYS Fluent 15.0, which employs the finite volume method discretization technique. In terms of numerical settings, the Semi-Implicit Method for Pressure-Linked Equations (SIMPLE) algorithm was used for the pressure-velocity coupling [251], with a bounded second-order implicit advancement in time. A second-

order upwind scheme has been used for both the momentum equation and transported scalars for the RANS calculations, whilst a bounded central differencing scheme has been employed for the momentum equations in LES calculations. Since the Sigma model is not included in the default SGS stress closures available in ANSYS Fluent, it has been implemented in the code via a User Defined Function.

All of the LES solutions were calculated for a physical time of 0.02 s, equal to the residence time in the domain, in order to reach a statistically steady state, with an additional 0.04 s for statistical averaging. A time-step equal to 2×10^{-5} s was employed for the calculations on mesh #1, and a smaller time-step of 1.5×10^{-5} s was used for meshes #2 and #3.

The steady-stated RANS calculations for both the non-reactive and the reactive have been carried out on mesh #3.

5.2 Non-reactive case N29S054

The numerical results for the non-reactive N29S054 case are reported in this section. This case has a jet axial bulk velocity of 66.0 m/s and a swirl number equal to 0.54. The peculiar feature of this case is the presence of two distinct RZs: the first one is stabilised on the bluff-body face while the second one, due to vortex breakdown, has the form of a closed bubble and is located along the burner axis further downstream. From the experimental findings, the first RZ stagnates at x=25 mm downstream of the burner outlet over the bluff-body face and the second one presents a first stagnation point located at x=50 mm along the axis and a second one at x=110 mm. This second recirculating region is associated with a peak negative velocity of about -6 m/s at x=85 mm [229]. The simulation of 0.06 s of physical time on mesh #3 with the Smagorinsky SGS model took about 132 hours on a 48 cores cluster. The use of WALE and Sigma models did not result in any significant computational overhead, whilst the Dynamic procedure resulted in an increase in the computational time of about 24% with respect to the Smagorinsky model.

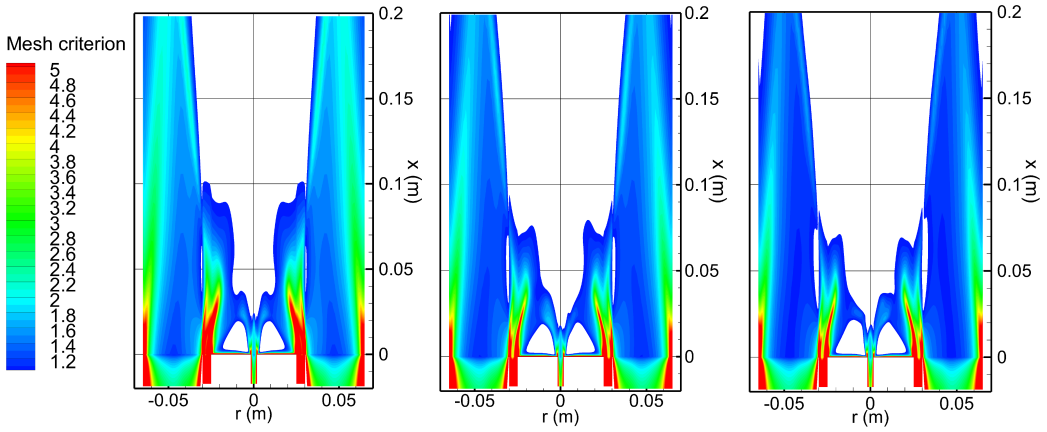

Figure 5.1: Case N29S054 - Mesh quality criterion, Equation (2.79), contours for (from left to right) mesh #1, #2 and #3.

5.2.1 Mesh resolution impact

The suitability of the three different meshes for LES has been assessed using the a-priori criterion reported in Equation (2.79). Figure 5.1 shows distributions of the ratio $\Delta/\frac{\mathcal{L}}{12}$ for the three meshes, where $\mathcal{L}$ has been evaluated from a precursor steady RANS simulation carried out with the realizable $k-\epsilon$ model. The regions where the criterion in Equation (2.79) is satisfied are clipped out in the figure. It can be seen how, according to the proposed criterion, the most critical regions for mesh refinement are represented by the inner and outer shear layers at the burner outlet. Also, it can be noted that these two regions appear to be under-resolved, especially in mesh #1. The shear layers resolution is improved in mesh #2, although, according to the criterion, the numerical grid is still too coarse in these regions to resolve 80% of the turbulent kinetic energy. A mesh satisfying the criterion everywhere in the domain has not been considered in the present investigation due to the elevated number of cells that such a computational grid would require. As detailed in Section 5.1, the difference between mesh #2 and #3 lies in the increased refinement of the latter in the axial direction up to x=0.2 m. The increased axial resolution has a significant impact on the results, especially away from the burner, and this will be discussed more in the detail for the reactive case in Section 5.3.1.

All of the considered SGS stress models have been able to predict the presence of the two RZs on the three considered meshes. The numerical results for the

main RZs features are summarised in Table 5.2. From the figures reported, it can be seen that a good prediction for both the RZs has been obtained. As expected, the results are converging towards the experimental measurements with refined numerical grids. The Sigma model provides the most accurate results among the considered SGS models. On the most refined mesh, this model predicts that the first RZ stagnates at x=28 mm, compared to an experimental value of 25 mm. The caclulated locations of the stagnation points associated with the bubble-like RZ are x=43 mm and x=109 mm. Also, the magnitude and the location of the negative velocity peak within the secondary RZ are predicted with a reasonable accuracy.

5.2.2 Mean and RMS velocity components

A comparison between experimental and calculated axial mean velocity values is shown in Figure 5.2 at x=10, 40, 70 and 100 mm. Overall, a satisfactory matching between numerical and experimental values has been observed. In the first section, there is a spurious negative velocity dip in all the numerical results around r=30 mm, and this is probably due to a coarse resolution of the outer shear layer region. A trace of this spurious peak is still visible in the downstream section in the standard Smagorinsky results, whilst all the other SGS models are in reasonable agreement with the experimental data. Further downstream, a good matching between numerical predictions and experimental data has been achieved.

The same comparison for the mean tangential velocity component is reported in Figure 5.3, with an overall good agreement with the experiments. At x=40 mm the Smagorinsky and the Dynamic models provide a better prediction of the peak located at r=16 mm. Away from this radial location, the standard Smagorinsky model deviates slightly from the experimental values, whilst the other models are matching the experimental data closely. All of the considered SGS models are in good agreement with the experiments in the downstream sections, with a slight under-prediction of the experimental values along the axis.

A comparison between the experimental and the calculated axial and tangential velocity RMS fluctuations at x=10, 20, 40 and 70 mm is reported in

		Mesh #1	Mesh #2	Mesh #3
Smagorinsky	x_{1rz}	35 mm	31 mm	30 mm
	x_{2rz}	40/95 mm	42/101 mm	42/106 mm
	U_{neg}	-5.81 m/s	-6.04 m/s	-6.14 m/s
	x_{neg}	70 mm	61 mm	59 mm
Dynamic Smagorinsky	x_{1rz}	37 mm	32 mm	30 mm
	x_{2rz}	43/99 mm	41/106 mm	44/116 mm
	U_{neg}	-7.21 m/s	-6.44 m/s	-6.11 m/s
	x_{neg}	65 mm	72 mm	73 mm
WALE	x_{1rz}	37 mm	30 mm	29 mm
	x_{2rz}	42/104 mm	42/111 mm	42/113 mm
	U_{neg}	-6.90 m/s	-5.75 m/s	-6.13 m/s
	x_{1rz}	67 mm	62 mm	70 mm
Sigma	x_{1rz}	36 mm	30 mm	28 mm
	x_{2rz}	42/101 mm	43/117 mm	43/109 mm
	U_{neg}	-6.86 m/s	-6.02 m/s	-6.36 m/s
	x_{neg}	62 mm	71 mm	75 mm

Table 5.2: Case N29S054: LES predictions for the RZs main features - Calculated location of the stagnation points associated with the first (x_{1rz}) and the second (x_{2rz}) RZs together with the peak negative velocity value (U_{neg}) and its location (x_{neg}) associated with the latter.

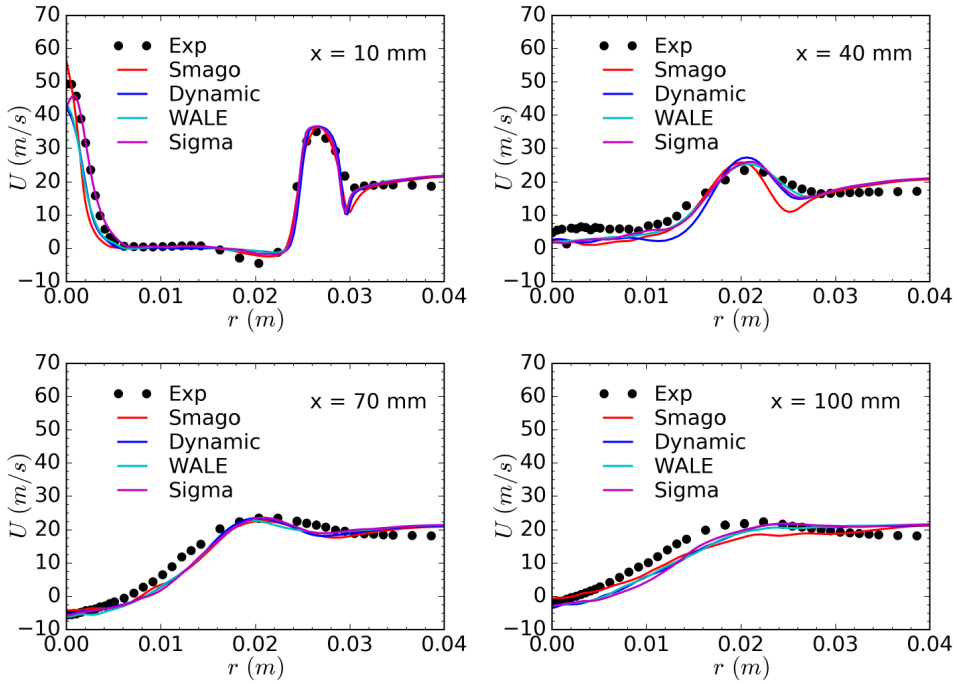

Figure 5.2: Case N29S054 - Calculated (mesh #3) and experimental mean axial velocity profiles at different axial locations.

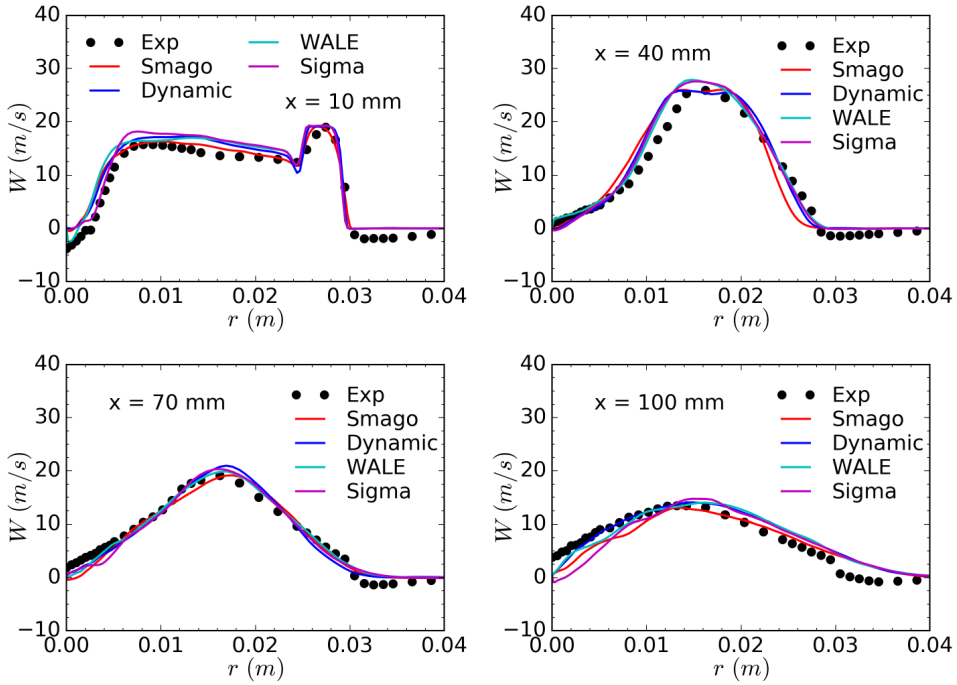

Figure 5.3: Case N29S054 - Calculated (mesh #3) and experimental mean tangential velocity profiles at different axial locations.

Figures 5.4 and 5.5, respectively. For the axial velocity fluctuations at x=10 mm, the two spikes observed experimentally at r=24 mm and r=29 mm are captured by the CFD calculations, although the calculated peak values are smaller than the measured values. The Smagorinsky model overestimates the axial U_{rms} value more significantly than the other SGS stress models. At x=20 mm the predictions of peak values are improved with respect to the upstream section, and further downstream a good agreement between numerical and experimental results can be observed.

For the tangential velocity RMS values, the first experimental spike at x=10 mm is hardly visible in the numerical results, whilst the second peak is well predicted by all of the considered SGS models apart from the Smagorinsky model. At x=0.02 m, the axial W_{rms} value is well predicted by all of the models. Also, the first spike is still not reproduced correctly, whilst a good prediction for the second peak experimental value can be observed (again, the Smagorinsky model underestimates this value). A good matching between numerical and experimental data can be observed further downstream, with a tendency to slightly over-predict the W_{rms} values along the burner axis.

5.2.3 Flow instabilities

An assessment of the unsteady jet behaviour has been carried out, taking advantage of the LES ability to predict flow instabilities. Experimentally, the presence of jet precession and the associated frequency have been assessed by postprocessing of the high speed Mie scattering imaging in a region centered around a spatial jet locator at x=12.3 mm and r=2.3 mm. Although no direct evidence of jet precession has been observed experimentally for this case, the presence of this kind of flow instability has been reported for a similar case, where the experimental jet precession frequency observed for a swirl number of $S_g = 0.45$ is equal to 26 Hz [231].

Following the approach outlined in [252], a combination of visual inspection of the flowfield together with a Fast Fourier Transform (FFT) analysis of the instantaneous axial velocity signal evaluated at the same spatial location considered in the experimental investigation (i.e. x=12.3 mm, r=2.3 mm) was used

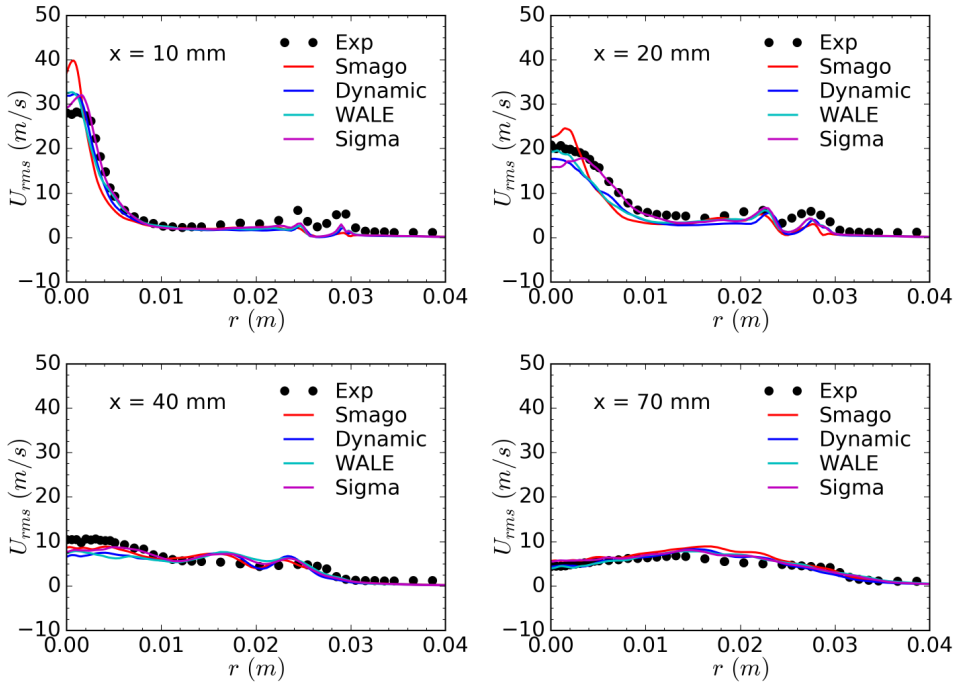

Figure 5.4: Case N29S054 - Calculated (mesh #3) and experimental axial velocity RMS fluctuations at different axial locations.

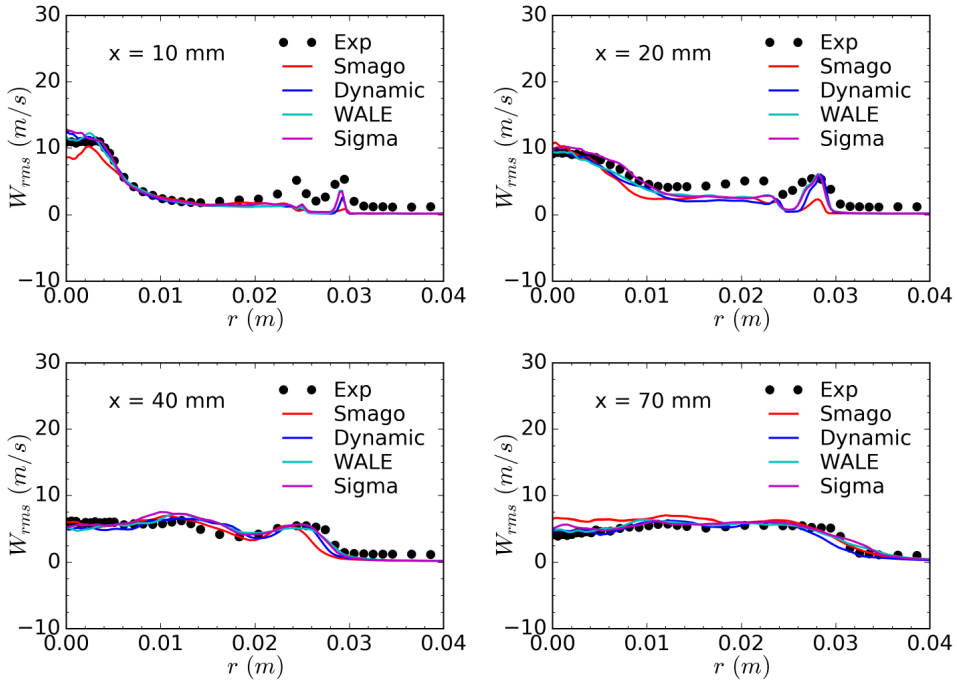

Figure 5.5: Case N29S054 - Calculated (mesh #3) and experimental tangential velocity RMS fluctuations at different axial locations.

in the present work to assess the presence of flow instabilities and evaluate the related characteristic frequencies. The power spectrum of the calculated instantaneous axial velocity signal on mesh #3 with the Sigma model shows a peak corresponding to a precession frequency of 27 Hz. A visual representation of the jet precession motion is shown in Figure 5.6 in terms of instantaneous axial velocity contours between t=0 s and t=0.0369 s.

In general, it can be concluded that LES has been confirmed to be a suitable tool for the prediction of the considered non-reactive swirling flow and of the related complex phenomena (i.e. flow recirculation, vortex breakdown). Good quantitative predictions for the mean velocity component have been obtained on a sufficiently refined mesh, especially employing more advanced SGS stress models with respect to the standard Smagorinsky model. The proposed mesh quality metric showed that the numerical grid is undersized in the shear layers region, and this can explain the slight deviation between the calculated and the measured location of the first RZ stagnation point. The use of more advanced SGS models also appears to improve the prediction of the velocity RMS fluctuations. Overall, the Sigma model provides the most accurate results for this case among the considered SGS closures. Further, it was shown that LES has the potential to predict flow instabilities associated with swirling flows.

5.2.4 Steady-state RANS results

The simulation of the reactive case on mesh #3 with the realizable $k-\epsilon$ model took about 24 hours on a 48 cores cluster. Due to the inherently unsteady nature of the flow, and to the presence of flow instabilities, the calculation showed a fluctuating behaviour and it was not possible to reach a completely stable solution. Also, due to the intrinsic limitations of the steady RANS approach, no information on the RMS quantities and flow instabilities are obtained. Nevertheless, the RANS simulation is able to reproduce the main time-averaged features of the flow, at least from a qualitative point of view. In particular, the presence of two distinct RZs, the first one stabilised over the bluff-body face and the second one having the form of a closed bubble further downstream, is predicted correctly. The first RZ is predicted to stagnate at x=32 mm, compared to an experimental

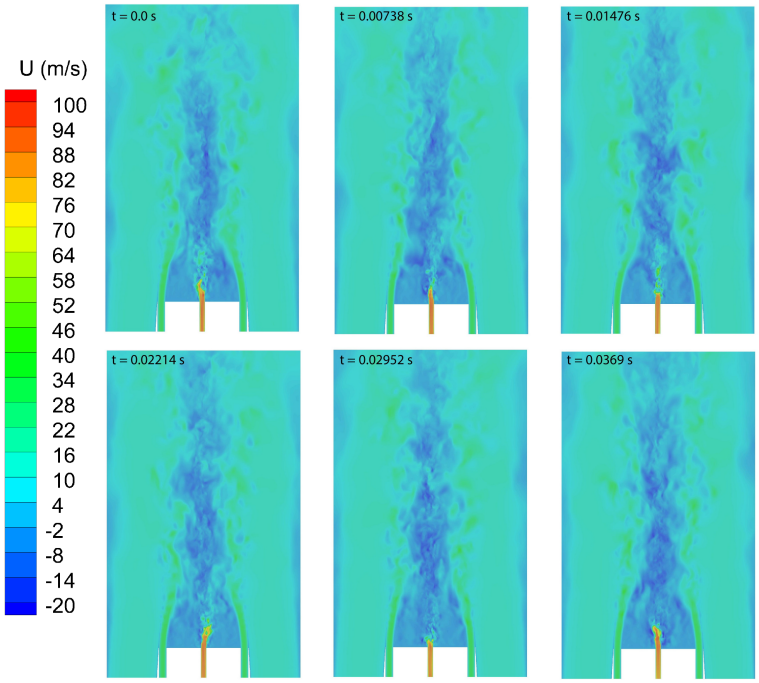

Figure 5.6: Case N29S054 - Calculated (Sigma model - mesh #3) instantaneous axial velocity contours at different simulation times.

value of 25 mm and a prediction obtained with the Sigma SGS model on the same mesh of 28 mm. The calculated shape of the second RZ results elongated with respect to the experimental observation. The two stagnation points associated with this RZ are located at x=52 and 154 mm, compared to the experimental locations corresponding to x=50 and 110 mm, and the calculated locations with the Sigma model on the same mesh being equal to x=43 and 109 mm.

A more detailed comparison between the results obtained with the steady RANS approach and the LES with the Sigma model on mesh #3 for the mean axial velocity component at the axial locations corresponding to the second RZ is reported in Figure 5.7, showing the calculated mean axial velocity profiles at x=70, 100 and 125 mm together with the experimental data. It can be noted how the Sigma model is able to provide a more accurate prediction of the axial velocity along the burner axis in all the considered axial locations. Also, at x=125 mm the steady-state calculations are still predicting a significantly negative axial velocity at r=0 mm, whilst the Sigma model is in close agreement with the experimental data, predicting a positive value of the axial velocity.

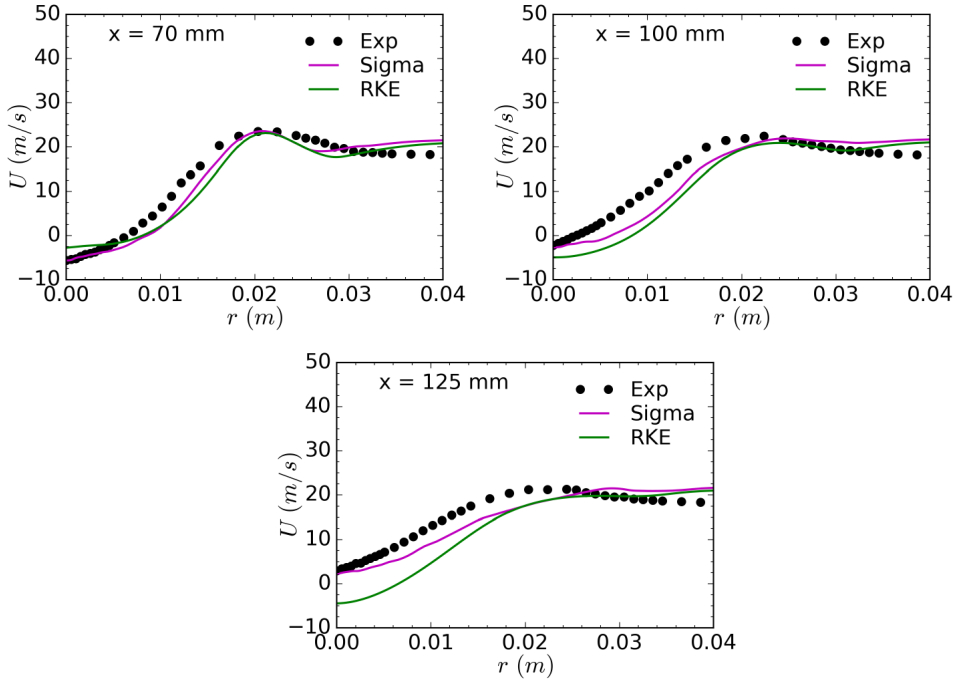

Figure 5.7: Case N29S054 - Calculated mean axial velocity profiles at different axial positions

5.3 Reactive case SMA1

In this section the results for the reactive case SMA1 are presented. This case is characterised by a jet bulk axial velocity of 66.3 m/s and a geometrical swirl number of 0.66. The jet flow is composed of a CNG-air mixture (with a 1:2 volume ratio), and thus the combustion regime is partially premixed. In the present calculations the CNG is treated as pure methane. The velocity flowfield is characterised by a single elongated RZ attached to the bluff-body which stagnates at a distance of about 110 mm from the burner outlet [230].

A real-colour picture of the flame taken from [253], together with contour plots of the instantaneous OH mass fraction and temperature from LES calculations (Sigma model on mesh #3), are shown in Figure 5.8. From the experiments, the flame looks asymmetric, with a visible length of about 200 mm and an evident neck zone downstream of the RZ. Further, extensive local extinction has been observed experimentally within the flame [230]. From the contour plots in Figure 5.8, it can be noted how the numerical calculations have been able to reproduce the neck contraction in the flame (it is worth noting that James at al.

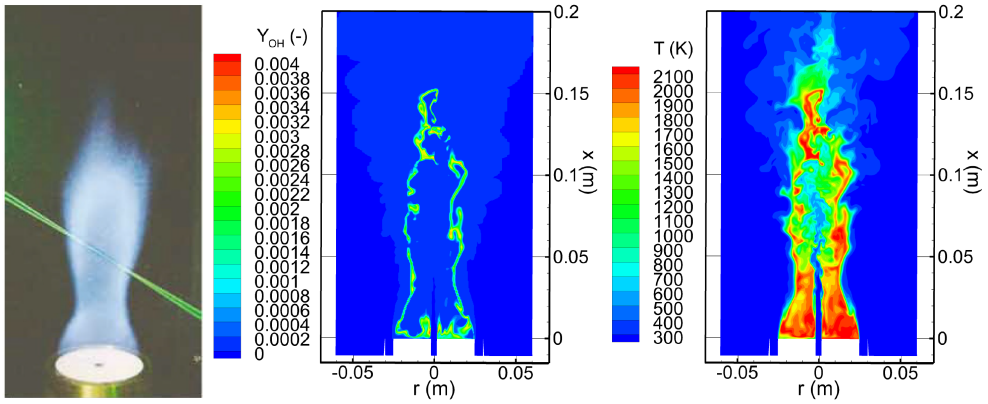

Figure 5.8: Case SMA1 from left to right: real-colour picture of the flame from from [253] and calculated (Sigma model on mesh #3) instantaneous OH mass fraction and instantaneous temperature.

[254] had difficulty in predicting this feature in their numerical investigation of the same case case). Also, the extensive local extinction observed experimentally has been predicted by CFD calculations thanks to the progress variable approach ability to account for this phenomenon [192], as can be noted in the instantaneous temperature contour plot shown in the same figure. The simulation of a physical time of 0.06 s on mesh #3 with the Smagorisnky model resulted in a computational time of about 199 hours on a 48 cores cluster. Also in this case, the increase in the computational cost associated with the Sigma and the WALE models resulted to be less than 5% with respect to the Smagorinsky model, whilst the computational time associated with the Dynamic model for the same physical time on the same mesh was equal to 277 hours.

5.3.1 Mesh resolution impact

In terms of the assessment of the mesh refinement impact on the numerical results, the same a-priori mesh quality criterion employed for the non-reactive case, Equation (2.79), has been applied to the reactive case as well. Plots of $\Delta/\frac{\mathcal{L}}{12}$ for the three meshes are shown in Figure 5.9, where regions corresponding to a value less than unity are clipped out. Similarly to the findings for the non-reactive case, it can be noted from Figure 5.9 that the inner and outer shear layers are still the most challenging regions in terms of mesh resolution, with an improvement between mesh #1 and mesh #2 and a very small improvement in the near-burner

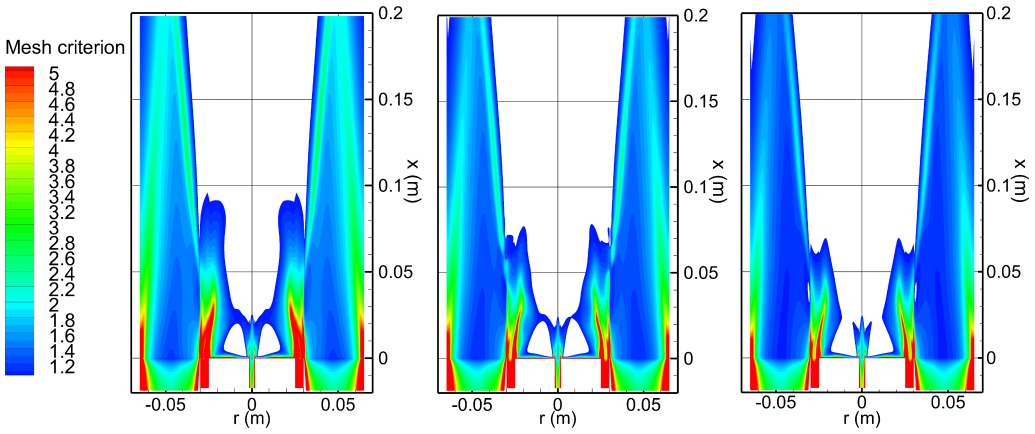

Figure 5.9: Case SMA1 - Mesh quality criterion, Equation (2.79), contours for (from left to right) mesh #1, #2 and #3.

	Mesh #1	Mesh #2	Mesh #3
Smagorinsky	0.49 mm	0.67 mm	0.86 mm
Dynamic	0.79 mm	0.87 mm	0.88 mm
WALE	0.67 mm	0.78 mm	0.85 mm
Sigma	0.80 mm	0.85 mm	0.93 mm

Table 5.3: SMA1 case - LES results for the stagnation point locations.

region from mesh #2 to #3.

The four different SGS models have been employed on the three meshes, for a total of 12 calculations. The presence of a single RZ attached to the bluff body has been predicted correctly in all of the simulations, and the calculated stagnation point locations are summarised in Table 5.3. Also in this case, the calculated positions converge towards the experimental values as the mesh is refined. The Sigma model provides the most accurate predictions for the stagnation point location on mesh #3, with a calculated value of x=93 mm compared to the experimental figure of 110 mm. The discrepancy between the calculated and the experimental values can be due to the insufficient mesh resolution in the shear layers. Furthermore, it can be noted how the Dynamic and the Sigma models are able to provide a reasonable prediction even on the coarser mesh, whilst WALE and the Smagorinsky model are more sensitive to mesh refinement, as it will now be detailed further.

Since the mesh resolution has been found to have a significant impact on the

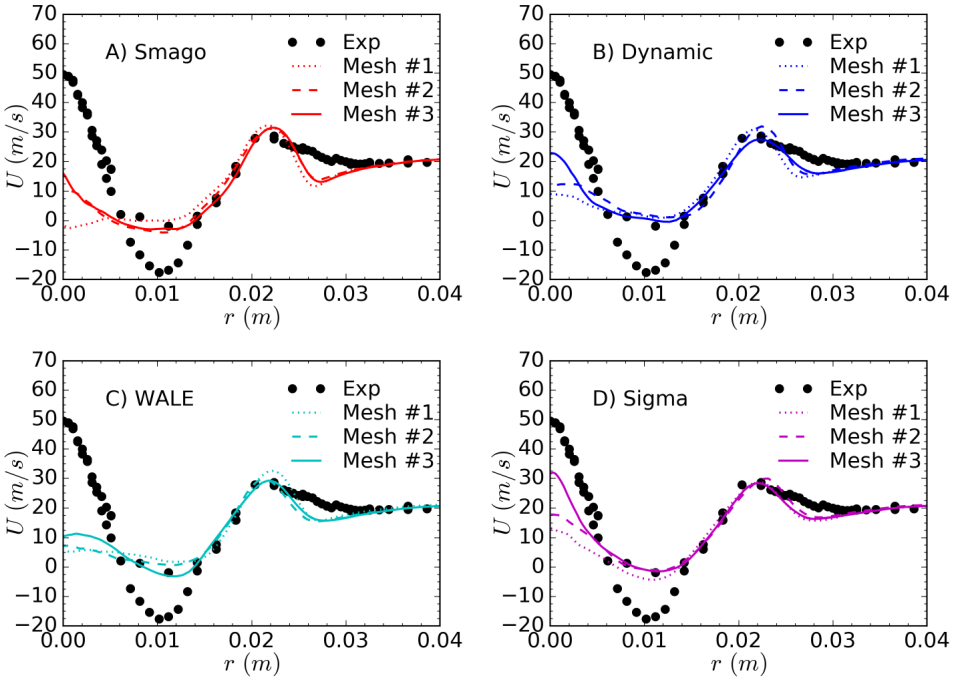

Figure 5.10: Case SMA1 - Mesh size impact on axial jet penetration: mean axial velocity profiles at x=40 mm.

accuracy of the numerical predictions, a more in depth analysis of the effects of mesh resolution on the numerical results for the SMA1 case has been carried out, with a particular focus on the following three features:

- Jet penetration prediction, for which the mean axial velocity profiles at x=40 mm are reported in Figure 5.10.
- Flame stabilization on the bluff body surface, for which the mean temperature profiles at x=10 mm are shown in Figure 5.11.
- Temperature field prediction away from the burner, for which the mean temperature profiles at x=120 mm are reported in Figure 5.12.

From Figure 5.10, it can be seen how mesh refinement has a marked impact on the prediction of one of the most challenging features of this case, i.e. the axial jet penetration. With the most refined grid, the Sigma model is providing the most accurate prediction for this feature, followed by the Dynamic model. In general, the Sigma model was observed to be the less sensitive model to mesh size. Nevertheless, a non-negligible improvement in the prediction of this feature

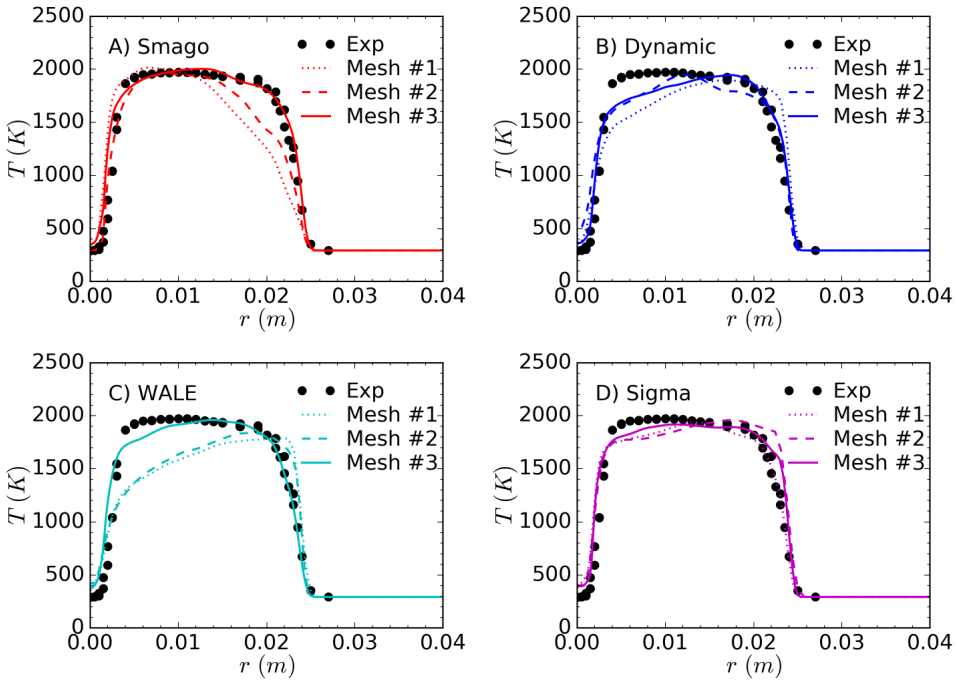

Figure 5.11: Case SMA1 - Mesh size impact on flame stabilization on the bluff body: mean axial velocity profiles at x=10 mm.

with this SGS model was observed over the refined meshes. In particular, it is worth noting the improvement between meshes #2 and #3, due to the higher axial resolution of the latter.

The effects of mesh refinement on the flame stabilization on the bluff body are shown in Figure 5.11. It can be noted how the numerical results are improved on the more refined numerical grids. The Smagorinsky and WALE models are found to be quite sensitive to the mesh resolution in this location, while the Sigma and the Dynamic models are giving more consistent results regardless of mesh resolution. In particular, the Sigma model appears to be able to give an acceptable prediction for this particular feature even on the coarser mesh.

Finally, the impact of mesh resolution on the temperature predictions away from the burner is shown Figure 5.12. It can be seen that the Smagorinsky model is very sensitive to mesh resolution in this section. On the other hand, WALE resulted to be the less sensitive model to grid refinement in this section, whilst the Sigma and Dynamic models over-predicted the axial temperature value noticeably on mesh #1. Overall, improvements in the accuracy with more refined numerical

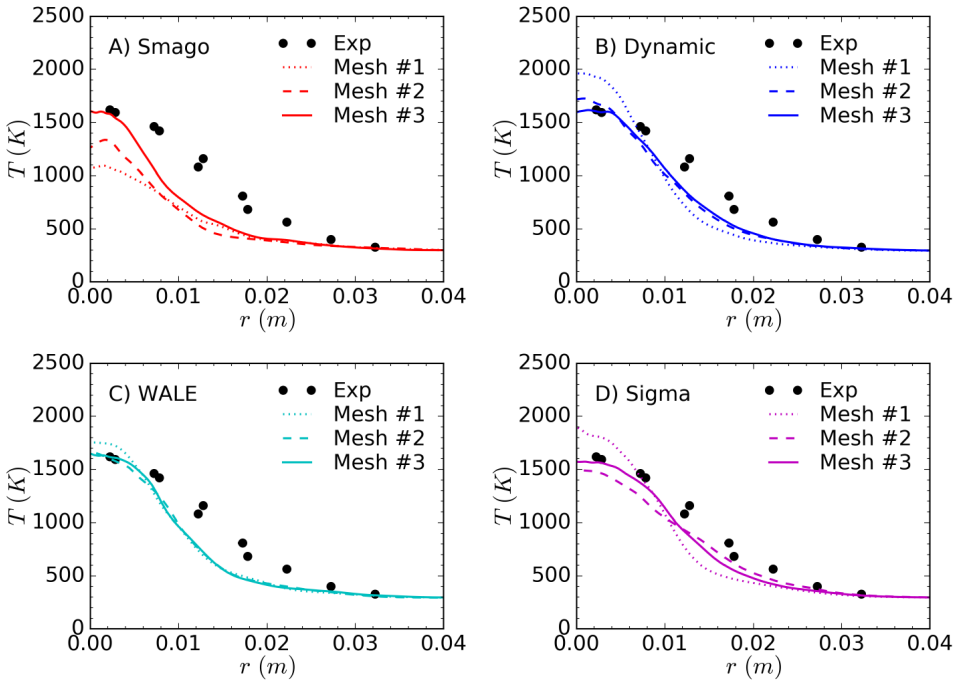

Figure 5.12: Case SMA1 - Mesh size impact on the calculated temperature away from the burner: mean axial velocity profiles at x=120 mm.

grids can be noted for all of the SGS models. It can be concluded that mesh resolution is crucial to the accuracy of the LES calculations in the reactive case, both in the shear layers and in the low-turbulence region away from the burner. Although mesh #3 is still too coarse to satisfy the criterion in Equation (2.79), an improvement of the results with respect to mesh #2 can be seen both in the shear layers and in the low turbulent region away from the burner.

5.3.2 Mean and RMS velocity components

A comparison between the numerical results obtained on mesh #3 with the different SGS models and the experimental data for the mean axial velocity at x=10, 40, 70 and 150 mm is shown in Figure 5.13. A good agreement with the experimental data is obtained in the first section, although the presence of a spurious negative dip at r=30 mm, as noted in the non-reactive case, is present in this case as well. At x=40 mm, the jet decay is over-predicted by all of the SGS models, with the Sigma and Dynamic models closer to the measured values. As reported also in [189] for the investigation of the SMA2 case, an accurate jet pen-

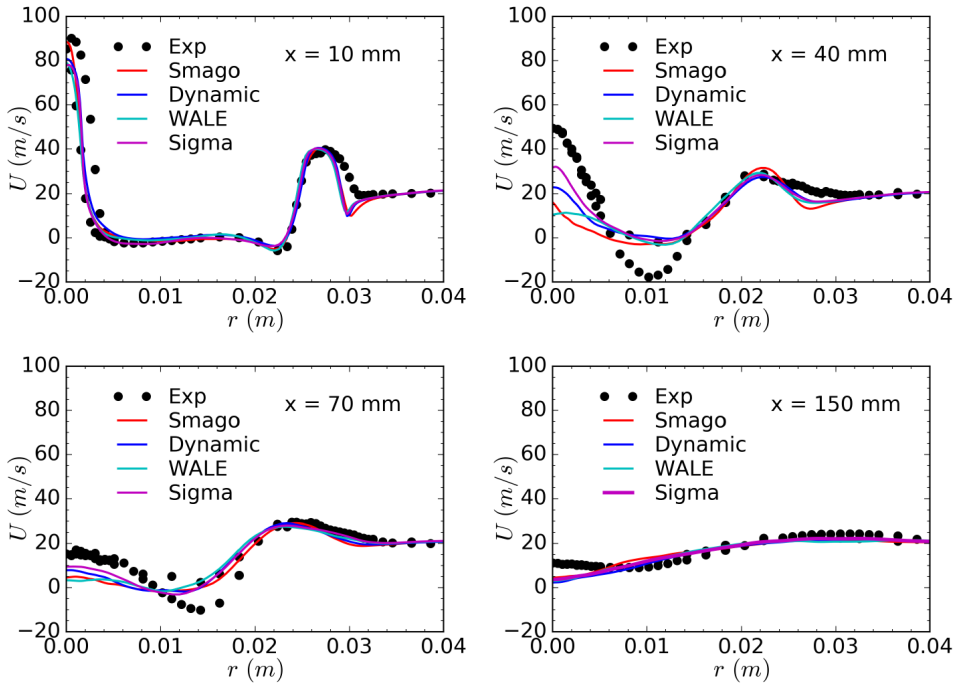

Figure 5.13: Case SMA1 - Calculated and experimental mean axial velocity profiles at different axial locations.

etration prediction appears to be a very challenging task for the SMA flames. In the sections downstream, all of the models are underestimating the experimental axial value, with the Sigma model providing the most accurate prediction among the considered models, whilst a good agreement with the measurements is found away from the burner axis.

A comparison between the experimental and calculated mean tangential velocity is reported in Figure 5.14. At x=10 mm, the double-humped profile observed experimentally is reproduced correctly by all models, although the first peak value is slightly underestimated, whilst the central values are overestimated. In their numerical investigation of the same case, James et al. [254] failed to predict the correct tangential velocity shape in this section. At x=40 mm, the numerical results are in reasonable agreement with the experimental values, even if all of the SGS models, except Sigma, are failing to predict the short plateau observed experimentally at r=15 mm. At x=70 mm, the Sigma model is still providing a more accurate prediction of the experimental values between r=15-20 mm. Further downstream, all the models are in good agreement with the experimental

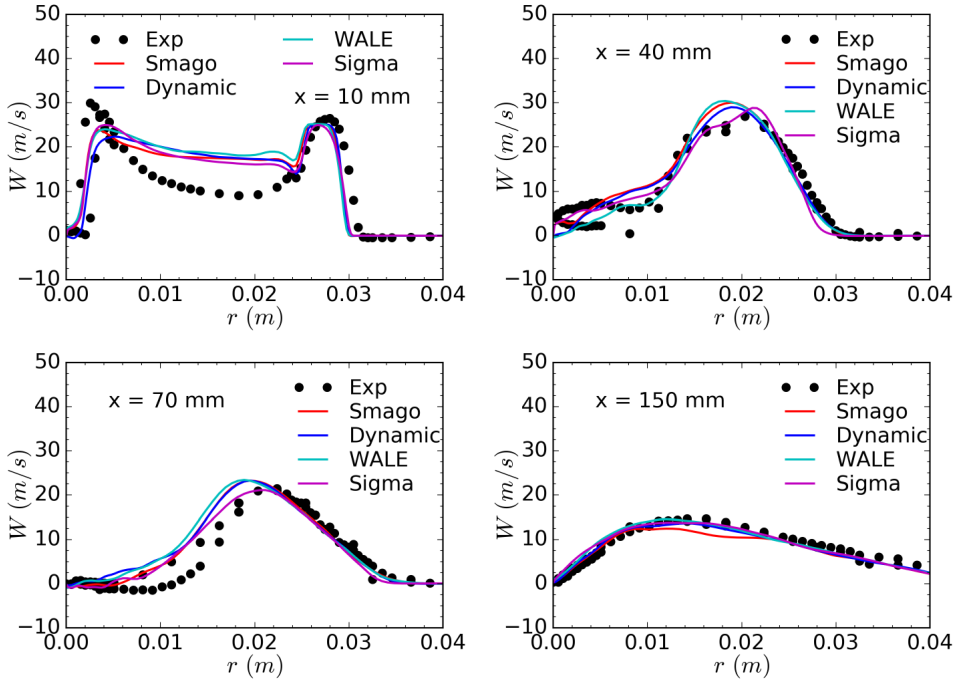

Figure 5.14: Case SMA1 - Calculated and experimental mean tangential velocity profiles at different axial locations.

measurements.

Experimental and numerical values of the RMS fluctuations of U and W at x=10, 40, 70 and 150 mm are reported in Figures 5.15 and 5.16, respectively. For the axial velocity fluctuations, at x=10 mm all the models are overestimating the axial value significantly. Also, the presence and location of the two spikes observed experimentally is well predicted, with the Smagorinsky model underestimating the peak values. At x=40 mm, all the models, except WALE, are still overpredicting the measured axial U_{rms} value, whilst a reasonable agreement with the experimental values is found away from the burner axis. At x=70 mm, the correct experimental axial value is recovered, and further downstream an overall good agreement with the measurements can be observed.

For the tangential velocity fluctuations, as shown in Figure 5.16, at x=10 mm the measured axial W_{rms} values are overestimated significantly by the calculations, whilst a fairly good prediction of the two peaks observed experimentally has been obtained with all the SGS models, except Smagorinsky. At x=0.04 mm a reasonable estimation of the axial value can be observed, whilst the measured

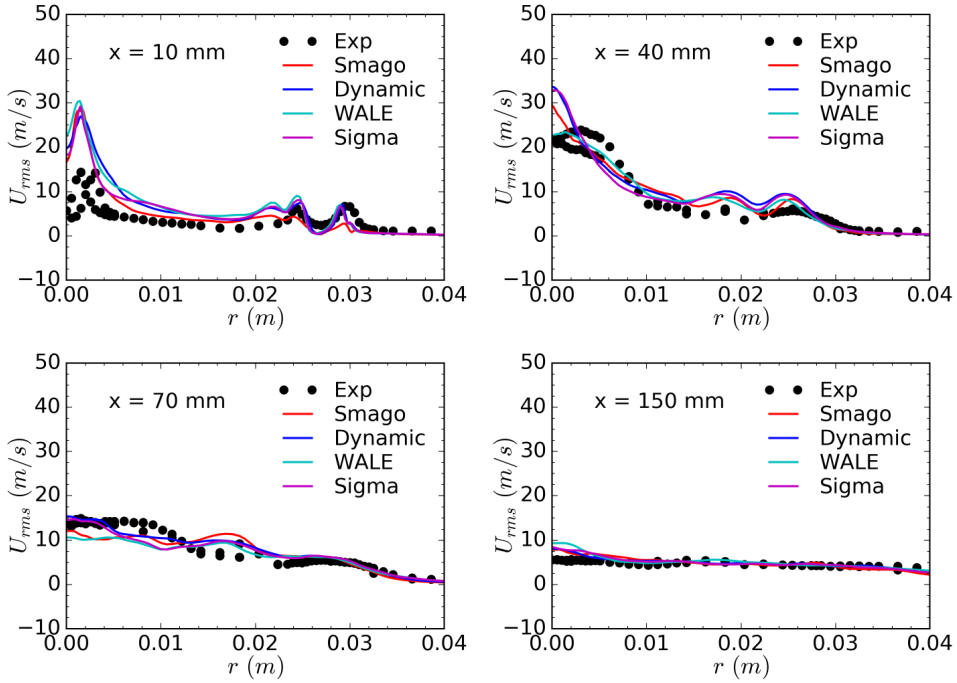

Figure 5.15: Case SMA1 - Calculated and experimental RMS axial velocity profiles at different axial locations.

values between r=7 mm and r=20 mm are over-predicted by all the SGS models. In the downstream section, a satisfactory overall agreement with the experimental values has been found, although the axial experimental value is slightly overestimated at x=150 mm.

5.3.3 Temperature and species

The calculated mean temperature is compared to the measured values at x=10, 25, 50 and 120 mm in Figure 5.17. The temperature values are well predicted by all models in the first section, with the Smagorinsky model performing slightly better close to the burner axis. At x=25 mm, the axial temperature is overestimated by all models, due to the incorrect jet penetration prediction, with the Sigma and the Dynamic model closer to the experimental axial value. The experimental peak temperature away from the axis is well estimated by all models, although the flame looks slightly broader than the experiments in this section. The latter feature can be observed also at x=0.05 m. Also, in this section the axial temperature is predicted correctly (slightly overestimated by the Smagorinsky

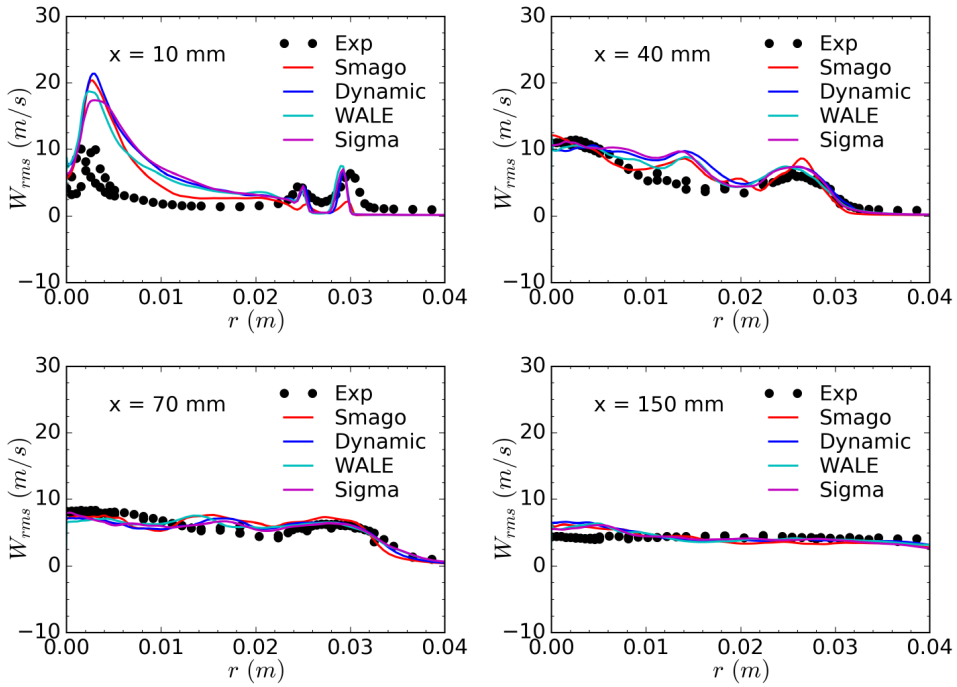

Figure 5.16: Case SMA1 - Calculated and experimental RMS tangential velocity profiles at different axial locations.

model) whilst the peak value is over-predicted and shifted outwards with respect to the experimental measurements. Overall, a good estimation of the experimental temperature profiles and its axial values can be observed further downstream, although the radial extent of the flame is slightly underestimated in these sections, with the Sigma and the Dynamic models closer to the measurements.

Comparisons between the experimental and the numerical values for the mean mass fraction of CO_2, H_2O and OH at the same axial locations considered for the temperature profiles are reported in Figures 5.18, 5.19 and 5.20, respectively. Overall, the species predictions are satisfactory and reflect the general picture outlined when discussing the temperature field. The carbon dioxide mass fraction is underestimated significantly in the first two sections, especially close to the burner axis, while an improvement in the predictions can be observed in the downstream sections. The calculated H_2O mass fraction is in good agreement with the measured values at x=10 mm, and follows the same trend described for the temperature predictions in the remaining sections. For the numerical prediction of the radical species OH, the connection with the calculated temperature

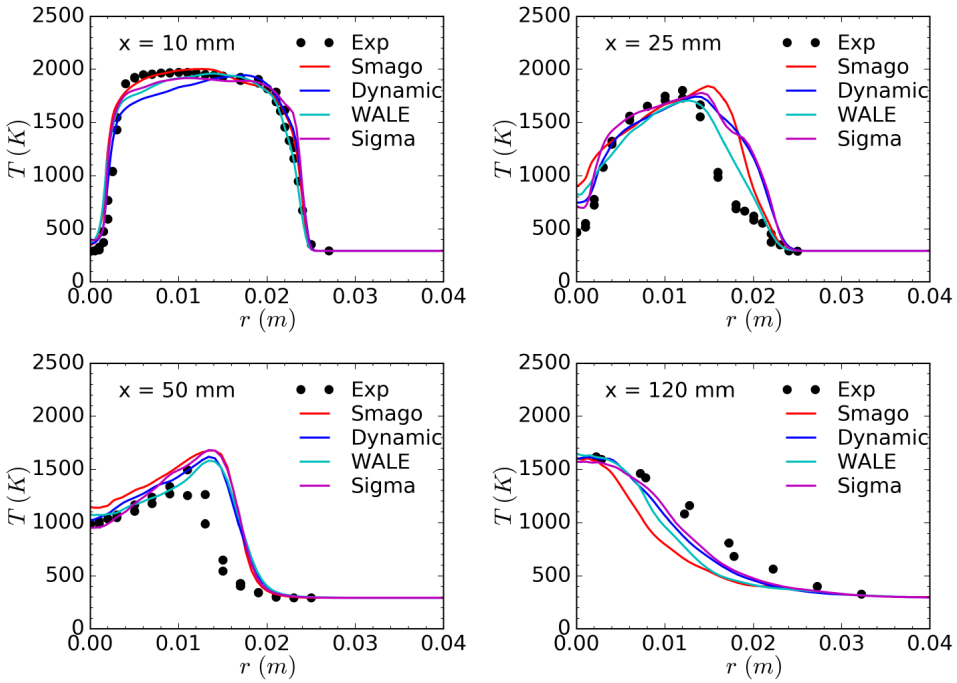

Figure 5.17: Case SMA1 - Calculated and experimental mean temperature profiles at different axial locations.

field is less straightforward. At x=10 mm a general under-prediction of the experimental OH levels has been observed, with the Smagorinsky model performing better close to the burner axis, while the Sigma model gives a better prediction of the overall profile shape and of the experimental values away from the axis. The same general underestimation of OH levels is observed at x=25 mm, although the peak observed in the experiments is reproduced qualitatively by all models, with the Sigma model better matching the measured value. At x=50 mm, a reasonable prediction of the measured OH level is provided, and the Sigma model is able to correctly predict the maximum OH value observed in the experiments. In the downstream section, all the models are able to reproduce the shape of the experimental data, although the axial OH levels are underestimated significantly and the radial broadness of the profile is under-predicted as well (with the Sigma model again closer to the experimental values).

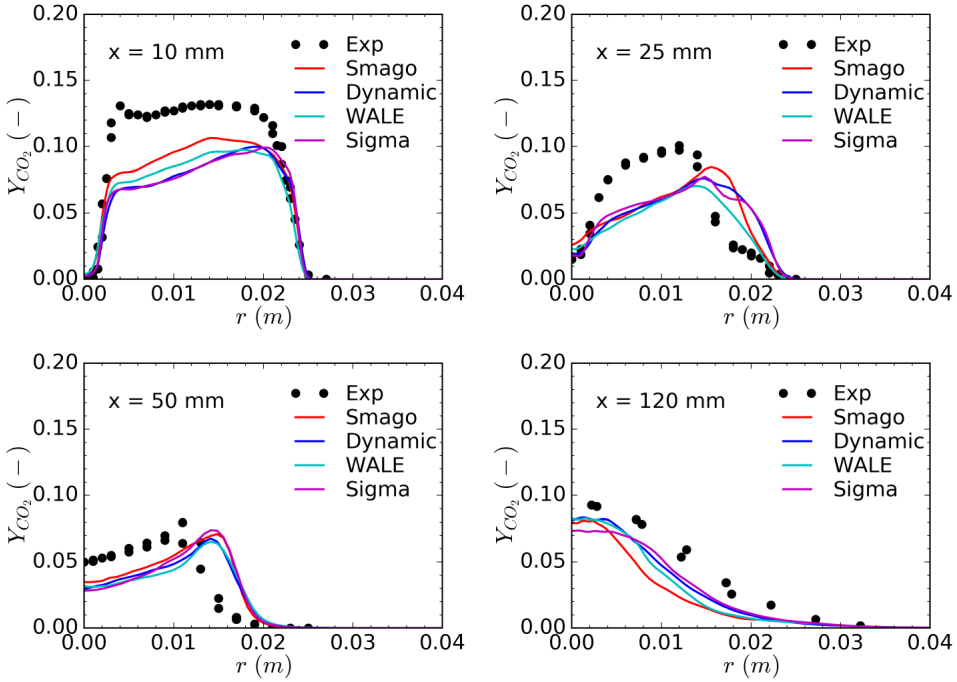

Figure 5.18: Case SMA1 - Calculated and experimental mean CO_2 mass fraction profiles at different axial locations.

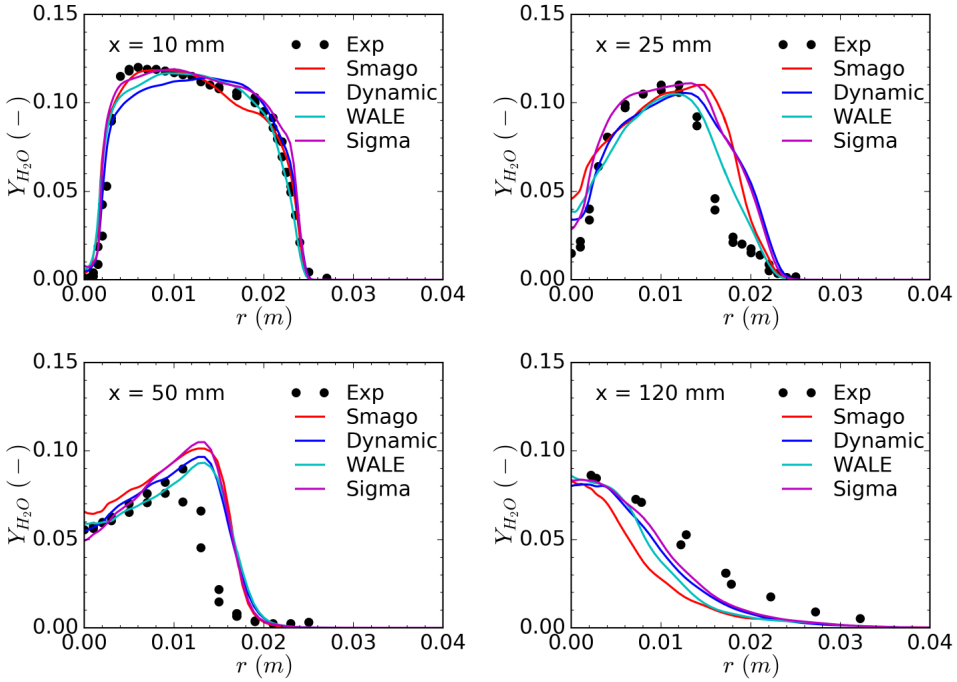

Figure 5.19: Case SMA1 - Calculated and experimental mean H_2O mass fraction profiles at different axial locations.

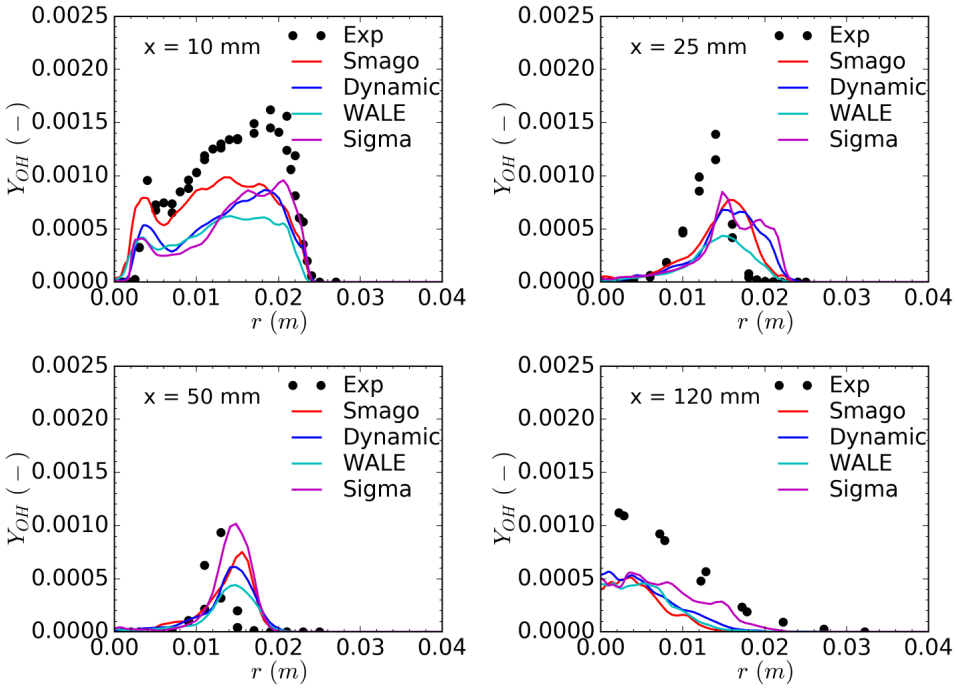

Figure 5.20: Case SMA1 - Calculated and experimental mean OH mass fraction profiles at different axial locations.

5.3.4 Flow instabilities

Finally, an analysis of the time-dependant results obtained for the reactive case has been performed. In particular, Al-Abdeli et al. [232] reported that, although no clear jet precession or other form of periodic instabilities have been observed in this case, Mie scattering movie clips showed that the tip of the jet is subject to irregular bending, and a FFT analysis of the instantaneous axial velocity within the jet (at x=12.3 mm and r=2.3 mm) revealed a characteristic peak around 100 Hz. The numerical results somewhat confirm these experimental findings. In fact, employing the same technique used for the non-reactive case, no clear precession jet motion has been observed in any of the calculations carried out. However, as evident in the power spectrum (calculated from the Sigma model results on mesh #3) shown in Figure 5.21, a characteristic peak at around 80 Hz is present, and irregular (non-periodic) jet bending has been reproduced as well. Again, as for the non-reactive case, this confirms the potential of LES calculation to predict flow instabilities in both reactive and non reactive flows.

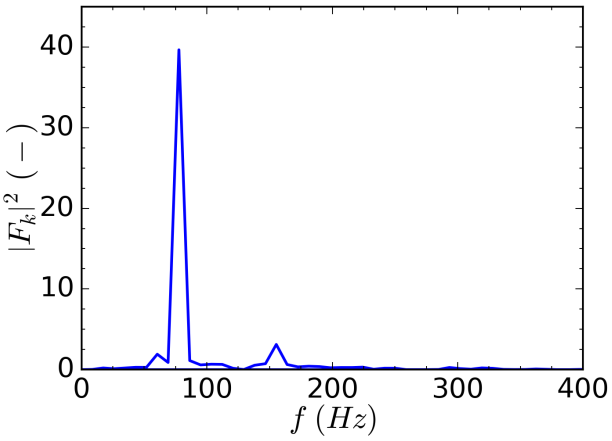

Figure 5.21: Case SMA1 - Power spectrum of the instantaneous axial velocity signal sampled at x=0.0123 m and r=0.0023 m from the Sigma model calculation on mesh #3.

5.3.5 Steady-state RANS results

The calculation of a steady-state RANS solution on mesh #3 for the reactive case took about 32 hours on a 48 cores cluster. The observations made in Section 5.2.4 on the inability of the steady RANS approach to account for flow unsteadiness apply also to the reactive case. Also in this case, the realizable $k-\epsilon$ approach is able to predict the main features of the flow, such as the presence of a single RZ attached to the bluff-body, and the characteristic neck contraction of the flame. The calculated stagnation point associated with the RZ is located 65 mm downstream of the burner, whilst the Sigma model predicts a location of x=93 mm on the same numerical grid and the experimental location is equal to x=110 mm.

Also, due to a less accurate estimation of the velocity field within the RZ with respect to LES, the steady RANS calculation is not able to correctly predict the stabilisation of the flame above the bluff-body face. A comparison between the mean temperature contours calculated with the realizable $k-\epsilon$ and the Sigma model on mesh #3 is shown in Figure 5.22, together with the calculated 2D velocity streamlines within the RZ. It can be seen how the less accurate prediction of the velocity field over the bluff-body obtained with the RANS model has a dramatic impact on the temperature field, resulting in the failure to predict the stabilisation of the flame over the bluff-body face. Also, the steady-state calcu-

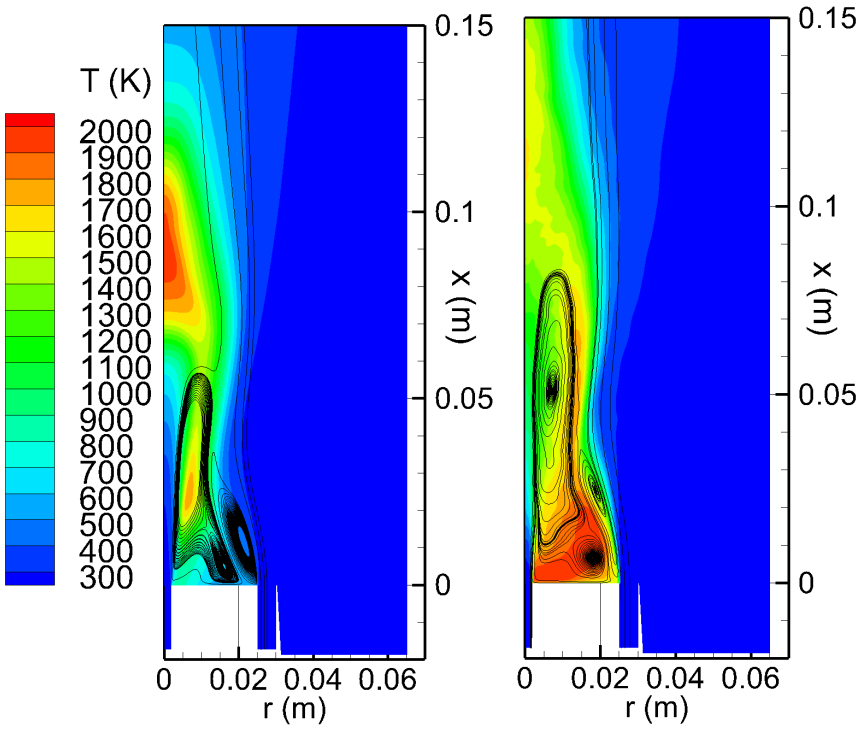

Figure 5.22: Case SMA1 - Mean temperature contours and 2D streamlines calculated with the realizable $k-\epsilon$ (left) and the Sigma model (right) on mesh #3.

lation appears to underpredict the length of the flame with respect to LES and experimental measurements.

A detailed comparison between the calculated mean temperature and axial velocity profiles with the realizable $k-\epsilon$ and the Sigma model above the bluff-body at x=10 mm is reported in Figure 5.23. It can be observed that the Sigma model is able to provide a better representation of the recirculating flow field above the bluff-body, with a calculated axial velocity dip radial location equal to about 0.021 mm, which is very close to the experimental observations. The position of this velocity dip is shifted towards the burner axis in the realizable $k-\epsilon$ calculations, and the velocity field within the RZ is predicted less accurately with respect to the Sigma model. This has a significant impact on the temperature prediction at x=10 mm, with the LES calculation able to accurately predict the flame stabilisation over the bluff-body face.

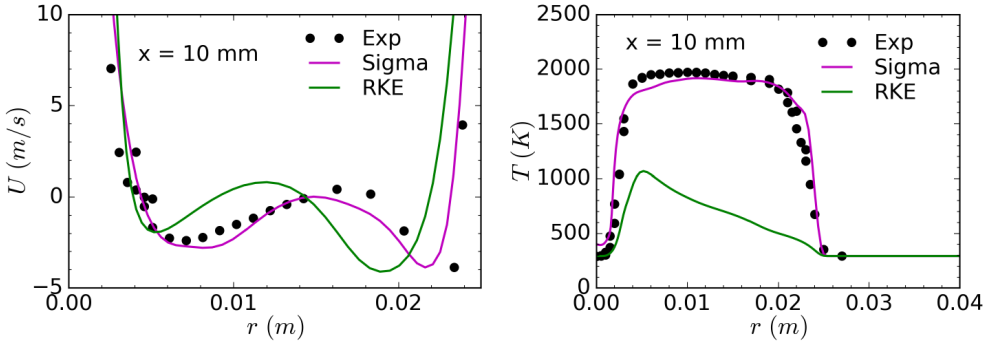

Figure 5.23: Case SMA1 - Calculated mean axial velocity (left) and temperature (right) profiles at x=10 mm.

5.4 Summary

A non-reactive and a reactive partially-premixed cases from the Sydney swirl flames series were simulated using both RANS and LES approaches. The RANS calculations were carried out in steady-state using the realizable $k-\epsilon$ model. The LES calculations were focused on the assessment of performances of four different SGS stress models (Smagorinsky, Dynamic, WALE and Sigma) on three different meshes, for a total of 24 LES simulations.

For the non-reactive case, a good estimation of the main features of the two RZs and reasonable predictions of the mean and fluctuating velocity components have been reached with the LES approach, with more precise results obtained using more advanced SGS models on a refined numerical grid. Overall, the Sigma model was able to provide more accurate results on all the three considered meshes with respect to the other SGS models considered. The ability of LES to predict flow instabilities typical of swirling flows has been confirmed for both cases, with jet precession predicted in the non-reactive case and the reproduction of the non-periodic instability of the jet tip observed experimentally in the reactive case. The steady-state RANS calculations were able to reproduce the main flow field features, even if the predictions were less accurate with respect to the LES calculations on the same computational grid. Also, due to the intrinsic limitations of the steady-state RANS approach, no information about the unsteady nature of the flow were obtained.

For the reactive case, the FGM method has been employed for chemistry

tabulation together with a presumed-PDF approach for turbulence-chemistry interaction. Although reasonably accurate results have been obtained for the main velocity and temperature fields with LES, some features have been found to be very challenging to reproduce (e.g. the axial jet penetration). Also in this case, the Sigma model has given the more accurate results among the considered SGS models. Further, the reactive case has been found to be more sensitive to the numerical grid size both near the burner and further downstream. The a-priori mesh quality criterion employed in the present work, based on the evaluation of the turbulent integral length from a precursor RANS calculation, has been found to be representative of the mesh suitability, in particular in the highly-turbulent shear layer regions close to the burner. Among the considered SGS stress models, the Sigma model appeared to be less sensitive to the grid resolution, providing acceptable results even on relatively coarse meshes. Also in this case the steady-state RANS calculation was able to predict the main features of the considered case, such as the presence of a single RZ and the neck contraction of the flame, at least from a qualitative point of view. A less accurate prediction of the flow field within the RZ leads to inability to correctly predict the flame stabilisation over the bluff-body face.

Finally, due to the ability of the considered experimental setup to reproduce flow features that are typical of industrial configurations (e.g. flow recirculation, vortex breakdown, flow instabilities), the study carried out in this chapter can provide useful insights for the modelling of such complex devices, that are usually characterised by limited or no experimental in-flame measurements for results validation. Steady-state RANS calculations still represent the common practice for the investigation of such devices. It has been shown that this approach is characterised by well-known limitations (e.g. inability to cope with the unsteady nature of the flow) and reduced accuracy with respect to LES calculations. Nevertheless, these calculations are able to provide useful insights about the mean characteristics of the flow field at a reasonable computational cost. On the other hand, LES is able to account for the unsteady nature of swirling reactive flows. The use of advanced closures for SGS stresses and a sufficient mesh resolution are key to obtaining accurate results. Further, the a-priori mesh quality metric used

in the present work can be employed for assessing the suitability of the employed mesh for LES, in particular in the critical regions dominated by highly-turbulent shear layers. Also, due to a reduced sensitivity to the mesh size, the use of SGS stress models based on sound physical principles, such as the Sigma model, can result in a significant advantage when modelling complex geometries, where it is usually necessary to find a compromise between grid refinement and calculation time.

Chapter 6

CFD analysis of a MGT combustor

The present chapter presents the results obtained in the CFD analysis of the Turbec T-100 combustor under both air-fired and diluted conditions. Preliminarily, a description of the mesh and the numerical settings employed in the calculations is provided. Afterwards, the results obtained for the DLR cases outlined in Section 3.2 are introduced. These cases are employed to validate the model against the data provided by the DLR experimental investigation of the MGT system. Finally, the numerical results obtained for the air-fired and diluted cases from the PACT experimental campaign are reported, highlighting the impact of CO_2 and H_2O dilution on the operation of the device.

6.1 Mesh and numerical settings

Mesh generation for industrial gas turbine combustors can be a particularly challenging task, and this is due to the complex geometries typical of these devices. In addition to the geometrical complexity, the complicated nature of the physical processes associated with modern combustors poses additional challenges to the generation of a suitable numerical grid.

The combustor employed by the Turbec T-100 MGT is described in detail in Section 3.2. With respect to the actual combustor geometry, the following modifications have been introduced at the modelling stage:

- The three pins that are used to connect the outer casing to the flame tube have been removed.

- The main fuel injection system has been simplified by removing the nozzle and the toroidal chamber. Instead, the main fuel inlet section consists of 15 circular sections issuing directly into the corresponding main swirler vanes.

- The flame tube has been extended downstream in order to allow more room for dilution to take place and avoid possible numerical issues related to the presence of reverse flow in the exhaust outlet section.

The numerical grid has been generated using ANSYS ICEM 15.0. In order to minimize the influence of the boundary conditions on the flame region, the entire combustor geometry has been modelled, with the modifications outlined above. Due to the significant complexity of the burner section, which includes the swirlers and the pilot and main fuel injection systems, an unstructured tetrahedral mesh has been employed in this region. Prism layers have been generated on the walls of the unstructured region for a better prediction of the boundary layer physics, especially in the non-adiabatic calculations involving Conjugate Heat Transfer (CHT). On the other hand, it is desirable to employ a structured hexahedral mesh in the relatively less complex region downstream of the burner section, including the dilution holes. Although this region is relatively simple compared to the burner section, the presence of the dilution holes represents a significant complication from a topological point of view. An O-grid block has been associated with each dilution hole in order to enhance the mesh quality for these features. The resulting blocking structure is quite complex, and is represented in Figure 6.1.

In order to avoid numerical errors arising from interpolation between the structured and the unstructured regions, the use of a conformal interface between the two is highly recommended. Normally, the interface between a fully tetrahedral and a hexahedral mesh is made conformal by taking advantage of the flexibility of the tetra elements, and leaving the more rigid hexa elements unaltered. Unfortunately, when prism layers are present in the tetra mesh, they cannot be adjusted to match the corresponding hexahedral elements in the structured re-

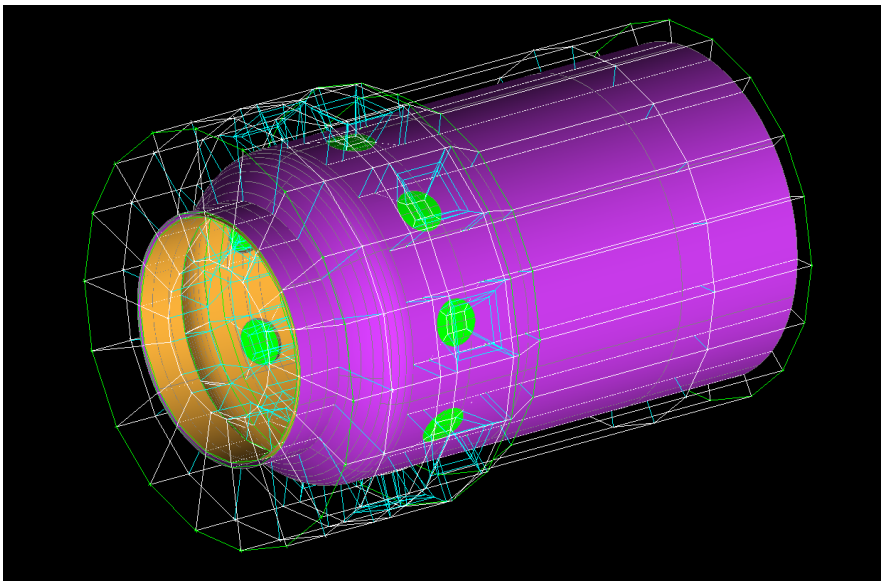

Figure 6.1: Blocking structure employed to generate the hexahedral mesh in the structured region.

gion, and therefore the creation of a conformal interface in this case is particularly challenging. In this work, the advanced meshing capabilities of ANSYS ICEM have been employed to develop a novel methodology to generate a conformal interface between the tetra-with-prisms and the hexahedral mesh. In detail, a pre-inflation technique for the prism layers has been coupled with the use of the existing quadrilateral faces at the interface on the structured region side. The details of the resulting conformal mesh are illustrated in Figure 6.2. On the right hand side of Figure 6.2 it can also be noted that the solid parts of the combustor have been included in the computational domain, and this is in order to account for the CHT within the device.

The same numerical grid used for the RANS calculations of all the considered cases has been employed for the LES modelling of the baseline case at 80 kW power output. As it is often the case when dealing with LES analysis of industrial devices, the maximum number of elements that can be employed is controlled by the available computational resources, and the mesh is often under-resolved for a proper LES calculation. In this case, an upper limit of 15 million elements in the cell count has been identified. The employed numerical grid consists of about 14.9 M elements, 3.9 M of which are solid cells employed for CHT calculations.

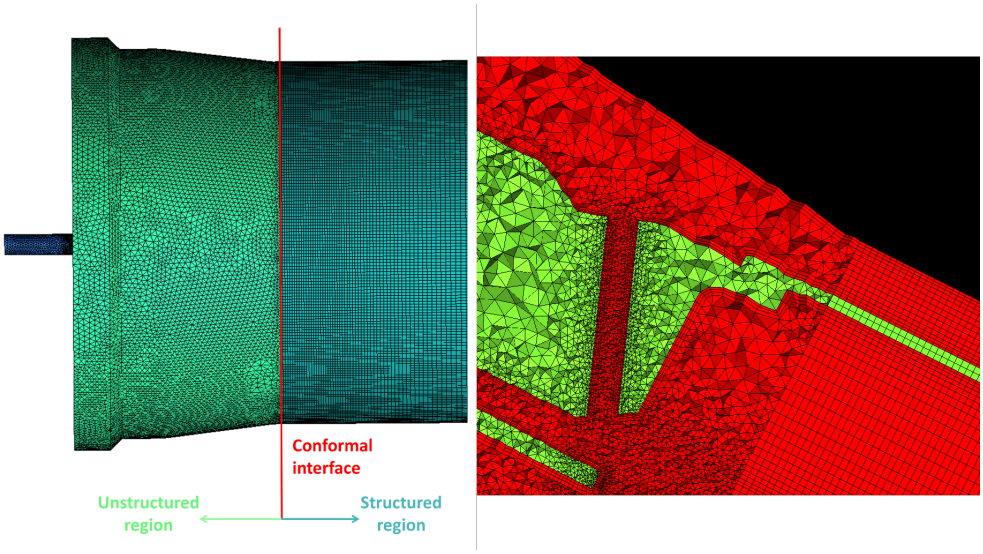

Figure 6.2: Separation between the structured and unstructured regions (left) and details of the resulting conformal interface between the two regions (right).

All of the calculations have been carried out using the commercial CFD code ANSYS Fluent 15.0. Similar to the numerical settings employed for the CFD investigation of the lab-scale burner described in Chapter 5, the SIMPLE algorithm has been used for the pressure-velocity coupling. A second-order upwind scheme has been used for both the momentum equation and transported scalars for the RANS calculations, whilst a bounded central differencing scheme has been employed for the momentum equations in the LES case, together with a bounded second-order implicit advancement scheme in time.

In terms of boundary conditions, fully developed velocity profiles have been used for the fuel and oxidizer inlet sections, with the mass flow rates specified accordingly to the experimental measurements. In the LES calculation, stochastic unsteady perturbations generated using the vortex method [105] were added to the mean velocity components. For the exhaust outlet section, a Dirichlet condition was employed for the pressure and a zero-gradient condition was enforced for all of the other flow variables.

In order to reduce the cell count, a suitable wall-treatment has been employed in both the RANS and LES calculations. For RANS, the scalable wall-functions formulation has been used [63], whilst the Werner-Wengle near-wall treatment [100] has been employed for LES.

Due to the very compact design of the device, CHT is expected to have a significant impact on the results and therefore it has been accounted for in all the calculations. In order to assess the impact of CHT, the baseline 80 kW case of the PACT experimental campaign has been investigated under adiabatic conditions as well.

The RANS calculations have been carried out using the realizable $k-\epsilon$ model, whilst the LES calculation relies on the Sigma model for the SGS stress closure. The combustion thermo-chemistry has been tabulated in terms of the mixture fraction Z and the progress variable c following the FGM approach, as detailed in Section 4.4. The turbulence-chemistry interaction have been accounted for by employing a presumed-PDF approach, where the joint-PDF $P(Z, c)$ has been evaluated as the product of two β-functions.

The progress variable definition presented in Equation (2.146) has been employed for all the calculations. Therefore, NOx emissions have been evaluated according to the post-processing approach discussed in Section 2.3.5. It should be noted that an accurate quantitative calculation of NOx production is an extremely challenging task. The methodology adopted in the present work is aimed at predicting the NOx variation trends, rather than provide precise quantitative values, in order to assess the effects of dilution on pollutant emissions [63].

In detail, the thermal NOx reaction rates have been evaluated using rate coefficients from [255]. Prompt NOx production has been calculated using a global kinetic model proposed by [256] for a C_2H_4-air flame, and a correction function to account for alkane hydrocarbon fuels different from ethylene has been employed, as described in [63]. Further, NOx formation due to the N_2O-intermediate mechanism has been evaluated using the kinetic rate constants provided by [257].

Also, NOx reburn reactions from CH, CH_2 and CH_3 have been considered, by assuming a general reburning mechanism having the form

$$CH_i + NO \longrightarrow HCN + \text{products} \qquad \text{(R 6.1)}$$

The rate constants for the ruburn reactions are taken from [258].

One of the main advantages of this approach is that it allows us to evaluate the relative contribution of each route to the overall NOx production. In all of the considered cases the thermal route resulted to be the most important mechanism

for NOx production, the thermal NOx generation being between one and three orders of magnitude higher than that due to the other routes.

Transport equations for the Favre-averaged mass fraction of the species involved in the NOx calculation (e.g. NO, NO_2, HCN) are solved on the frozen flowfield obtained from the precursor CFD calculations. The instantaneous source terms for the involved species come from the overall contribution of the different mechanisms listed above (i.e. thermal, prompt, N_2O-intermediate and reburn). The Favre-averaged source terms, which have to be provided in order to close the transport equations, are evaluated from the instantaneous values by means of PDF-averaging. A β-function PDF of the temperature has been employed to evaluate the Favre-averaged source terms. In order to build the PDF, the mean temperature value is taken from the results of the precursor CFD calculation, whilst a suitable transport equation for the temperature variance is solved, as detailed in [63].

The mixture density is retrieved directly from the look-up table generated by integration of the laminar flamelet library. Given the very lean overall equivalence ratio and the relatively low dilution levels considered, the thermal conductivity and molecular viscosity are considered to be equal to those of air. Values for the molecular transport properties have been taken from [259].

6.2 DLR baseline cases

The boundary conditions for two DLR cases considered in the present work are reported in Section 3.2. In the experimental findings from [236], as shown in Figure 6.3, the shape of the flame is observed to switch from a closed cone in the $N = 75.0$ case, to a open cone in the $N = 92.5$ case (where N is expressed as the percentage of the nominal shaft rotating speed). Also, due to the higher value of the fuel split ratio s in the latter case, most of the combustion process takes place in the premixed main stage, and the high temperature region associated with the flame appears to be more spread with respect to the $N = 75.0$ case.

The flame shapes obtained from the CFD calculations are reported in Figure 6.4, showing the temperature isosurface at 2000 K for the two cases. From a

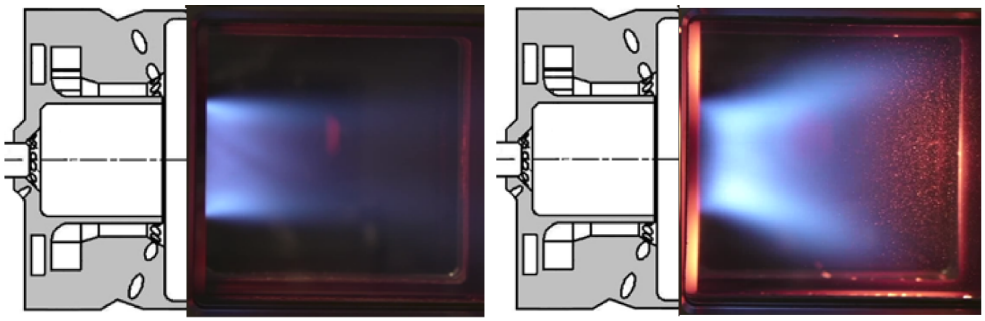

Figure 6.3: Flame pictures at $N = 75.0$ (left) and $N = 92.5$ (right) working points (from [236]).

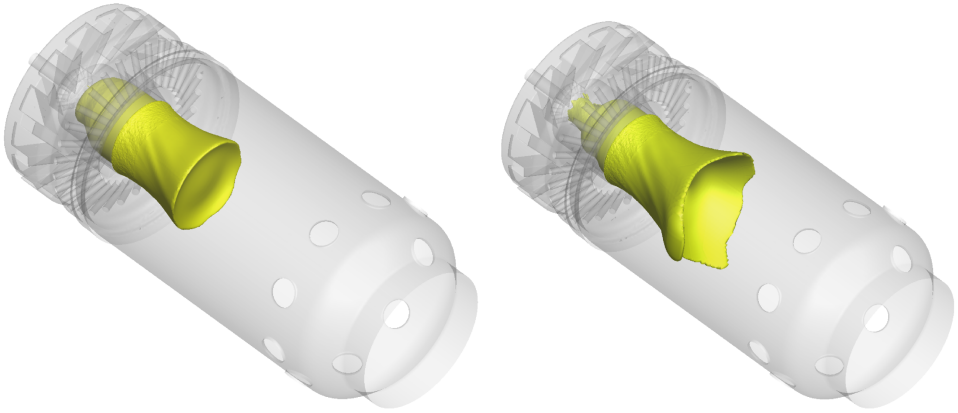

Figure 6.4: Calculated temperature isosurface at 2000 K for the $N = 75.0$ (left) and the $N = 92.5$ (right) cases.

comparison with Figure 6.3, it can be observed how the CFD model is able to predict the flame shape shift from a closed to an open cone between the two cases.

Unfortunately, no flowfield measurements within the combustor are available. From the numerical results, confirmed by the experimental findings obtained in an atmospheric pressure test rig and reported in [236], the velocity field within the combustor chamber is characterised by the presence of two RZs: an outer recirculation zone (ORZ) of toroidal shape and an inner recirculation zone (IRZ) having the form of a closed bubble and generated by vortex breakdown of the swirling flow issuing from the main swirler. It is interesting to note that the realizable $k - \epsilon$ model is able to predict these features, that are typical of swirl-stabilised combustors [23], at least from a qualitative point of view. This confirms

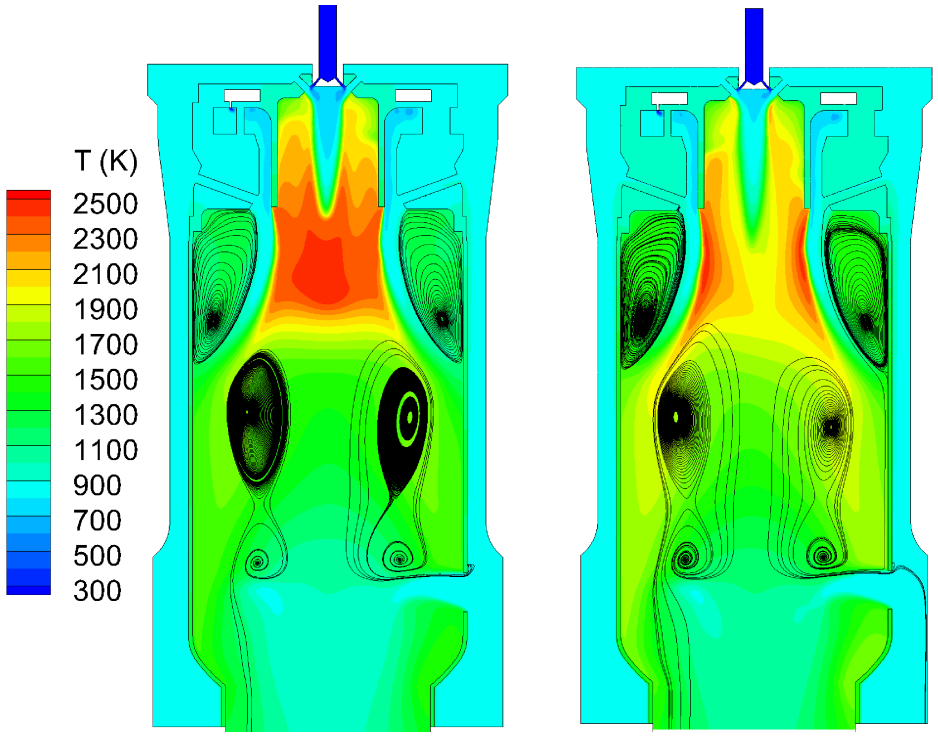

Figure 6.5: Calculated temperature contours together with 2D streamlines on the combustor mid-plane for the $N = 75.0$ (left) and the $N = 92.5$ (right) cases.

the observations made in Chapter 5 on the ability of the steady RANS approach to predict these features.

The flow field for the two cases is depicted in Figure 6.5 in terms of 2D streamlines on the combustor mid-plane, together with the temperature contours on the same plane. The presence of the ORZ and the IRZ is clearly visible in both cases. From a comparison with the experimental findings of [236], it appears that the CFD calculations tend to overestimate the length of the cold jet associated with the pilot flame structure. This can be due to the shortcomings of the turbulence model and to the unsuitability of the premixed flamelet library to reproduce the non-premixed combustion process taking place in the pilot region.

The location of the reaction zone has been assessed by means of the progress variable source term contour plots shown in Figure 6.6. In both cases, the chemical reactions associated with the main combustion process are particularly intense in the shear layers between the ORZ and the IRZ. In the $N = 75.0$ case, the main stage reaction zone is attached to the pilot dome tip and is localised in a small zone close to the burner outlet plane. Also, it can be seen how in this case the

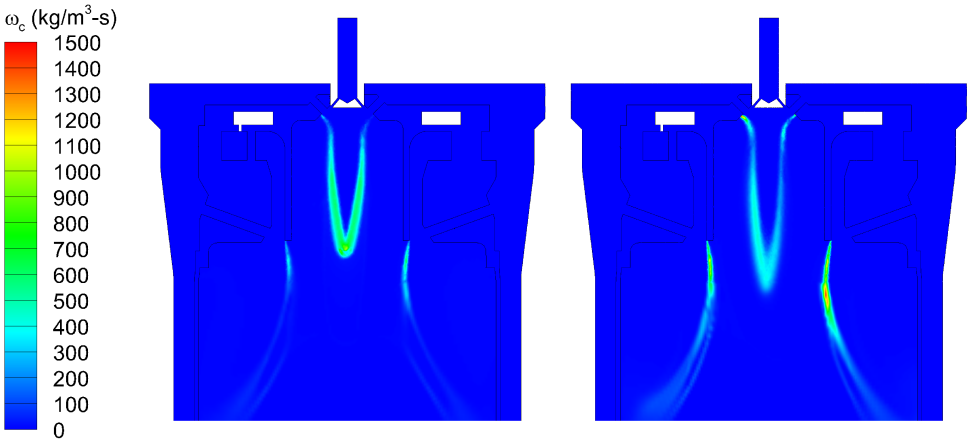

Figure 6.6: Calculated progress variable source term contours on the combustor mid-plane for the $N = 75.0$ (left) and the $N = 92.5$ (right) cases.

contribution of the pilot flame to the overall combustion process is more significant, due to a lower value of the fuel split ratio. In the $N = 92.5$ case, most of the combustion takes place in the main stage, and the region of the maximum reaction rate appears to be lifted and more widespread with respect to the former case. These findings are in agreement with the experimental OH* chemiluminescence measurements for the two cases reported in [235].

For the $N = 92.5$ case, pollutant emissions at the exhaust outlet are reported in [236]. The measurements have been taken while operating the MGT equipped with its original combustion chamber, i.e. without the modifications necessary to guarantee optical access. Therefore, the additional heat losses associated with the fitting of the optically accessible window to the combustor are not present and the experimental data can be readily compared with the CFD results. The calculated and measured NOx [1], CO and unburned hydrocarbons (UHC) concentration at the combustor outlet for the $N = 92.5$ case are summarised in Table 6.1, together with the calculated values for the $N = 75.0$ case. The calculated NOx and CO concentrations are in good agreement with the experimental values in the former case. The observed overprediction of the UHC levels can be due to the inability of the premixed flamelet library to provide an accurate description of the dilution

[1] In this chapter, NOx are considered to consist of the NO species only, since NO_2 production has been found to be negligible with respect to NO. Also, all the figures reported for NOx emissions are "wet" and not normalised to a given oxygen concentration.

	CFD $N = 92.5$	Exp $N = 92.5$	CFD $N = 75.0$
NOx	11	8	19
CO	4	3	< 1
UHC	13	3	42

Table 6.1: Pollutant emissions (ppmv) at the combustor outlet.

of the hot combustion process with cold air downstream of the flame [198].

Although no experimental measurements for pollutant emissions are reported for the $N = 75.0$ case, the calculated results can be compared against the general trends reported in [236] at different N values. Overall, from the experiments, CO emissions are observed to increase sharply for values of N lower than 85, reaching a value of about 200 ppm at $N = 80.0$. UHC and NOx emissions increase slightly at low N values, reaching a value of 5 and 12 ppm, respectively, at $N = 80.0$. The general trend for UHC and nitrogen oxides is reproduced correctly by the CFD calculations, although the predicted figure of 42 ppm for UHC is probably too high, for the same reasons outlined for the $N = 92.5$ case. Carbon monoxide emissions for the $N = 75.0$ case appears to be substantially underpredicted, and the fact that the calculated value is lower than the one reported for the $N = 92.5$ case is in contrast with the observed experimental trends. This issue in the prediction of super-equilibrium CO at low power outputs can be related to the inability of the premixed flamelet library to describe the dilution process with cold air that takes place before the combustion outlet [198]. Also, at low loads, the fuel split s is reduced significantly, and the relative importance of the non-premixed pilot stage with respect to the main stage is therefore augmented. The use of a premixed flamelet library to represent the thermo-chemistry of the combustion process under these conditions may be less appropriate with respect to the operation at high power outputs, where most of the combustion takes place in the premixed main stage.

Overall, the CFD model appears to be able to reproduce the main features of the two investigated cases, i.e. flame shape, location of the reaction zone, vortex breakdown, presence and shape of the characteristic RZs. The numerical

predictions for NOx and CO are also in good quantitative agreement with the experimental measurements for the $N = 92.5$ case. The use of premixed flamelets to represent the the combustion process is likely to be less appropriate for the $N = 75.0$ case, and this is due to the increased contribution of the non-premixed pilot flame to the overall combustion process. The non accurate prediction of same features (e.g. the length of the cold core associated with the pilot flame, CO emissions at partial load) can be due to shortcomings in the steady RANS approach and in the use of a premixed flamelet library for the representation of the complex phenomena taking place in the device.

6.3 PACT cases

This section introduces the numerical results obtained for the CFD analysis of the Turbec T-100 combustor under the conditions investigated experimentally at the PACT facility. Overall, six cases have been considered, at two different electrical power output. In the first two cases, the MGT is operated at a power output of 80 kW, under air-fired and CO_2-diluted conditions. In the latter four cases, the electric power output has been reduced to 65 kW, and the cases comprise air-fired, CO_2-diluted, steam-diluted, and combined carbon dioxide- and steam-diluted operation. The boundary conditions for all the cases investigated are reported in Table 3.6.

6.3.1 80 kW power output

Both cases at 80 kW power output have been modelled employing the numerical grid described in Section 6.1, which includes the solid parts of the combustor for CHT calculations. In order to assess the impact of CHT on the results, the baseline case has been simulated on the same numerical grid under adiabatic conditions, i.e. without including CHT. Therefore, the mesh for the adiabatic calculation consists of 11 M fluid elements, and does not include any solid part of the combustor.

Temperature contour plots for both the adiabatic and the CHT calculations of the baseline case are shown in Figure 6.7. It can be noted how, as expected,

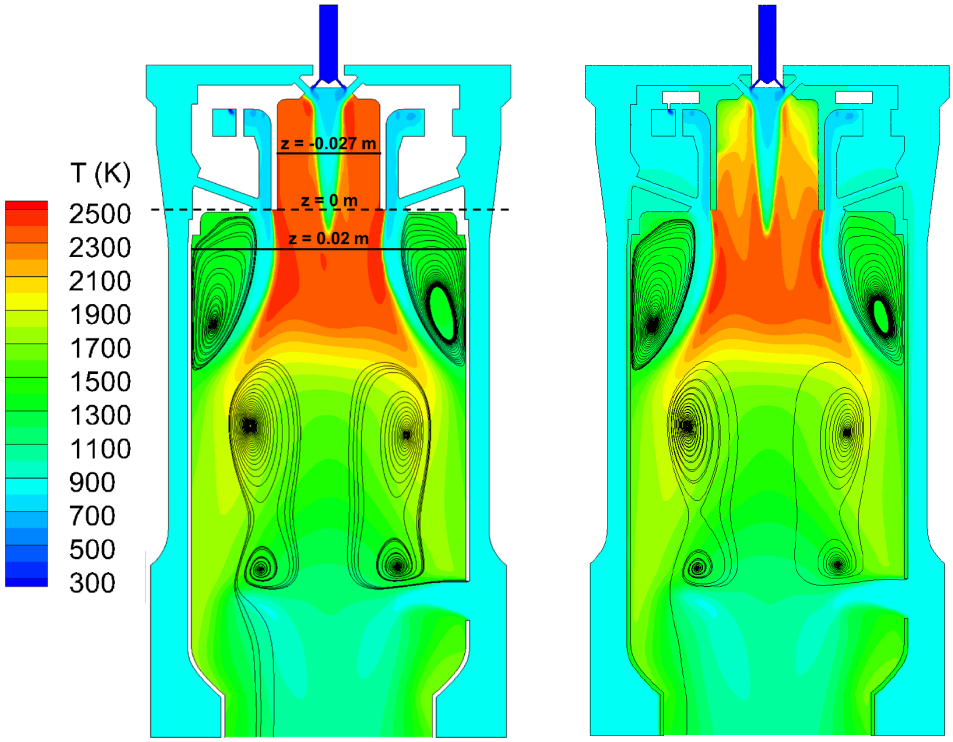

Figure 6.7: Baseline 80 kW case: calculated temperature contours together with 2D streamlines on the combustor mid-plane for the adiabatic (left) and the CHT (right) calculations.

taking into account the CHT has a significant impact on the temperature field. This is due to the very compact geometry of the device, which results in high temperature gradients and therefore in non-negligible conductive heat transfer through the walls. This effect is particularly evident in the pilot region, where thin walls separate the hot pilot flame zone from the relatively cold premixing chamber.

Overall, CHT has the effect of reducing the temperature levels at walls and within the flame. The effects of CHT on the temperature in both the pilot and the main flame regions are illustrated in detail in Figure 6.8, showing the calculated radial temperature profiles at two different axial locations for both adiabatic and CHT calculations. The position of the first axial location, corresponding to z=-0.027 m, is shown on the left hand side of Figure 6.7 and corresponds to the mid point of the pilot dome in the axial direction. The calculated temperature profiles for this location show how CHT has a significant impact on the temperature field

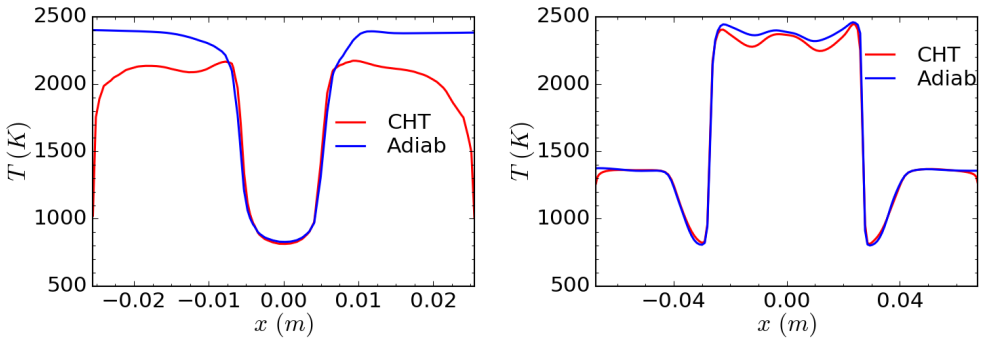

Figure 6.8: Baseline 80 kW case: calculated radial temperature profiles at z=-0.027 m (left) and z=0.2 m (right)for the adiabatic and the CHT calculations.

in the pilot region, especially close to the walls. The calculated wall temperature in the adiabatic case is very high (the wall radial location corresponds to 0.0255 m in the plot, which is equal to the inner radius of the pilot dome), and this is beyond the structural limit for steel. It can be observed that accounting for CHT has the effect of reducing the calculated wall temperature significantly, to a value slightly above 1000 K. The calculated temperature profiles reported on the right hand side of Figure 6.8 show the effects of CHT in the main flame region. The plot is taken at the axial location z=0.02 m, i.e. 2 cm downstream of the burner outlet section, as illustrated in Figure 6.7. CHT has been found to have a non-negligible impact on the main combustion stage as well, with the peak temperature within the flame being reduced by up to 100 K with respect to the adiabatic calculation.

Since CHT has a significant impact on the temperature field within the combustor, it can be expected that it affects other aspects of the combustion process, such as the pollutant formation. In particular, thermal NOx production has been found to be the dominant mechanism for nitrogen oxides formation in the combustor. The production of NOx via the thermal mechanism is extremely sensitive to the in-flame temperature and also to the spatial extension of the hot regions within the flame [243], and therefore accounting for CHT can have a significant impact on the predicted thermal NOx production. The calculated NO source term due to the thermal mechanism for both the adiabatic and the CHT calculation on the combustor mid-plane is shown in Figure 6.9. It can be seen how, due to the reduced temperature levels within the flame, thermal NO production

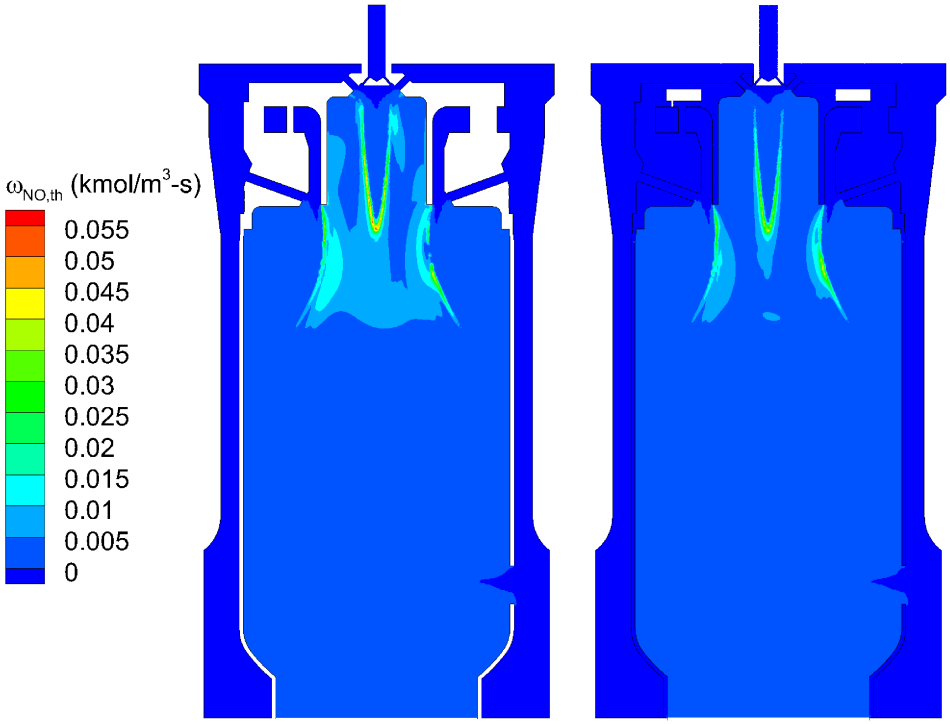

Figure 6.9: Baseline 80 kW case: calculated thermal NO source term contours on the combustor mid-plane for the adiabatic (left) and the CHT (right) calculations.

is reduced significantly when including CHT in the CFD model, with respect to the adiabatic calculation. As a result, the overall NOx emissions at the combustor outlet are reduced from 24 ppmv in adiabatic conditions to 16 ppmv when accounting for CHT effects. Therefore, since CHT has been found to have a noticeable impact on the results for the baseline 80 kW case, it has been included in all the following calculations.

At the power output considered in this section, only the baseline and CO_2-diluted operation have been investigated in the PACT experimental campaign. The boundary conditions for the two 80 kW cases considered in the present work are reported in Table 3.6. The baseline and the diluted cases are characterised by a similar operating pressure, whilst the oxidizer inlet temperature in the combustion chamber is slightly higher in the former case. In the CO_2-diluted case, carbon dioxide is injected at the compressor inlet with a mass flow rate of 0.03472 kg/s. This results in an increase in the CO_2 concentration in the oxidizer stream from 0.0003 (which is the carbon dioxide concentration in the air composition reported in Table 3.5) to 0.0285. As reported in Section 4.4, even this relatively low carbon

dioxide dilution has a non-negligible impact on the combustion process. In fact, the adiabatic flame temperature of the mixture is reduced from 2503 K in the baseline case to 2451 K in the diluted operation, whilst the maximum laminar flame speed is lowered from 1.48 to 1.24 m/s.

The impact of the dilution on the operation of the combustor is shown in Figure 6.10, in terms of the calculated temperature contours on the combustor mid-plane, together with 2D streamlines, for the baseline and the CO_2-diluted cases. The shape of the flame appears to be similar for the two cases, and is the same open cone shape as observed in the $N = 92.5$ case for the DLR experiments. The similarity in the shape of the flame is expected, since both the air-fired and the diluted cases have been calculated with the same fuel split ratio, as reported in Section 3.2. Also, both cases are characterised by the presence of a toroidal ORZ and of a large IRZ which acts as an aerodynamic flameholder. The length of the cold core associated with the pilot flame appears to be longer in the diluted case, and this is probably due to the higher fuel and oxidizer mass flow rates associated with this case, which results in a higher axial velocity. In this respect, it is worth observing that the modifications in the flow field are due to both the direct impact of the diluting species on the operation of the combustor and to the fact that, as reported in Table 3.6, diluted operation leads to different oxidizer and fuel volumetric flow rates with respect to air-fired operation at the same power output.

The temperature levels within the flame in the diluted case are lower with respect to the baseline case, due to the thermal and chemical effects of CO_2 dilution on the combustion process. As a result, the maximum temperature value in the computational domain is lowered from 2471 to 2406 K.

A quantitative analysis of the effect of carbon dioxide dilution on the temperature field is reported in Figure 6.11, showing the radial temperature profiles for both cases at z=0.02 m. It can be noted how the enhanced carbon dioxide presence in the combustion environment has the effect of reducing the temperature levels within the flame and in the ORZ. Also, the extended axial length of the cold pilot jet core in the CO_2-diluted case is evident in the plot, with the temperature dip due to this feature evident in the former case and not present in

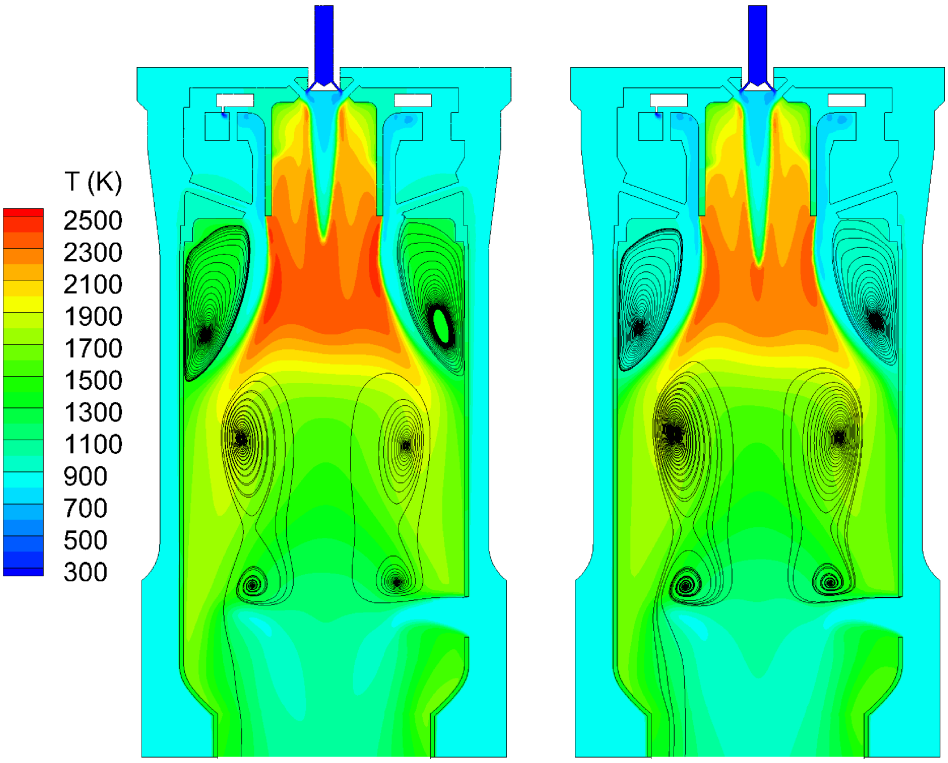

Figure 6.10: 80 kW power output: calculated temperature contours together with 2D streamlines on the combustor mid-plane for the baseline (left) and the CO_2-diluted (right) cases.

the air-fired case. Within the flame, a temperature reduction up to about 100 K is observed.

Even if carbon dioxide dilution has a relatively small impact on the flame shape in the considered case, it has been found to modify the location of the flame stabilisation point, as well as to affect the characteristics of the IRZ. The modifications in the velocity field are due to the different mass flow rates and physical properties of the mixture [184]. In particular, the changes in the density are related to both the changes directly due to CO_2 dilution (and therefore to the different mixture composition) and to the impact of dilution on the temperature field. The flame stabilisation point is identified as the axial location where the turbulent flame speed s_T is equal to the axial velocity component U. The turbulent flame speed is calculated employing the model from Zimont [143]. In this model, s_T is evaluated as a function of the local laminar flame speed and of the turbulent variables. Therefore, CO_2 dilution has an impact on s_T due to both

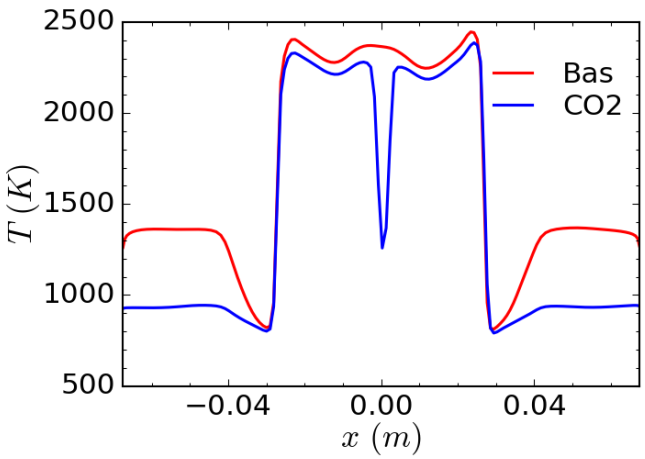

Figure 6.11: 80 kW power output: calculated radial temperature profile at z=0.02 m for the baseline and the CO_2-diluted cases.

	$P_{IRZ,1}$	$P_{IRZ,2}$	P_{stab}
Baseline	0.073	0.181	0.066
CO_2	0.074	0.178	0.061

Table 6.2: 80 kW power output: axial location (m) of the IRZ stagnation points and of the flame stabilisation point for the baseline and the CO_2-diluted cases.

the changes in the laminar flame speed (see Section 4.4) and to the modifications induced in the velocity and turbulent fields.

The axial locations of the stagnation points associated with the IRZ and of the flame stabilisation point for the two considered cases are reported in Table 6.2. The CO_2-diluted case is characterised by a slightly shorter IRZ. In fact the axial length of the IRZ is reduced from 10.8 cm in the air-fired operation to 10.4 cm in the diluted case. Also, in the latter case, the location of the flame stabilisation point is moved upstream, closer to the burner outlet, by 0.5 cm.

The calculated exhaust gas temperature and composition, in terms of main species and pollutant emissions, for the two cases are reported in Table 6.3. The carbon dioxide content in the exhaust gas is increased from 1.69% in air-fired operation to 4.40% in the CO_2-diluted case. The enhanced carbon dioxide content in the latter case would benefit significantly the post-combustion carbon capture process [15, 260]. The higher efficiency of the carbon capture process in

	Baseline	CO_2
CO_2	1.69	4.40
O_2	17.18	16.75
H_2O	4.13	3.97
NOx (ppmv)	16	4
CO (ppmv)	2	2
UHC (ppmv)	8	9
T_{out} (K)	1184	1151

Table 6.3: 80 kW power output: calculated exhaust gas composition (% vol) and combustor outlet temperature for the baseline and the CO_2-diluted cases.

the diluted case is counterbalanced by the lower combustor outlet temperature, which results in a lower electric efficiency in the MGT operation, as highlighted by the higher fuel consumption in the CO_2-diluted with respect to the baseline case reported in Table 3.6. Also, due to the lower in-flame temperature observed in the former case, NOx emissions are reduced significantly with respect to air-fired operation. The considered dilution level does not have a significant impact on the CO emissions and also UHC emissions do not show any significant increase, in line with the experimental findings for the considered power output and dilution levels [238].

LES simulation of the baseline 80 kW case

In addition to the RANS calculations described above, the baseline case at 80 kW power output has been investigated employing the LES approach for turbulence modelling. As stressed in Section 6.1, due to the very high computational burden associated with the LES simulation of industrial combustors, the maximum number of cells employable is dictated by the available computational resources, and is often not enough for a proper LES calculation. The suitability of the numerical grid for the LES simulation of the considered case has been evaluated by means of the criterion reported in Equation (2.79), where the integral turbulent length scale $\mathcal{L}$ has been calculated from the RANS results for the same case. The

resulting distribution of the ratio $\Delta/\frac{\mathcal{L}}{12}$ on the combustor mid-plane is reported in Figure 6.12, in which the regions satisfying the criterion have been clipped out. It is worth pointing out that, since a near-wall treatment is employed in the present LES calculation, the mesh criterion does not apply to the near-wall regions.

The upper limit of 15 M elements due to computational constraints, combined with the complexity of the geometry and of the physical processes taking place within the device, results in the necessity to compromise between the cell size necessary to satisfy the criterion and the overall cell count. The main concept followed in the generation of the numerical grid is to maximise the number of elements available for the discretisation of the most critical regions and phenomena within the combustor (i.e. the mixing between the fuel and oxidizer in the pilot region, the shear layers at the burner outlet, the high gradients associated with the presence of the dilution holes) and employ a coarser discretisation for the regions in the domain that are not characterised by the presence of chemical reactions, mixing and elevated gradients.

Following this approach, a relatively coarse mesh was employed in the annular section between the outer cases and the flame tube, which is used to convey the oxidizer coming from the recuperator to the dilution holes and to the burner region. The numerical grid results to be too coarse with respect to the mesh criterion represented in Figure 6.12 also within the main swirler. Further, although the mesh has been refined locally to improve the resolution of relevant physical phenomena, the criterion expressed by Equation (2.79) is not satisfied in some areas of the critical regions mentioned above. In particular, the highly turbulent regions resulting from the mixing of the oxidizer and the fuel streams in the pilot stage appears to be under-resolved in proximity of the injecting nozzles. Also, in the critical regions of the shear layers found at the burner outlet and between the ORZ and the IRZ, which correspond to the location of the main reaction zone, the mesh does not satisfy the criterion. The under-resolution of the grid in this region is particularly evident in the structured part of the mesh. In fact, due to the low flexibility of structured meshes, it is not possible to refine the grid locally without incurring a dramatic increase in the overall cell count. The same

applies to the dilution holes region, where high gradients are present due to the fact that the dilution air is injected at an almost orthogonal angle with respect to the main flow direction within the combustion chamber. Although the mesh has been refined locally in this region, in order to better resolve the expected elevated gradients, the cell size is not small enough to satisfy the criterion in the regions where the dilution air mixes with the hot combustion products. Also, a relatively coarse grid has been employed within the low-turbulence hot region located at the centre of the combustion chamber. Although this is not evident from mesh criterion plots, a more refined mesh in this part of the domain could improve the accuracy of the results significantly, accordingly to the results of the study presented in Chapter 5.

Despite the shortcomings related to the numerical grid, a LES simulation for the baseline 80 kW case has been performed in order to verify the suitability of the present mesh for LES and develop guidelines for a further refinement in the future, to assess the differences between RANS and a coarse LES results, and also to obtain some insights on the unsteady behaviour of the flow field within the combustor. Following the findings of the study reported in Chapter 5, the Sigma model has been employed as a SGS stress model in order to reduce the sensitivity of the results to mesh resolution.

The residence time within the domain for this case has been evaluated from the precursor RANS calculation as

$$t_r = \frac{\int_V \rho dV}{\dot{m}_{tot}} \tag{6.1}$$

where $\dot{m}_{tot}$ is the total mass flow rate entering the system, equal to the summation of the oxidizer and fuel mass flow rates. According to Equation (6.1), the residence time within the domain is 0.015 s. The LES calculation has been run for a physical time of 0.02 s in order to reach a statistically steady solution, plus an additional physical time of 0.04 s in order to collect statistics for the evaluation of time-averaged quantities. A time step size of 2.0×10^{-6} s was employed. The total computational time for a physical solution of 0.06 s on a 48 cores cluster was equal to about 1200 hours, compared to the 72 hours necessary to reach a converged steady-state RANS solution with the realizable $k - \epsilon$ model.

The calculated instantaneous and time-averaged temperature contours on the

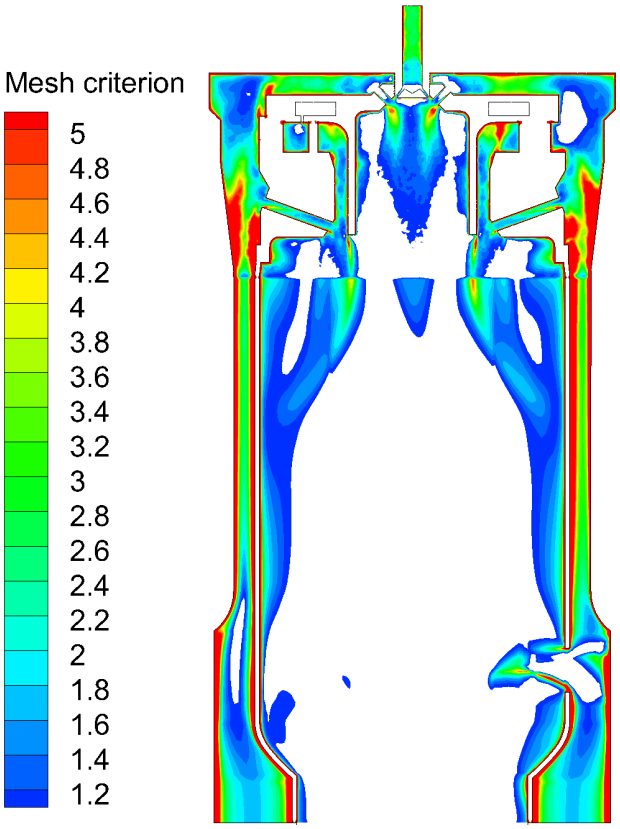

Figure 6.12: Baseline 80 kW case: mesh quality criterion, Equation (2.79), contours on the combustor mid-plane.

combustor mid-plane are reported in Figure 6.13, together with the contours obtained from the steady-state RANS calculation. From a comparison between the time-averaged LES and the steady-state RANS temperature fields, it can be noted how the former is characterised by a more spread high temperature region in the main flame region with respect to the latter. Also, the calculated time-averaged LES peak temperature values appear to be lower with respect to RANS. On the other hand, as expected, the instantaneous temperature field is characterised by higher peak values with respect to the time-averaged one. Further, it can also be noted how the cold jet core associated with the pilot flame is shorten with respect to the RANS calculations.

As shown by the 2D streamlines reported in Figure 6.13, the time-averaged flow-field within the chamber is still dominated by the presence of a toroidal ORZ and a central IRZ due to vortex breakdown. With respect to the RANS calculations, the axial length of the IRZ is shorter and therefore it does not

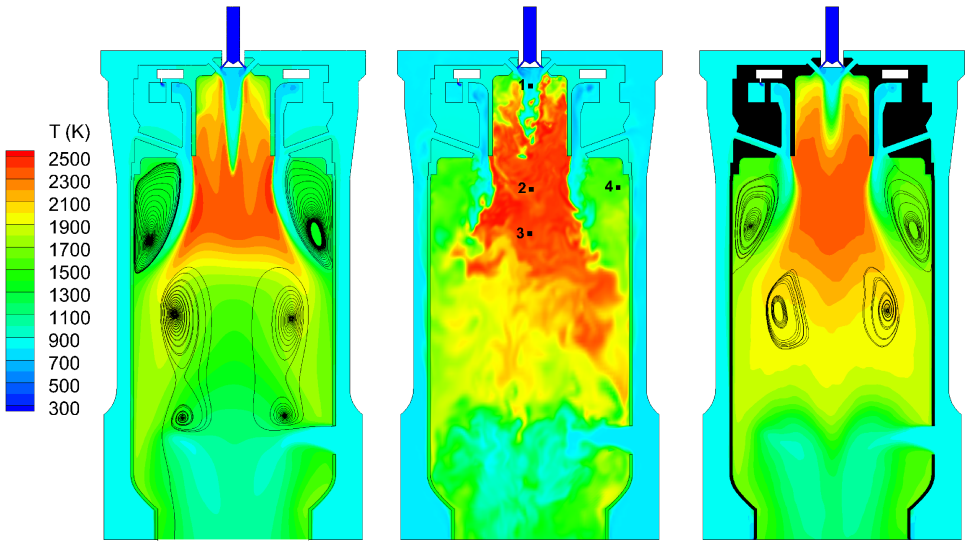

Figure 6.13: Baseline 80 kW case temperature contours on the combustor mid-plane: steady-state RANS with 2D streamlines (left), instantaneous LES with monitoring points location (centre), time-averaged LES with 2D streamlines (right).

interact with the dilution air jets. Also, the different size and shape of the IRZ with respect to the steady-state RANS results has an impact of the flame shape.

The locations of four monitoring points are highlighted on the instantaneous temperature contours in Figure 6.13 and reported in Table 6.4, together with the monitored variables. The monitoring points have been employed in order to evaluate the statistically steady behaviour of the solution within the sampling interval used to collect the statistics to calculate time-averaged quantities. The time-series obtained for the instantaneous axial velocity at Point 1 (located in the mixing region within the pilot stage) and the instantaneous temperature at Point 2 (corresponding to the hot region within the main flame) within the sampling interval are reported in Figure 6.14. It can be seen how the solution appears to have a statistically-steady behaviour within the considered sampling interval.

The times-series obtained for the monitored quantities in Table 6.4 have also been employed to assess the presence of flow instabilities within the combustor, following the same methodology as the one employed in Chapter 5. The FFTs of the time-series showed that no dominant frequencies are present in any of the monitored locations, suggesting that no periodic flow instabilities are present.

	x (m)	y (m)	z (m)	Variables
Point 1	0	0	-0.047	u
Point 2	0	0	0.024	u, T
Point 3	0	0	0.053	u
Point 4	0.06	0	0.023	u, T

Table 6.4: Baseline 80 kW LES: monitoring points location and monitored variables.

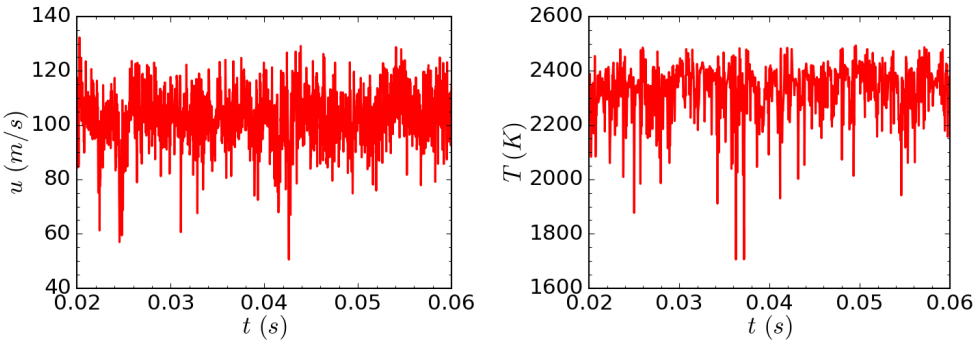

Figure 6.14: Baseline 80 kW case: time-series for the instantaneous axial velocity u at Point 1 (left) and the instantaneous temperature T at Point 2 (right).

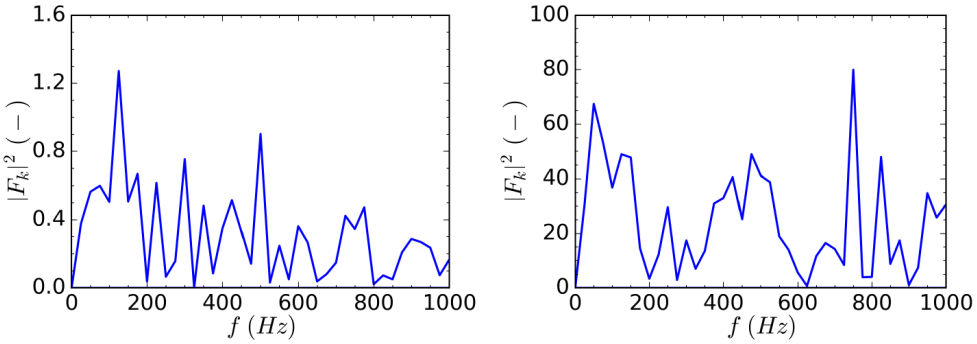

Figure 6.15: Baseline 80 kW case: calculated power spectra for the time-series of the instantaneous axial velocity u at Point 1 (left) and of the instantaneous temperature T at Point 2 (right).

As an example, the power spectra obtained from the two time-series reported in Figure 6.14 are shown in Figure 6.15. The absence of flow instabilities in the LES solution has been confirmed by visual inspection of the instantaneous temperature and velocity field as well as by the stable behaviour of the device observed experimentally.

Overall, the LES calculation of the baseline 80 kW case confirmed the observations made in Chapters 2 and 5 on the potential and drawbacks of the LES approach. In particular, the main flow-field features predicted by LES are in agreement with the steady-state RANS calculation of the same case. Nevertheless, significant quantitative differences are observed (e.g. flame shape, temperature distribution within the flame, shape and size of the RZs, length of the pilot jet structure). Given the limitations of the numerical grid employed for the LES calculation, it would be advisable to employ a more refined mesh in order to assess the reliability of the LES results more in detail, possibly in combination with in-flame experimental measurements.

6.3.2 65 kW power output

The boundary conditions for the four cases considered for CFD modelling at 65 kW power output are reported in Table 3.6. These cases comprise conventional air-firing as well as carbon dioxide, steam and combined CO_2 and H_2O dilution. The operating pressure at this power output is lower with respect to 80 kW, and

ranges from 3.645 bar in the air-fired case to 3.445 bar when steam injection is considered. The oxidizer temperature at the combustor inlet is comprised between 828.1 K in the baseline case and 813.6 K in the CO_2-diluted case.

In the CO_2-diluted case, the diluting species is injected at the compressor inlet with a mass flow rate equal to 0.03472 kg/s, resulting in an increase in the carbon dioxide mole fraction in the oxidizer from 0.0003 in the air-fired case to 0.0310 in the CO_2-diluted case. In the steam-diluted case, the diluting species is introduced at the compressor outlet with a mass flow rate of 0.01111 kg/s, which increases the H_2O mole fraction in the oxidizer stream from 0.0099 (which is the value considered for pure air, as reported in Table 3.5) to 0.0354. Finally, in the combined injection case, carbon dioxide and steam are injected with mass flow rates of 0.03472 and 0.01111 kg/s, respectively. This results in an increased mole fraction of both diluting species in the oxidizer stream. In particular, the CO_2 and H_2O mole fractions in the oxidizer are equal to 0.0328 and 0.0348, respectively.

As reported in Section 4.4, the considered dilution levels have been found to have a significant impact on the combustion process in 1D premixed flamelets calculated under the same conditions considered in the experiments and in the CFD calculations. The resulting adiabatic flame temperature and maximum laminar flame speed values for the four considered cases are reported in Table 6.5. It can be noted that, as observed in Chapter 4, steam dilution has a smaller impact on the combustion process with respect to carbon dioxide. The most significant differences with respect to conventional air-firing is observed in the combined injection case, with the calculated reduction in the adiabatic flame temperature exceeding 100 K, and the related laminar flame speed value reducing from a maximum value of 1.62 m/s in the baseline case to 1.24 m/s.

The impact of dilution on the operation of the Turbec T-100 combustor is depicted in Figure 6.16, showing the calculated temperature contours on the combustor mid-plane, together with 2D streamlines, for the four cases considered at 65 kW power output. It can be noted how the shape of the flame is not affected significantly by dilution under the present modelling assumptions. As in the 80 kW cases, the velocity field within the combustor is dominated by the presence of a large IRZ, which is employed to stabilise the flame, in both the

	T (K)	s_L (m/s)
Baseline	2508	1.62
CO_2	2447	1.31
H_2O	2471	1.50
Combined	2405	1.24

Table 6.5: 65 kW power output: calculated adiabatic flame temperature and maximum laminar flame speed for the four considered cases.

air-fired and diluted operations. The most evident effect of dilution is a general reduction in the in-flame temperature. In agreement with the 1D calculations reported in Table 6.5, the most marked temperature reduction is observed in the combined dilution case, followed by the carbon dioxide- and steam-diluted operation. Also, dilution appears to extend the length of cold pilot jet core with respect to the air-fired case, this effect being more evident in the combined dilution case. The possible reasons behind this phenomenon have been outlined when discussing the 80 kW cases.

A quantitative comparison of the temperature levels reached within the flame is reported in Figure 6.17, showing the calculated temperature profiles at z=0.02 m for the four cases at the considered electrical power output. The temperature plots at this axial location confirm the general remarks made above. In particular, from temperature values at the combustor axis it can be noted how the cold core of the pilot flame does not reach this axial location in the baseline case, whilst all the diluted cases are characterised by a temperature dip that corresponds to the cold pilot flame region. Within the main stage flame, the air-fired case is characterised by a significantly higher temperature with respect to the diluted cases. Also, the CO_2 and the combined cases are characterised by a lower temperature in the ORZ region with respect to the baseline and steam-diluted operation.

The calculated axial locations for the stagnation points associated with the IRZ and for the flame stabilisation point in the four cases are summarised in Table 6.6. The reasons behind the modifications in the flow-field and in the flame stabilisation point induced by the diluted operation have been illustrated when discussing the 80 kW cases. From the data reported in Table 6.6, it can be

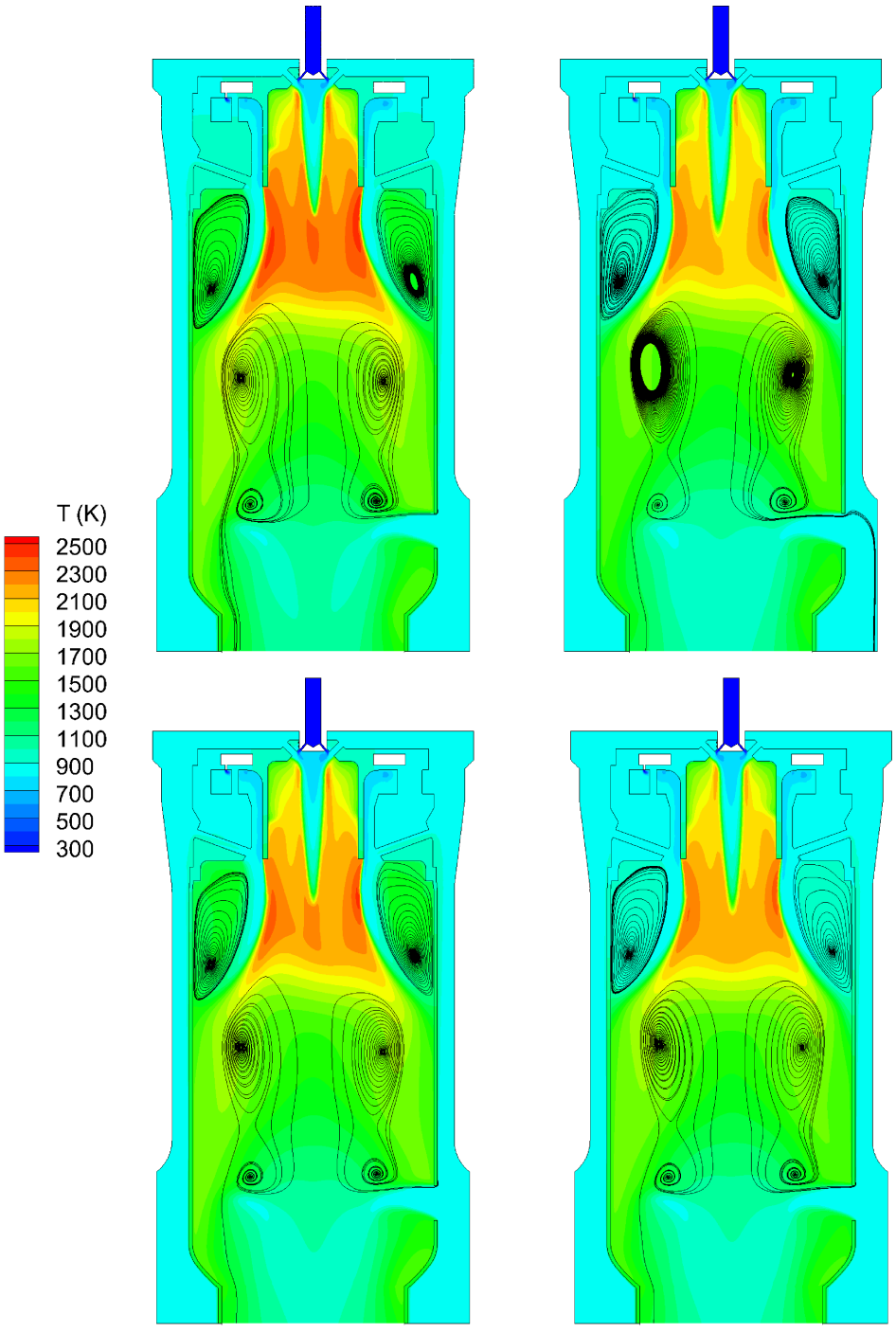

Figure 6.16: 65 kW power output: calculated temperature contours together with 2D streamlines on the combustor mid-plane for the baseline (top-left), the CO_2-diluted (top-right), the H_2O-diluted (bottom-left) and the combined dilution (bottom-right) cases.

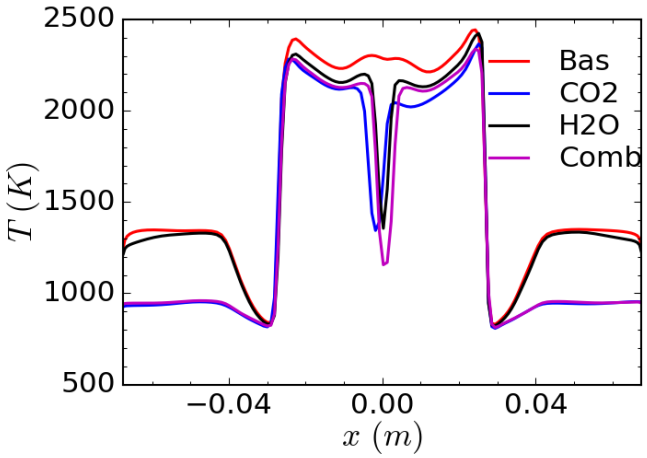

Figure 6.17: 65 kW power output: calculated radial temperature profile at z=0.02 m for the four cases investigated.

	$P_{IRZ,1}$	$P_{IRZ,2}$	P_{stab}
Baseline	0.073	0.180	0.061
CO_2	0.071	0.177	0.059
H_2O	0.072	0.175	0.060
Combined	0.076	0.172	0.064

Table 6.6: 65 kW power output: axial location (m) of the IRZ stagnation points and of the flame stabilisation point for the four cases.

seen as the most marked differences can be observed between the baseline and the combined dilution cases. In particular, the first stagnation point associated with the IRZ in the latter case is located 0.3 cm downstream with respect to the former, and the axial length of the IRZ is reduced from 10.6 to 9.6 cm. Also, the axial location of the flame stabilisation point is moved 0.3 cm downstream in the combined dilution case with respect to the air-fired operation.

The volumetric exhaust gas composition and the calculated combustor outlet temperature are reported in Table 6.7. Also in this case, the CO_2-diluted operation is characterised by a lower combustor outlet temperature and a lower overall electrical efficiency with respect to the baseline case. The carbon dioxide concentration in the exhausts is increased from 1.59 to 4.45, with all the related beneficial effects on the efficiency of the carbon capture process. In the case of the

	Baseline	CO_2	H_2O	Combined
CO_2	1.59	4.45	1.49	4.69
O_2	17.40	17.12	17.08	16.43
H_2O	3.93	3.60	6.27	6.20
NOx (ppmv)	10	1	3	1
CO (ppmv)	1	< 1	< 1	< 1
UHC (ppmv)	14	29	19	19
T_{out} (K)	1174	1120	1145	1137

Table 6.7: 65 kW power output: calculated exhaust gas composition (% vol) and combustor outlet temperature for the baseline and the CO_2-diluted cases.

STIG cycle, i.e. when steam dilution is considered, the main advantage is related to the higher electrical efficiency that can be obtained with respect to air-fired operation, resulting in a lower fuel consumption for the same electrical power output in the former case, as reported in Table 3.6. Steam dilution also results in lower nitrogen oxides emissions with respect to air-firing, although the reduction in NOx is slightly smaller with respect to CO_2 and combined dilution, due to the relatively higher temperature values typical of steam dilution with respect to the former cases. The combined dilution case results in both a higher concentration of CO_2 in the exhaust gas and in a slightly smaller fuel consumption with respect to the baseline case. Also, NOx are reduced significantly due to the noticeable in-flame temperature reduction obtained with combined CO_2 and steam dilution. The prediction of carbon monoxide emissions seems to be affected by the same issues reported in Section 6.2, i.e. the inability of the premixed flamelet ability to predict super-equilibrium CO concentrations at partial load. The trend predicted for UHC emissions appears more sensible, with an increase in UHC levels for the air-fired case at 65 kW compared with the same case at 80 kW. Also, carbon dioxide dilution appears to increase the UHC levels.

One of the main advantages of diluted operation is the reduction in thermal NOx production with respect to conventional air-firing. The impact of dilution on nitrogen oxides production is illustrated in Figure 6.18, showing the calculated

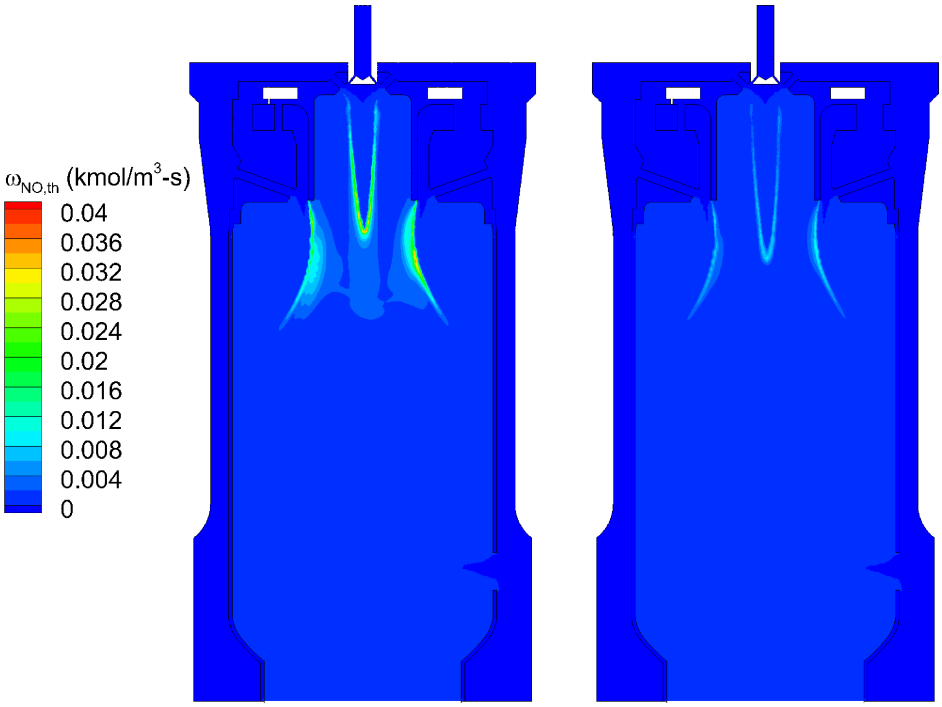

Figure 6.18: Baseline 65 kW case: calculated thermal NO source term contours on the combustor mid-plane for the air-fired (left) and the combined CO_2 and steam injection (right) cases.

NO source term due to the thermal mechanism for the baseline and the combined injection cases. It can be seen how the noticeable decrease in in-flame temperature obtained in the diluted case, which is of the order of 100 K as estimated in the 1D calculations and confirmed in the CFD analysis, results in a dramatic reduction in the thermal NO source term. This, in turn, results in noticeably lower NOx emissions in the diluted operation, as reported in Table 6.7.

Overall, the diluted operation of the MGT results in significant modifications with respect to conventional air-firing. In particular, carbon dioxide dilution results a in a reduced efficiency with respect to conventional air-combustion. This energy penalty can be compensated when considering post-combustion carbon capture in the economy of the system. In fact, the diluted operation is characterised by a higher CO_2 concentration in the exhaust gas, which would benefit greatly the chemical CO_2 capture process. Steam injection, on the other hand, increases the overall mass flow rate through the turbine and results in an improved electrical efficiency. By injecting both diluting species at the same time, it is pos-

sible to combine the benefits of both solutions, i.e. an increase in carbon dioxide concentration in the exhausts for a more efficient carbon capture process, and an improvement in the MGT efficiency with respect to CO_2-diluted operation.

With a focus on the combustion process, a diluted operation is characterised by lower temperature levels within the flame and by a reduced flame speed with respect to the baseline case. The reduction in the in-flame temperature has the beneficial effect of lowering nitrogen oxides emissions significantly, and this is due to the reduced production of thermal NOx. Further, the increased carbon dioxide and/or steam content in the oxidizer stream modifies the characteristcs of the IRZ, and results in modifications in the location of the flame stabilisation point with respect to conventional air-combustion. Also, it should be noted that the lowering in the flame speed results in a reduced flammability range for the diluted mixture, as shown in the 1D calculations reported in Section 4.4. This effect is more evident when combined CO_2 and steam injection is considered. Although the combustion process under diluted conditions has been observed to be stable in both the experiments and the CFD calculation in all the considered cases, the shrinking of the flammability range due to the enhanced CO_2 and H_2O presence can be problematic when considering higher dilution levels. This is due to the fact that the device is already operated close to the lean flammability limit under air-fired conditions in order to control NOx emissions.

The numerical prediction of emissions in gas turbines is an extremely challenging task. The CFD model appears to be able to provide a satisfactory prediction of the effects of dilution on NOx and UHC emissions, at least in terms of expected trends. On the other hand, the model is not able to correctly predict super-equilibrium CO at partial load, due to limitations related to the premixed flamelet library employed to parametrise the combustion thermo-chemistry in this study. Since no direct species measurements at the combustor outlet are available for the PACT cases, NO emissions measured at the outlet section of the exhaust gas exchanger (details on the measurements are reported in Section 3.2) are compared with the calculated NO emissions at the combustor outlet in Figure 6.19, for both the 80 kW and 65 kW power outputs. It can be seen how the CFD model is able to predict the overall NO emissions trend at both the power

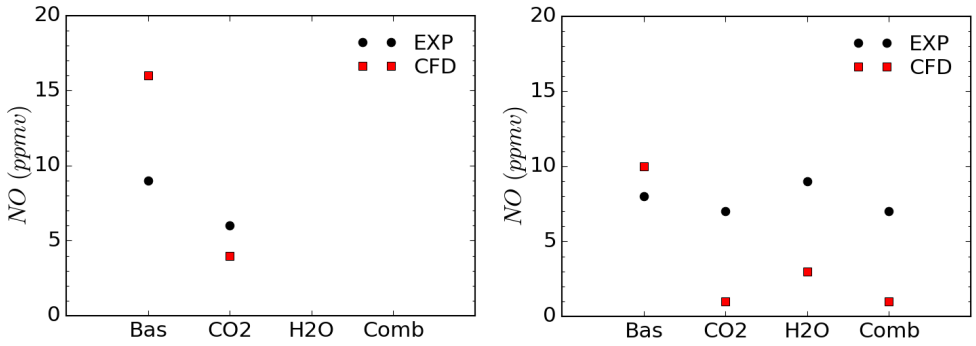

Figure 6.19: Calculated and measured NO emissions for the 80 kW (left) and the 65 kW (right) cases.

output levels considered, although the accuracy of the calculated figures changes from case to case. Again, it is worth pointing out again that the post-processing methodology adopted in the present study is mainly aimed at predicting trends, rather than the exact value of the NOx emissions in each case.

6.4 Summary

A complete CFD model for the combustion chamber of the Turbec T-100 MGT has been developed in order to simulate its air-fired and diluted operation. The computational domain employed for the calculations consists of both fluid and solid cells, to account for CHT effects. A numerical grid consisting of 15 M elements has been generated to discretise the domain. Unstructured tetra elements with prism layers on the walls have been employed in the complex burner region, whilst a structured hexa grid has been used in the rest of the domain. The advanced meshing capabilities of ANSYS ICEM 15.0 have been employed in order to develop a novel method to generate a conformal interface between the structured and the unstructured regions.

The datasets coming from two different experimental campaigns have been used in order to set-up and validate the numerical calculations. The experimental data from DLR have been used to set-up and validate the steady-state RANS calculations for two different air-fired cases. The numerical results are in good agreement with the experimental observations in terms of flame shape, observed

flow field and location and shape of the reaction zones. Reasonable quantitative predictions for NOx, UHC and CO emissions have been obtained for the high power output case. At partial load, the model has been able to predict the correct trend for both NOx and UHC emissions, whilst it failed to predict super-equilibrium CO, and this is probably due to limitations in the premixed flamelet database used to represent the combustion thermo-chemistry.

A total of six air-fired and diluted cases from the PACT experimental dataset have been simulated employing RANS steady-state calculations. The CFD model is able to predict the effects of carbon dioxide and steam dilution on the operation of the device. In particular, the impact of dilution on temperature levels, velocity flow-field and pollutant emissions has been assessed, and the results are in good agreement with the theoretically expected behaviour and the experimental observations. Again, the model has been able to predict the expected trends for UHC and NOx emissions.

The baseline 80 kW case from the PACT experimental campaign has been modelled using a LES approach with the Sigma SGS model. Due to the available computational resources, the employed numerical grid is undersized with respect to the grid solution required for a proper LES calculation. The LES results are characterised by the same main features highlighted by steady-state RANS calculations. Nevertheless, significant quantitative differences with respect to the RANS calculation have been found, e.g. in the temperature levels within the flame and in the size and shape of the RZs. Also, an assessment of the unsteady behaviour of the flow-field as been carried out, and no evidence in the presence of flow instabilities has been observed.

Chapter 7

Conclusions and future work

CCS represents an attractive option to reduce greenhouse gas emissions due to the combustion of fossil fuels. With respect to gas-fired power generation, post-combustion carbon capture is regarded as the most feasible solution in the short term. The energy penalty associated with the CO_2 capture process can be reduced by resorting to modified cycles, such as EGR and STIG. These cycles are characterised by an enhanced presence of CO_2 and/or H_2O in the combustion environment. CFD can be a useful tool to assess the effects of dilution on the combustion process and to develop novel combustor designs. In this context, the main aims of this thesis are the assessment of the effects of carbon dioxide and steam dilution on natural gas combustion and the development of an accurate CFD model for the diluted operation of industrial gas turbine combustors. The main conclusions drawn from the work carried out in the thesis are reported in Section 7.1 and suggestions for further work on the topic are made in Section 7.2.

7.1 Conclusions

The aims and objectives of the present thesis have been outlined in Section 1.5 and include the assessment of the impact of CO_2 and H_2O dilution on gas combustion and the development of a CFD model for the investigation of diluted combustion in realistic industrial configurations.

Preliminarily, a critical review of the methodologies available for turbulent combustion modelling and of the studies regarding diluted combustion in the

literature has been carried out in Chapter 2.

In order to assess the impact of the enhanced presence of carbon dioxide and steam in the combustion environment, a fundamental numerical study has been carried out in Chapter 4. A simple flame configuration, i.e. a 1D laminar steady premixed flame, has been chosen to represent the combustion process. This configuration has been modelled, by employing a detailed chemical mechanism on a computational grid sufficiently refined to resolve the flame structure, under air-fired and diluted conditions at ambient and MGT-like temperature and pressure conditions. The dilution levels considered in the study are similar to those observed in the EGR and STIG operation of the Turbec T-100 MGT in the experimental campaign carried out at the PACT facility, as reported in Chapter 3.

The detailed calculations showed that the considered dilution levels have a non-negligible impact on the combustion process, at both ambient and MGT-like conditions. The modifications in the combustion process with respect to conventional air-firing are due to both thermal and chemical effects, the former being related to the different physical properties of the mixture under diluted conditions and the latter due to the direct participation of the diluting species in the combustion chemistry. According to the results obtained in the considered simplified configuration, thermal effects have a more marked impact with respect to the chemical ones. Nevertheless, the latter cannot be neglected, and have a more pronounced impact at MGT-like pressure and temperature conditions.

The latter observation has important implications when considering the CFD modelling of diluted operation of realistic devices. In fact, the CFD model needs to be able to account for detailed chemistry and finite-rate effects in order to predict the impact of the diluting species on the combustion chemistry.

Further, an assessment of the impact of dilution on the radiative heat transfer in 1D laminar premixed flames has been performed by employing an optically thin model together with the SNB-CK model to evaluate the optical properties of the mixture. It has been observed that radiation has a more marked impact on the temperature field in the diluted cases with respect to air-fired flames, although the latter are characterised by a higher flame temperature with respect to the

former. Nevertheless, under the considered dilution levels, the chemical source term has been found to be greater than the radiative source term by about three orders of magnitude within the reaction zone. For this reason, together with the elevated computational costs associated with the accurate evaluation of the optical properties of the mixture in a 3D CFD simulation, radiative heat transfer has not been included in the CFD calculations performed in the present work.

The findings of the fundamental study carried out in Chapter 4 have been employed to formulate guidelines for the CFD modelling of diluted combustion. In particular, the critical review of the turbulent combustion modelling techniques presented in Chapter 2 allowed us to pinpoint the tabulated chemistry combined with a presumed-PDF approach as the best compromise between the need to incorporate detailed chemistry and finite rate effects in the CFD model and the necessity to control the computational cost associated with the numerical calculations. In order to assess the suitability of the FGM/presumed-PDF approach to model swirling partially-premixed flames, a numerical investigation of a non-reactive and of a partially-premixed case of the Sydney burner swirling flames series has been performed and the results obtained are outlined in Chapter 5. Both steady-state RANS and LES turbulence modelling techniques have been employed in the study, with the aim of highlighting their main advantages and drawbacks. Also, the sensitivity of the different SGS stress models to mesh refinement has been assessed by employing three different numerical grids.

The FGM/presumed-PDF approach has been found to be able to provide encouraging results for the considered partially-premixed case. In the steady-state RANS calculations, the most significant features of both the non-reactive and reactive cases have been predicted successfully, at least from a qualitative point of view. The accuracy on these predictions can be improved significantly with LES, especially when employing more refined numerical grids and advanced SGS stress closures. Also, the LES calculations correctly predicted the presence of flow instabilities which has been observed experimentally. The improvement in the results accuracy obtained with LES comes at the price of the significantly higher computational cost associated with this approach, especially when considering the sensitivity of the LES results to the mesh size. In fact, it has been observed that

mesh refinement is key in order to obtain accurate results with LES, especially for the reactive case. The sensitivity of the LES results to grid refinement can be reduced by employing a sound numerical formulation for the SGS stress closure, such as the one provided by the Sigma model. Further, the Sigma model provided the most accurate results among the considered SGS stress models on all the numerical grids.

The findings from the fundamental study on diluted natural gas combustion carried out in Chapter 4 and the CFD analysis of the lab-scale burner presented in Chapter 5 have been used to develop a CFD model for the Turbec T-100 MGT combustor. The numerical results have been validated against two air-fired cases which have been investigated experimentally at DLR. The CFD results are in good agreement with the experimental observations, in terms of flame shape, presence of IRZ and ORZ and location and shape of the reaction zone. With respect to pollutant formation, the model provided good quantitative predictions for CO and NOx at the nominal power output, whilst the calculated figure for UHC is slightly overpredicted. At partial load, the CFD model is able to reproduce the expected trends for NOx and UHC emissions, whilst it struggles to predict the super-equilibrium carbon monoxide emissions. Overall the model appears to be in good agreement with the experimental data, with the main sources of uncertainty being identified in the turbulence model and in the use of a premixed flamelet library to parametrise the complex phenomena taking place in the device.

Successively, the CFD model has been employed to simulate the air-fired and diluted operation of the device, by considering six cases from the experimental campaign carried out at the PACT facility. The steady-state RANS calculations of the PACT cases have been employed to assess the impact of CO_2 and H_2O dilution on the operation of the device at two different power outputs, i.e. 80 and 65 kW. The baseline 80 kW case has been investigated with and without accounting for CHT, in order to assess the impact of this heat transfer mechanism on the operation of the device, which has been found to be significant. Therefore, the CHT effects have been included in all the other modelled cases.

For all the considered cases, the CFD model successfully predicted the impact

of dilution on the in-flame temperature, the flow-field within the combustor, the flame stabilisation and pollutant emissions. The numerical results are in good agreement with the detailed 1D calculations in terms of the observed reduction in the in-flame temperature due to the diluted operation.

In terms of pollutant emissions, the considered levels of CO_2 dilution do not appear to have a significant impact on the calculated CO emissions at 80 kW. On the other hand, an increase in UHC emissions has been observed with diluted operation, and this increase is more marked at partial load. Similar to what has been observed in the DLR cases, the calculated trend for UHC appears to be correct, whilst the model is not able to predict the expected trend for the CO emissions at partial load. One of the main advantages of diluted combustion is the possibility to reduce the NOx emissions significantly with respect to air-fired operation, and this is due to a reduction in the production of thermal NO. The calculated trends for NOx emissions confirm this observation, and are in line with the experimental observations.

Finally, although the resulting numerical grid appears not to be refined enough in order to satisfy the mesh criterion of Equation (2.79) in some critical regions, a LES investigation of the baseline 80 kW case from the PACT dataset has been performed in addition to the steady-state RANS calculations. Following the findings of the study carried out in Chapter 5, the Sigma model has been employed for the SGS stresses in order to reduce the result sensitivity to the size of the numerical grid, especially given the coarse mesh size employed in some regions within the domain. Consistently with the findings reported in Chapter 5, the resulting time-averaged flow field showed the same main features observed in the steady-state RANS calculations, but some significant quantitative differences are present. The LES calculation has also been employed to obtain some insights on the unsteady behaviour of the combustor. In particular, no evidence of flow instabilities has been observed in the LES results in the considered case.

7.2 Future work

Although the CFD model employed in the present work provided satisfactory results in the prediction of both air-fired and diluted operation of an industrial MGT combustor, some possible sources of inaccuracy have been identified. The first one is related to the dubious ability of the premixed flamelet library employed in the present work to represent the complex phenomena taking place in the device, as observed also in [198]. A possible solution to this problem would be the creation of two flamelet libraries, one based on premixed flamelets as the one used in the present work, and the second one employing non-premixed flamelets. The most relevant representation for the local combustion thermo-chemistry between the two libraries can be identified by employing a flame index that allows for the identification of the local combustion regime, as suggested by [261] and [262].

The second source of inaccuracy is related to the use of a steady-state RANS approach for turbulence modelling. As suggested by the study carried out in Chapter 5, LES can improve the accuracy of the numerical results significantly, especially when used with sufficiently refined numerical grids and advanced SGS closures such as the Sigma model. Also, LES can provide additional information on the unsteady behaviour of the device that cannot be obtained with a steady-state RANS approach, as showed by the numerical investigation of flow instabilities performed in Chapters 5 and 6. In this respect, the main bottleneck associated with the application of LES to industrial combustors is clearly related to its elevated computational cost. In the future, it would be advisable to employ a more refined grid with respect to the one used in present study for the LES modelling of the Turbec T-100 combustor.

The lack of in-flame detailed measurements in the PACT facility cases can also represent an issue when it comes to detailed validation of the numerical results. Although this is a common problem when dealing with industrial devices, it would be advantageous to have some experimental insight on the flame behaviour and of the flow-field under diluted combustion, perhaps considering the use of a combustion chamber with optical access similar to the one described in [235], in future experimental tests.

It would also be interesting to investigate higher levels of CO_2 and H_2O di-

lution levels, in order to assess the experimental operational limits of the MGT system and of its combustion chamber under diluted conditions. CFD analyses could also be used to suggest modifications in the design of the combustion chamber in order to optimise its diluted operation. The numerical investigation of higher dilution levels would probably need to include radiative heat transfer in the system, which has been neglected in the CFD analyses carried out in this thesis on the grounds of the observations made in Section 4.3. In fact, with a higher concentration of participating species such as CO_2 and H_2O, the relative importance of radiation with respect to the chemical heat release can be expected to be more significant. The use of narrow-band models, such as the SNB-CK, in complex CFD calculations is ruled out by the computational burden associated with these models. On the other hand, simplified models, such as the WSGG, are not suitable for applications where the oxidizer composition differs significantly from that of air. A good compromise would probably be represented by a full spectrum model, such as the FSCK which, as reported in Section 2.3, has been observed to perform significantly better than the standard WSGG model approach in conditions departing from conventional air-firing at a reasonable computational cost.

Bibliography

[1] British Petroleum. *BP Energy Outlook: 2016 edition*. BP plc, 2016.

[2] IPCC. *Climate change 2013 - The physical science basis*. Cambridge University Press, 2013.

[3] IEA. *Energy and Climate Change*. IEA Publications, 2015.

[4] COP-21 Paris Agreement. `https://unfccc.int/resource/docs/2015/cop21/eng/l09r01.pdf`, 2015.

[5] IEA. *World energy outlook 2013*. IEA Publications, 2013.

[6] IEA. *Technology roadmap: Carbon Capture and Storage*. IEA Publications, 2013.

[7] H.I.H. Saravanamuttoo. *Gas Turbine Theory*. Pearson Prentice Hall, 2009.

[8] M. P. Boyce. *Gas turbine engineering handbook (4th edition)*. Elsevier, 2012.

[9] IEA. *Energy technology perspectives*. IEA Publications, 2012.

[10] IEA/UNIDO. *Tehcnology roadmap: Carbon Capture and Storage in industrial applications*. IEA Publications, 2013.

[11] Global CCS Institute. *The global status of CCS*. Global Carbon Capture and Storage Institute Ltd., 2015.

[12] P. Jansohn, T. Griffin, I. Mantzaras, F. Marechal, and F. Clemens. Technologies for gas turbine power generation with CO2 mitigation. *Energy Procedia*, 4:1901–1908, 2011.

[13] A. M. ElKady, A. Evulet, A. Brand, T. P. Ursin, and A. Lynghjem. Application of exhaust gas recirculation in a DLN F-Class combustion system for postcombustion carbon capture. *Journal of Engineering for Gas Turbines and Power*, 131:51–55, 2009.

[14] Y. Tanaka, M. Nose, M. Nakao, K. Saitoh, E. Ito, and K. Tsukagoshi. Development of low NOx combustion system with EGR for 1700 C-Class gas turbine. *Mitsubishi Heavy Industries Technical Reviews*, 50(1):1–6, 2013.

[15] H. Li, G. Haugen, M. Ditaranto, Da. Berstad, and K. Jordal. Impacts of exhaust gas recirculation (EGR) on the natural gas combined cycle integrated with chemical absorption CO2 capture technology. *Energy Procedia*, 4:1411–1418, 2011.

[16] T. Heppenstall. Advanced gas turbine cycles for power generation: a critical review. *Applied Thermal Engineering*, 18(910):837 – 846, 1998.

[17] H. Haselbacher. Performance of water/steam injected gas turbine power plants consisting of standard gas turbines and turbo expanders. *International Journal of Energy Technology and Policy*, 3:12–23, 2005.

[18] W. De Paepe, F. Delattin, S. Bram, and J. De Ruyck. Steam injection experiments in a microturbine a thermodynamic performance analysis. *Applied Energy*, 97:569 – 576, 2012.

[19] H. K. Versteeg and W. Malalasekera. *An Introduction to Computational Fluid Dynamics: The Finite Volume Method*. Pearson Education Limited, 2007.

[20] D. Veynante and L. Vervisch. Turbulent combustion modeling. *Progress in Energy and Combustion Science*, 28(3):193 – 266, 2002.

[21] A. H. Lefebvre and D. R. Ballal. *Gas turbine combustion - alternative fuels and emissions*. CRC Press, 2010.

[22] R. W. Bilger, S. B. Pope, K. N. C. Bray, and J. F. Driscoll. Paradigms in turbulent combustion research. *Proceedings of the Combustion Institute*, 30(1):21 – 42, 2005.

[23] I. Chterev, C. W. Foley, D. Foti, S. Kostka, A. W. Caswell, N. Jiang, A. Lynch, D. R. Noble, S. Menon, J. M. Seitzman, and T. C. Lieuwen. Flame and flow topologies in an annular swirling flow. *Combustion Science and Technology*, 186(8):1041–1074, 2014.

[24] M. D. Turrell, P. J. Stopford, K. J. Syed, and E. Buchanan. CFD simulation of the flow within and downstream of a high-swirl lean premixed gas turbine combustor. *ASME Turbo Expo: Power for Land, Sea and Air*, 1:31–38, 2004.

[25] H. Barths, N. Peters, N. Brehm, A. Mack, M. Pfitzner, and V. Smiljanovski. Simulation of pollutant formation in a gas-turbine combustor using unsteady flamelets. *Symposium (International) on Combustion*, 27(2):1841 – 1847, 1998.

[26] E. Riesmeier, S. Honnet, and N. Peters. Flamelet modeling of pollutant formation in a gas turbine combustion chamber using detailed chemistry for a kerosene model fuel. *Journal of Engineering for Gas Turbines and Power*, 126(4):899–905, 2004.

[27] M. C. Cameretti, R. Piazzesi, F. Reale, and R. Tuccillo. Combustion simulation of an Exhaust Gas Recirculation operated micro-gas turbine. *Journal of Engineering for Gas Turbines and Power*, 131(5):1–10, 2009.

[28] L. Y. M. Gicquel, G. Staffelbach, and T. Poinsot. Large Eddy Simulations of gaseous flames in gas turbine combustion chambers. *Progress in Energy and Combustion Science*, 38(6):782–817, 2012.

[29] H. Pitsch. Large-Eddy Simulation of turbulent combustion. *Annual Review of Fluid Mechanics*, 38(1):453–482, 2006.

[30] J. Janicka and A. Sadiki. Large eddy simulation of turbulent combustion systems. *Proceedings of the Combustion Institute*, 30(1):537–547, 2005.

[31] N. Peters. Combustion theory. CERFC Summer School - Princeton University, 2010.

[32] P. Sabia, M. Lubrano Lavadera, P. Giudicianni, G. Sorrentino, R. Ragucci, and M. de Joannon. CO2 and H2O effect on propane auto-ignition delay times under mild combustion operative conditions. *Combustion and Flame*, 162(3):533 – 543, 2015.

[33] A. N. Mazas, D. Lacoste, and T. Schuller. Experimental and numerical investigation on the laminar flame speed of CH4/O2 mixtures diluted with CO2 and H2O. *ASME Turbo Expo: Power for Land, Sea and Air*, 2:411–421, 2010.

[34] K. Andersson and Filip J. Flame and radiation characteristics of gas-fired O2/CO2 combustion. *Fuel*, 86(56):656 – 668, 2007.

[35] A. G. Clements, S. Black, J. Szuhnszki, K. Stechly, A. Pranzitelli, W. Nimmo, and M. Pourkashanian. LES and RANS of air and oxy-coal combustion in a pilot-scale facility: Predictions of radiative heat transfer. *Fuel*, 151:146 – 155, 2015.

[36] R. Marsh, J. Runyon, A. Giles, S. Morris, D. Pugh, A. Valera-Medina, and P. Bowen. Premixed methane oxycombustion in nitrogen and carbon dioxide atmospheres: measurement of operating limits, flame location and emissions. *Proceedings of the Combustion Institute*, 2016. In Press.

[37] S B Pope. *Turbulent flows*. Cambridge University Press, 2000.

[38] T. Poinsot and D. Veynante. *Theoretical and Numerical Combustion*. R. T. Edwards, Inc., 2005.

[39] N. Peters. *Turbulent Combustion*. Cambridge University Press, 2000.

[40] H. Pitsch. Unsteady flamelet modeling of differential diffusion in turbulent jet diffusion flames. *Combustion and Flame*, 123(3):358–374, 2000.

[41] H. Pitsch and H. Steiner. Large-eddy simulation of a turbulent piloted methane/air diffusion flame (Sandia flame D). *Physics of Fluids*, 12(10):2541–2554, 2000.

[42] P. Bradshaw. *An introduction to turbulence and its measurements*. Pergamon Press, Oxford, 1971.

[43] J. H. Ferziger and M. Perić. *Computational Methods for Fluid Dynamics*. Springer, 1999.

[44] K. Hanjalić. Turbulence and transport phenomena modelling and simulation, 2006.

[45] A. Lipatnikov. *Fundamentals of Premixed Turbulent Combustion*. Taylor & Francis, 2012.

[46] L. F. Richardson. *Weather Prediction by Numerical Process*. Cambridge University Press, 1922.

[47] M. van Dyke. *An album of fluid motion*. Parabolic Press, Stanford, 1982.

[48] A. Kolmogorov. The local structure of turbulence in incompressible viscous fluid for very large Reynolds' numbers. *Doklady Akademiia Nauk SSSR*, 30:301–305, 1941.

[49] O. Reynolds. On the dynamical theory of incompressible viscous fluids and the determination of the criterion. *Philosophical Transactions of the Royal Society of London A: Mathematical, Physical and Engineering Sciences*, 186:123–164, 1895.

[50] D. C. Wilcox. *Turbulence Modeling for CFD*. DCW Industries, 2004.

[51] H. Schlichting. *Boundary-layer theory*. McGraw-Hill, 1979.

[52] A. Leonard. Energy cascade in large-eddy simulations of turbulent fluid flows. In *Turbulent Diffusion in Environmental PollutionProceedings of a Symposium held at Charlottesville*, volume 18, Part A of *Advances in Geophysics*, pages 237 – 248. Elsevier, 1975.

[53] C. Meneveau and J. Katz. Scale-invariance and turbulence models for large-eddy simulation. *Annual Review of Fluid Mechanics*, 32:1–32, 2000.

[54] J. H. Ferziger. Large eddy numerical simulations of furbulent flows. *AIAA Journal*, 15(9):1261–1267, 1977.

[55] Y. Zhiyin. Large-eddy simulation: past, present and the future. *Chinese Journal of Aeronautics*, 28(1):11 – 24, 2015.

[56] C. K. Law. *Combustion physics*. Cambridge University Press, 2010.

[57] I. G. Shepherd, J. B. Moss, and K. N. C. Bray. Turbulent transport in a confined premixed flame. *Symposium (International) on Combustion*, 19(1):423 – 431, 1982.

[58] J. Boussinesq. *Théorie de L'Écoulement Tourbillonnant Et Tumultueux Des Liquides*. Gautier-Villars et fils, Paris.

[59] B. Baldwin and H. Lomax. Thin-layer approximation and algebraic model for separated turbulent flows. AIAA paper 78-257.

[60] P. R. Spalart and S. R. Allmaras. A one-equation turbulence model for aerodynamic flows. AIAA paper 92-0439.

[61] B. E. Launder and D. B. Spalding. *Mathematical Models of Turbulence*. Academic Press, 1972.

[62] B. E. Launder and D. B. Spalding. The numerical computation of turbulent flows. *Computer Methods in Applied Mechanics and Engineering*, 3(2):269 – 289, 1974.

[63] ANSYS, Inc. *ANSYS Fluent theory guide - Release 15.0*, 2015.

[64] D. C. Wilcox. Reassessment of the scale-determining equation for advanced turbulence models. *AIAA Journal*, 26(11):1299 – 1310, 1988.

[65] K. Hanjalić. Some resolved and unresolved issues in modelling nonequilibrium and unsteady turbulent flows. In W. Rodi and G. Bergeles, editors, *Engineering Turbulence Modelling and Experiments 3*, pages 3–18, 1996.

[66] K. Hanjalić. Advanced turbulence closure models: a view of current status and future prospects. *International Journal of Heat and Fluid Flow*, 15(3):178 – 203, 1994.

[67] T. Shih, W. W. Liou, A. Shabbir, Z. Yang, and J. Zhu. A new $k - \epsilon$ eddy viscosity model for high Reynolds number turbulent flows. *Computers and Fluids*, 24:227–238, 1995.

[68] V. Yakhot, S. A. Orszag, S. Thangam, T. B. Gatski, and C. G. Speziale. Development of turbulence models for shear flows by a double expansion technique. *Physics of Fluids A*, 4(7):1510–1520, 1992.

[69] F. R. Menter. Two-equation eddy-viscosity turbulence models for engineering applications. *AIAA Journal*, 32(8):1598 – 1605, 1994.

[70] R. B. Langtry and F. R. Menter. Correlation-based transition modeling for unstructured parallelized computational fluid dynamics codes. *AIAA Journal*, 47(12):2894 – 2906, 2009.

[71] P. A. Durbin. Near-wall turbulence closure modeling without damping functions. *Theoretical and Computational Fluid Dynamics*, 3(1):1–13, 1991.

[72] J. C. Rotta. Statisticne theorie nichthomegen turbulenz. *Zeitschrift fur Physik*, 129:547–572, 1951.

[73] K. Hanjalić. Second-moment turbulence closures for CFD: Needs and prospects. *International Journal of Computational Fluid Dynamics*, 12(1):67–97, 1999.

[74] P. Sagaut. *Large eddy simulation for incompressible flows*. Springer, 2002.

[75] U. Piomelli. Large-eddy simulation: achievements and challenges. *Progress in Aerospace Sciences*, 35(4):335 – 362, 1999.

[76] T. S. Lund. Turbulence modelling and simulation the use of explicit filters in large eddy simulation. *Computers and Mathematics with Applications*, 46(4):603 – 616, 2003.

[77] S. T. Bose, P. Moin, and D. You. Grid-independent large-eddy simulation using explicit filtering. *Physics of Fluids*, 22:1 – 11, 2010.

[78] F. M. Denaro. What does finite volume-based implicit filtering really resolve in large-eddy simulations? *Journal of Computational Physics*, 230(10):3849 – 3883, 2011.

[79] J. W. Deardorff. A numerical study of three-dimensional turbulent channel flow at large Reynolds numbers. *Journal of Fluid Mechanics*, 41(02):453–480, 1970.

[80] C. Speziale. Turbulence modelling for time-dependent RANS and VLES. *AIAA Journal*, 36(2):173 – 184, 1998.

[81] F. Mathey and J. P. Chollet. Subgrid-scale model of scalar mixing for large eddy simulations of turbulent flows. In *Direct and large eddy simulation*, volume II, pages 103–114. Kluwer Academic Publishers, 1997.

[82] C. G. Speziale. Galilean invariance of subgrid-scale stress models in the large-eddy simulation of turbulence. *Journal of Fluid Mechanics*, 156:55–62, 7 1985.

[83] M. Klein, C. Kasten, Y. Gao, and N. Chakraborty. A-priori direct numerical simulation assessment of sub-grid scale stress tensor closures for turbulent premixed combustion. *Computers and Fluids*, 122:1 – 11, 2015.

[84] C. Fureby, G. Tabor, H. Weller, and A. Gosman. A comparative study of subgrid scale models in homogeneous isotropic turbulence. *Physics of Fluids*, 9(5):1416–1429, 1997.

[85] J. Smagorinsky. General circulation experiments with the primitive equations. *Monthly Weather Review*, 91(3):99–164, 1963.

[86] M. Germano, U. Piomelli, P. Moin, and W. H. Cabot. A dynamic subgrid-scale eddy viscosity model. *Physics of Fluids A: Fluid Dynamics*, 3(1991):1760–1765, 1991.

[87] F. Nicoud, H. B. Toda, O. Cabrit, S. Bose, and J. Lee. Using singular values to build a subgrid-scale model for large eddy simulations. *Physics of Fluids*, 23(8), 2011.

[88] F. Nicoud and F. Ducros. Subgrid-scale stress modelling based on the square of the velocity gradient tensor. *Flow, Turbulence and Combustion*, 62(3):183–200, 1999.

[89] M. Rieth, F. Proch, O. T. Stein, M. W. A. Pettit, and A. M. Kempf. Comparison of the Sigma and Smagorinsky LES models for grid generated turbulence and a channel flow. *Computers and Fluids*, 99:172–181, 2014.

[90] A. Rittler, F. Proch, and A. M. Kempf. LES of the Sydney piloted spray flame series with the PFGM/ATF approach and different sub-filter models. *Combustion and Flame*, 162(4):1575–1598, 2015.

[91] F. Proch and A. Kempf. Modeling heat loss effects in the large eddy simulation of a model gas turbine combustor with premixed flamelet generated manifolds. *Proceedings of the Combustion Institute*, 35(3):3337–3345, 2014.

[92] D. K. Lilly. A Proposed Modification of the Germano-Subgrid-Scale Closure Method. *Physics of Fluids a-Fluid Dynamics*, 4(3):633–635, 1992.

[93] H. Baya Toda, K. Truffin, and F. Nicoud. Is the dynamic procedure appropriate for all Sgs models? In *V European Conference on Computational Fluid Dynamics*, 2010.

[94] I. B. Celik, Z. N. Cehreli, and I. Yavuz. Index of resolution quality for Large Eddy Simulations. *Journal of Fluids Engineering*, 127:949–958, 2005.

[95] S. B. Pope. Ten questions concerning the large-eddy simulation of turbulent flows. *New Journal of Physics*, 6:35, 2004.

[96] U. Piomelli, P. Moin, and J. H. Ferziger. Model consistency in large eddy simulation of turbulent channel flows. *Physics of Fluids*, 31(7):1884–1891, 1988.

[97] G. Boudier, L. Y. M. Gicquel, and T. J. Poinsot. Effects of mesh resolution on large eddy simulation of reacting flows in complex geometry combustors. *Combustion and Flame*, 155:196–214, 2008.

[98] M. Breuer, B. Kniazev, and M. Abel. Development of wall models for LES of separated flows using statistical evaluations. *Computers and Fluids*, 36(5):817 – 837, 2007.

[99] P. J. Mason and N. S. Callen. On the magnitude of the subgrid-scale eddy coefficient in large-eddy simulations of turbulent channel flow. *Journal of Fluid Mechanics*, 162:439–462, 1986.

[100] H. Werner and H. Wengle. Large-eddy simulation of turbulent flow over and around a cube in a plate channel. In *Eighth Symposium on Turbulent Shear Flows*, pages 155–168, 1991.

[101] U. Piomelli and E. Balaras. Wall-layer models for large-eddy simulations. *Annual Review of Fluid Mechanics*, 34(1):349–374, 2002.

[102] U. Piomelli. Wall-layer models for large-eddy simulations. *Progress in Aerospace Sciences*, 44(6):437 – 446, 2008. Large Eddy Simulation - Current Capabilities and Areas of Needed Research.

[103] G. R. Tabor and M. H. Baba-Ahmadi. Inlet conditions for large eddy simulation: A review. *Computers and Fluids*, 39(4):553–567, 2010.

[104] A. M. Kempf. LES validation from experiments. *Flow, Turbulence and Combustion*, 80(3):351–373, 2008.

[105] F. Mathey, D. Cokljat, J. P. Bertoglio, and E. Sergent. Assessment of the vortex method for Large Eddy Simulation inlet conditions. *Progress in Computational Fluid Dynamics*, 6(1-3):58–67, 2006.

[106] A. Kempf, M. Klein, and J. Janicka. Efficient generation of initial- and inflow-conditions for transient turbulent flows in arbitrary geometries. *Flow, Turbulence and Combustion*, 74(1):67–84, 2005.

[107] I. Glassman and R. A. Yetter. *Combustion - 2nd Edition*. Elsevier, 2008.

[108] K. K. Kuo. *Principles of combustion*. Wiley, 1986.

[109] P. Clavin. Premixed combustion and gasdynamics. *Annual Review of Fluid Mechanics*, 26(1):321–352, 1994.

[110] Y. B. Zel'dovich and D. A. Frank-Kamenetskii. A theory of thermal flame propagation. *Zhurnal Fizicheskoi Khimii*, 12(1):100 – 105, 1938.

[111] L. P. H. de Goey, J. A. van Oijen, V. N. Kornilov, and J .H. M. ten Thije Boonkkamp. Propagation, dynamics and control of laminar premixed flames. *Proceedings of the Combustion Institute*, 33(1):863 – 886, 2011.

[112] K. N. C. Bray, P. Domingo, and L. Vervisch. Role of the progress variable in models for partially premixed turbulent combustion. *Combustion and Flame*, 141(4):431 – 437, 2005.

[113] R. W. Bilger. The structure of diffusion flames. *Combustion Science and Technology*, 13(1-6):155–170, 1976.

[114] S. P. Burke and T. E. W. Schumann. Diffusion flames. *First Symposium (International) on Combustion*, pages 2 – 11, 1928.

[115] A. Linan. The asymptotic structure of counterflow diffusion flames for large activation energies. *Acta Astronautica*, 1:1007 – 1039, 1973.

[116] H. Pitsch and N. Peters. A consistent flamelet formulation for non-premixed combustion considering differential diffusion effects. *Combustion and Flame*, 114(12):26 – 40, 1998.

[117] N. Peters. Laminar flamelet concepts in turbulent combustion. *Symposium (International) on Combustion*, 21(1):1231 – 1250, 1988.

[118] N. Peters. Laminar diffusion flamelet models in non-premixed turbulent combustion. *Progress in Energy and Combustion Science*, 10(3):319 – 339, 1984.

[119] R. Borghi. On the structure and morphology of turbulent premixed flames. In C. Casci and C. Bruno, editors, *Recent Advances in the Aerospace Sciences.*, pages 117–138. Springer, 1985.

[120] K. N. C. Bray. Turbulent flows with premixed reactants. In P. A. Libby and F. A. Williams, editors, *Turbulent Reacting Flows*. Springer Berlin Heidelberg, 1980.

[121] N. Peters. The turbulent burning velocity for large-scale and small-scale turbulence. *Journal of Fluid Mechanics*, 384:107–132, 1999.

[122] N. Peters and J. Göttgens. Scaling of buoyant turbulent jet diffusion flames. *Combustion and Flame*, 85(1):206 – 214, 1991.

[123] K. N. C. Bray and N. Peters. Laminar flamelets in turbulent flames. In P. A. Libby and F. A. Williams, editors, *Turbulent Reacting Flows*, pages 63 – 113. London Academic Press, 1994.

[124] R. Borghi. Turbulent combustion modelling. *Progress in Energy and Combustion Science*, 14(4):245 – 292, 1988.

[125] B. Cuenot and T. Poinsot. Effects of curvature and unsteadiness in diffusion flames. Implications for turbulent diffusion combustion. *Symposium (International) on Combustion*, 25(1):1383 – 1390, 1994.

[126] W. M. Pitts. Assessment of theories for the behavior and blowout of lifted turbulent jet diffusion flames. *Symposium (International) on Combustion*, 22(1):809 – 816, 1989.

[127] R. Cabra, J. Y. Chen, R. W. Dibble, A. N. Karpetis, and R. S. Barlow. Lifted methaneair jet flames in a vitiated coflow. *Combustion and Flame*, 143(4):491 – 506, 2005.

[128] P. Domingo, L. Vervisch, and D. Veynante. Large-eddy simulation of a lifted methane jet flame in a vitiated coflow. *Combustion and Flame*, 152(3):415 – 432, 2008.

[129] L. Vervisch. Using numerics to help the understanding of non-premixed turbulent flames. *Proceedings of the Combustion Institute*, 28(1):11 – 24, 2000.

[130] H. Phillips. Flame in a buoyant methane layer. *Symposium (International) on Combustion*, 10(1):1277 – 1283, 1965.

[131] L. J. Hartley and J. W. Dold. Flame propagation in a nonuniform mixture: analysis of a propagating triple-flame. *Combustion Science and Technology*, 80(1-3):23–46, 1991.

[132] A. Bourlioux, B. Cuenot, and T. Poinsot. Asymptotic and numerical study of the stabilization of diffusion flames by hot gas. *Combustion and Flame*, 120(12):143 – 159, 2000.

[133] T. Plessing, P. Terhoeven, N. Peters, and M. S. Mansour. An experimental and numerical study of a laminar triple flame. *Combustion and Flame*, 115(3):335 – 353, 1998.

[134] D. B. Spalding. Combustion mixing and chemical reaction in steady confined turbulent flames. *Symposium (International) on Combustion*, 13(1):649 – 657, 1971.

[135] D. B. Spalding. Development of the eddy-break-up model of turbulent combustion. *Symposium (International) on Combustion*, 16(1):1657 – 1663, 1977.

[136] R. Saïd and R. Borghi. A simulation with a cellular automaton for turbulent combustion modelling. *Symposium (International) on Combustion*, 22(1):569 – 577, 1989.

[137] B. F. Magnussen and B. H. Hjertager. On mathematical modeling of turbulent combustion with special emphasis on soot formation and combustion. *Symposium (International) on Combustion*, 16(1):719 – 729, 1977.

[138] B. F. Magnussen. On the structure of turbulence and a generalized eddy dissipation concept for chemical reaction in turbulent flow. In *19th AIAA Aerospace Sciences Meeting*, 1981.

[139] I. R. Gran and B. F. Magnusses. A numerical study of a bluff-body stabilized diffusion flame. part 2. influence of combustion modeling and finite-rate chemistry. *Combustion Science and Technology*, 119(1-6):191–217, 1996.

[140] A. De, E. Oldenhof, P. Sathiah, and D. Roekaerts. Numerical simulation of Delft jet in hot coflow flames using the Eddy Dissipation Concept model for turbulence-chemistry interaction. *Flow, Turbulence and Combustion*, 87(4):537–567, 2011.

[141] A. R. Kerstein, W. T. Ashurst, and F. A. Williams. Field equation for interface propagation in an unsteady homogeneous flow field. *Phys. Rev. A*, 37:2728–2731, 1988.

[142] F. C. Gouldin. Combustion intensity and burning rate integral of premixed flames. *Symposium (International) on Combustion*, 26(1):381–388, 1996.

[143] V. Zimont, W. Polifke, M. Bettelini, and W. Weisenstein. An efficient computational model for premixed turbulent combustion at high Reynolds numbers based on a turbulent flame speed closure. *Journal of Engineering for Gas Turbines and Power*, 120:526–532, 1998.

[144] K. N. C. Bray and J. B. Moss. A unified statistical model of the premixed turbulent flame. *Acta Astronautica*, 4(3):291 – 319, 1977.

[145] K. N. C. Bray, P. A. Libby, and J. B. Moss. Flamelet crossing frequencies and mean reaction rates in premixed turbulent combustion. *Combustion Science and Technology*, 41(3-4):143–172, 1984.

[146] K. N. C. Bray, M. Champion, and P. A. Libby. The interaction between turbulence and chemistry in premixed turbulent flames. In R. Borghi and S. N. B. Murthy, editors, *Turbulent Reactive Flows*, pages 541–563. Springer US, 1989.

[147] T. Mantel and R. Borghi. A new model of premixed wrinkled flame propagation based on a scalar dissipation equation. *Combustion and Flame*, 96(4):443 – 457, 1994.

[148] P. A. Libby and Bray K. N. C. Countergradient diffusion in prexmied turbulent flames. *AIAA Journal*, 19:205–213, 1981.

[149] K. N. C. Bray, P. A. Libby, G. Masuya, and J. B. Moss. Turbulence production in premixed turbulent flames. *Combustion Science and Technology*, 25(3-4):127–140, 1981.

[150] S. B. Pope. The evolution of surfaces in turbulence. *International Journal of Engineering Science*, 26:445–469, 1988.

[151] F. E. Marble and J. E. Broadwell. The coherent flame model for turbulent chemical reactions. Tech. Rep. TRW-9-PU, Project Squid., 1977.

[152] P. J. O'Rourke and F. V. Bracco. Two scaling transformations for the numerical computation of multidimensional unsteady laminar flames. *Journal of Computational Physics*, 33(2):185 – 203, 1979.

[153] T. D. Butler and P .J. O'Rourke. A numerical method for two dimensional unsteady reacting flows. *Symposium (International) on Combustion*, 16(1):1503 – 1515, 1977.

[154] N. Peters. The premixed turbulent flame in the limit of a large activation energy. *Journal of Non-Equilibrium Thermodynamics*, 7(1):25–38, 1982.

[155] T. Landenfeld, A. Sadiki, and J. Janicka. A turbulence-chemistry interaction model based on a multivariate presumed beta-PDF method for turbulent flames. *Flow, Turbulence and Combustion*, 68(2):111–135, 2002.

[156] K. N. C. Bray, M. Champion, P. A. Libby, and N. Swaminathan. Finite rate chemistry and presumed PDF models for premixed turbulent combustion. *Combustion and Flame*, 146(4):665 – 673, 2006.

[157] C. Huang and A. N. Lipatnikov. Comparison of presumed PDF models of turbulent flames. *Journal of Combustion*, 2012:1–15, 2012.

[158] S. B. Pope. Pdf methods for turbulent reactive flows. *Progress in Energy and Combustion Science*, 11(2):119 – 192, 1985.

[159] C. Dopazo. Recent developments in PDF methods. In P. A. Libby and F. A. Williams, editors, *Turbulent Reactive Flows*, pages 375–474. Academic Press, 1994.

[160] D. C. Haworth. Progress in probability density function methods for turbulent reacting flows. *Progress in Energy and Combustion Science*, 36(2):168 – 259, 2010.

[161] F. A. Williams. *Combustion Theory - 2nd edition*. Benjamin Cummings, 1985.

[162] S. K. Liew, K. N. C. Bray, and J. B. Moss. A stretched laminar flamelet model of turbulent nonpremixed combustion. *Combustion and Flame*, 56(2):199 – 213, 1984.

[163] J. S. Kim and F. A. Williams. Extinction of diffusion flames with nonunity lewis numbers. *Journal of Engineering Mathematics*, 31(2):101–118, 1997.

[164] D. C. Haworth, M. C. Drake, S. B. Pope, and R .J. Blint. The importance of time-dependent flame structures in stretched laminar flamelet models for turbulent jet diffusion flames. *Symposium (International) on Combustion*, 22(1):589 – 597, 1989.

[165] H. Pitsch, M. Chen, and N. Peters. Unsteady flamelet modeling of turbulent hydrogen-air diffusion flames. *Symposium (International) on Combustion*, 27(1):1057 – 1064, 1998.

[166] A. Yu. Klimenko. Multicomponent diffusion of various admixtures in turbulent flow. *Fluid Dynamics*, 25(3):327–334, 1990.

[167] R. W. Bilger. Conditional moment closure for turbulent reacting flow. *Physics of Fluids A*, 5(2):436–444, 1993.

[168] A. Y. Klimenko and R. W. Bilger. Conditional moment closure for turbulent combustion. *Progress in Energy and Combustion Science*, 25(6):595 – 687, 1999.

[169] F. Gao and E. E. OBrien. A large eddy simulation scheme for turbulent reacting flows. *Physics of Fluids A*, 5(6):1282–1284, 1993.

[170] A. W. Cook and J. J. Riley. A subgrid model for equilibrium chemistry in turbulent flows. *Physics of Fluids*, 6(8):2868–2870, 1994.

[171] N. Branley and W. P. Jones. Large eddy simulation of a turbulent non-premixed flame. *Combustion and Flame*, 127(12):1914 – 1934, 2001.

[172] A. Cavaliere and M. de Joannon. Mild combustion. *Progress in Energy and Combustion Science*, 30(4):329 – 366, 2004.

[173] C. Y. Liu, G. Chen, N. Sipöcz, M. Assadi, and X. S. Bai. Characteristics of oxy-fuel combustion in gas turbines. *Applied Energy*, 89(1):387 – 394, 2012.

[174] S. Richter, J. Ermel, T. Kick, M. Braun-Unkhoff, C. Naumann, and U. Riedel. The influence of diluent gases on combustion properties of natural gas: A combined experimental and modeling study. *Journal of Engineering for Gas Turbines and Power*, 138:1 – 9, 2016.

[175] J. Kestin, J. V. Sengers, B. Kamgar Parsi, and J. M. H. Levelt Sengers. Thermophysical properties of fluid H2O. *Journal of Physical and Chemical Reference Data*, 13(1):175–183, 1984.

[176] Y. Xie, J. Wang, M. Zhang, J. Gong, W. Jin, and Z. Huang. Experimental and numerical study on laminar flame characteristics of methane oxy-fuel mixtures highly diluted with CO2. *Energy & Fuels*, 27(10):6231–6237, 2013.

[177] F. Liu, H. Guo, G. J. Smallwood, and Ö. L. Gülder. The chemical effects of carbon dioxide as an additive in an ethylene diffusion flame: implications for soot and NOx formation. *Combustion and Flame*, 125(12):778 – 787, 2001.

[178] F. Halter, F. Foucher, L. Landry, and C. Mounaïm-Rousselle. Effect of dilution by nitrogen and/or carbon dioxide on methane and iso-octane air flames. *Combustion Science and Technology*, 181(6):813–827, 2009.

[179] Gas Research Intitute. Gri mechanism version 3.0. `http://www.me.berkeley.edu/gri-mech/`, 2000.

[180] C. K. Westbrook and F. L. Dryer. Chemical kinetic modeling of hydrocarbon combustion. *Progress in Energy and Combustion Science*, 10(1):1 – 57, 1984.

[181] L. Qiao, Y. Gan, T. Nishiie, W.J.A. Dahm, and E.S. Oran. Extinction of premixed methane/air flames in microgravity by diluents: Effects of radiation and lewis number. *Combustion and Flame*, 157(8):1446 – 1455, 2010.

[182] N. Hinton and R. Stone. Laminar burning velocity measurements of methane and carbon dioxide mixtures (biogas) over wide ranging temperatures and pressures. *Fuel*, 116:743 – 750, 2014.

[183] S. de Persis, F. Foucher, L. Pillier, V. Osorio, and I. Gökalp. Effects of O2 enrichment and CO2 dilution on laminar methane flames. *Energy*, 55:1055 – 1066, 2013.

[184] J. Runyon, R. Marsh, A. Valera-Medina, A. Giles, S. Morris, D. Pugh, Y. Sevcenko, and P. Bowen. Methane-oxygen flame stability in a generic premixed gas turbine swirl combustor at varying thermal power and pressure. *Proceedings of ASME Turbo Expo*, 4B, 2015.

[185] O. Gicquel, N. Darabiha, and D. Thvenin. Laminar premixed hydrogen-air counterflow flame simulations using flame prolongation of ILDM with differential diffusion. *Proceedings of the Combustion Institute*, 28(2):1901 – 1908, 2000.

[186] J. A. van Oijen and L. P. H. De Goey. Modelling of premixed laminar flames using Flamelet Generated Manifolds. *Combustion Science and Technology*, 161(1):113–137, 2000.

[187] B. Naud, R. Novella, J. M. Pastor, and J. F. Winklinger. RANS modelling of a lifted H2/N2 flame using an unsteady flamelet progress variable approach with presumed PDF. *Combustion and Flame*, 162(4):893 – 906, 2015.

[188] C. Olbricht, F. Hahn, A. Ketelheun, and J. Janicka. Strategies for presumed PDF modeling for LES with premixed flamelet-generated manifolds. *Journal of Turbulence*, 11(38):1–18, 2010.

[189] C. Olbricht, A. Ketelheun, F. Hahn, and J. Janicka. Assessing the predictive capabilities of combustion LES as applied to the Sydney flame series. *Flow, Turbulence and Combustion*, 85(3):513–547, 2010.

[190] C. F. Lietz. *Large eddy simulation of gas turbine combustors using flamelet manifolds method*. PhD thesis, University of Texas, Austin, 2015.

[191] S. Rida, S. Chakravorty, J. Basani, S. Orsino, and N. Ansari. An assessment of flamelet generated manifold combustion model for predicting combustor performance. *ASME Turbo Expo: Turbine Technical Conference and Exposition*, 4A:30–37, 2015.

[192] C. D. Pierce and P. Moin. Progress-variable approach for large-eddy simulation of non-premixed turbulent combustion. *Journal of Fluid Mechanics*, 504:73–97, 4 2004.

[193] P. D. Nguyen, Luc Vervisch, Vallinayagam Subramanian, and Pascale Domingo. Multidimensional flamelet-generated manifolds for partially premixed combustion. *Combustion and Flame*, 157(1):43 – 61, 2010.

[194] W. J. S. Ramaekers, J. A. van Oijen, and L. P. H. de Goey. A priori testing of flamelet generated manifolds for turbulent partially premixed methane/air flames. *Flow, Turbulence and Combustion*, 84(3):439–458, 2010.

[195] A. Ketelheun, C. Olbricht, F. Hahn, and J. Janicka. Premixed generated manifolds for the computation of technical combustion systems. *ASME Turbo Expo: Power for Land, Sea and Air*, 2:695–705, 2009.

[196] B. Fiorina, O. Gicquel, L. Vervisch, S. Carpentier, and N. Darabiha. Approximating the chemical structure of partially premixed and diffusion counterflow flames using FPI flamelet tabulation. *Combustion and Flame*, 140(3):147 – 160, 2005.

[197] A. W. Vreman, B. A. Albrecht, J. A. van Oijen, L. P. H. de Goey, and R. J. M. Bastiaans. Premixed and nonpremixed generated manifolds in large-eddy simulation of Sandia flame D and F. *Combustion and Flame*, 153(3):394 – 416, 2008.

[198] G. Goldin, Z. Ren, H. Forkel, L. Lu, V. Tangirala, and H. Karim. Modeling CO with Flamelet Generated Manifolds. Part 1: flamelet configuration. *Proceedings of the ASME Turbo Expo*, 2:1141–1151, 2012.

[199] C. M. Müller, H. Breitbach, and N. Peters. Partially premixed turbulent flame propagation in jet flames. *Symposium (International) on Combustion*, 25(1):1099 – 1106, 1994.

[200] J. A. van Oijen and L. P. H. de Goey. Predicting NO formation with Flamelet Generated Manifolds. In *Proceedings of the 4th European Combustion Meeting*, pages 1–5, 2009.

[201] A. Boucher, N. Bertier, and F. Dupoirieux. A method to extend flamelet manifolds for prediction of NOx and long time scale species with tabulated chemistry. *International Journal of Sustainable Aviation*, 1(2):181–202, 2014.

[202] A. Ketelheun, C. Olbricht, F. Hahn, and J. Janicka. NO prediction in turbulent flames using LES/FGM with additional transport equations. *Proceedings of the Combustion Institute*, 33(2):2975 – 2982, 2011.

[203] M. A. Rajhi, R. Ben-Mansour, M. A. Habib, M. A. Nemitallah, and K. Andersson. Evaluation of gas radiation models in CFD modeling of oxy-combustion. *Energy Conversion and Management*, 81:83 – 97, 2014.

[204] M. Di Domenico, P. Gerlinger, and M. Aigner. Development and validation of a new soot formation model for gas turbine combustor simulations. *Combustion and Flame*, 157(2):246 – 258, 2010.

[205] J. H. Lienhard. *A heat transfer textbook*. Prentice Hall PTR, 1981.

[206] M. F. Modest. *Radiative Heat Transfer Second Edition*. Academic Press, 2003.

[207] W. L. Grosshandler. Radiative heat transfer in nonhomogeneous gases: A simplified approach. *International Journal of Heat and Mass Transfer*, 23(11):1447 – 1459, 1980.

[208] R. Viskanta and M.P. Mengüc. Radiation heat transfer in combustion systems. *Progress in Energy and Combustion Science*, 13(2):97 – 160, 1987.

[209] V. Kez, F. Liu, J. L. Consalvi, J. Ströhle, and B. Epple. A comprehensive evaluation of different radiation models in a gas turbine combustor under conditions of oxy-fuel combustion with dry recycle. *Journal of Quantitative Spectroscopy and Radiative Transfer*, 172:121 – 133, 2016.

[210] W. A. Fiveland. Discrete ordinates solutions of the radiative transport equation for rectangular enclosures. *Journal of Heat Transfer*, 106(4):699–706, 1984.

[211] F. C. Lockwood and N. G. Shah. A new radiation solution method for incorporation in general combustion prediction procedures. *Symposium (International) on Combustion*, 18(1):1405 – 1414, 1981.

[212] M. F. Modest. Further development of the elliptic PDE formulation of the P_N approximation and its Marshak boundary conditions. *Numerical Heat Transfer, Part B: Fundamentals*, 62(2-3):181–202, 2012.

[213] J. Taine. A line-by-line calculation of low-resolution radiative properties of CO2-CO-transparent nonisothermal gases mixtures up to 3000 k. *Journal of Quantitative Spectroscopy and Radiative Transfer*, 30(4):371 – 379, 1983.

[214] W. Malkmus. Random Lorentz band model with exponential-tailed S^{-1} line-intensity distribution function. *Journal of the Optical Society of America*, 57(3):323–329, 1967.

[215] A. G. Clements, R. Porter, A. Pranzitelli, and M. Pourkashanian. Evaluation of FSK models for radiative heat transfer under oxyfuel conditions. *Journal of Quantitative Spectroscopy and Radiative Transfer*, 151:67 – 75, 2015.

[216] M. F. Modest. Narrow-band and full-spectrum k-distributions for radiative heat transfercorrelated-k vs. scaling approximation. *Journal of Quantitative Spectroscopy and Radiative Transfer*, 76(1):69 – 83, 2003.

[217] A. A. Lacis and V. Oinas. A description of the correlated k distribution method for modeling nongray gaseous absorption, thermal emission, and

multiple scattering in vertically inhomogeneous atmospheres. *Journal of Geophysical Research: Atmospheres*, 96:9027–9063, 1991.

[218] D. G. Goodwin, H. K. Moffat, and R. L. Speth. Cantera: An object-oriented software toolkit for chemical kinetics, thermodynamics, and transport processes. `http://www.cantera.org`, 2016. Version 2.2.1.

[219] P. Rivire and A. Soufiani. Updated band model parameters for H2O, CO2, CH4 and CO radiation at high temperature. *International Journal of Heat and Mass Transfer*, 55(1314):3349 – 3358, 2012.

[220] M. F. Modest. The weighted-sum-of-gray-gases model for arbitrary solution methods in radiative transfer. *Journal of Heat Transfer*, 113(3):650 – 656, 1991.

[221] T. F. Smith, Z. F. Shen, and J. N. Friedman. Evaluation of coefficients for the Weighted Sum of Gray Gases model. *Journal of Heat Transfer*, 104(4):602 – 608, 1982.

[222] R. Johansson, B. Leckner, K. Andersson, and F. Johnsson. Account for variations in the H2O to CO2 molar ratio when modelling gaseous radiative heat transfer with the weighted-sum-of-grey-gases model. *Combustion and Flame*, 158(5):893 – 901, 2011.

[223] T. Kangwanpongpan, F.H.R. Franca, R. C. da Silva, P. S. Schneider, and H. J. Krautz. New correlations for the weighted-sum-of-gray-gases model in oxy-fuel conditions based on HITEMP 2010 database. *International Journal of Heat and Mass Transfer*, 55:7419 – 7433, 2012.

[224] P. Nakod, G. Krishnamoorthy, M. Sami, and S. Orsino. A comparative evaluation of gray and non-gray radiation modeling strategies in oxy-coal combustion simulations. *Applied Thermal Engineering*, 54(2):422 – 432, 2013.

[225] R. Porter, F. Liu, M. Pourkashanian, A. Williams, and D. Smith. Evaluation of solution methods for radiative heat transfer in gaseous oxy-fuel

combustion environments. *Journal of Quantitative Spectroscopy and Radiative Transfer*, 111(14):2084 – 2094, 2010.

[226] P. J. Coelho. Numerical simulation of the interaction between turbulence and radiation in reactive flows. *Progress in Energy and Combustion Science*, 33(4):311 – 383, 2007.

[227] Y. M. Al-Abdeli and A. R. Masri. Review of laboratory swirl burners and experiments for model validation. *Experimental Thermal and Fluid Science*, 69:178–196, 2015.

[228] Y. Al-Abdeli and A. Masri. Stability characteristics and flowfields of turbulent non-premixed swirling flames. *Combustion Theory and Modelling*, 7(4):731–766, 2003.

[229] Y. M. Al-Abdeli and A. R. Masri. Recirculation and flowfield regimes of unconfined non-reacting swirling flows. *Experimental Thermal and Fluid Science*, 27(5):655–665, 2003.

[230] A. R. Masri, P. A. M. Kalt, Y. M. Al-Abdeli, and R. S. Barlow. Turbulencechemistry interactions in non-premixed swirling flames. *Combustion Theory and Modelling*, 11(5):653–673, 2007.

[231] Y. M. Al-Abdeli and A. R. Masri. Precession and recirculation in turbulent swirling isothermal jets. *Combustion Science and Technology*, 176(5-6):645–665, 2004.

[232] Y. M. Al-Abdeli, A. R. Masri, G. R. Marquez, and S. H. Starner. Time-varying behaviour of turbulent swirling nonpremixed flames. *Combustion and Flame*, 146(1-2):200–214, 2006.

[233] P. A. Pilavachi. Mini- and micro-gas turbines for combined heat and power. *Applied Thermal Engineering*, 22(18):2003 – 2014, 2002.

[234] Turbec SpA. T-100 micro turbine system technical description, 2004. Technical report D 14127-03.

[235] M. Hohloch, R. Sadanandan, A. Wiendhorn, W. Meier, and M. Aigner. OH* chemiluminescence and OH-PLIF measurements in a micro gas turbine combustor. *ASME Turbo Expo: Power for Land, Sea and Air*, 2:655–664, 2010.

[236] T. O. Monz, M. Stöhr, O'Loughlin W., J. Zanger, M. Hohloch, and M. Aigner. Experimental characterization of a swirl stabilized MGT combustor. *ASME Turbo Expo: Power for Land, Sea and Air*, 4:1–15, 2015.

[237] M. Zanger, T. Monz, and M. Aigner. Experimental investigation of the influence of combustor cooling on the characteristics of a FLOX-based micro gas turbine combustor. In *Progress in Gas Turbine Performance*, pages 165–184, 2013.

[238] T. Best, K. N. Finney, D. B. Ingham, and M. Pourkashanian. Impact of CO2-enriched combustion air on micro-gas turbine performance for carbon capture. *Energy*, 115, Part 1:1138 – 1147, 2016.

[239] U. Ali, T. Best, K. N. Finney, C. Font Palma, K. J. Hughes, D. B. Ingham, and M. Pourkashanian. Process simulation and thermodynamic analysis of a micro turbine with post-combustion CO2 capture and exhaust gas recirculation. *Energy Procedia*, 63:986 – 996, 2014.

[240] U. Ali, C. Font Palma, K. J. Hughes, D. B. Ingham, L. Ma, and M. Pourkashanian. Thermodynamic analysis and process system comparison of the exhaust gas recirculated, steam injected and humidified micro gas turbine. *ASME Turbo Expo: Power for Land, Sea and Air*, 3, 2015.

[241] M. Cadorin, M. Pinelli, A. Vaccari, R. Calabria, F. Chiariello, P. Massoli, and E. Bianchi. Analysis of a micro gas turbine fed by natural gas and synthesis gas: MGT test bench and combustor CFD analysis. *Journal of Engineering for Gas Turbines and Power*, 137, 2012.

[242] R. J. Kee, M. E. Coltrin, and P. Glarborg. *Chemical reactive flow: theory and practice*. John Wiley and Sons, Inc., 2003.

[243] R. C. Flagan and J. H Seinfeld. *Fundamentals of air pollution engineering.* Prentice Hall, Inc., 1988.

[244] Z. Chen, X. Qin, B. Xu, Y. Ju, and F. Liu. Studies of radiation absorption on flame speed and flammability limit of CO2 diluted methane flames at elevated pressures. *Proceedings of the Combustion Institute*, 31(2):2693 – 2700, 2007.

[245] J. Göttgens, F. Mauss, and N. Peters. Analytic approximations of burning velocities and flame thicknesses of lean hydrogen, methane, ethylene, ethane, acetylene, and propane flames. *Symposium (International) on Combustion*, 24(1):129 – 135, 1992.

[246] O. Lucca-Negro and T. O'Doherty. Vortex breakdown: a review. *Progress in Energy and Combustion Science*, 27(4):431 – 481, 2001.

[247] P. Ghose, J. Patra, A. Datta, and A. Mukhopadhyay. Prediction of soot and thermal radiation in a model gas turbine combustor burning kerosene fuel spray at different swirl levels. *Combustion Theory and Modelling*, 20(3):457–485, 2016.

[248] R. Prieler, M. Demuth, D. Spoljaric, and C. Hochenauer. Numerical investigation of the steady flamelet approach under different combustion environments. *Fuel*, 140:731 – 743, 2015.

[249] L .C. B .S. Reis, J. A. Carvalho, M. A. R. Nascimento, L. O. Rodrigues, F. L. G. Dias, and P. M. Sobrinho. Numerical modeling of flow through an industrial burner orifice. *Applied Thermal Engineering*, 67(12):201 – 213, 2014.

[250] Y. Yang and S. K. Kær. Large-eddy simulations of the non-reactive flow in the Sydney swirl burner. *International Journal of Heat and Fluid Flow*, 36:47–57, 2012.

[251] S. V. Patankar and D. B. Spalding. A calculation procedure for heat, mass and momentum transfer in three-dimensional parabolic flows. *International Journal of Heat and Mass Transfer*, 15(10):1787–1806, 1972.

[252] K. K. J. Ranga Dinesh and M. P. Kirkpatrick. Study of jet precession, recirculation and vortex breakdown in turbulent swirling jets using LES. *Computers and Fluids*, 38(6):1232 – 1242, 2009.

[253] A. R. Masri, P. A. M. Kalt, and R. S. Barlow. The compositional structure of swirl-stabilised turbulent nonpremixed flames. *Combustion and Flame*, 137(1-2):1–37, 2004.

[254] S. James, J. Zhu, and M. S. Anand. Large eddy simulations of turbulent flames using the filtered density function model. *Proceedings of the Combustion Institute*, 31 II:1737–1745, 2007.

[255] R. K. Hanson and S. Salimian. Survey of rate constants in H/N/O systems. In W.C. Gardiner, editor, *Combustion chemistry*. Springer, 1984.

[256] G. G. De Soete. Overall reaction rates of NO and N2 formation from fuel nitrogen. *Symposium (International) on Combustion*, 15(1):1093–1102, 1975.

[257] P. C. Malte and D. T. Pratt. Measurement of atomic oxygen and nitrogen oxides in jet-stirred combustion. *Symposium (International) on Combustion*, 15(1):1061–1070, 1975.

[258] C. T. Bowman. Chemistry of gaseous pollutant formation and destruction. In W. Bartok and A.F. Sarofim, editors, *Fossil fuel combustion*. J. Wiley and Sons, 1991.

[259] K. Kadoya, N. Matsunaga, and A. Nagashima. Viscosity and thermal conductivity of dry air in the gaseous phase. *Journal of Physical and Chemical Reference Data*, 14:947–970, 1985.

[260] M. Akram, S. Blakey, and M. Pourkashanian. Influence of gas turbine exhaust CO2 concentration on the performance of post combustion carbon capture plant. *Proceedings of the ASME Turbo Expo: turbine technical conference and exposition*, 3:1–9, 2015.

[261] H. Yamashita, M. Shimada, and T. Takeno. A numerical study on flame stability at the transition point of jet diffusion flames. *Symposium (International) on Combustion*, 26(1):27 – 34, 1996.

[262] E. Knudsen and H. Pitsch. A general flamelet transformation useful for distinguishing between premixed and non-premixed modes of combustion. *Combustion and Flame*, 156(3):678 – 696, 2009.